

Expanding the Functionality of Piezo-Particulate Composites

Khanbareh, Hamideh

DOI

[10.4233/uuid:aab2497d-6eec-4956-8c15-8f5fdedc94f3](https://doi.org/10.4233/uuid:aab2497d-6eec-4956-8c15-8f5fdedc94f3)

Publication date

2016

Document Version

Final published version

Citation (APA)

Khanbareh, H. (2016). *Expanding the Functionality of Piezo-Particulate Composites*. [Dissertation (TU Delft), Delft University of Technology]. <https://doi.org/10.4233/uuid:aab2497d-6eec-4956-8c15-8f5fdedc94f3>

Important note

To cite this publication, please use the final published version (if applicable).
Please check the document version above.

Copyright

Other than for strictly personal use, it is not permitted to download, forward or distribute the text or part of it, without the consent of the author(s) and/or copyright holder(s), unless the work is under an open content license such as Creative Commons.

Takedown policy

Please contact us and provide details if you believe this document breaches copyrights.
We will remove access to the work immediately and investigate your claim.

Expanding the Functionality of Piezo-Particulate Composites

Hamideh Khanbareh

Expanding the Functionality of Piezo-Particulate Composites

Proefschrift

ter verkrijging van de graad van doctor
aan de Technische Universiteit Delft,
op gezag van de Rector Magnificus prof. ir. K.C.A.M. Luyben,
voorzitter van het College voor Promoties,
in het openbaar te verdedigen op woensdag 8 juni 2016 om 15:00 uur
door

Hamideh KHANBAREH

Master of Science in Aerospace Engineering, Delft University of Technology, Delft,
the Netherlands

geboren te Teheran, Iran.

This dissertation has been approved by the promoters:

Prof. Dr. Ir. S. van der Zwaag

Prof. Dr. W.A. Groen

Composition of the doctoral committee:

Rector Magnificus

voorzitter

Prof. Dr. Ir. S. van der Zwaag

Technische Universiteit Delft, promotor

Prof. Dr. W.A. Groen

Technische Universiteit Delft, promotor

Independent members:

Prof. Dr. C.R. Bowen

University of Bath, UK

Prof. Dr. D.M. de Leeuw

Max Planck Institute for Polymer Research, Germany

Prof. Dr. J. Schmitz

Technische Universiteit Twente

Prof. Dr. B. Dam

Technische Universiteit Delft

Prof. Dr. Ir. J.R. van Ommen

Technische Universiteit Delft



This research was carried out under project number M62.3.11438 in the framework of the Research Program of Materials innovation institute (M2i) in the Netherlands (www.m2i.nl)

ISBN 978-94-91909-36-8

Copyright © 2016 by Hamideh Khanbareh

All rights reserved. No part of the material protected by this copyright notice may be reproduced or utilized in any form or by any means, electronic or mechanical, including photocopying, recording, or by any information storage and retrieval system, without prior written permission from the author.

Printed in the Netherlands.

Contents

1	Introduction	1
1.1	Introduction	1
1.2	Different functionalities of ferroelectric materials	2
1.2.1	Ferroelectricity	2
1.2.2	Pyroelectricity	3
1.2.3	Piezoelectricity	5
1.3	Piezoelectric electroceramic-polymer composites	6
1.3.1	Effect of topology on electroactive properties of electroceramic-polymer composites	7
1.3.2	Effect of intrinsic properties of the polymer matrix on electroactive properties of electroceramic-polymer composites	8
1.4	Scope of the thesis	11
2	Structure and properties of particulate PT-epoxy composites	15
2.1	Introduction	15
2.2	Experimental procedure	16
2.2.1	Composite manufacturing	16
2.3	Results	19
2.3.1	Microstructure of composites	19
2.3.2	Dielectric properties	19
2.3.3	Piezoelectric and pyroelectric properties	21
2.4	Discussion	25
2.5	Conclusions	33
3	Computational modeling of structure formation during dielectrophoresis in piezoparticle-polymer systems	35
3.1	Introduction	35
3.2	Dielectrophoresis modelling	36
3.2.1	Background	36

3.2.2	Mechanical modeling	37
3.2.3	Dielectrophoretic force	38
3.2.4	Viscous drag	38
3.2.5	Algorithmic aspects	38
3.3	Simulations	39
3.3.1	Performance parameters	39
3.3.2	Single particle orientation	41
3.3.3	Two particle interaction	42
3.3.4	Multi-particle interaction	43
3.4	Conclusions	47
4	Ferroelectric characteristics of particulate PZT-epoxy composites	51
4.1	Introduction	51
4.2	Theory	52
4.3	Experimental procedure	55
4.3.1	Composite manufacturing	55
4.3.2	Measurement procedure	55
4.4	Results and Discussion	56
4.5	Conclusions	61
5	In-situ structuring and poling of PZT-epoxy composites	63
5.1	Introduction	63
5.2	Experimental procedure	64
5.2.1	Composite manufacturing	64
5.2.2	Measurement procedure	65
5.3	Results and discussion	65
5.3.1	Microstructure of composites	65
5.3.2	Functional properties	66
5.4	Conclusions	70
6	Structure and properties of PT-polyethylene oxide composites, and accurate determination of their pyroelectric properties	71
6.1	Introduction	71
6.2	Experimental procedure	74
6.2.1	Composite manufacturing	74
6.2.2	Measurement procedure	75
6.3	Novel device for pyroelectric measurements	75
6.3.1	Basic concept	75
6.3.2	Temperature controller and noise analysis	75
6.4	Results and discussion	81
6.4.1	Microstructure of composites	81
6.4.2	Dielectric results	81
6.4.3	Piezoelectric analysis	82

6.4.4	Pyroelectric properties	84
6.4.5	Poling study	85
6.5	Conclusions	88
7	Enhancing the sensitivity of PZT-polyurethane composites by reducing the dielectric permittivity of the matrix	91
7.1	Introduction	91
7.2	Experimental procedure	92
7.2.1	Composite manufacturing	92
7.2.2	Measurement procedure	94
7.3	Results and discussion	95
7.3.1	Microstructure analysis	95
7.3.2	Properties of composites	101
7.4	Conclusions	107
8	High temperature PT-polyetherimide composites	109
8.1	Introduction	109
8.2	Experimental procedure	110
8.2.1	Composite manufacturing	110
8.2.2	Measurement procedure	112
8.3	Results and discussion	113
8.3.1	Microstructure analysis	113
8.3.2	Thermo-mechanical analysis	113
8.3.3	Dielectric, piezoelectric and pyroelectric analysis	113
8.4	Conclusions	118
	Summary	121
	Samenvatting	125
A	Effect of topological imperfections on the electromechanical properties of structured particulate composites	143
A.1	Introduction	143
A.2	Theory	144
A.2.1	Piezoelectric constitutive equations	144
A.2.2	Homogenization of 0-3 composites	146
A.2.3	Homogenization of 1-3 composites	148
A.2.4	Experimental determination of c_{VP}	150
A.3	Theoretical predictions using imperfection parameters	151
A.3.1	Single chain imperfections	151
A.3.2	Aggregated chain imperfections	155
A.4	Conclusions	161
	Acknowledgments	163

Curriculum Vitae	167
List of Publications	169

Introduction

1.1 Introduction

Multifunctional systems that can provide performance-tailored functionality as well as adaptability have emerged in recent years. Researchers are seeking to design materials that include autonomic structures that can sense, diagnose and respond to external stimuli without human intervention [1, 2]. Adaptive structures that allow readjustment of functionality, shape and mechanical properties on demand [3, 4], as well as self-sustaining systems with structurally integrated power harvest, storage and transmission capabilities are also under investigation [5–8].

Multifunctional materials, designed to improve the overall system performance, are typically composites of several distinct materials phases, in which each phase performs a different function. These materials can be designed to meet specific requirements through tailored properties. The properties in a system can be integrated on several dimensional scales with increasing inter-connectivity between phases as the scale decreases. Three different types of materials multifunctionality can be realized [1, 9] through addition, colocation and integration of the phases. The material selection process is done to satisfy the requirements of more than one function and the best candidate of multifunctional materials for performance-tailored structures is most likely to be realized by the integration type [9, 10].

An important group of materials, often studied for integration with others to create multifunctional materials, are stimulus responsive materials that react to a certain stimulus by altering some of their physical properties. Among these types of materials, piezoceramics have gained significant attention for a wide variety of applications in sensing and actuation, due to their strong actuation power, piezo sensitivity, as well as wide dynamic frequency [1]. However, piezoceramics also have deficiencies, such as brittleness and lack of formability. Recently, particulate piezoelectric ceramics have been combined with inert or piezoelectric polymers to form flexible functional composites [11, 12]. In such composites the overall functionalities of the material is controlled by the intrinsic properties of the constituent ceramic and polymer phases, their morphology as well as the pattern of connectivity. New

developments in polymer synthesis have led to a variety of advanced flexible composites with functionalities in multiple domains of piezo- and pyroelectric in a wide temperature range. Moreover the micro/macro architecture design and optimization, using a range of polymer processing techniques, has resulted in enhanced performance of the composites in piezoelectric sensing, as well as actuation fields.

The relationship between the piezoelectric, pyroelectric and ferroelectric materials is schematically shown in Fig. 1.1. A dielectric material is an electrical insulator that can be polarized under an electric field. A group of dielectrics that show a change of strain or stress due to an applied external electric field, or conversely to the change of the polarization due to a mechanical excitation are called piezoelectrics. Pyroelectrics are a group of piezoelectrics that show a change of polarization due to a change in temperature. Ferroelectric materials, as a subgroup of pyroelectrics, have both pyroelectric and piezoelectric properties. Therefore due to the presence of multiple properties in a ferroelectric system, multiple functionalities can be integrated by a proper design of these materials.

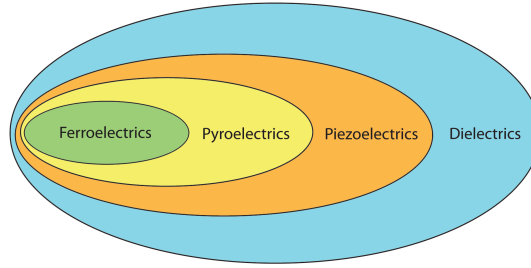


Figure 1.1: The relationship between the piezoelectric, pyroelectric and ferroelectric materials.

In this chapter the phenomena of ferro-, piezo- and pyroelectricity in relation to ferroelectric materials are briefly reviewed, in order to create a basic understanding of the behavior of electroceramic-polymer composites. This is followed by a review of the design rules for performance optimization of piezoelectric particulate composites used in this thesis, namely topology, processing and selection of the polymer phase.

1.2 Different functionalities of ferroelectric materials

1.2.1 Ferroelectricity

In ferroelectric materials the spontaneous electric polarization can be reversed by the application of an external electric field. These materials maintain a spontaneous electric polarization in the absence of an imposed applied field below a certain phase transition temperature, known as the Curie temperature (T_c). Ferroelectric crystals possess regions with uniform polarization called ferroelectric domains. Within a domain, all the electric dipoles are aligned in the same direction. There may be many domains in a crystal separated by interfaces called domain walls. The multiple ferroelectric domains of a single crystal can be combined to a unified domain by application of an appropriate electric field. A very

strong field can lead to the reversal of the polarization in the domain, known as domain switching [13, 14]. The polarization reversal can be observed by measuring the ferroelectric hysteresis as shown in Fig. 1.2. In ferroelectric materials a polarization (P) versus electric field (E) hysteresis loop exists, as shown in Fig. 1.2, that is characterized by quantities such as the saturation polarization (P_S), remnant polarization (P_R) and coercive field (E_C). The hexagons with gray and white regions schematically represent repartition of two polarization states in the material (e.g. in grains of a ceramic) at different fields.

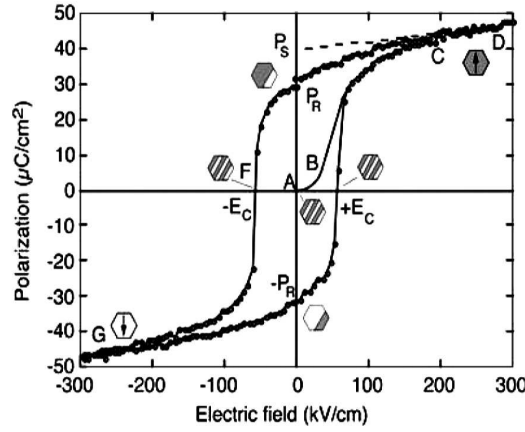


Figure 1.2: Ferroelectric (P-E) hysteresis loop measured on a (111)-oriented sol-gel PZT film [13].

1.2.2 Pyroelectricity

Pyroelectricity is the generation of an electrical charge due to a change in temperature [15]. The total pyroelectric coefficient, measured at constant stress, is the sum of primary pyroelectric coefficient and secondary pyroelectric effect due to piezoelectric contribution from thermal expansion. The primary pyroelectric constant of a material, $p_{primary}$, is defined as temperature dependence of the spontaneous polarization when the material is able to expand freely. A secondary contribution, $p_{secondary}$, can occur if the material is constrained, resulting in a piezoelectric contribution [15]. Both effects are illustrated in Fig. 1.3, in which pyroelectricity is visualized as one side of a triangle. Each corner represents energy states in the crystal: mechanical, electrical, and thermal energy. D , σ and S stand for electrical displacement, entropy and strain respectively. A small change in one of the variables produces a corresponding change in the other [16].

The primary pyroelectric effect, $p_{primary}$, is defined as the gradient of the polarization-temperature curve at a particular temperature:

$$p_{primary} = \frac{\Delta P}{\Delta T} \quad (1.1)$$

where P and T denote polarization and temperature respectively. For a small ΔT and at a temperature sufficiently below the Curie temperature, it can be regarded as a constant for a

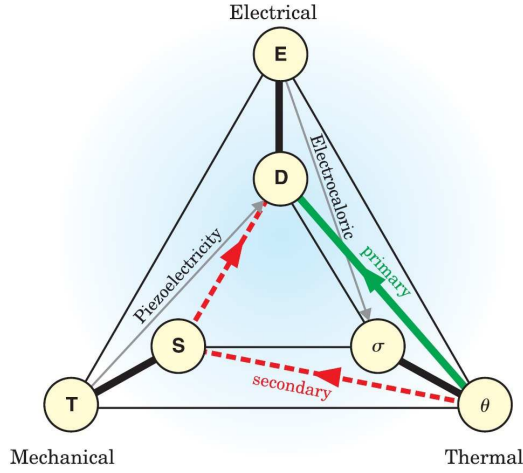


Figure 1.3: Primary and secondary pyroelectric contributions [15].

given material and temperature. Although the pyroelectric coefficient is a vector, since the measuring electrodes are generally placed along a principal crystallographic direction, the coefficient is often regarded as a scalar. The $p_{primary}$ is normally negative, since the spontaneous polarization of a pyroelectric decreases upon heating towards the Curie temperature, and it is dominant for ferroelectric materials. For ease of calculations the absolute value of $p_{primary}$ is presented throughout the thesis.

For a piezoelectric material under constant stress, a temperature change leads to a dimension change due to thermal expansion. This phenomenon results in an additional piezoelectrically induced charge. This coupled effect of thermal deformation and piezoelectricity is expressed by the secondary pyroelectric effect, $p_{secondary}$, and is defined as:

$$p_{secondary} = \left(\frac{\delta D}{\delta e} \right)_{E,T} \left(\frac{\delta e}{\delta T} \right)_{E,\sigma} = \left(\frac{\delta D}{\delta \sigma} \right)_{E,T} \left(\frac{\delta \sigma}{\delta e} \right)_{E,T} \left(\frac{\delta e}{\delta T} \right)_{E,\sigma} = d\alpha \quad (1.2)$$

where e , c , and α are the strain, elastic stiffness and thermal expansion coefficient of the material respectively [17, 18].

Pyroelectric materials develop an electric current upon experiencing a temperature change as shown in Fig. 1.4. A change in temperature of the sample leads to a change in the net dipole moment and spontaneous polarization, which results in a change in the quantity of surface charges. The free charges flow to compensate for the change, which leads to the pyroelectric current flow, i_p , in the circuit defined as [15, 19, 20]:

$$i_p = AP \frac{dT}{dt} \quad (1.3)$$

where A is the electroded area of the pyroelectric material, p is the component of the pyroelectric coefficient normal to the electrodes, and dT/dt is the rate of temperature change with time. This equation holds, provided that measurements are carried out under constant stress and electric field, so as to avoid piezoelectric, ferroelastic and ferroelectric contributions.

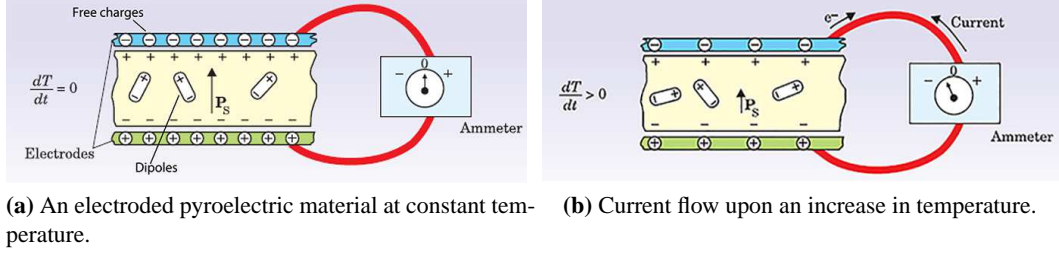


Figure 1.4: Development of pyroelectric current [15].

Pyroelectric materials have been used in wide range of applications such as infrared detectors, thermal imaging, radiometers and pollution monitoring [21]. To select a material for each application, several figures of merit (FOM) have been defined, that can be calculated from the thermal, electrical and optical properties of the materials. The most frequently used FOM is:

$$F = \frac{p}{\epsilon_r} \quad (1.4)$$

where ϵ_r and p are the dielectric constant and pyroelectric coefficient of the material measured at constant stress at the operating temperature of the device.

1.2.3 Piezoelectricity

The piezoelectric effect is related either to the change of strain or stress due to an applied external electric field, or conversely to the change of the polarization due to a mechanical excitation [22]. The piezoelectric properties of ferroelectric materials can be described by the linear matrix equations:

$$\begin{pmatrix} x \\ D \end{pmatrix} = \begin{pmatrix} S^E & d_t \\ d & \epsilon_e \epsilon^X \end{pmatrix} \begin{pmatrix} X \\ E \end{pmatrix} \quad (1.5)$$

The stress X and the electric field E are the independent variables, while the strain x and electric displacement D are the dependent variables; s , ϵ , and d are the elastic compliance, the dielectric and the piezoelectric constant respectively, while the superscripts of these variables denote the physical quantities held constant during determination. All variables are tensors and that the suffix t denotes a transposed tensor.

The piezoelectric constants are third rank tensors as they couple a second tensor to an external electric field vector E_k or dielectric displacement vector D_k . Due to the symmetry of the mechanical tensor variables ($X_{ij} = X_{ji}$) the strain tensor can be compacted into a first rank tensor. Therefore that the piezoelectric constants are converted into second rank tensors with the first index denoting the direction of the applied field specified from 1 to 3, while the second index denotes the strain direction, denoted 1 to 6. For instance, Eq. 1.5 can

then be rewritten in a complete form for ferroelectric ceramics with a perovskite structure of symmetry poled in the thickness or third dimension as:

$$\begin{pmatrix} S_1 \\ S_2 \\ S_3 \\ S_4 \\ S_5 \\ S_6 \\ D_1 \\ D_2 \\ D_3 \end{pmatrix} = \begin{pmatrix} s_{11}^E & s_{12}^E & s_{13}^E & s_{14}^E & s_{15}^E & s_{16}^E & d_{11} & d_{21} & d_{31} \\ s_{21}^E & s_{22}^E & s_{23}^E & s_{24}^E & s_{25}^E & s_{26}^E & d_{12} & d_{22} & d_{32} \\ s_{31}^E & s_{32}^E & s_{33}^E & s_{34}^E & s_{35}^E & s_{36}^E & d_{13} & d_{23} & d_{33} \\ s_{41}^E & s_{42}^E & s_{43}^E & s_{44}^E & s_{45}^E & s_{46}^E & d_{14} & d_{22} & d_{34} \\ s_{51}^E & s_{52}^E & s_{53}^E & s_{54}^E & s_{55}^E & s_{56}^E & d_{15} & d_{25} & d_{35} \\ s_{61}^E & s_{62}^E & s_{63}^E & s_{64}^E & s_{65}^E & s_{66}^E & d_{16} & d_{26} & d_{36} \\ d_{11} & d_{12} & d_{13} & d_{14} & d_{15} & d_{16} & \epsilon_{11}^T & \epsilon_{12}^T & \epsilon_{13}^T \\ d_{21} & d_{22} & d_{23} & d_{24} & d_{25} & d_{26} & \epsilon_{21}^T & \epsilon_{22}^T & \epsilon_{23}^T \\ d_{31} & d_{32} & d_{33} & d_{34} & d_{35} & d_{36} & \epsilon_{31}^T & \epsilon_{32}^T & \epsilon_{33}^T \end{pmatrix} \begin{pmatrix} T_1 \\ T_2 \\ T_3 \\ T_4 \\ T_5 \\ T_6 \\ E_1 \\ E_2 \\ E_3 \end{pmatrix} \quad (1.6)$$

Thus in perovskite ferroelectric ceramics there are five independent elastic compliances, two dielectric permittivities and three piezoelectric constants. The key parameters such as piezoelectric charge coefficients, d_{ij} , the piezoelectric voltage coefficients, g_{ij} , and the energy efficiency, Q_{ij} , can be obtained using:

$$d_{ij} = \frac{e_{ij}}{C_{ij}} \quad (1.7)$$

$$g_{ij} = \frac{d_{ij}}{\epsilon_{ij}} \quad (1.8)$$

$$Q_{ij} = d_{ij} \cdot g_{ij} \quad (1.9)$$

where C_{ij} and e_{ij} are the elastic moduli (for a constant electric field), and piezoelectric stress moduli (for a constant strain or constant electric field).

1.3 Piezoelectric electroceramic-polymer composites

Ferroelectric materials generally belong to one of two families: The first class consists of ferroelectric ceramics which offer high electromechanical coupling ($k_p = 0.5 - 0.8$), a wide range of permittivities ($\epsilon = 100 - 3000$), low dielectric and mechanical losses as well as high thermal stability [23,24]. However, these materials are brittle and difficult to shape, and they possess a large acoustic impedance resulting in a more difficult acoustic match to soft media such as tissues and water. Moreover, despite their relatively high charge constants (d_{33}) that are beneficial for actuation, their high capacitance reduces the voltage sensitivity (g_{33}) quite drastically (see Eq. 1.8) [23,25].

The second group consists of ferroelectric polymers which have a low acoustic impedance as well as low permittivity, which can be advantageous in certain situations, such as in pyroelectric detectors [26,27]. They are rather flexible and ductile and can be manufactured with various processing techniques. The ferroelectric polymers show a low electromechanical coupling factor ($k_t = 0.2 - 0.3$) and low thermal stability and quality factors ($Q_m = 10 - 20$) which make them useful for underwater operation or for broad-band applications [25,28].

Piezoelectric polymers exhibit a low permittivity and a high piezoelectric sensitivity (g_{33}), which can be interesting in applications such as touch and impact sensing [25,27].

Potentially, attractive combinations of mechanical, thermal, dielectric, acoustic and electroactive properties and an adequate processability can be achieved by embedding ferroelectric ceramic particles within a polymer matrix, in which the ferroelectric activity is provided by the ceramic phase, and the flexibility is provided by the polymer phase. Such composites can overcome the limitations of both ceramics and polymers, and provide new avenues to sensing applications.

1.3.1 Effect of topology on electroactive properties of electroceramic-polymer composites

In the multiphase composites, the pattern of connectivity of the two phases plays a crucial role, as far as overall physical and electromechanical properties are concerned. Connectivity describes the interspatial relationships in a multiphase material. According to Newnham, in a two-phase system, a set of universal terminological conventions (Fig. 1.5) can be used to show different patterns of self-connections of the constituent phases [29].

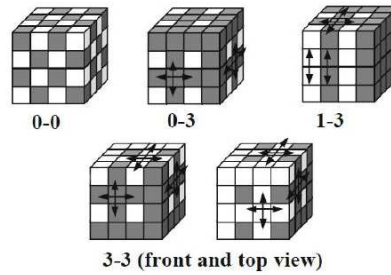


Figure 1.5: Illustration of the terminological conventions of diphasic composite-particulate connectivity (Adapted from Newnham et al. [29])

The connectivity pattern can be expressed with two digits, denoting the connectivity of the filler and that of the matrix respectively. The random particle distribution, or 0-3 composites with unconnected equiaxed particles in a fully self-connected matrix, and a fibrous distribution, or 1-3 composites with continuous ceramic fibers fully aligned in one dimension, represent the lower and upper bounds as far as the final properties of the composites are concerned. An intermediate state between the 0-3 (particulate) and 1-3 (fibrous) state can be obtained by applying an dielectrophoresis (DEP) treatment on a semi-dilute solution of particles in a viscous matrix (such as the most polymer systems prior to curing) [30–32]. As a result of the local electromechanical field the particles reorient and reposition themselves in thread-like structures. Under ideal processing conditions, long and well separated particulate threads form, which can span the full electrode to electrode spacing, closely approaching the topology of perfect 1-3 composites. For a given particulate concentration, the alignment of the particles in the thread-like structure leads to a marked increase in piezoelectric properties while the high mechanical flexibility due to the polymer matrix is

maintained [31, 33–35]. Various properties of ideal 0-3 (series) and 1-3 (parallel) composites as a function of the volume fraction of the filler are shown in Fig. 1.6. The polymer matrix (epoxy) and piezo ceramic (lead titanate) are chosen arbitrarily. The properties are simulated according to the mixed connectivity model (MCM) presented in Chapter 2.

As shown in Fig. 1.6, composites with 0-3 connectivity only show attractive piezoelectric properties at very high ceramic volume fractions [36]. One major reason can be attributed to inefficient poling state of the ceramic particles at low volume fractions [37]. Due to the lower resistivity and permittivity of the ceramic phase, the electric flux concentrates more effectively on the polymer phase and does not affect the ceramic particles efficiently. At high ceramic contents the thickness of the polymer layer separating the ceramic particles becomes smaller. Such a lower polymer layer thickness facilitates the poling of the composite, as a smaller fraction of the applied external electric field is imposed on the polymer matrix rather than on the poling of the ceramic particles.

On the other hand, the 1-3 connectivity composites show in general a higher performance in terms of electroactive properties, albeit at a higher manufacturing cost. The approach of combining an electroceramic powder with a polymer matrix, which has been used throughout this work, is widely considered to be an attractive option, since it allows mass production of cost effective piezoelectric and pyroelectric materials that could in a reliable way impart special properties to various structures by a coating process.

1.3.2 Effect of intrinsic properties of the polymer matrix on electroactive properties of electroceramic-polymer composites

Electrical conductivity

Particulate 0-3 composites are interesting candidates for demanding long term applications due to their ease of fabrication, tunable electroactive properties, high mechanical stability, ability to cover large area, versatile product size range and low manufacturing cost [38–40]. Moreover, they can be flexible, if properly selected polymer matrix material is used and the ceramic volume fraction is kept low. However, below the percolation threshold, there is no continuous path of connected particles from one electrode to another. In such cases, the poling efficiency as well as the electroactive properties depend even more strongly on the electrical conductivity of the polymer matrix [41–43].

Recent investigations have shown that the electrical conductivity of the constituents has a significant effect on dielectric, piezoelectric and pyroelectric properties of the particulate composites [44–48]. It has been reported that enhanced electrical conductivity of the matrix shortens the build-up time of the electric field acting on the ceramic particles, thus leading to higher poling efficiency in those composites. Moreover, the piezoelectric and pyroelectric properties of the composites also improve significantly [42, 49]. One way to improve the electrical conductivity of the composites is to introduce a small volume fraction of a conductive third phase [50–52]. Sakamoto et al. reported that an addition of carbon black in lead zirconate titanate-polyurethane (PZT-PU) 0-3 composite results in efficient poling at relatively low electric field and in a short time frame as well as superior pyroelectric and

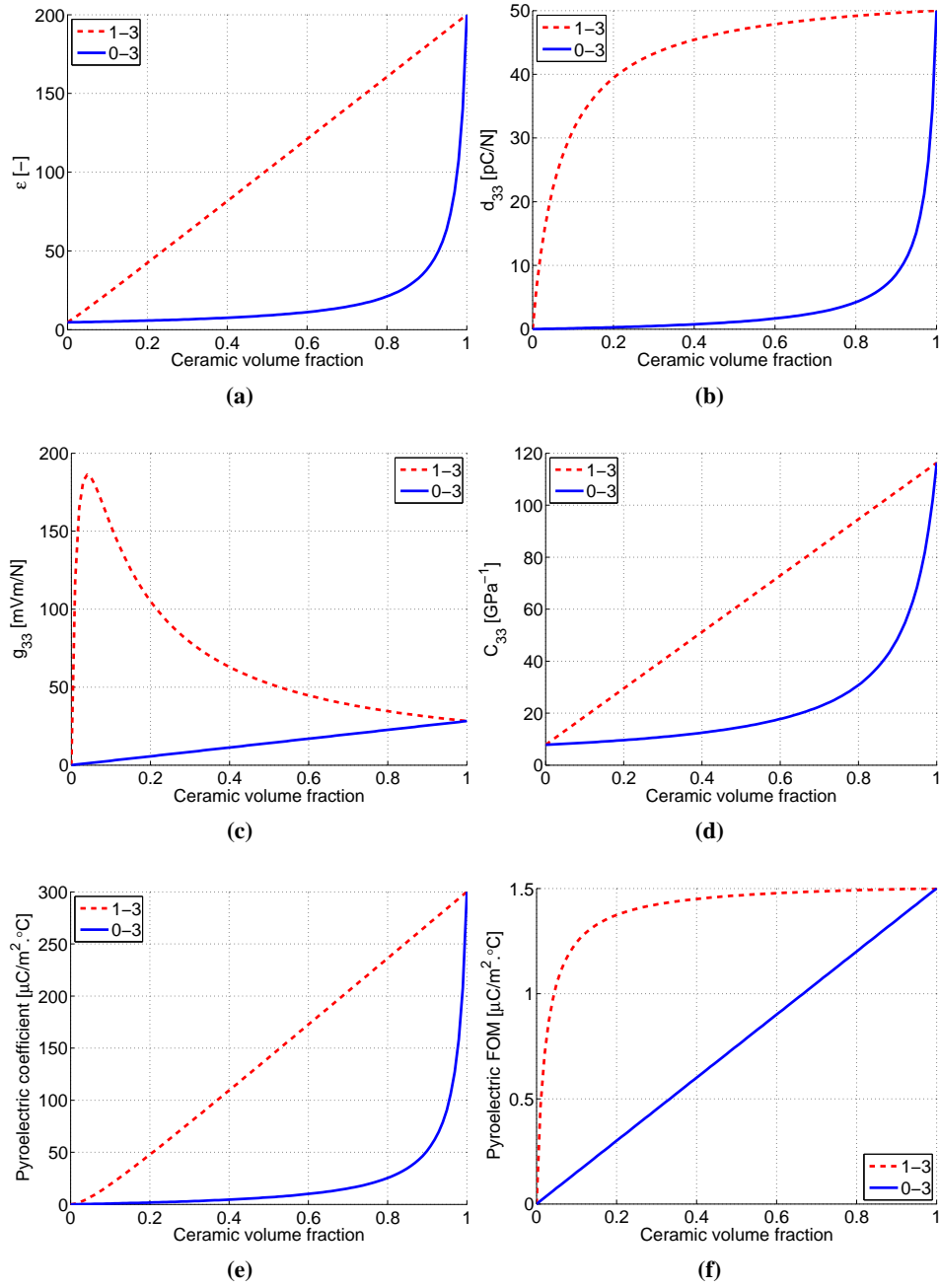


Figure 1.6: Electroactive and mechanical properties of 0-3 and 1-3 composites. Values of volume fraction, 0 and 1, indicate arbitrarily selected properties of polymer matrix (epoxy) and piezo ceramic (lead titanate) respectively.

piezoelectric coefficients [46]. The same group has reported that PZT-polyvinylidene fluoride (PZT-PVDF) 0-3 composites containing polyaniline, either as a separate phase or as a coating of ceramic particle, also show superior properties in all respects in comparison to the other composites [44, 45, 47]. Ploss et al. have also observed a significant improvement in pyroelectric properties of PZT-PU composites by using a matrix doped with lithium perchlorate (LiClO_4) [53, 54]. The mechanism of ionic conduction in doped polymer-ceramic composites is demonstrated by Furukawa et al. [55, 56]. The improvement of the pyroelectric coefficient from $6 \mu\text{C.m}^{-2}.\text{°C}^{-1}$ to $50 \mu\text{C.m}^{-2}.\text{°C}^{-1}$ after doping has been reported. These results have stimulated the application of other polymeric materials with higher conductivity to further enhance the pyroelectricity. Chau et al. [48] reported on the application of polyethylene oxide (PEO), a well known polymer electrolyte used for lithium battery, in pyroelectric composites. In PZT-PEO composites the pyroelectric and piezoelectric coefficients of the samples were greatly enhanced, when compared with other PZT-polymer composites with negligible conductivity.

Dielectric permittivity

The piezoelectric voltage sensitivity, g_{33} (Eq. 1.8), as well as pyroelectric FOM (Eq. 1.4) are directly proportional to the piezoelectric charge constant and pyroelectric coefficient, respectively, and inversely dependent on the permittivity of the material. Our earlier research has shown that optimization of the electrical as well as mechanical properties of the polymer matrix plays an important role in controlling the piezoelectric charge and output voltage of the diphasic composites, as presented in the Appendix [57]. The sensitivities can be further optimized by adding a gaseous phase to the polymer matrix to form of a porous medium.

Porous polymers, foamed to various low densities, find use in a wide range of applications that require properties such as weight-reduction, insulation, buoyancy, energy dissipation, mass transport as well as convenience and comfort [58]. More recent advances include polymeric foam scaffolds for tissue engineering [59], shape memory polymer foams for biomedical and aerospace applications [60–63], membranes for gas separation or filtration [64, 65], polymeric electrolytes in lithium-ion batteries [66, 67] and hydrogen storage [68, 69]. Investigation of ultra low permittivity dielectrics for the next generations of microchips in the field of electronic materials has encouraged development of porous polymer structures which show a clear relation between decreasing permittivity and increasing porosity [58, 70, 71]. A significant reduction in the permittivity of the piezo composites results in enhanced piezoelectric and pyroelectric performance of the composite sensors.

High performance properties

The interest for high temperature piezoelectric sensor materials for application in automotive, aerospace and energy has been growing significantly [72]. In automotive electronics, the current operating environments reach temperatures of 150 °C , and temperatures as high as 500 °C are expected for the near future. The aerospace industry has even tougher high

temperature requirements, when sensors often need to be placed close to the engine for adequate sensitivity to monitor the engine health. Therefore, piezoelectric materials that can function at high temperatures without failure are desired for structural health monitoring or nondestructive evaluation of the next generation turbines. Another major motivation for the development of high temperature electronic materials can be attributed to the exploration of new sources for energy production, such as nuclear and wind power as well as geothermal energy. Wind and geothermal energy capacities are growing as the leading forms of renewable energy worldwide. Wind and steam turbines will benefit from the development of high temperature sensors for structure health monitoring, ensuring enhanced lifetime and reliability, less maintenance and downtime, thus reducing the overall cost of renewable energy sources [73, 74].

The operating temperature range of a piezoceramic-polymer transducers is limited by the sensing capability of the piezoceramic at elevated temperatures, increased conductivity and mechanical attenuation, variation of the piezoelectric properties with temperature, and most importantly the glass transition temperature of the polymer matrix. High T_c piezo-ceramics can be embedded in high temperature polymers to overcome this problem. High performance amorphous polyimides are interesting candidates for the applications mentioned above [75–80]. To achieve an adequate combination of mechanical, thermal and electroactive properties ferroelectric ceramic particles are embedded within properly modified polymers of this family.

1.4 Scope of the thesis

This thesis presents several new composite materials and relates the effect of topology, processing and intrinsic properties of the constituent materials to piezo-, pyro-, and ferroelectric properties of the di-phase and tri-phase composites.

Chapter 2 describes the materials development and characterization of 0-3, as well dielectrophoretically structured quasi 1-3 composites based on lead titanate (PT) in an epoxy matrix. These composites consist of isolated equiaxed granulate particles in an inert, electrically insulating polymer presenting two distinct configurations of (0-3) or randomly distributed and (1-3) or chain-like structure. These systems can be regarded as the reference system for the systems investigated in the subsequent chapters. Two parameters, the inter-particle distance and the percentage of 1-3 connectivity, are used to evaluate the degree of structuring. Piezoelectric and pyroelectric sensitivities of the composites are investigated as a function of these parameters.

Chapter 3 deals with the computational modeling of structure formation during dielectrophoresis. A novel multiphysics finite element model is presented for semi-qualitative simulation of the structure formation in a medium of dielectric particles suspended in a liquid between parallel plate electrodes. The performance of the model is illustrated in a number of fundamental cases. The influence of parameters such as size, aspect ratio and heterogeneity of the particles is studied for the purpose of obtaining insight into the ideal conditions required to obtain a specific structure.

Chapter 4 describes the ferroelectric characteristics of PZT-epoxy particulate composites. The properties of dielectrophoretically structured PZT-polymer particulate composites are studied at high electric fields and compared to those of 0-3 composites. Polarization and strain response of PZT-polymer particulate composites, both 0-3 and quasi 1-3 types, are investigated. The properties of the composites are evaluated, and compared with those of the bulk ceramic. An analytical model is developed to describe the electromechanical strain of composites with a chain-like arrangement of the ceramic particles.

In chapter 5 the integration of process steps in the production of quasi 1-3 composites via DEP is described. A simultaneous combination of dielectrophoresis and poling is applied at room temperature, while the polymer is in the liquid state, followed by subsequent curing. This new processing route is applied in an uncured thermoset system, while the polymer matrix still possesses a relatively high electrical conductivity. Composites with different degrees of alignment are produced by altering the magnitude of the applied electric field. The effect of processing route on the degree of structuring as well as poling efficiency and the functional properties of the composites is investigated.

In chapter 6 electrically conductive PT-polyethylene oxide (PEO) composites are presented. PT particles are dispersed in PEO polymer at varying volume fractions, and composite films are cast. The dielectric, piezoelectric and pyroelectric properties are determined. From these data the piezoelectric voltage coefficients, as well as pyroelectric figures of merit of the composite films are calculated. The obtained values are compared with that of PT-epoxy composites in order to determine the effect of electrical conductivity of the polymer matrix on the poling efficiency and the final properties. A novel method is applied to test the pyroelectric properties of these materials at low frequency. The signal analysis procedure mathematically mimics the ideal lock-in character via a unique combination of Fast Fourier Transform (FFT) with Heaviside threshold to filter residual noise. The phase difference between the peaks of the temperature and current waves is calculated using a folded correlation.

Chapter 7 describes the development of tri-phase PZT-porous polyurethane composites. The main goal is to reduce the dielectric constant of the polymer matrix, and improve flexibility and conformability of traditional diphasic flexible piezo-composites consisting of ceramic particles in a dense polymeric matrix. This is achieved by adding a third (gaseous) phase to the system. The presence of the gaseous component in the polymer matrix lowers its dielectric constant and increases its piezoelectric voltage constant.

In Chapter 8 high temperature PT-polyetherimide (PEI) composites, as promising candidates for high temperature piezoelectric sensing applications, are presented. Lead titanate (PT) ceramic particulates are incorporated into a polyetherimide (PEI) polymer matrix at two specific volume fractions. A conventional dielectrophoretic structuring, as described in Chapter 2, is used to induce chain-like particle configuration, followed by curing the matrix to form free standing films. Subsequently poling is performed under high voltages and at temperatures above the glass transition temperature of the partially imidized matrix. Free standing composites are subsequently imidized to form fully imidized films. The piezoelectric and pyroelectric properties of the films are tested at elevated temperatures.

Finally, the main findings of this work are compiled in the summary.

In the Appendix, the Virtual Particle Mori Tanaka (VPMT) method, a model for the effect of topological imperfections on the electromechanical properties of structured particulate composites is presented. This novel method is developed, based on the Mori-Tanaka method with Eshelby tensors for piezoelectric composite materials, to predict the effective electro-elastic properties d_{33} and g_{33} of structured granular piezoelectric composites. The method achieves an improved accuracy by means of a single parameter related to the spatial distribution of imperfectly aligned rod-like PZT particles and is found to have excellent prediction capabilities. Extending the approach, several newly defined functions are presented to capture the drop in the piezoelectric composite's electro-elastic properties as a function of topological imperfections. These imperfections are related to longitudinal and lateral inter-particle spacings and the topology of the chain-like structures themselves. The functions are evaluated in detail and show physically consistent behavior.

Structure and properties of particulate PT-epoxy composites *

2.1 Introduction

Among various kinds of commercially available ferroelectric materials for sensing applications, lead titanate (PT) is generally regarded as a good pyroelectric material because of a large spontaneous polarization, a small relative dielectric constant, and a large pyroelectric coefficient [81, 82]. As far as functional PT-polymer composites are concerned, the overall piezoelectric voltage coefficient and pyroelectric responsivity can be optimized by combining the high electroactivity of the ceramic phase and the low dielectric constant of the polymer. The pattern of connectivity of the two phases plays a crucial role in the overall physical and electromechanical properties are concerned. Structuring the ceramic particles in PZT-polymer composites, by means of dielectrophoresis (DEP), has been shown to improve the piezoelectric properties of these materials over those of random composites, by forming chains of aligned and closely connected particles, when the matrix polymer is still in its low viscosity state [30, 31, 33]. The enhanced electromechanical properties of quasi 1-3 composites can be explained by the higher degree of parallel connectivity in these systems compared to 0-3 composites. In the current work, Bowen's model [33] and the mixed connectivity model (MCM) [83] are used to assign structuring parameters to the composites based on which the piezoelectric and pyroelectric properties of the composites are evaluated.

*This work has been published as: Khanbareh, H. , van der Zwaag and S., Groen, W. A., Effect of dielectrophoretic structuring on piezoelectric and pyroelectric properties of lead titanate-epoxy composites, Journal of Smart Materials and Structures, 23 105030, 2014.

2.2 Experimental procedure

2.2.1 Composite manufacturing

Lead titanate (PT) powder was calcined at 800 °C for 2 h to create a single phase PbTiO_3 . The agglomerated powder was then dry-milled, using 5-mm zirconium balls for 2 h in a single G90 jar mill. The particle size distribution of milled powder in an aqueous solution with 10% isopropyl alcohol, measured by a Beckman Coulter LS230 laser diffraction analyzer was found to be $d(10) = 2.4 \mu\text{m}$, $d(50) = 4.5 \mu\text{m}$, and $d(90) = 8.1 \mu\text{m}$. The powder was stored in a drying oven at 120 °C for 24 h prior to the experiment to avoid moisture adsorption. A two component epoxy system (Epotek 302-3M, Epoxy (diglycidyl ether of bisphenol-A (DGEBA) resin and poly(oxypropyl)-diamine (POPD) multifunctional aliphatic amine curing agent, as shown in Fig. 2.1, was used.

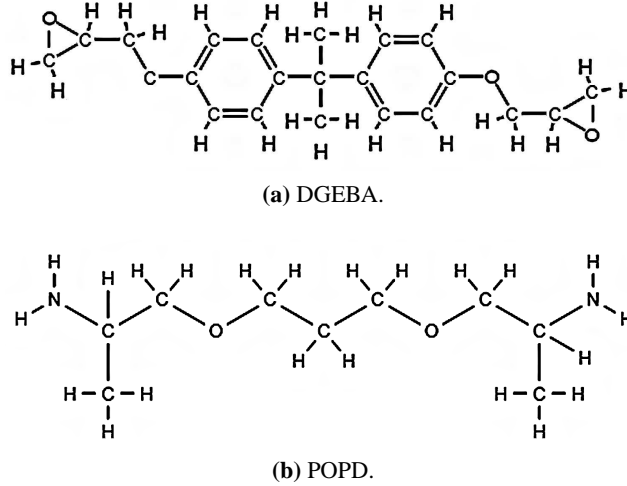


Figure 2.1: Chemical structure of the epoxy components.

The glass transition temperature (T_g) of the epoxy was determined by differential scanning calorimetry (DSC) using a Perkin-Elmer Sapphire DSC. Samples were heated at a rate of 20 °C/min under a nitrogen atmosphere. For the epoxy cured at 50 °C for 3 h followed by a post-curing step at 100 °C for 1 h a T_g of 60 °C was measured. At room temperature, the epoxy is viscous (at 800-1600 cPs) and has a low dielectric constant (at 1 kHz) of approximately 4.6, which makes it an interesting option for dielectrophoresis (DEP) as also reported earlier [30]. To fabricate the composites, the ceramic content was calculated using following equation:

$$M_c = M_p \left(\frac{\rho_c}{\rho_p} \right) \left(\frac{\phi_c}{1 - \phi_c} \right) \quad (2.1)$$

where M is the mass, ρ is the density, and ϕ is the volume fraction. The subscript c and p denote the ceramic and polymer properties, respectively. The PT particles were dispersed

in the resin component of the epoxy and mixed at a speed of 1000 RPM for 15 min using a planetary mixer (SpeedMixer DAC 150.1 FVZ, Hauschild). Subsequently, the hardener was added and the composite resin was again mixed at 1500 RPM for 3 min. Finally the uncured ceramic-polymer mixture was degassed and poured into a mold consisting of a 1 mm thick Teflon sheet with 15 mm diameter circular cut-outs. The sheet was then placed between two layers of 50 μm thick Aluminum foil serving as the temporary electrodes for the application of the electric field for DEP as shown in Fig. 2.2.

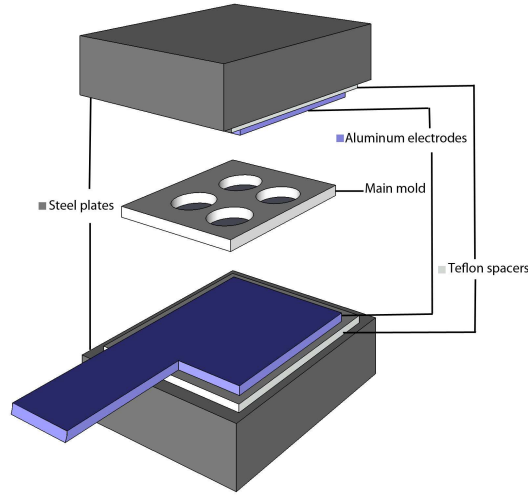


Figure 2.2: Schematic drawing of the mold used for dielectrophoresis processing of composites.

The whole set-up was placed between two bolted steel plates with additional Teflon spacers separating the electrodes from the steel plates to apply pressure and produce flat samples. Structuring of the particles in the as-yet uncured composite was realized by a dielectrophoresis process, in which an electric field of 2 kV/mm and a frequency of 1200 Hz was applied to the composite medium of particles dispersed in the uncured epoxy resin. The electric field was applied using a function generator (Agilent, 33210A) coupled to a high voltage amplifier (Radiant Technologies Inc., T6000HVA-2) at room temperature (RT) for 1 h (i.e. well into the curing stage) followed by 5 h heating at 50 °C to obtain a fully cured matrix. The peak to peak output voltage of the high voltage amplifier, the phase angle and the leakage current were verified with an oscilloscope (Agilent, DSO-x 2004A).

The randomly dispersed samples were obtained in a similar manner only without applying an electric field and by oven curing at 50 °C for 5 h. The completely cured disk-shaped samples of 15 mm diameter and 1 mm thickness were polished to remove the top epoxy layer and post cured at 100 °C for 1 h to remove moisture. Finally, gold electrodes of 9.2 mm diameter and 50 nm thickness were deposited on both sides of the composite samples by sputtering (Balzers Union, SCD 040) and poled at 9 kV/mm at 80 °C in a water-cooled Julabo, SE Class III, 12876 oil bath for a 1 h. The samples were then cooled to room temperature in the presence of the poling field. In order to remove the injected charges during the polarization and the trapped charges due to impurities, the samples were stored

at 100 °C for 24 h with their electrodes short circuited prior to the measurements.

Measurement procedure

The dielectric constants of the composites were determined using the parallel plate capacitor method with an Agilent 4263B LCR meter (Japan) at 1 V and 1 kHz. The piezoelectric coefficients, d_{33} , were determined using a Berlincourt type M3001 d_{33} meter, KCF technologies (State College, PA). The pyroelectric characterization was performed based on the change in total charge at the electrodes due to a change in sample temperature using the direct method [84]. The sample was placed in an Agilent 16339A component test fixture with its electrodes connected to the measurement device as shown in Fig. 2.3, and heated uniformly using an integrated programmable heater. The heating cycle was from 25 °C to 70 °C. The maximum temperature is lower than the poling temperature of the composites. The heating rate was controlled by a PID controller and kept constant at 1 °C/min during the measurement.

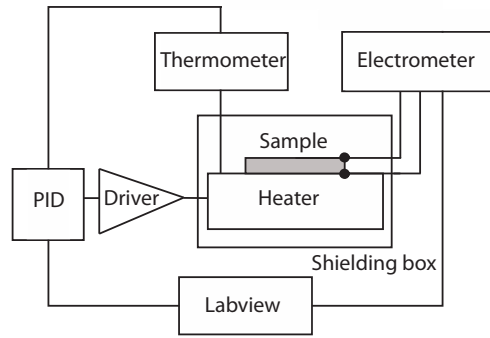


Figure 2.3: Schematic diagram of the set-up for the direct pyroelectric current measurement.

The depolarization current, flowing between the two contacts of the sample, was monitored with an Agilent 4339B high resistance meter as shown in Fig. 2.3. The temperature was monitored with a K-type thermocouple and stored in a computer. Calibration of the setup was undertaken using a single crystal LiTaO_3 prior to measurements. The heating cycle normally started from room temperature. The pyroelectric coefficient was calculated using Eq. 1.3. The constant heating rate, dT/dt , was chosen as 1 °C/min over the whole temperature range. The measurement of I_p gives a direct plot of $p(T)$ over the range of the temperature. Electrical conductivity measurements were carried out by means of a broadband spectrometer (Novocontrol) at 1 kHz, using an Agilent E4991A impedance analyzer. The microstructures of the samples were observed using a field emission-scanning electron microscope (FE-SEM) (JEOL, JSM-7500F), operated in backscattered electron mode. Samples sectioned parallel to the particle chains were embedded in a room temperature curing epoxy and polished with 1 μm diamond paste.

2.3 Results

2.3.1 Microstructure of composites

The effect of DEP structuring on the SEM microstructures of the composite samples is shown in Fig. 2.4. A clear difference can be observed between random and structured samples in particular for 10-20 % PT composites. It can be seen that during dielectrophoresis, ceramic particles construct chain like structures along the electric field direction. The degree of alignment, which affects the final dielectric and electroactive properties of the composites, depends on the force acting on the particles as a consequence of imposed electric field. This driving force behind the attraction between particles is a function of the amplitude and frequency of the electric field, the dielectric properties of both matrix and ceramic particles as well as the size of the particles [30, 85]. Although the gravitational forces also affect the motion of particles in the fluid matrix, they are not taken into account since no sedimentation was observed in the microstructures.

2.3.2 Dielectric properties

The measured dielectric constant values are presented in Fig. 2.5 for PT volume fractions from 10% to 50%. The analytical model used to explain the piezoelectric properties of the random or 0-3 composites is the model proposed by Yamada et al. [36]. In this model the composite is assumed as a uniform distribution of ellipsoidal particles in an isotropic polymer matrix. The dielectric constant of the composite in the poling direction is given by:

$$\epsilon_{random} = \epsilon_m \left(1 + \frac{n\phi(\epsilon_c - \epsilon_m)}{n\epsilon_m + (\epsilon_c - \epsilon_m)(1 - \phi)} \right) \quad (2.2)$$

where ϵ is the dielectric constant, and ϕ is the volume fraction of the ceramic phase. The subscript c , m , and $random$ refer to the ceramic, polymer matrix and 0-3 composite properties, respectively and n is the inverse of the depolarization factor for an ellipsoidal particle in the direction of applied electric field. The good agreement between the measured and theoretical values indicates a 0-3 connectivity pattern. In the current work n was obtained as a fitting parameters by the least square method in such a way to minimize the difference between the experimental data and the model predictions. The best fit of the experimental data to model predictions was obtained for $n = 4.48$.

Dielectric properties of the structured composites are fitted to Bowen's model [33] as shown in Fig. 2.5. According to this model, the composite is considered as a collection of particles aligned as chain-like structures along a specific direction separated by polymer gaps. The equation for the permittivity for such a composite is as follows:

$$\epsilon_{structured} = \phi_c \left(\frac{R\epsilon_c\epsilon_m}{\epsilon_c + R\epsilon_m} \right) + (1 - \phi_c)\epsilon_m \quad (2.3)$$

where $\epsilon_{structured}$ is the dielectric constant of dielectrophoretically structured 1-3 composites, and R is the ratio of average particle size to the effective interparticle distance, which influences the fraction of the applied electric field acting on the ceramic particles. The input

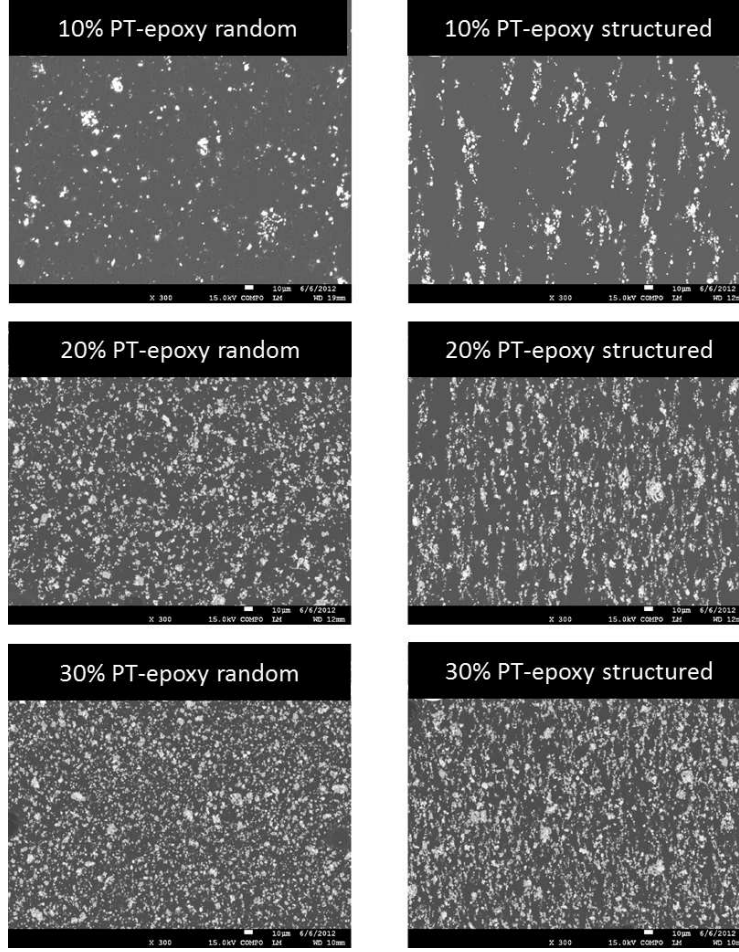


Figure 2.4: SEM microstructures of random and structured PT-epoxy composites with different PT volume fractions.

parameters for both random and structured composite modeling are listed in Table 2.1. It is assumed that the piezoelectric properties of the particles are equal to the bulk ceramic values, as particle properties could not be measured directly. The value of R obtained for the best fit of the experimental data to Bowen's model was 11.2.

Material	ϵ at 1 kHz	d_{33} (pC/N)	d_{31} (pC/N)	Y (GPa)	s_{11} (TPa^{-1})	s_{12} (TPa^{-1})	s_{33} (TPa^{-1})	α ($10^{-6}K^{-1}$)
PT	200 [81]	50 [81]	-4.2 [81]	126.7 [18]	7.35	1.5	1.5	3.57 [18]
Epoxy	4.6	0	0	1.7 [11]	128 [86]	256 [86]	256 [86]	56

Table 2.1: Properties of ceramic inclusions and polymer matrix.

The electrical conductivity of random and structured composites are shown in Fig. 2.6 for different PT volume fractions at two different temperatures which is in agreement with the dielectric results presented previously (Fig. 2.5). Conductivity enhancement is observed at

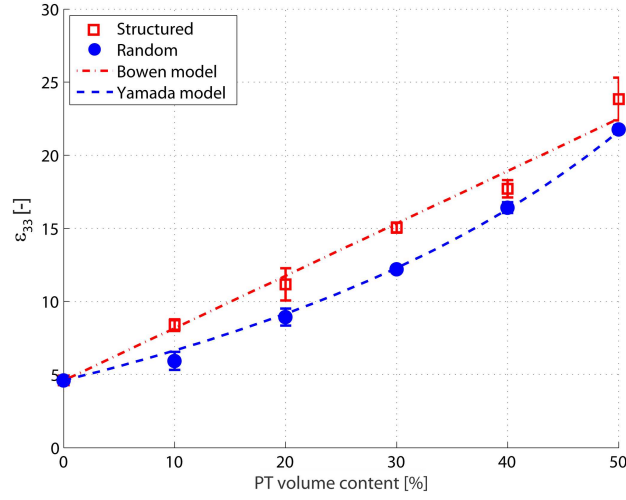


Figure 2.5: Measured dielectric constant values for structured and random composites with their associated models.

higher temperatures and higher ceramic volume fractions.

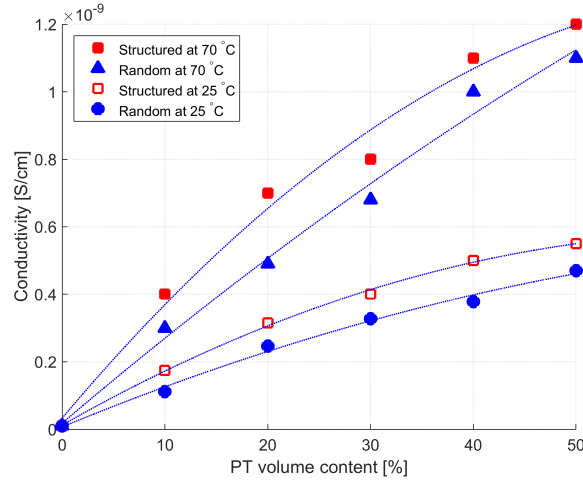


Figure 2.6: Electrical conductivity (at 1 kHz) versus ceramic volume fraction of PT-epoxy composites. Lines are added to guide the eye.

2.3.3 Piezoelectric and pyroelectric properties

The influence of DEP structuring on piezoelectric charge constant, d_{33} , of the composites is shown in Fig. 2.7 where the experimentally observed d_{33} values of both structured and random composites are compared with their associated models. The experimental data for random composites are fitted to Yamada's model [36] as described below. The piezoelectric

charge constant, d_{33} , of the composite in the poling direction is given by:

$$d_{33\text{random}} = \frac{\phi \alpha n \epsilon_{\text{random}} d_{33c}}{n \epsilon_{\text{random}} + \epsilon_c - \epsilon_{\text{random}}} \quad (2.4)$$

where α is the poling ratio of the ceramic particles. The other parameters were introduced earlier with equation 2.2. The best fit of the experimental data to the model predictions was obtained when $\alpha = 1$. To describe the piezoelectric charge constant in structured composites, the analytical model proposed by Van den Ende et al. [31] is applied. This model is an extension of Bowen's model [33], in which the d_{33} of composites are obtained by modeling the particle-matrix sequences in the chains as two capacitors in series in the electrical domain, and two springs in series in the mechanical domain. The equation for d_{33} of 1-3 composite is given by:

$$d_{33\text{structured}} = \frac{(1 + R)^2 \epsilon_m \phi_c d_{33c} Y_c}{\epsilon_c + R \epsilon_m [(1 + R \phi_c) Y_c + (1 - \phi_c) R Y_m]} \quad (2.5)$$

where Y_m and Y_c are elastic moduli of the polymer matrix and that of the ceramic in the direction of chains respectively, while R is the ratio of average particle size to the effective interparticle distance in the direction of electric field. As shown in Fig. 2.7, the values for both 0-3 and 1-3 composites match reasonably well to the models. The best fit of the model to the experimental data was obtained for an R of 11.7 which is in a good agreement with the value of R obtained for the dielectric constant data.

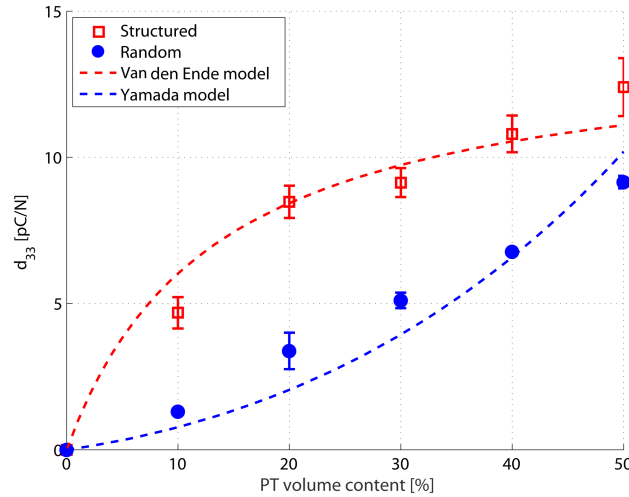


Figure 2.7: d_{33} values for structured and random composites with their associated model predictions.

The pyroelectric coefficient, p , is obtained from the reversible pyroelectric current after three runs of the thermally stimulated discharge current measurement, using equation Eq. 1.3, for random and structured composites, for PT volume fractions from 10% to 50%. A small change in the intensity of the discharge current was observed during the first and second runs due to the space charges. The third heating cycle shows no reduction in the

current, thus a reversible pyroelectric current was established. The effect of structuring on pyroelectric coefficient of PT-epoxy composites at 25 °C for various PT content is shown in Fig. 2.8. The pyroelectric coefficient increases as the PT content in the composites increases, and there is a mild improvement due to structuring.

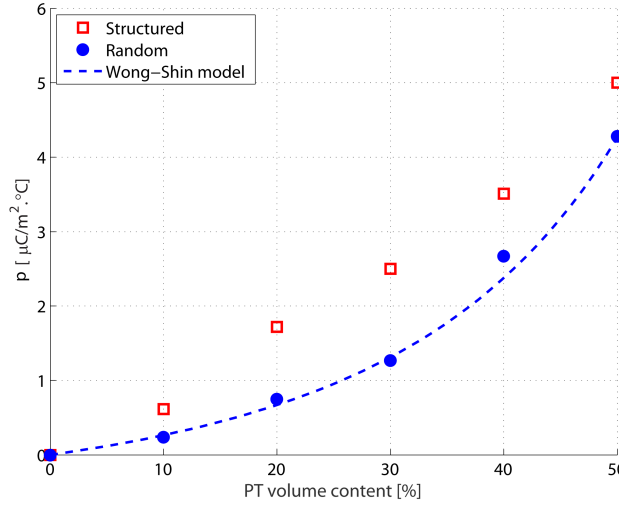


Figure 2.8: Pyroelectric behavior of PT-epoxy composites.

In order to verify the validity of the results, comparisons with existing models were carried out. The model proposed by Wong and Shin [42] can be used to determine the pyroelectric properties of the random composites. This model considers the composite as a system consisting of spherical ceramic particles, uniformly dispersed in a continuous medium in which the electrical conductivities affect the internal fields in the 0-3 composites and thus accumulation of charge at the ceramic-polymer interfaces occurs. Fig. 2.8 shows the predictions of the model compared with the experimental results for random PT-epoxy composites for $\sigma_m = 10^{-15}$ S/cm and $\sigma_c = 10^{-13}$ S/cm at 25 °C indicating a good agreement. With increasing the volume fraction of the pyroelectric constituents, the overall pyroelectric coefficient of the composite increases as well. This model only applies to random composites and does not take the effect of phase connectivity into account.

The pyroelectric figure of merit (FOM), calculated by dividing the pyroelectric coefficient of the composite by its dielectric permittivity (see Eq. 1.4) is shown in Fig. 2.9, for PT volume fractions from 10% to 50%. The pyroelectric FOM increases as the PT content composites increases, and an improvement is observed due to structuring.

Fig. 2.10 shows the typical behavior of pyroelectric coefficient as a function of temperature for PT-epoxy composites. The 30%-PT-epoxy composite shows a considerable increase in the value of $p(T)$ above 60 °C. This transition temperature agrees well with the measured glass transition temperature of the polymer matrix cured using the above mentioned scheme. The increase may be due to the fact that at temperatures above the T_g of the polymer there is an increase of the free volume contributing to a high current [87]. Similar behavior has been observed in PZT-PU [46, 87], PTCa-PEKK [88, 89] and PZT-PVDF composites [90].

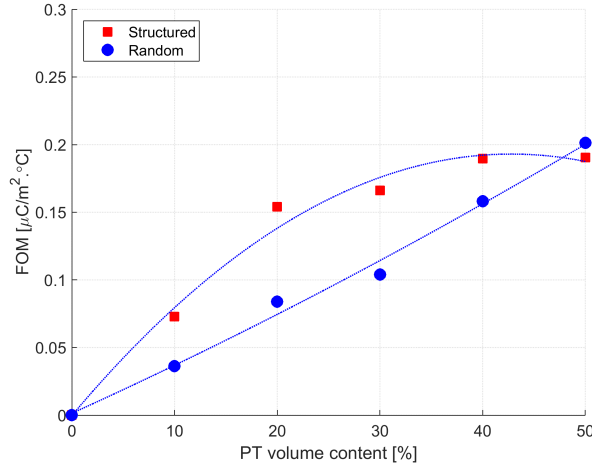


Figure 2.9: Pyroelectric FOM of random and structured PT-epoxy composites as a function of PT content. Lines are added to guide the eye.

In order to verify the effect of glass-rubber transition on the pyroelectric current, a poled 30% PT-epoxy composite was post-cured at 150 °C for 1 h, and the T_g and the reversible pyroelectric current were subsequently measured. Interestingly, the new transition point in the pyroelectric coefficient-temperature curve corresponds well with the increased glass transition temperature of 80 °C.

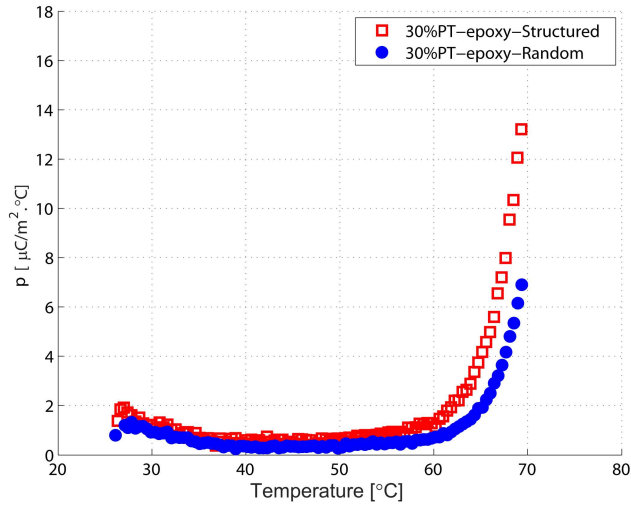


Figure 2.10: Temperature dependance of the pyroelectric coefficient for random and structured 30%-PT-epoxy composites.

The pyroelectric coefficient of random and structured composites, as a function of PT volume content, at two different temperatures of 25 °C and 70 °C, is shown in Fig 2.11. Signif-

icant improvement in pyroelectric coefficient is observed, at 70 °C, especially for high PT volume fractions.

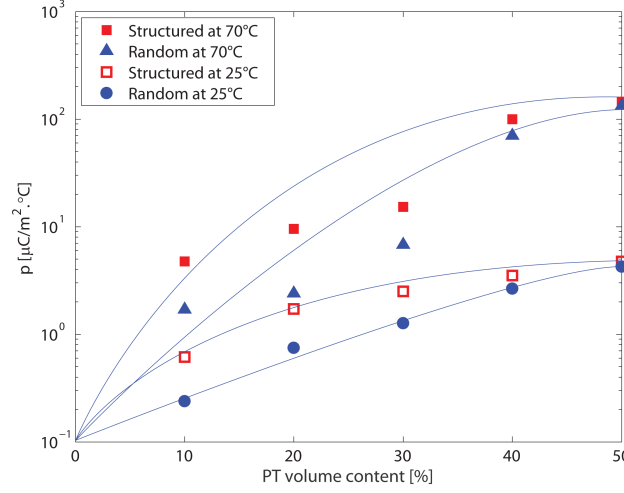


Figure 2.11: Temperature dependent pyroelectric behavior of PT-epoxy composites. Lines are added to guide the eye.

2.4 Discussion

The higher ϵ , d_{33} and p values obtained for the dielectrophoretically structured composites, compared to random composites, show that aligning the ceramic particles enhances the dielectric, piezoelectric, and pyroelectric properties for every volume fraction of PT. In earlier work it was shown that the degree of increase depends on amplitude and frequency of the applied field and on the viscosity of the polymer matrix. No dielectrophoretic alignment of piezoelectric ceramic particles below 1 kHz was observed in epoxy systems at low ceramic content [30, 91]. In this work, the frequency level was adjusted to obtain the highest phase angle of Lissajous plots for each volume fraction in early stages of curing [91]. Although conditions are adequate for alignment, the phase angle never reaches 90°, so losses are still present. However, the dielectrophoretic force in this system is enough to induce alignment in the 0-3 systems up to 50 % volume fraction PT as shown in Fig. 2.5 to Fig. 2.12, which was also reported by Van den Ende [92]. During the dielectrophoresis process, PT particles are redistributed to form chains in the electric field direction, hence resulting in anisotropic dielectric properties. Since the effective volume fraction of the ceramic phase is higher parallel to the direction of applied electric field, the properties are also enhanced in that direction.

The shape parameter, n , obtained from the best fit of Yamada's model to the dielectric constant experimental data gives a reasonably good correlation to d_{33} . However, in general this model gives the best prediction of d_{33} for high ceramic volume fractions [36]. One reason for this deviation could be the difference in the poling ratio depending on the ce-

ramic volume fraction, since the effective electric field sensed by the particles is weaker in the low volume fraction composites. The effect of dielectrophoretic ordering on the piezoelectric charge constant as shown in Fig. 2.7 is found to be most pronounced at lower PT volume fractions. According to the Van den Ende model (Eq. 2.5), from 0 to 10% ceramic volume fraction a rapid increase in d_{33} is expected, which is in agreement with the theory for anisotropic piezoelectric particles spanning the length of the composites in a 1-3 manner [93]. However, the slope of the change observed experimentally is lower than the theoretical predicted value, showing that at 10% the composite still has a significant 0-3 character. At 50% ceramic content an enhancement of 25% in d_{33} is observed, which indicates that although the particles are more likely to be constrained in their movement at high ceramic volume fraction, the application of an electric field induces a higher degree of parallel connectivity. The increase in 1-3 connectivity due to a coalescence of ceramic grains in the thickness direction results in an increase in quasi-continuous ceramic paths between the electrodes [94].

The piezoelectric voltage coefficient, g_{33} , calculated by dividing the d_{33} of the composites by their relative permittivity are plotted as a function of the PT volume fraction in Fig. 2.12. The maximum value obtained for the random composites is 48 mV.m/N at a PT volume fraction of 50%, while for the structured composite, a value of 85.6 mV.m/N is obtained at a PT volume fraction of 20%. Compared to pure PT with g_{33} of 33 mV.m/N, both random and structured composites show superior voltage sensitivity.

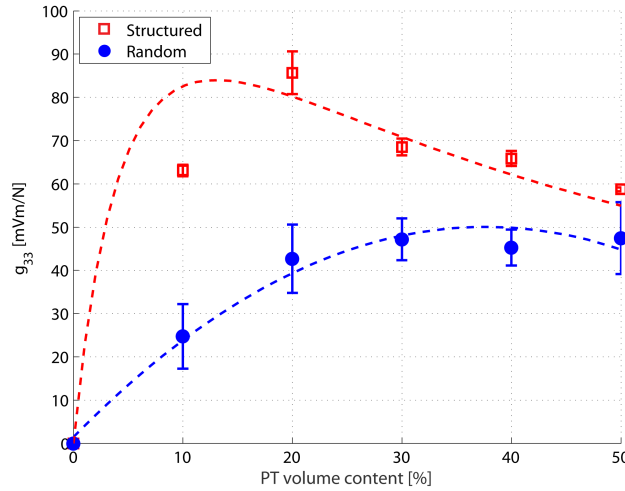


Figure 2.12: g_{33} values for structured and random composites.

For the structured composites, the d_{33} increment is higher than that of dielectric constant especially at lower volume fractions. Therefore, the voltage coefficient of these composites exhibits a maximum at low volume fraction of PT. The position of the peak depends on the stiffness ratio of the piezoelectric phase over the polymer matrix [31,95]. At higher volume fractions than 20%, the derivative of d_{33} decreases rapidly to zero while the derivative of ϵ is constant, so the g_{33} values of structured composites drop rapidly.

The superior electroactive properties of quasi 1-3 composites, compared to 0-3 composites, can be related to the effect of ceramic particle structuring. Bowen's model introduces the interparticle distance as the structuring parameter. Fitting the model to the experimental data for ϵ and d_{33} resulted in close R values of 11.2 and 11.7 respectively. The interparticle distances calculated from the R value obtained from the dielectric constant data are plotted for different PT volume fractions in Fig. 2.13, for both random and structured composites. The obtained interparticle distances decrease with increasing PT volume fraction. A significant difference between interparticle distances for random and structured samples is observed at low ceramic volume fractions.

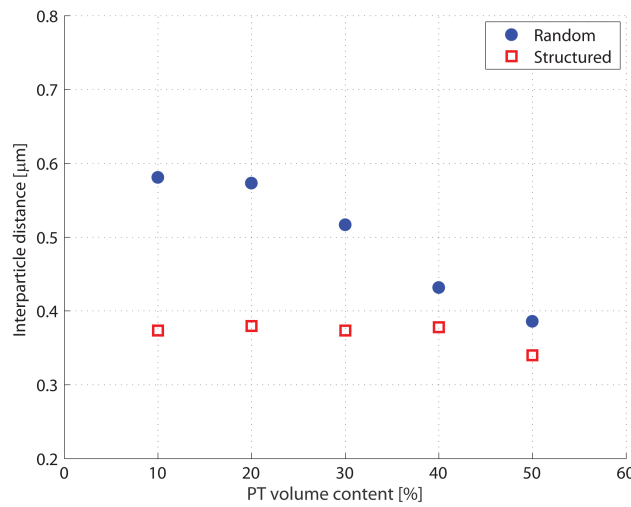


Figure 2.13: Estimated values of average interparticle distance obtained from Bowen's model (Eq. 2.3).

The effect of ceramic interparticle distance on piezoelectric and pyroelectric properties of random as well as structured composites is shown in Fig. 2.14. Data points with the same volume fraction are connected by lines. The slope of the constant volume fraction line shows the sensitivity of the functional property to the DEP structuring. The change in interparticle distance with DEP is higher for low ceramic volume fractions. Comparing the effect of DEP structuring on d_{33} and p reveals that at high ceramic volume fractions the piezoelectric charge constant is more sensitive to the change in interparticle distance than the pyroelectric coefficient.

The mixed connectivity model is used as the second tool to estimate the 1-3 connectivity as a structuring parameter in order to understand the effect of dielectrophoretic alignment of particles on the electroactive properties of the composites [83]. This model considers that both parallel and series connectivity exist in the composite, giving a tri-phasic system. In this model the properties depend on the parameters n and m , which are related to the connectivity of the composite (Fig. 2.15). The ceramic is represented as a cube of dimensions m where a fraction of it, n , connects both electrodes in the form of a parallelepiped. Thus the composite is considered as having mixed connectivity of 0-3 and 1-3. The ceramic volume fractions are given in Table 2.2.

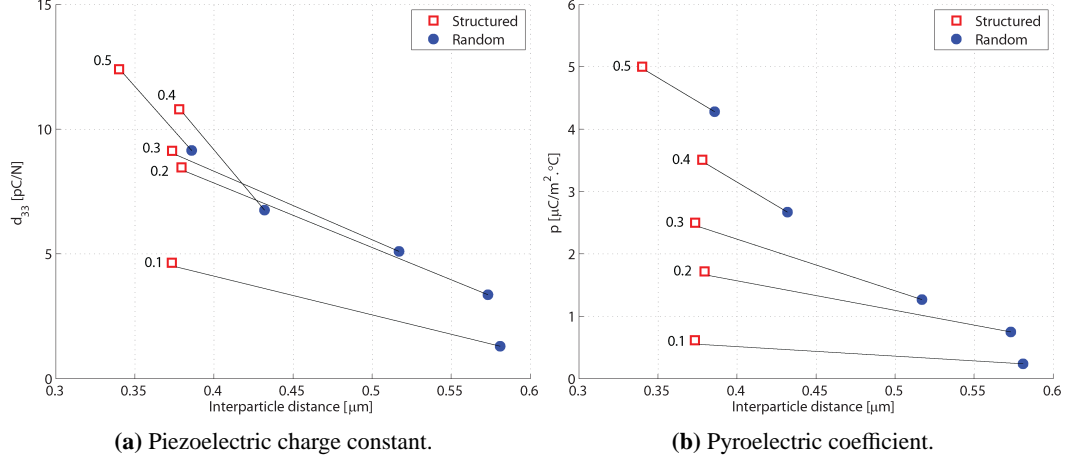


Figure 2.14: Functional properties of PT-epoxy composites as a function of interparticle distance calculated from Bowen's model (Eq. 2.3). Constant volume fraction lines are also shown.

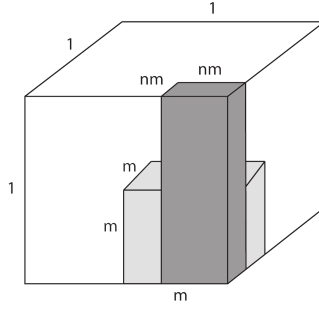


Figure 2.15: Mixed connectivity cube [83].

Volume fractions	Ceramic	Matrix	Series
Series	m	1-m	
Parallel	$(mn)^2$	$1 - m^2$	$m^2(1 - n^2)$
Total	$m^3 + n^2m^2(1 - m)$		

Table 2.2: Volume fractions of the phases used in the mixed connectivity model [12].

The expression for the d_{33} given by this model is:

$$d_{33} = s_{33} \left(\frac{\phi_c^{par} d_{33}^c}{s_{33}^c} + \frac{\phi_m^{par} d_{33}^m}{s_{33}^m} + \frac{\phi_{ser} d_{33}^{ser}}{s_{33}^{ser}} \right) \quad (2.6)$$

$$s_{33} = \frac{\phi_c^{par}}{s_{33}^c} + \frac{\phi_m^{par}}{s_{33}^m} + \frac{\phi_{ser}^{par}}{s_{33}^{ser}} \quad (2.7)$$

$$s_{33_{ser}} = \phi_{ser}^c s_{33_{ser}}^c + \phi_{ser}^m s_{33_{ser}}^m + \Delta s_{33} \quad (2.8)$$

$$\Delta s_{33} = \frac{(d_{33}^c - d_{33}^m)^2 \phi_{ser}^c \phi_{ser}^c}{a_1} - 2 \frac{[(d_{33}^c - d_{33}^p)a_3 - (s_{33}^c - s_{33}^p)a_1]^2 \phi^c \phi^m}{(a_1 a_2 - 2a_3^2)a_1} \quad (2.9)$$

Auxillary defenitions:

$$a_1 = \epsilon_0(\phi^c \epsilon^c + \phi^m \epsilon^m) \quad (2.10a)$$

$$a_2 = \phi^m(s_{11}^c + s_{12}^c) + \phi^c(s_{11}^m + s_{12}^m) \quad (2.10b)$$

$$a_3 = \phi^m d_{31}^c + \phi^c d_{31}^m \quad (2.10c)$$

where s_{ij} and d_{ij} are the elastic compliance and the piezoelectric coefficient respectively. The subscripts i and j refer to the direction of the response and applied stimulus, respectively. The superscripts c and m and the subscripts ser and par denote ceramic and matrix constituents, and series and parallel phases respectively. Using this model the composite properties can be represented as contour plots as a function of the connectivity parameters n and m [83]. The contour charts, using the mixed connectivity cube model, for dielectric constant, g_{33} , pyroelectric coefficient, and pyroelectric FOM for PT-epoxy composites can be found in Figs. 2.16 to 2.19. The constant volume fraction curves, from 0.1 to 0.9, have also been included in the form of dashed lines. The permittivity charts reflects similar behavior as the raw materials from which the composites are made from. The pyroelectric coefficient charts show a large region in the $n - m$ plane with a small pyroelectric coefficient at low ceramic volume fractions. The pyroelectric FOM charts are obtained by taking the ratio of p/ϵ . The pyroelectric FOM does not exceed that of the ceramic. However, this is not the case for g_{33} , which is calculated by dividing the d_{33} of the composites by their permittivity. The highest g_{33} can be observed for low ceramic volume fractions, at high n values.

Fig. 2.20 shows a contour chart of d_{33} for random and structured PT-epoxy composites, obtained using the mixed connectivity model. Each experimental data point is located in the intersection of the known value of volume fraction of the composite and the corresponding value of the d_{33} . The n and m values are found by the least square method in such a way to minimize the difference between the experimental data and the model predictions. The values of n and m increase for both random and structured composites with increasing ceramic volume fraction. The percentage of 1-3 connectivity, calculated as the the volume fraction of the ceramic phase in parallel connectivity ($\frac{(nm)^2}{m^3+n^2m^2}$), is shown as a function of the ceramic volume fraction in Fig. 2.21.

The 1-3 connectivity character of the composites depends both on the ceramic loading fraction and the DEP structuring. At each constant volume fraction, the structured composite has a higher degree of 1-3 connectivity compared to the random composite. Higher efficiency of dielectrophoresis is observed at lower ceramic content. However, the maximum percentage of 1-3 connectivity in the ceramic phase for the structured composites hardly exceeds 9% even at high PT volume fractions, which can be due to very low particle size to sample thickness ratio [12]. As also reported by Pardo et al., for mixed connectivity PZT-epoxy systems, a higher grain size to sample thickness ratio is beneficial for the piezoelectric

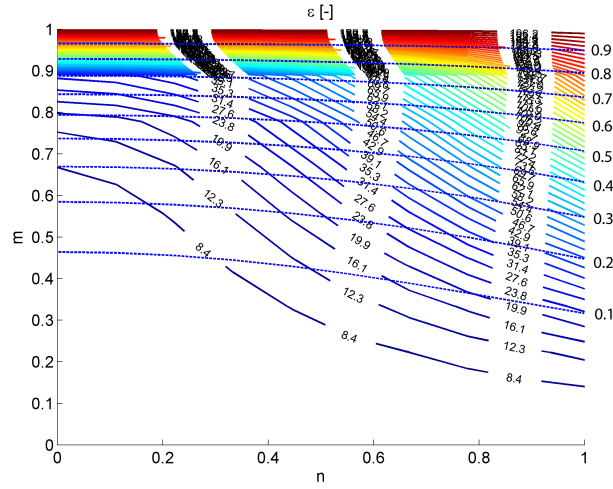


Figure 2.16: ϵ contour chart for the PT-epoxy composites using the MCM. Dashed lines show the constant volume fraction curves, from 0.1 to 0.9.

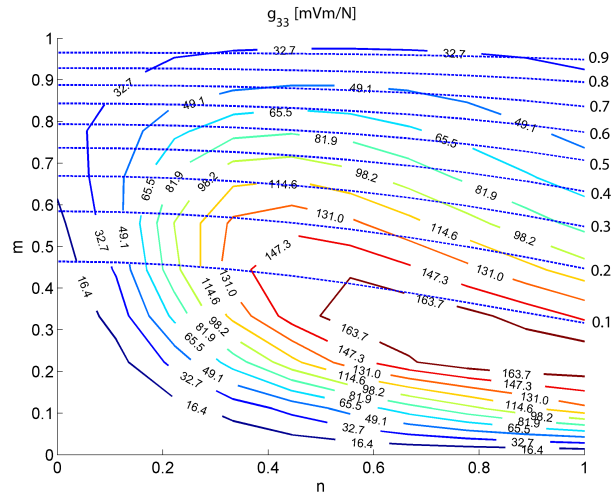


Figure 2.17: g_{33} contour chart for the PT-epoxy composites using the MCM. Dashed lines show the constant volume fraction curves, from 0.1 to 0.9.

properties and poling efficiency [96] regardless of the volume fraction of the ceramic. Comparing Fig. 2.20 with the contour plot of permittivity, one can observe that the n values for d_{33} are slightly lower than those of permittivity chart. So, there is a tendency for permittivity to show higher 1-3 connectivity character compared to d_{33} , which was also reported by Dias [83]. Plots of the average d_{33} and p value at each volume fraction versus the percentage of 1-3 connectivity are shown in Fig. 2.22, for random and structured composites. The constant volume fraction lines slope shows the sensitivity of the properties to the percent-

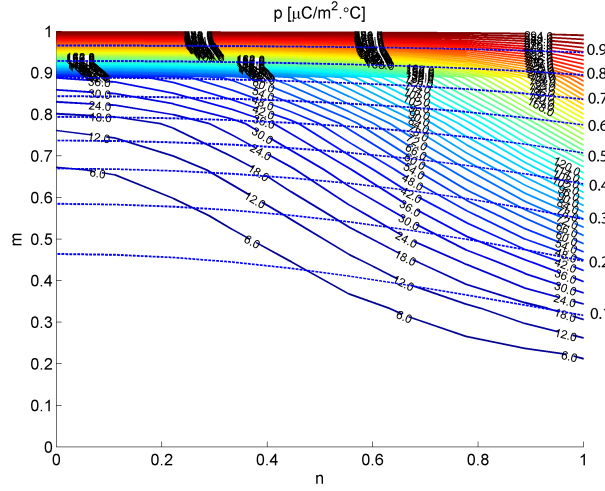


Figure 2.18: p contour chart for the PT-epoxy composites using the MCM. Dashed lines show the constant volume fraction curves, from 0.1 to 0.9.

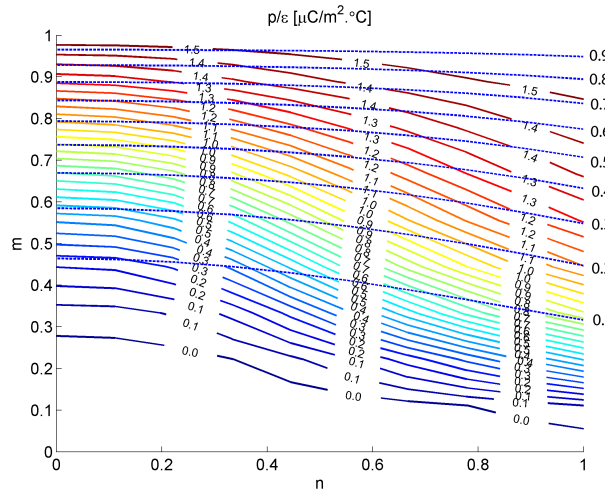


Figure 2.19: Pyroelectric FOM contour chart for the PT-epoxy composites using the MCM. Dashed lines show the constant volume fraction curves, from 0.1 to 0.9.

age of 1-3 connectivity. Higher sensitivity of the functional properties to DEP structuring is observed at higher ceramic content, although the absolute DEP induced 1-3 connectivity is larger at lower volume fractions. These results agree well with the effect of interparticle distance calculated from the piezo- and pyroelectric properties of the composites using Bowen's model.

The maximum observed value of pyroelectric coefficient at room temperature is lower than that reported for other 0-3 composite systems, for instance PTCa-PEEK [94], PTCa-

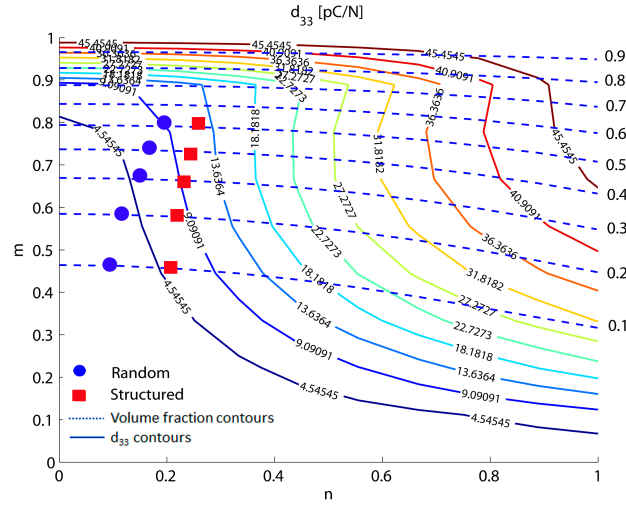


Figure 2.20: d_{33} contour chart for the PT-epoxy composites using the MCM. Dashed lines show the constant volume fraction curves, from 0.1 to 0.9.

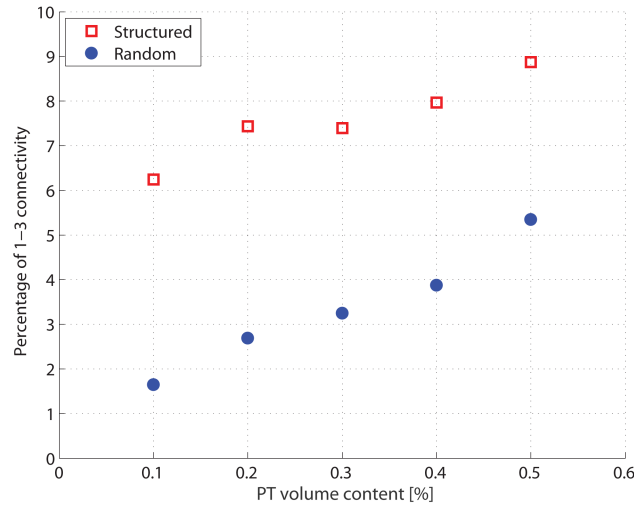


Figure 2.21: Estimated percentage of 1-3 connectivity obtained from the MCM.

PVDF [97] and PTCa-PEKK [98]. Part of this difference is likely to be due to the relatively thick samples (1 mm) employed, for which it is difficult to ensure that the whole sample changes temperature at the same rate [99]. It has been found that for PTCa-PVDF composites a reduction in thickness from 100 μm down to 50 μm improves significantly the pyroelectric performance [12]. Moreover, it has been reported by Dias et. al. [12] that for a composite system of ceramic of low resistivity embedded in high resistivity polymer matrix, the pyroelectric coefficient measured by the direct method could be substantially lower than that obtained using the dynamic method. The authors argument is that the py-

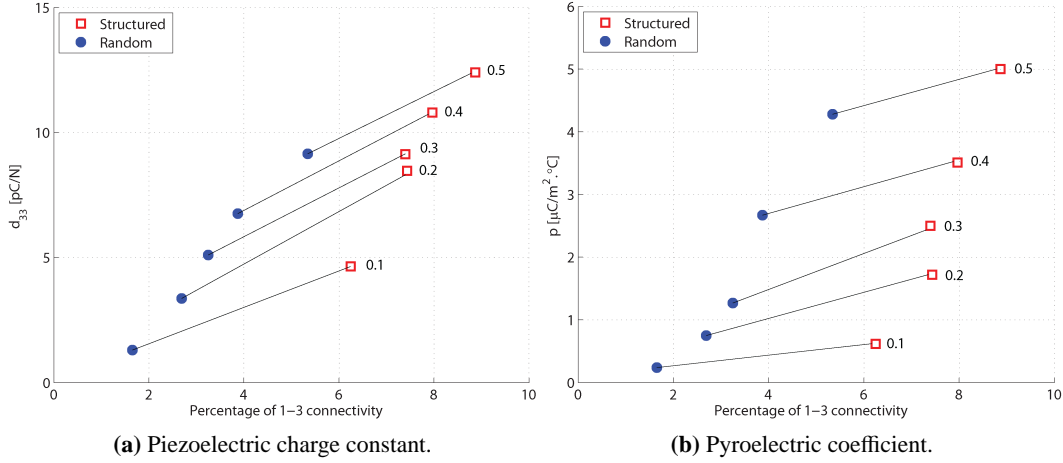


Figure 2.22: Functional properties of PT-epoxy composites as a function of degree of structuring calculated from the MCM. Constant volume fraction lines are also included.

roelectric charge, generated when heating the sample, discharges through the resistance of ceramic phase, due to very low electrical conductivity of the matrix, and therefore not contribute to the measured pyroelectric current. This phenomenon can be prevented in dynamic testing at higher frequencies compared to the electrical time constant, RC , of the ceramic. Nevertheless the direct method to measure the pyroelectric coefficient of the PT-epoxy composites is used in this chapter, which provides us with a good indication of pyroelectricity between samples of similar compositions. Another possible reason for the relatively low value of pyroelectric coefficient could be associated with the dielectric mismatch between the two constituent phases, leading to a poor poling of the ceramic phases in the composites. However, alignment of filler particles into a chain like structure forms a semi-continuous path of high susceptibility phase and enhances filler particle polarization, compared to a 0-3 composite. As demonstrated in Fig 2.11, with increasing temperature from 25 °C to 70 °C, a significant improvement in pyroelectric coefficient of both random and structured composites is observed, especially at high PT volume fractions. The observed behavior is associated with the change in electrical conductivity of the polymer matrix at higher temperatures. Fig. 2.6 shows conductivity enhancement with increasing temperature and ceramic content, which results in more efficient poling at higher temperatures and higher ceramic content, especially in presence of particle chains. Moreover, the problem of discharging the generated pyroelectric charge due to high resistivity of the matrix at room temperature can be circumvented at 70 °C, which enhances the performance of the composites.

2.5 Conclusions

This chapter shows that a significant improvement in dielectric, piezoelectric and pyroelectric properties of 0-3 composites can be achieved by dielectrophoretic alignment of the

ferroelectric ceramic particles inside a polymer matrix. The degree of structuring, as well as the electrical properties of the constituents, are the most important parameters controlling the overall properties of the composites. Two structuring parameters, the interparticle distance and the percentage of 1-3 connectivity, are derived from Bowen's model and the mixed connectivity model. The degree of structuring calculated according to both models correlate well with the increase in piezoelectric and pyroelectric sensitivities of the composites.

Computational modeling of structure formation during dielectrophoresis in piezoparticle-polymer systems *

3.1 Introduction

Piezoelectric ceramics are widely used in sensing, actuation and energy harvesting applications due to their high permittivity, thermal stability, and electromechanical coupling. However, these materials suffer from inherent brittleness, and lack of formability, which limits their use for applications in which mechanical flexibility is required. Ductile and flexible piezoelectric polymers, which have a modest sensitivity and a low thermal stability, are found in less demanding applications. By embedding piezoelectric ceramics in a polymer matrix one can combine the superior piezoelectric and mechanical properties, allowing for high piezoelectric coupling characteristics with increased flexibility and toughness. In such multiphase composites, the volume fraction of the phases, their morphology, the pattern of connectivity as well as the dielectric and electrical properties of the two phases control the overall physical and electromechanical properties [30, 31, 100]. As discussed in Chapter 2, an intermediate state between the 0-3 (particulate) and 1-3 (fibrous) state can be obtained by dielectrophoresis (DEP) treatment on a semi-dilute solution of particles in a viscous matrix (such as the most polymer systems prior to curing) [30–32]. Under ideal processing conditions, long and well separated particulate threads form which span the entire electrode to electrode spacing, approaching the topology of perfect 1-3 composites. For a given particulate concentration, the alignment of the particles in the thread-like structure leads to a marked increase in piezoelectric properties while the high mechanical flexibility due to the polymer matrix is maintained [31, 33–35].

*This work has been published as: Gutiérrez, M.A., Khanbareh, H., van der Zwaag, S., Computational modelling of structure formation during dielectrophoresis in particulate composites, Computational Materials Science, Vol. 112, Part A, 1 pp. 139146, 2016.

The quality of particle alignment in the thread-like structure is the key parameter in controlling the overall properties of the composites [35, 101–103]. Enhancing the alignment quality, by means of decreasing the inter-particle distance, has been shown to significantly improve the dielectric, piezoelectric and pyroelectric properties of particulate composites [32]. The effect of processing parameters on thread formation has been experimentally demonstrated for high aspect ratio particles in a thermoset matrix [11]. The orientation angle of the particles in the DEP composites has been shown to be dependent on the applied electric field, time, and aspect ratio of the particles. To date, all research into DEP structuring of piezoceramic particulate-polymer composites has been of an experimental nature. Furthermore, the quality of the structure formation has only been determined after consolidation of the polymer matrix, and additional processing. It is the aim of the present chapter to present a 2D computational model for the structuring of particulate composites when the matrix is still in its fluid state. The performance of the model is illustrated for a number of fundamental cases. The influence of parameters such as size, aspect ratio and heterogeneity of the particles on the thread or chain formation is analyzed. The quality of the chain-like structure created is investigated through a chain perfection degree, which is defined using a set of geometric parameters, that correlates to the overall performance of piezoelectric composites.

3.2 Dielectrophoresis modelling

3.2.1 Background

The dielectrophoretic force is defined as the action experienced by a polarized particle immersed in an electric field E . In the ideal case that the particle can be modeled by means of an infinitesimal dipole moment p , it will experience a force:

$$F = p \cdot \nabla E \quad (3.1)$$

and a torque:

$$M = p \times E \quad (3.2)$$

In addition to the infinitesimal dipole idealization, these equations are based on the assumption that the electric field itself is not influenced by the dipole [104, 105].

For the case of structure formation during dielectrophoresis, however, none of the above assumptions hold. Particles need to be viewed as finite domains with an own polarization P , that will contribute to the electric field E in the surrounding medium. This contribution will also induce a force on neighboring particles. This situation can be treated analytically by means of higher-order multipoles [85, 104, 106, 107]. Alternatively, and especially for the purpose of simulation of structure formation with several particles involved in which emphasis is given to the qualitative behavior of the system rather than to the accuracy of the results, numerical methods such as finite elements provide a meaningful alternative.

The current study is limited to a two-dimensional rectangular domain, which can be viewed as an idealization of a thin three-dimensional quadrangular domain Ω^l filled with a viscous liquid of a dielectric permittivity ε^l and viscosity η , which is confined between two plates separated by a distance d , and containing a single layer of particles $\{\Omega_i^p\}_{i=1}^n$ with dielectric permittivity ε^p and mass density γ restricted to move on the mid-plane. The particles have thickness l . This renders a computationally treatable model of an experimental setup [31] used to observe structure forming in dielectrophoretic manufacturing of piezoelectric polymers. A schematic representation of the geometry of this model is given in Figs 3.1 and 3.2.

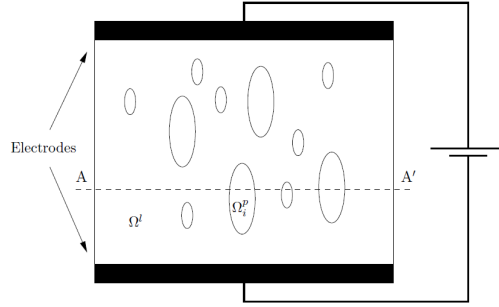


Figure 3.1: Schematic representation of the geometrical model.

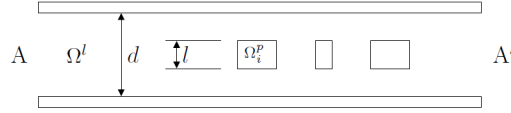


Figure 3.2: Cross section of the geometrical model along line AA' of Fig. 3.1.

3.2.2 Mechanical modeling

In the context of the simplification introduced in Section 3.2.1, the particles Ω_i^p can be modeled as linear elastic solids in plane-stress conditions. The motion of each individual particle is obtained by solving Cauchy equation:

$$\nabla \cdot T + b = \gamma \ddot{u} \quad \text{in } \Omega_i^p; \quad (3.3)$$

$$Tn = t \quad \text{on } \partial\Omega_i^p, \quad (3.4)$$

where T is the stress tensor, b is the body force density, γ is the mass density, u is the displacement field, t is the boundary traction and n is the outward normal vector at the boundary $\partial\Omega_i^p$. For a proper description of the particle motion, geometrical non-linearity is considered.

The body force b consists of a dielectrophoretic contribution b_d and an equivalent viscous drag term b_v , while the boundary traction t is of a purely dielectrophoretic nature. These forces will be characterized in Sections 3.2.3 and 3.2.4.

3.2.3 Dielectrophoretic force

The Laplace equation

$$\nabla^2 V = 0 \quad (3.5)$$

is solved for the potential V in $\bigcup_{i=1}^n \Omega_i^p \cup \Omega^l$ with adequate boundary conditions to obtain the electric field E and the polarization field P as derived quantities. This polarization is associated to the bound volume and surface charge densities in the particles according to the expressions:

$$\rho = -\nabla \cdot P \quad \text{in } \Omega_i^p \quad (3.6)$$

$$\sigma = P \cdot n \quad \text{on } \partial\Omega_i^p \quad (3.7)$$

From these charge densities, dielectrophoretic body and surface forces are computed as:

$$b_d = \rho E t = \sigma E \quad (3.8)$$

3.2.4 Viscous drag

As the particles $\{\Omega_i^p\}_{i=1}^n$ are immersed in a fluid, they will experience viscous drag upon motion. A simplified model is adopted for this purpose. It is assumed that the fluid interacts with the particle along the top and bottom flat surfaces, and that the rate of shear is linear between the particle and the upper and lower confining plates, see Fig. 3.3. If a Newtonian fluid is considered, this leads to a distributed shearing force on the surface amounting to

$$\tau = \eta \frac{v}{(d-l)/2} \quad (3.9)$$

This shearing force is reworked into an equivalent body force as

$$b_v = \frac{2\tau}{l} \quad (3.10)$$

where the factor two is introduced to account for the contribution of both sides.

3.2.5 Algorithmic aspects

The model, described in Section 3.2, can be viewed as a coupled transient mechanical-electrostatic system. The model was simulated efficiently in the multiphysics finite element package COMSOL, making use of the electromagnetism and the solid mechanics modules.

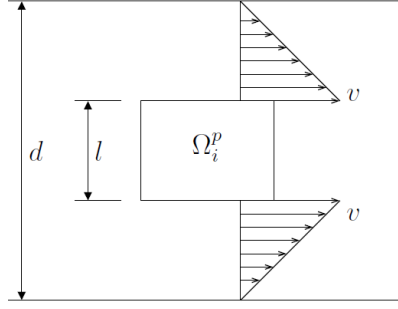


Figure 3.3: Schematic representation of the assumed velocity field for computation of the viscous drag force.

A single finite element domain is generated for the domain $\bigcup_{i=1}^n \Omega_i^p \cup \Omega^l$ respecting the internal boundaries between particles and fluid. The electrostatic problem stated in Section 3.2.3 is solved in the entire domain to obtain the dielectrophoretic forces (A.8). These are used as body force and boundary traction in the mechanical problem 3.2.2. However, the latter is solved only for the particles $\{\Omega_i^p\}_{i=1}^n$, that are regarded as unconstrained entities, in order to obtain the displacement and velocity field at each time step. After updating the position of all particles, the mesh in the liquid domain Ω^l is adapted. For this purpose, a moving mesh technique is adopted in combination with automatic remeshing [108].

During structure formation the particles will eventually collide and get attached. This is modeled by means of contact constraints to prevent domain overlapping. A difficulty arises here, because the software requires that pairs of boundaries needing a contact constraint be specified beforehand. However these pairs cannot be objectively predicted. Preliminary runs of each case were carried out in order to identify the positions along the particulate boundaries coming in contact during structuring [109].

3.3 Simulations

In this section a number of fundamental cases are investigated to show the performance of the model. To gain insight into the ideal conditions required to obtain the desired structure, the influence of parameters such as size, aspect ratio and particle size distribution is particularly studied.

3.3.1 Performance parameters

The quality of the structure evolution is studied by means of a set of objective geometric parameters describing a structure as shown schematically in Fig. 3.4. These parameters also relate to the resulting performance of the piezoelectric composite.

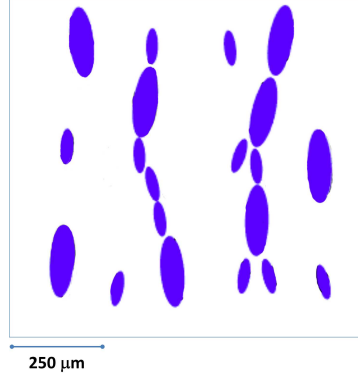


Figure 3.4: Schematic structure of particle system.

Average orientation

One of the objective parameters commonly used to describe orientational order of an ensemble of elongated particles is the order parameter, \bar{P}_2 ,

$$\bar{P}_2 = \overline{\frac{3}{2} \cos^2 \beta - \frac{1}{2}}, \quad (3.11)$$

where β is the angle between the dominating dimension of the particle and the electric field [110]. Parameter \bar{P}_2 ranges between zero for a random microstructure and one for a fully aligned situation. The geometrical parameter is calculated using the image processing toolbox of MATLAB. A sequence of plots of the particle positions and orientations at various stages of the structuring process are obtained. To calculate the \bar{P}_2 parameter, skeletonization is performed, which is a specialized use of erosion operation. A skeleton is a central line resulting from morphological thinning that successively erodes pixels from the boundary until no more thinning is possible, at which point the remaining approximates the skeleton. Finally the angle between every two vertically adjacent skeletons within a chain, the angle between the dominating dimension of the particle as well as the electric field and the \bar{P}_2 parameter are calculated.

Average distance

Another indicator of the performance of a piezoelectric composite is the distance d between closest particles within a formed chain. In an optimal situation, all elongated particles have formed chains with no gaps in between, leading to $d = 0$. It is not feasible to give a formal, objective definition of this parameter, as it depends on the actual resulting structure. Therefore, the involved pairs of particles for which d is computed need to be identified first. These are obviously the same for which contact constraints have been defined during the simulation, as described in Section 3.2.5. The inter-particle distance is calculated via the Euclidean distance transform of the binary image. For each pixel in the binary image, the

distance transform assigns a number that is the distance between that pixel and the nearest nonzero pixel of binary image. As a result, a grayscale image is produced, in which every pixel within a feature is assigned a value that is its straight line distance from the nearest background pixel. This is analogous to a dilation of the particles with constant speed until the growing border meets the border of the neighbouring particles. Subsequently, on each merging point between every two particles two distance values are identified with respect to both particles within a chain. The sum of these two values is the final inter-particle distance.

Chain perfection degree

The quality of the dielectrophoretically formed chains is estimated using a newly defined chain perfection degree, which topologically compares the microstructure to an ideal structure, composed of perfect chains spanning from one electrode to the other. In order to quantify the perfection degree of a chain, one should be able to detect the chain in the first place. Using the image processing toolbox, the snapshots are transformed to binary images, followed by calculation of the sum of pixels in every column. Finally the sum value is plotted versus the column position. Peaks in the resulting spectrum correspond to the chain position. The intercolumnar distance between the peaks shows the lateral distance between the formed chains. Results of the chain identification process are presented for two example of nine identical particles system (section 3.3.4), as well as several particles of different size (section 3.3.4). Once the chains are identified, the chain perfection degree can be calculated. The total chain perfection degree (PD_c) is composed of a global perfection degree (PD_g) as well as a local perfection degree (PD_l).

$$PD_c = PD_g \times PD_l$$

$$PD_c = \left(P_{2c} \times \frac{L - d}{L_{ic}} \right) \times \left(\bar{P}_2 \times \left(1 - \frac{\sum d}{a} \right) \right) \quad (3.12)$$

where P_{2c} is the order parameter of the chain, L is the actual chain length, L_{ic} is the ideal chain length, d is the inter-particle distance and \bar{P}_2 is the the average order parameter of individual particles within a chain.

3.3.2 Single particle orientation

Polarized particles, submitted to an electric field, experience a torque as expressed by equation (3.2) for an infinitesimal dipole idealization. The orientation behavior is studied for a range of particles with different aspect ratios, by evaluating the evolution of the \bar{P}_2 parameter in time, starting from the initial configuration at 45° with respect to the imposed electric field direction. The results are shown in Fig. 3.5. It is observed that the aspect ratio has little influence on the alignment behavior.

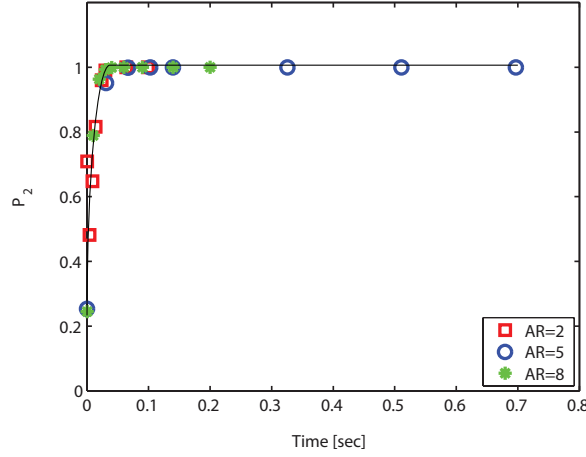


Figure 3.5: Evolution of \bar{P}_2 parameter for different aspect ratios: (1) Aspect ratio 2; (2) Aspect ratio 5; (3) Aspect ratio 8.

3.3.3 Two particle interaction

In contrast with Section 3.3.2, where the rotation induced by the imposed electric field is illustrated, the particle interaction resulting from the local variation of the electric field is shown here. Two situations are considered, each having two particles but at different initial positions.

First, two particles with an aspect ratio of five are symmetrically aligned with the electric field at a mutual distance equal to the particle length. Upon polarization, these particles will repel each other in horizontal direction. The evolution of the system is shown in Fig. 3.6. This simulation demonstrates that the centrosymmetrically aligned particles barely interact with each other once they are separated by a finite distance.

The same simulation is carried out for the same particles, but now placed initially in an off-centered position. Upon application of the electric field, the particles will not only feel the imposed homogenous field, but also the local field induced around each particle. As a result, two particles first rotate towards each other, but away from the equilibrium orientation angle. Consequently, the rotation is accompanied by a lateral and axial displacement that reduces the inter-particle distance (Fig. 3.6, $t = 0.5$ s). Both motions lead to the formation of connected chains at an off-axis angle with respect to the imposed field (Fig. 3.6, $t = 1$ s). To minimize the total energy of the system the chain rotates to align with the field (Fig. 3.6, $t = 1.5$ s). The simulations show that particle rotation precedes the lateral or axial displacement of the particles in accordance to experimental observations [31,38]. It follows that the chain formation does not only depend on filler and matrix properties, and applied electric field, but also on the initial configuration of particles with respect to each other.

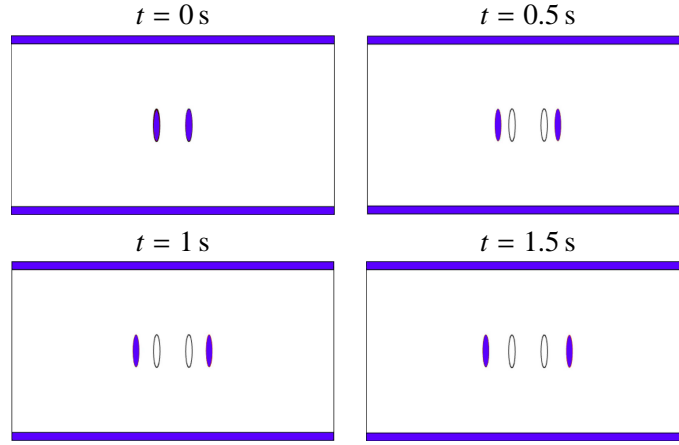


Figure 3.6: Positional evolution for two centro-symmetrically aligned particles. Empty and filled ellipsoids show the initial and actual positions respectively.

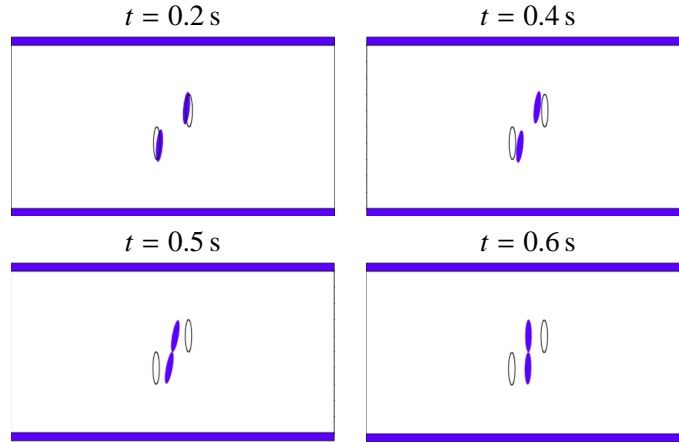


Figure 3.7: Positional evolution for two parallel particles positioned off-center. Empty and filled ellipsoids show the initial and actual positions respectively.

3.3.4 Multi-particle interaction

The structure evolution and chain formation is now analyzed for a number of cases involving more than two particles. The purpose is to predict which conditions can lead to optimal structures.

Nine identical particles system

The evolution of nine particles with an aspect ratio of three is evaluated using the inter-particle distance d and orientation parameter \bar{P}_2 . In the initial configuration, the particles

are placed on an 3×3 regular array. After the electric field is applied between the electrodes, two phases are clearly observed in the structure evolution. Once all particles have aligned to the imposed field (at $t = 0.1$ s), they start interacting until two chains of three particles and one chain of two particles have formed. This is illustrated in Fig. 3.8. In order to evaluate the chain quality, the chain identification process, as described in section 3.3.1, is applied on the four configurations shown in Fig. 3.8, and the resulting spectra are shown in Fig. 3.9. This figure shows the sum of the pixel values in every column plotted versus the column position. Each peak corresponds to a chain of particles and the intercolumnar distance between the peaks show the lateral distance between the formed chains. The time scale of the alignment phase is comparable with that of a single particle (see Section 3.3.2) and yet smaller than that for the chain formation phase as observed from the \bar{P}_2 evolution shown in Fig. 3.10. This observation corresponds well with the experimental results of the time dependent evolution of average orientation angle and average chain length as reported by Van den Ende et al. [38]. It should be noted that the \bar{P}_2 value does not increase continuously once the particles have made the initial alignment. There is a minor fluctuation in the \bar{P}_2 value as the particles experience minor temporary displacements in place.

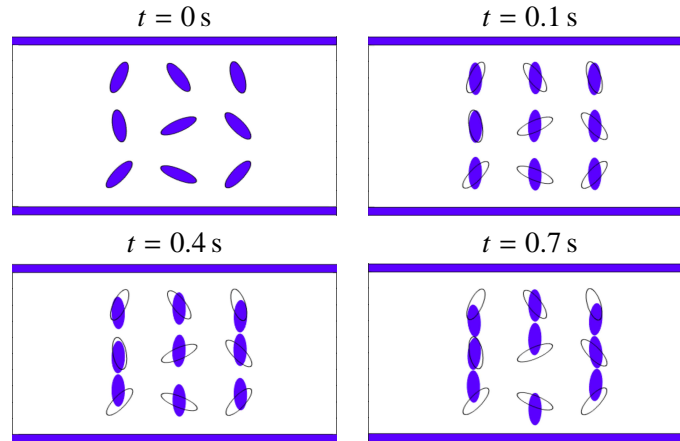


Figure 3.8: Evolution for nine identical particles initially placed on a square lattice. Empty and filled ellipsoids show the initial and actual positions respectively.

The inter-particle distance evolution is shown in Fig. 3.11. This suggests, that for the purpose of simulation of chain formation, it is sufficient to consider all particles to be aligned at the initial configuration. It has been shown that the final inter-particle distance tends to approach zero, the particles tend to be well connected within a chain. This agrees with the experimental observations of our earlier work, showing that regardless of the filler volume content, the inter-particle distance remains very small in dielectrophoretically structured composites [32]. The overall chain perfection degree as described in section 3.3.1 is calculated and plotted for four different time frames as shown in Fig. 3.12. Chains are labeled from left to right. A group of vertically oriented particles is considered a chain only if the

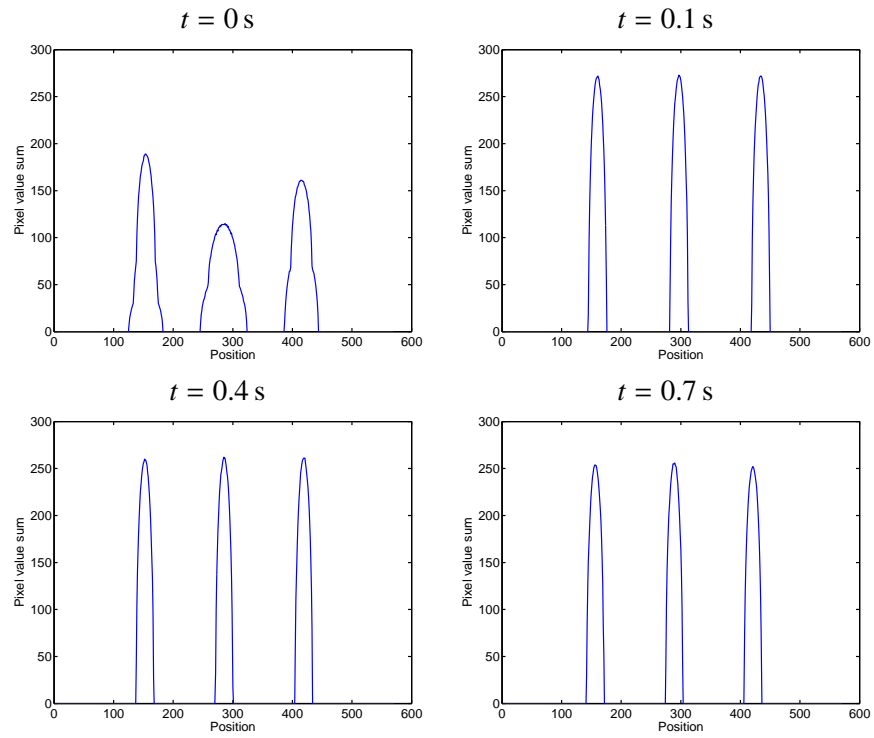


Figure 3.9: Chain identification process on the nine identical particles system.

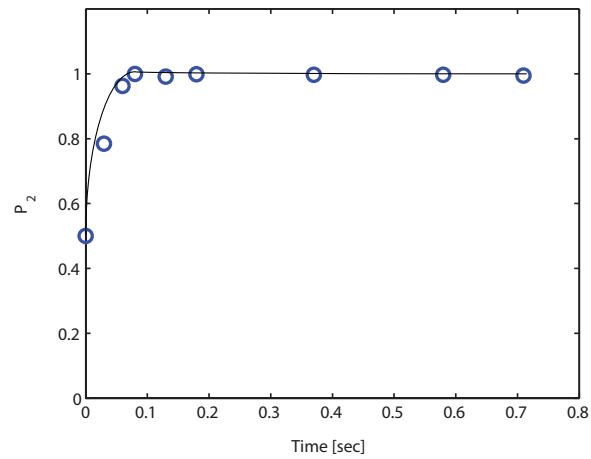


Figure 3.10: Evolution of the \bar{P}_2 parameter for nine identical particle system.

PD_c has a positive value. Therefore evolution of chain 1, and chain 3 during the dielectrophoresis process improves their PD_c from a negative value to 0.6 in 0.7 seconds. In other

words after 0.7 seconds the chain perfection degree of both chains approaches 60% of that of the ideal chain. In contrast to chain 1 and chain 3, chain 2 initially starts to form a chain, but the large inter-particle distance eventually results in a negative PD_c and ultimately to the dissolution of this particular chain.

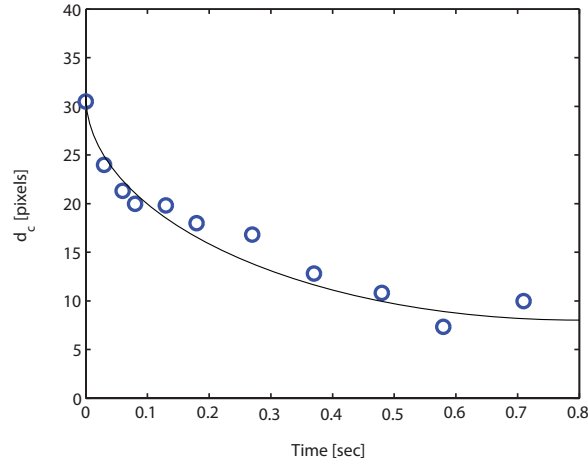


Figure 3.11: Evolution of the average inter-particle distance for nine identical particle system.

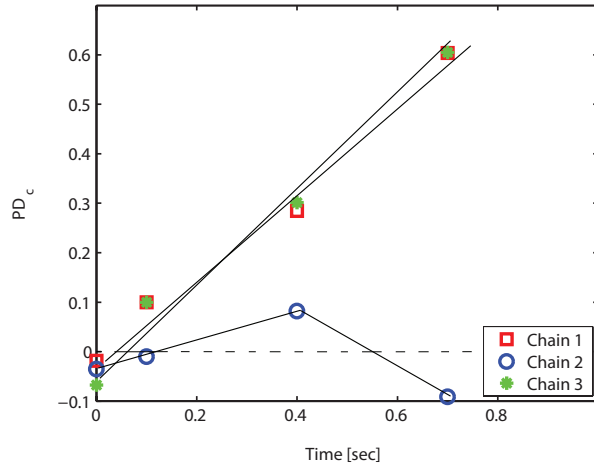


Figure 3.12: Evolution of the chain perfection degree (PD_c) parameter for nine identical particle system.

System containing particles of different aspect ratio

Subsequently, we study the case where one particle of an aspect ratio of five is combined with three particles with aspect ratio of 2.5, in order to study how heterogeneity can influ-

ence structure formation. As large particles create a more intense electric field it is expected that these act as a guide to determine the position of small particles. In this particular case, the three parallel particles are predicted to repel each other in the same fashion as the two parallel particles in Fig. 3.13. However, upon polarization the larger particle creates a more intense local field that ultimately leads to chain formation, as shown in Fig. 3.13. This shows that particle size is a key parameter in chain evolution process. Larger particles act as a guide for smaller particles, consequently dictating the kinetics and the final degree of orientation.

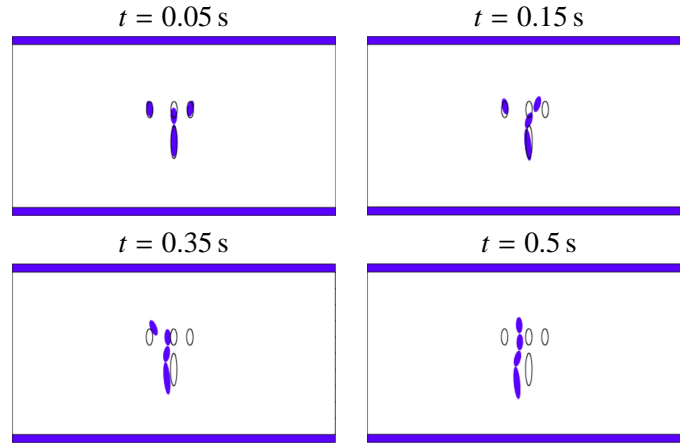


Figure 3.13: Structure evolution for the case of particles of different aspect ratio. Empty and filled ellipsoids show the initial and actual positions respectively.

System containing several particles of different size

A system combining several arbitrarily distributed big and small particles randomly distributed in space as shown in Fig. 3.14 is studied. It is observed, that after the electric field is applied, the small particles tend to fill in the gaps between big particles to form a chain. The output of the chain identification process is illustrated in Fig. 3.15. It can be seen that around $t = 0.1$ s four chains are identified. The total chain perfection degrees (PD_c) for $t = 0.1$ s and $t = 0.125$ s are calculated and plotted versus time as illustrated in Fig. 3.16. Chains are labeled from 1 to 4, from left to right respectively. At $t = 0.125$ s, chain 2 and chain 3 show perfection degrees of 0.7 and 0.5 respectively. For times shorter than $t = 0.1$ s individual chains can not be properly identified as shown in Fig. 3.15, and consequently, the the chain perfection degree can not be calculated.

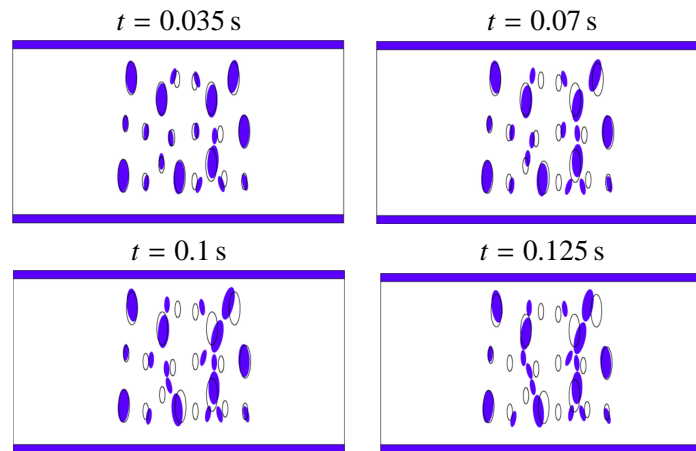


Figure 3.14: Structure evolution for the case of several particles of different size. Empty and filled ellipsoids show the initial and actual positions respectively.

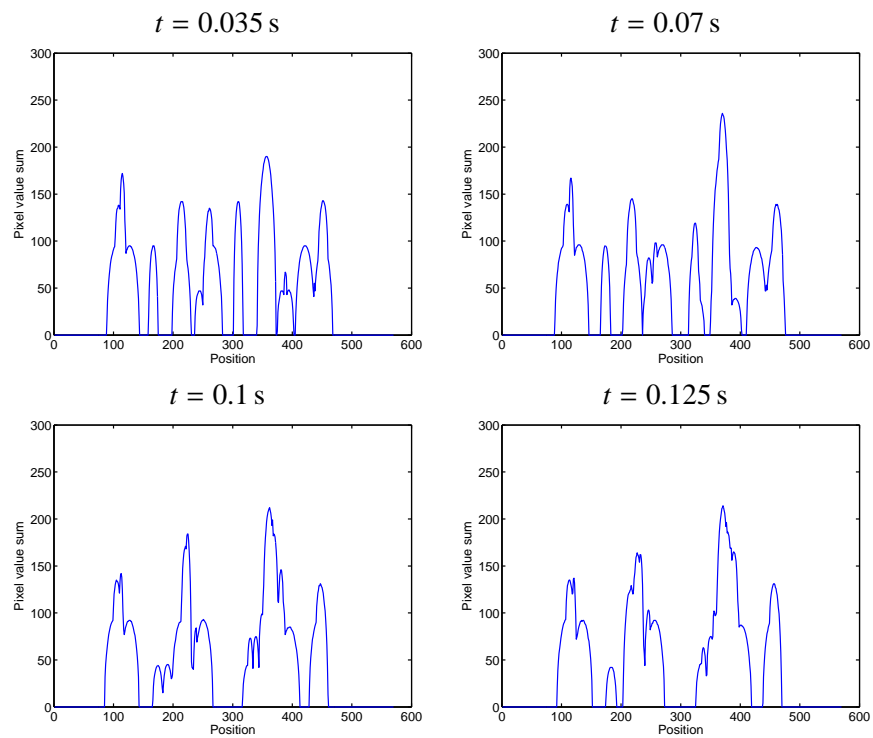


Figure 3.15: Output of the chain identification process for the case of several particles of different size.

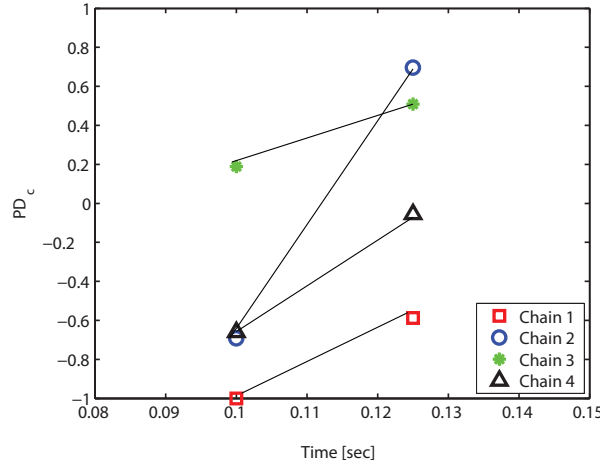


Figure 3.16: Evolution of the chain perfection degree (PD_c) parameter for a system of several particles of different size initially positioned randomly.

3.4 Conclusions

A numerical model is proposed to simulate the particle alignment and structure formation in a viscous matrix during dielectrophoresis for semi-dilute systems. The performance of the model is demonstrated in different systems. The general behavior after application of an electric field is summarized in two steps. First, reorientation of particles with respect to the imposed electric field occurs. Subsequently the orientation leads to thread formation in dilute systems. The model gives a quantitative handle on analyzing submodel performance in experimental systems.

The effect of particle aspect ratio has been shown to be of little importance on the alignment behavior of a single particle system. The initial configuration of a particle pair has been observed to be a key parameter in controlling the particle interaction. Repulsion is observed when a pair of particles are symmetrically aligned with the electric field, resulting in bare interaction after separation by a finite distance. However, chain formation is realized if the neighboring particles are initially located at off center positions. The effect of particle size and size distribution is investigated in a multi-particle system. Particle size distribution is found to be a key parameter in chain formation. Larger particles act as a guide for smaller particles, consequently dictating the kinetics and the final degree of orientation.

The quality of the structure evolution is investigated using a set of geometric parameters, which are estimated using image processing techniques. A new procedure to quantify the degree of chain formation and its quality is proposed and its value is demonstrated for the cases studied.

Ferroelectric characteristics of particulate PZT-epoxy composites

4.1 Introduction

Electroactive polymers showing significant deformation under electrical stimulation have attracted a lot of attention for new types of actuator materials due to their flexibility, low weight, high ductility and adequate strength, as well as ability to be molded into complex 3D configurations. However, they require very high electric fields (such as 200 MV/m) in order to present large strains [111–113]. Ceramic actuators, on the other hand, require lower electric fields, but they lack the flexibility and ductility of the polymers and normally require laborious high temperature processing [23].

The total strain, produced by a piezoelectric material under an electric field, consists of a strain due to piezoelectric effect and a strain due to electrostriction. Electrostriction refers to the strain induced by an applied electric field in all dielectrics, regardless of the symmetry. The effect, which is negligibly small in most materials, can be improved by increasing the dielectric constant of the material, so that the same electric field can induce higher polarization, and thus higher electrostrictive strain. One method to enhance the dielectric constant is by electron irradiation, as reported for P(VDF-TrFE) copolymers [114, 115]. Alternatively, the polymer material can be mixed with a filler of higher dielectric constant such as ceramics in the form of a composite structure to achieve a higher overall dielectric constant [116]. Therefore one might be interested in embedding high volume fractions of ceramic filler in a polymer in order to improve the permittivity. Unfortunately this would result in a higher stiffness which leads to lower actuation strains. An alternative solution is to optimize the connectivity pattern, the interspatial relationships between the constituent phases, in order to utilize a low volume fraction of the ceramic filler more efficiently. Structuring the ferroelectric ceramic particles in a polymer matrix by means of dielectrophoresis (DEP) has been shown to improve the piezoelectric properties (d_{33}) of these materials over those of random composites by forming columns of aligned particles in a form of quasi 1-3

composite [30, 31, 33, 117]. With the aim of designing new actuator materials with tunable electromechanical properties, which require a relatively low electric field and offer mechanical flexibility and ease of processing, the current chapter presents the evaluation of the actuation strain of PZT-epoxy composites. The effect of DEP structuring on the observed strain, as well as ferroelectric polarization behavior, as a function of the applied electric field is presented. Improved polarization, thus electrostrictive strain, as well as enhanced electromechanical properties, thus piezo-strain of the composite materials, results in more than doubling the overall strain compared to 0-3 composites. The enhanced actuation strain of quasi 1-3 composites is explained by a higher degree of parallel connectivity in these systems than in the unstructured 0-3 composites [32].

4.2 Theory

The total strain (S_{total}) produced by a piezoelectric material under an electric field can be expressed as the sum of piezo strain ($S_{piezoelectric}$) and strain due to electrostriction ($S_{electrostriction}$):

$$S_{total} = S_{piezoelectric} + S_{electrostriction} = d \cdot E + Q \cdot D^2 \quad (4.1)$$

where d is the piezoelectric charge coefficient, E is the applied electric field, D is the electric displacement, and Q is the polarization-related-electrostriction coefficient of the material. In this approach, the Maxwell strain, due to the electrostatic Coulomb attractive force between opposite charged faces of the dielectric material, is neglected as it is much smaller than the other two components. For linear dielectrics, the following equation for the electrostriction applies:

$$S_{electrostriction} = Q \cdot \epsilon_0^2 \cdot (\epsilon_r - 1)^2 \cdot E^2 \quad (4.2)$$

which relates the electrostriction strain ($S_{electrostriction}$) in the thickness direction of the film to the vacuum permittivity, ϵ_0 , the relative permittivity, ϵ_r , and the applied electric field, E [118]. Therefore, equation 4.1 can be rewritten as:

$$S_{total} = d \cdot E + M \cdot E^2 \quad (4.3)$$

where M is the electric field-related electrostriction coefficient of the material. For a fixed electric field, increasing the piezoelectric charge constant, or electrostriction coefficient will result in higher actuation strains.

The high field polarization, P , and strain, S , properties of structured composites are analytically derived, based on the model for the permittivity presented by Bowen for a composite consisting of an inert, non-piezo active polymer filled non-randomly by piezo active granular ceramic material [33]. In dielectrophoretically structured composites, closely packed particles within the chains experience more interaction in the direction of alignment than

homogeneously distributed particles in 0-3 composites. In this model, the composite material consists of two main phases, the non-piezoelectric polymer matrix, and the particle chain, connected in parallel in the electrical and mechanical domains. The particle chain itself includes particles and polymer in a serial connection. Particle size to interparticle distance ratio, being the dominant microstructural parameter, is given by R . The local electric field in the direction of the field in ceramic and polymer phases is given by:

$$\frac{E_p}{E_{applied}} = \frac{\epsilon_c \cdot (1 + R)}{\epsilon_c + R \cdot \epsilon_p} \quad (4.4)$$

$$\frac{E_c}{E_{applied}} = \frac{\epsilon_p \cdot (1 + R)}{\epsilon_c + R \cdot \epsilon_p} \quad (4.5)$$

where subscripts c and p represent ceramic and polymer, respectively. For a linear dielectric material, the induced polarization P_i , is the product of the dielectric constant and electric field. For ferroelectric materials, the spontaneous polarization, P_s , needs to be added. For 1-3 composites, each constituent material contributes to the total polarization in an amount proportional to their dielectric constants, and their volume fractions. To calculate the polarization, P , and strain, S , of structured composites the effective properties of the particle chains are calculated, and substituted for the properties of the active piezoelectric phase of fibrous 1-3 composites, as computed by Nelson [119]. The dielectric constant of a perfect 1-3 composite is given by:

$$\epsilon_{comp} = \epsilon_c \cdot \phi_c + \epsilon_p \cdot \phi_p - \frac{(d_{33c} - d_{33p})^2 \cdot s_{33comp} \cdot \phi_c \cdot \phi_p}{\epsilon_0 \cdot s_{33c} \cdot s_{33p}} \quad (4.6)$$

$$s_{33comp} = \frac{s_{33c} \cdot s_{33p}}{s_{33p} \cdot \phi_c + s_{33c} \cdot \phi_p} \quad (4.7)$$

where ϵ is the dielectric constant, ϵ_0 is the vacuum permittivity, s_{33} is the compliance, ϕ_c is the volume fraction of the ceramic and ϕ_p is the volume fraction of the polymer phase.

The effective compliance of a particle chain in the mechanical domain is calculated as:

$$s_{33eff} = \frac{s_{33p} + R \cdot s_{33c}}{1 + R} \quad (4.8)$$

The effective d_{33} of the chain is:

$$d_{33eff} = \frac{(1 + R) \cdot \epsilon_p}{\epsilon_c + R \cdot \epsilon_p} \cdot d_{33c} \quad (4.9)$$

The effective ϵ of the chain is:

$$\epsilon_{eff} = \frac{\epsilon_p \cdot (1 + R)}{\epsilon_c + R \cdot \epsilon_p} \cdot \epsilon_c \quad (4.10)$$

Substituting Eq. 4.8, Eq. 4.9 and Eq. 4.10 for s_{33c} , d_{33c} and ϵ_c in Eq. 4.6, and multiplying both sides of this equation by E_{app} and substituting Eq. 4.4 and Eq. 4.5 the induced polarization of the structured composite is found to be:

$$P_{DEP}(E_{app}) = P_c(E_c) \cdot \phi_c + \frac{\epsilon_c + R \cdot \epsilon_p}{\epsilon_c \cdot (1 + R)} \cdot P_p(E_p) - \frac{\left(\frac{\epsilon_p \cdot (1+R)}{\epsilon_c + R \cdot \epsilon_p} \cdot d_{33c}\right)^2 \cdot \phi_c \cdot \phi_p}{\epsilon_0 \cdot (\phi_c \cdot s_{33p} + \phi_p \cdot \frac{s_{33p} + R \cdot s_{33c}}{1+R})} \cdot E_{app} \quad (4.11)$$

The total strain, as shown earlier (Eq. 4.1), is a sum of piezoelectric and electrostrictive strains. The piezoelectric strain in a perfect 1-3 composite is derived by multiplying the analytical expression for d_{33} of the composite by the electric field, as shown by Nelson [119].

$$d_{33comp} = d_{33c} \cdot \frac{\phi_c \cdot s_{33p}}{\phi_c \cdot s_{33p} + \phi_p \cdot s_{33c}} \quad (4.12)$$

Multiplying the above analytical expression for d_{33} by the applied electric field, E_{app} , and substituting the Eq. 4.5, as well as the effective properties of the particle chain, Eq. 4.9 and Eq. 4.8, for d_{33c} and s_{33c} , the out-of-plane piezoelectric strain of a structured composite is given by:

$$S_{piezoelectric}(E_{app}) = S_c(E_c) \cdot \frac{\phi_c \cdot s_{33p}}{\phi_c \cdot s_{33p} + \phi_p \cdot \left(\frac{s_{33p} + R \cdot s_{33c}}{1+R}\right)} \quad (4.13)$$

Taking the polymer phase as being electrostrictive only, the total strain of the DEP composite, including electrostriction and piezoelectric strains according to Eq. 4.3 becomes:

$$S_{total} = S_c(E_c) \cdot \frac{\phi_c \cdot s_{33p}}{\phi_c \cdot s_{33p} + \phi_p \cdot s_{33c} \cdot \frac{s_{33p} + R \cdot s_{33c}}{1+R}} + \phi_p \cdot M_p \cdot E_p^2 + \phi_c \cdot M_{eff} \cdot E_c^2 \quad (4.14)$$

where M_p and M_{eff} are electric field related electrostrictive coefficients of the polymer and particle chain, respectively.

$$M_p = Q_p \cdot \epsilon_0^2 \cdot (\epsilon_p - 1)^2 \quad (4.15)$$

$$M_{eff} = Q_c \cdot \epsilon_0^2 \cdot (\epsilon_{eff} - 1)^2 = Q_c \cdot \epsilon_0^2 \cdot \left(\frac{\epsilon_p \cdot \epsilon_c \cdot (1 + R)}{\epsilon_c + R \cdot \epsilon_p} - 1\right)^2 \quad (4.16)$$

4.3 Experimental procedure

4.3.1 Composite manufacturing

Lead zirconate titanate ceramic powder (PZT5A4), a Niobium doped PZT powder with a Zr/Ti molar ratio of 52/48, was received from Morgan Electroceramics UK. The ceramic powder was calcined at 1150 °C for 1 h according to the optimized scheme reported by Van den Ende [11]. The agglomerated powder was then dry-milled, using 5-mm zirconium balls for 2 h in a single G90 jar mill. The particle size distribution of the milled powder in an aqueous solution with 10% isopropyl alcohol, measured by a Beckman Coulter LS230 laser diffraction analyzer, was found to be $d(50) = 2.5 \mu\text{m}$. The powder was stored in a drying oven at 120 °C for 24 h prior to the experiment, to avoid moisture adsorption. A two component epoxy system (Epotek 302-3M, Epoxy (diglycidyl ether of bisphenol-A (DGEBA) resin and poly(oxypropyl)-diamine (POPD) multifunctional aliphatic amine curing agent, was used.

The PZT particles were dispersed in the resin component of the epoxy to the specific volume fractions of 10%, 20%, 30%, 40% and 50% and mixed at a speed of 1000 RPM for 15 min, using a planetary mixer (SpeedMixer DAC 150.1 FVZ, Hauschild). Subsequently, the hardener was added, and the composite resin was again mixed at 1500 RPM for 3 min. Finally, the uncured ceramic-polymer mixture was degassed and poured into a mold consisting of a 1 mm thick Teflon sheet with circular 15 mm diameter cut-outs. 0-3 composites were cured at room temperature. To produce structured composites, the slurry was placed between two layers of 50 μm thick Aluminium foil serving as the temporary electrodes for the application of the electric field for DEP, as shown in Chapter 2. Dielectrophoresis process was performed using an electric field of 2 kV/mm and frequency of 2 kHz during curing of the composite at room temperature for 3 h.

4.3.2 Measurement procedure

The dielectric constants of the composites were determined using the parallel plate capacitor method with an Agilent 4263B LCR meter (Japan) at 1 V and 1 kHz. The piezoelectric coefficient, d_{33} , measurements were performed with a high precision PM300 Piezometer (Piezosystems) at 110 Hz and under a static and dynamic force of 10 N and 0.25 N, respectively. At least five samples for each composite system were tested. Ferroelectric polarization measurements were performed using a Radiant technologies Precision Multiferroic Test System at 1 Hz and under a double bipolar triangular pulse, with a peak from 0 to 18 kV/mm, as shown in Fig. 4.1.

Out-of-plane displacement measurements were performed using a photonic sensor, MTI-2100, with a 2032X high resolution module in combination with the Precision Multiferroic Test System, as shown in Fig. 4.1. The sensor utilizes adjacent pairs of light-transmitting and light-receiving fibers. It operates by measuring the interaction between the field of illumination of the transmitting, or source fibers, and the field of view of the receiving, or detector fibers. As the surface of the sample moves away from the sensor tip, the signal

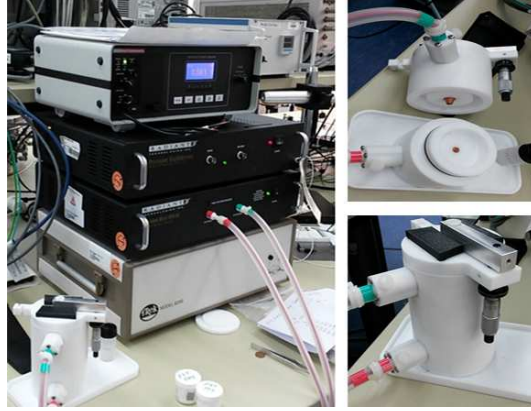


Figure 4.1: Ferroelectric polarization and strain test set-up. The test jig is shown in higher magnification.

decreases, and as the surface moves closer to the sensor tip, the signal increases. The probe is used in the high-resolution mode with a sensitivity of $0.000019 \mu\text{m}/\text{mV}$. The out-of-plane strain, S_{33} , was measured at 1 Hz under double bipolar alternating electric field, E , using:

$$S_{33} = \frac{\Delta t}{t} \quad (4.17)$$

where t is the thickness of the sample under test, and Δt is the change in thickness.

4.4 Results and Discussion

The typical electric displacement and strain behavior of PZT5A4 ceramic at 1 kHz is presented in Fig. 4.2. A maximum polarization of $42 \mu\text{C}\cdot\text{m}^{-2}$, a remanent polarization of $38 \mu\text{C}\cdot\text{m}^{-2}$, and a coercive field of $1.3 \text{ kV}/\text{mm}$ is observed.

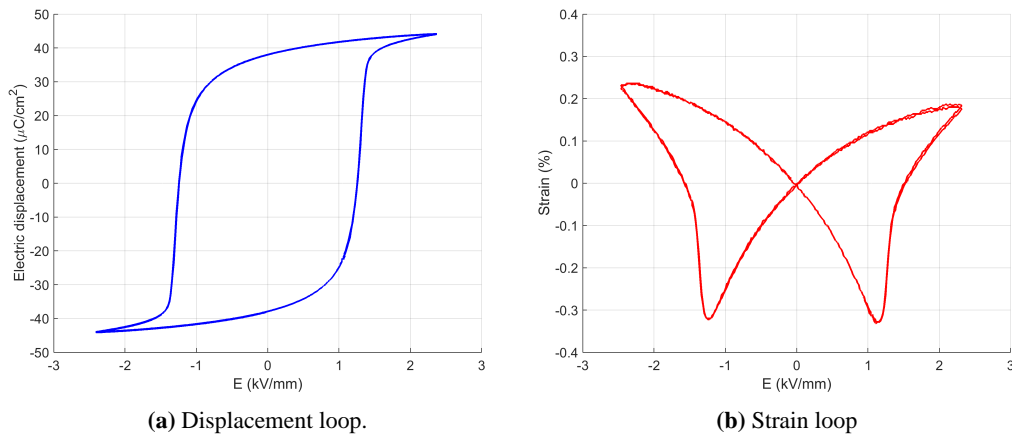


Figure 4.2: Ferroelectric hysteresis loops of PZT5A4 ceramic tested at 1 kHz.

The effect of dielectrophoretic structuring on the ferroelectric displacement and strain of the PZT-epoxy composites, for different PZT volume content, is shown in Fig. 4.3 and Fig. 4.4, respectively.

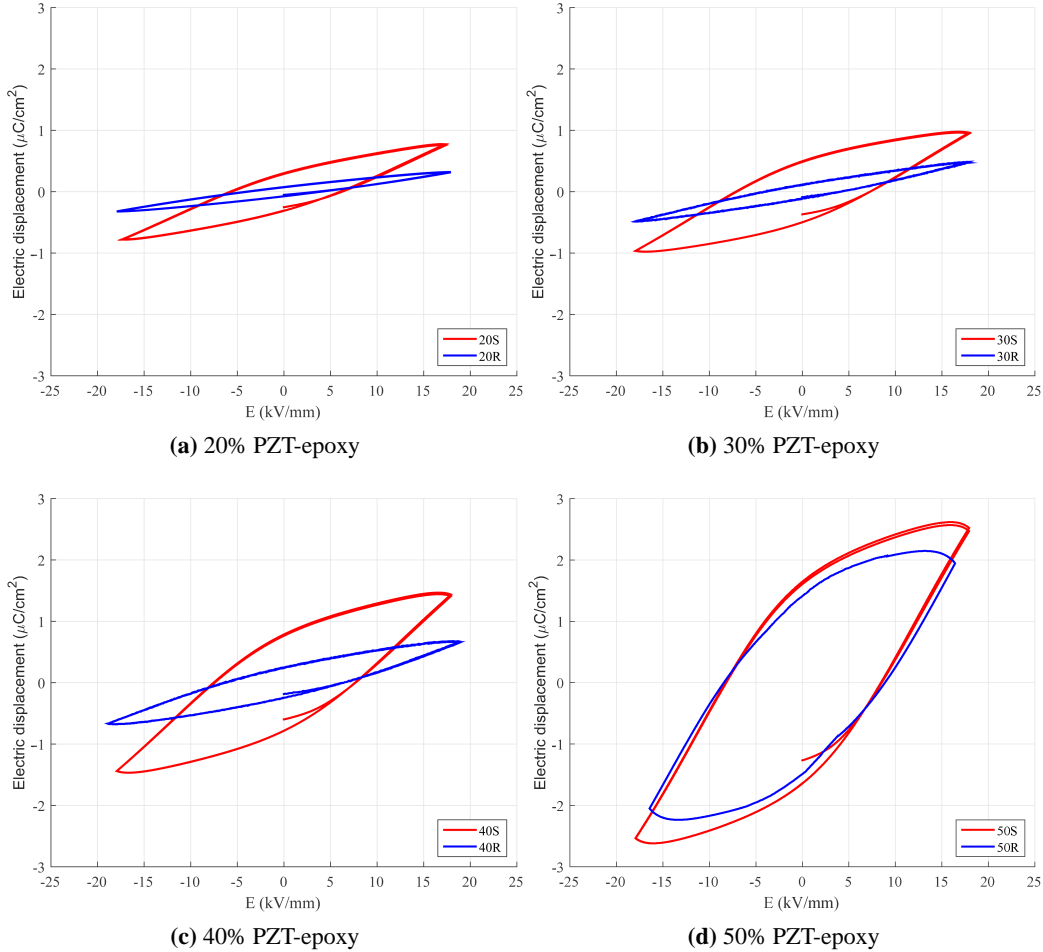


Figure 4.3: Effect of dielectrophoresis structuring on electrical displacement of of PZT-epoxy composites. *R* and *S* stand for random and structured composites.

With increasing the filler volume content the remanent polarization of the composite increases, while the coercive field remains constant at $9 \text{ kV}/\text{mm}$, which is approximately seven times higher than the coercive field of the bulk PZT5A4 ceramic. At all volume fractions, the dielectrophoretically structured composites exhibit higher polarizations than their non-structured counterparts. A maximum remanent polarization of $1.8 \mu\text{C}/\text{cm}^2$ is observed for the structured composite of 50% PZT-epoxy. Increasing the applied electric field above $18 \text{ kV}/\text{mm}$ resulted in an electrical break-down of the samples. In addition to the displacement-electric field (D-E) loop, polarization switching leads to strain-electric field hysteresis. The bipolar strain hysteresis loops plotted as a function of applied electric field,

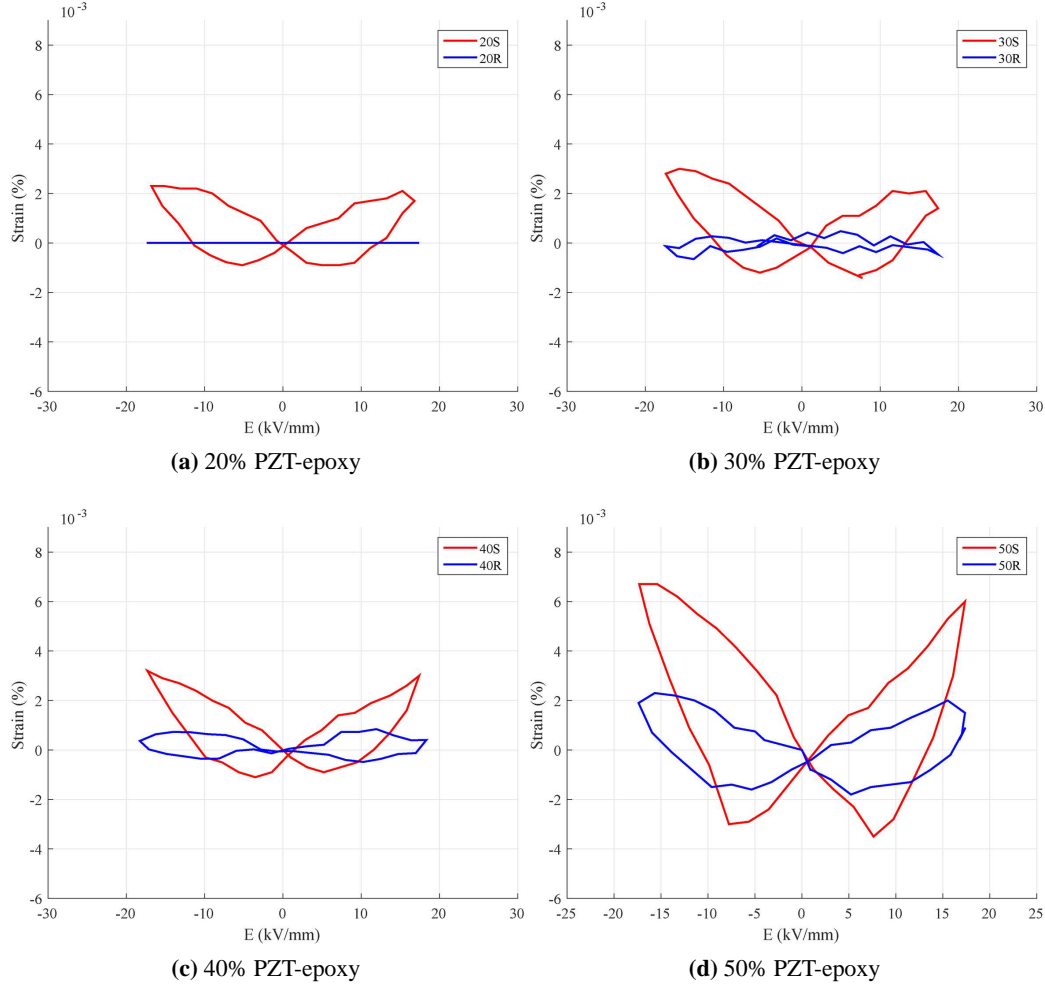


Figure 4.4: Effect of dielectrophoresis structuring on electromechanical strain of PZT-epoxy composites. *R* and *S* stand for random and structured composites.

so-called butterfly curves, are presented in Fig. 4.4. The shape of the strain response is similar to that of the bulk PZT5A4 ceramic [23]. As the electric field is applied, the converse piezoelectric effect results in strain. As the field increases, the strain is no longer linear with the field, as domains start switching. Switching is observed at a field of 9 kV/mm for random and structured composites, in agreement with the coercive field, as determined from the D-E loops. The maximum strain of 0.006 % is substantially lower than that of the bulk material (see Fig. 4.2).

The maximum observed strain at 18 kV/mm is extracted from Fig. 4.4, and presented as a function of ceramic volume fraction for random and structured composites in Fig. 4.5. A clear difference can be observed between random and structured samples. Random composites show no or very little strain at low PZT volume content below 30%. The effect

of structuring on the strain is already significant from 10% PZT-epoxy composite, and increases continuously up to 50% PZT. The predictions of the model presented earlier are also shown in Fig. 4.5. The input materials properties for modeling are listed in Table 4.1. The best fit of the model to the experimental data was obtained for $R = 20$ for structured and $R = 2$ for random composites respectively, which shows much lower interparticle distance for the structured composites with the same particle size. Such a strong reduction in particle distance along the chains formed in the quasi 1-3 composites has been confirmed by SEM [31].

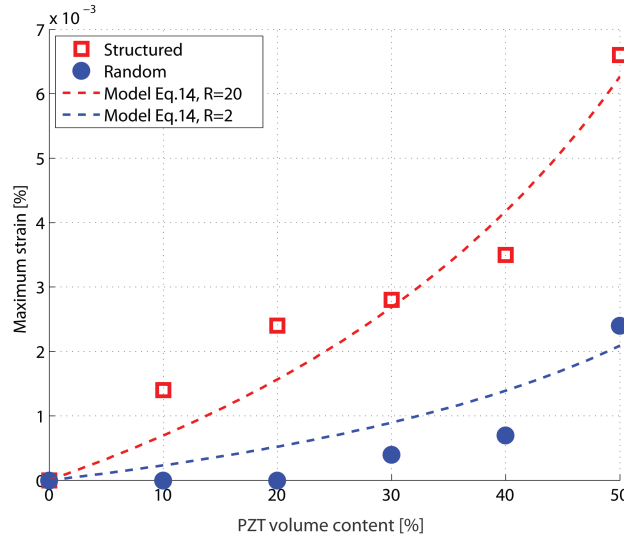


Figure 4.5: Maximum observed strain at the $E_{applied}$ of 18 kV/mm as a function of PZT content.

Material	ϵ at 1 kHz	d_{33} (pC/N)	P ($\mu\text{C}/\text{cm}^2$)	Y (GPa)	s_{33} (TPa) ⁻¹	s_{11} (TPa) ⁻¹	Q (m ⁴ /C ²)
PZT	1700 [81]	440 [81]	50	92 [18]	18.8 [120]	16 [120]	0.018 [121]
Epoxy	4.6	0	0	1.7 [11]	128 [86]	128 [86]	1

Table 4.1: Properties of ceramic inclusions and polymer matrix.

In order to understand the effect of dielectrophoretic alignment of particles on the electromechanical strain of the composites, the mixed connectivity model [83] is used to estimate the amount of 1-3 connectivity in these composites. This model considers that both parallel and serial connectivity can exist in a granular composite, giving a tri-phasic system. The detailed calculation procedure to extract the degree of 1-3 connectivity, the percentage of particles in direct contact along a chain spanning the thickness of the sample in the direction of the applied field, is explained in Chapter 2. The calculated percentage of 1-3 connectivity is shown as a function of ceramic volume fraction in Fig. 4.6.

A maximum of 4.6 % of parallel connectivity has been calculated for the structured composite of 50 vol% PZT. The maximum electromechanical strain of PZT-epoxy composites, with varying PZT content of 10%-50%, is plotted as a function of the degree of 1-3 con-

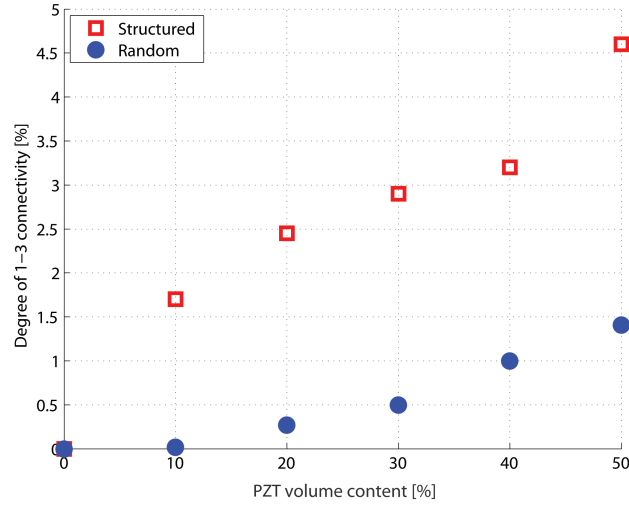


Figure 4.6: Degree of 1-3 connectivity as a function of PZT content.

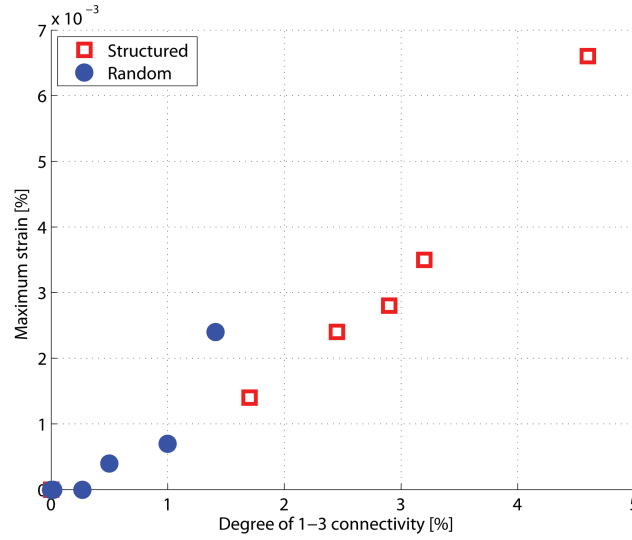


Figure 4.7: Maximum electromechanical strain of PZT-epoxy composites at the E_{applied} of 18 kV/mm as a function of degree of 1-3 connectivity.

nectivity in Fig. 4.7. Regardless of the volume fraction of the ceramic phase, increasing the parallel connectivity improves the maximum observed strain in structured composites, compared to the random composites.

The R values obtained, based on fitting the model developed in this work to the experimental data, are of the order of 20 and 2 for the structured and random composites respectively, which is another indication of the higher connectivity in the direction of the chains. Predictions of the normalized strain as a function of R for different PZT volume fractions in

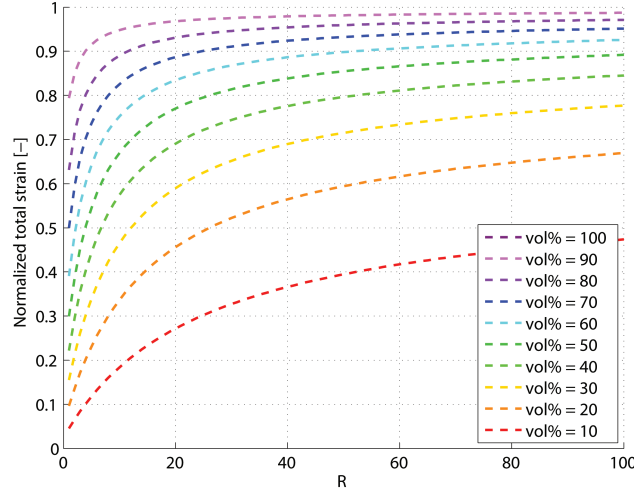


Figure 4.8: Predictions of the proposed model (Eq. 4.14) for the total strain of the composites normalized to the strain of bulk ceramic, as a function of R at the E_{applied} of 18 kV/mm, shown for different PZT volume fractions in PZT-epoxy composites.

PZT-epoxy composites is shown in Fig. 4.8. The strain values are normalized to the strain value for the bulk PZT5A4 ceramics under the applied electric field conditions. The figure shows a very clear increase in achievable strain for R values between 1 and 20. The rate of increase in maximum strain is highest at high loading fractions. This is in qualitative agreement with the dependence of g_{33} , the piezoelectric charge coefficient, of quasi 1-3 composites on volume fraction and degree of orientation, which reaches a maximum efficiency at a volume fraction of 10-20%, for R values between 10 and 20 [32]. Increasing the R value from 2 to 20 results in an improvement factor of 2-3 in the normalized strain values, which is in a good agreement with the experimental data in Fig. 4.5.

4.5 Conclusions

DEP structured PZT-polymer particulate composites, having superior low field piezoelectric constants compared to 0-3 granular particle composites, are studied at high electric fields. The ferroelectric polarization and strain loops are obtained at PZT volume fractions 10%-50%. The high electric field strain of the PZT-polymer composites is related to both the piezoelectric and electrostrictive properties of the constituent phases. The effect of interparticle distance on the final polarization and strain properties is modeled. The model predictions correlate well with experimental strain values for 0-3 and quasi 1-3 particulate composites. Increasing the amount of parallel connectivity leads to larger strains.

In-situ structuring and poling of PZT-epoxy composites *

5.1 Introduction

As stated and demonstrated in the previous chapters, the key parameters controlling the effective properties of the structured composites are the quality of particle alignment, as well as the poling efficiency. Improving the filler orientation while keeping the filler volume fraction low leads to a high electroactive sensitivity, while maintaining the flexibility levels of the composites [31, 33–35]. Enhancing the alignment quality, by means of decreasing the interparticle distance has been shown to significantly improve the dielectric, piezoelectric and pyroelectric properties of particulate composites [11, 32]. In conventional biphasic ferroelectric ceramic-polymer composites, the polymer phase normally has a lower permittivity and a lower electrical conductivity compared to the ceramic particles. Thus, a high AC field at elevated temperatures for an extended period of time is required for efficient poling [122, 123]. Hence, the poling process, as well as the resulting effective properties of the composites, remain a challenge in the production of such composites. Recent investigations have shown that the electrical conductivity of the constituents has a significant effect on the dielectric, piezoelectric and pyroelectric properties of the granular composites [100]. It has been reported that an enhanced electrical conductivity of the matrix shortens the build-up time of the electric field acting on the ceramic particles. Therefore, for an electrically conductive matrix efficient poling of the composites is possible even at room temperature, with short poling times and relatively low electric fields. The electrical conductivity of thermoset polymer matrices as well as their permittivity decrease upon curing. Thus, combining the DEP structuring, using an AC electric field, and DC poling conditions, while the matrix is in the liquid state can improve the poling efficiency of composites. Moreover, the

*This work has been submitted as: Khanbareh, H., van der Zwaag, S., Groen, W. A., In-situ poling and structuring of particulate piezoelectric composites, (under review, Journal of Intelligent Material Systems and Structures, 2016)

new proposed technique leads to cost effective single-step manufacturing of composite sensors. In the present work, the in-situ dielectrophoretic structuring and poling process of lead zirconate titanate-epoxy composites, upon application of AC and DC electric fields is investigated. The effect of processing parameters on the structuring configuration, as well as final properties of the composites, are demonstrated.

5.2 Experimental procedure

5.2.1 Composite manufacturing

Lead zirconate titanate ceramic powder (PZT5A4), a Niobium doped PZT powder with a Zr/Ti molar ratio of 52/48, was received from Morgan Electroceramics UK. The ceramic powder was calcined at 1150 °C for 1 h according to the optimized scheme reported by Van den Ende [11]. The agglomerated powder was then dry-milled using 5-mm zirconium balls for 2 h, using a single G90 jar mill. The particle size distribution of milled powder in an aqueous solution with 10% isopropyl alcohol, measured by a Beckman Coulter LS230 laser diffraction analyzer, was found to be $d(10) = 1.2 \mu\text{m}$, $d(50) = 2 \mu\text{m}$, and $d(90) = 8.5 \mu\text{m}$. The powder was stored in a drying oven at 120 °C for 24 h prior to the experiment, to avoid moisture adsorption. A two component epoxy system (Epotek 302-3M, Epoxy (diglycidyl ether of bisphenol-A (DGEBA) resin and poly(oxypropyl)-diamine (POPD) multifunctional aliphatic amine curing agent, was used. Both components were degassed separately in a vacuum oven at RT for 3 h prior to the experiment to avoid air void formation. The PZT particles were dispersed in the polymer resin to the specific volume fractions of 10%, 20%, 30%, 40% and 50%. Subsequently, the slurry was degassed for 5 min, then mixed with the hardener, and degassed for another 5 min. The slurry was then molded. The details of the mold layup are presented in [32]. Three sets of samples under specific combinations of AC and DC bias were prepared, as indicated in Table 5.1. The electric field was applied using a function generator (Agilent, 33210A), coupled to a high voltage amplifier (Radiant Technologies Inc., T6000HVA-2). The optimum frequency level was obtained for the highest phase angle of Lissajous plots for each volume fraction in early stages of the cure. Each set was exposed to the specific electric field for 3 h, then cured over-night at room temperature in the presence of the electric field. The samples were stored at 100 °C for 24 h, with their electrodes short circuited prior to the measurements, in order to remove the injected charges during the polarization and the trapped charges due to impurities.

Set	$E_{AC}(\text{kV/mm})$	$f_{AC}(\text{kHz})$	$E_{DC}(\text{kV/mm})$
Set 1	1	2	2
Set 2	0.1	2	2
Set 3	0	0	2

Table 5.1: Different combinations of AC and DC electric fields used for manufacturing of the composites. The AC field magnitudes apply to the peak values.

The first two sets result in quasi 1-3 composites with different degree of structuring, while Set 3 yields a 0-3 composite poled while curing. The properties of the obtained composites are compared with those of the reference samples, reported by Van den Ende et al. [31]. The reference composites were processed at a fixed applied field of $E_{AC} = 1$ kV/mm and $f = 4$ kHz, poled at 10 kV/mm at 100 °C in a silicone oil bath for a duration of 30 min. The microstructures of the samples were observed, using a field emission-scanning electron microscope (FE-SEM) (JEOL, JSM-7500F), operated in backscattered electron mode. Samples sectioned parallel to the formed particle chains were embedded in a room temperature curing epoxy, and polished with 1 μ m diamond paste.

5.2.2 Measurement procedure

The dielectric constants of the composites were determined using the parallel plate capacitor method with an Agilent 4263B LCR meter (Japan) at 1 V and 1 kHz. The curing study of the epoxy polymer as a function of temperature was performed using a broadband spectrometer (Novocontrol), in conjunction with a Cryostat high temperature sample cell, as well as an Agilent E4991A impedance analyzer at 1 V and 1 kHz. The piezoelectric coefficient, d_{33} , measurements were performed with a high precision PM300 Piezometer, Piezosystems, at 110 Hz and a static and dynamic force of 10 N and 0.25 N respectively.

5.3 Results and discussion

5.3.1 Microstructure of composites

Fig. 5.1 shows Scanning Electron Microscope (SEM) images of 20% PZT-epoxy composites prepared by means of conventional method and in-situ structuring and poling as defined in Table 5.1.

The average particle size, based on SEM microstructures matches well with the result of particle size analysis. Chain-like structures along the direction of the electric field are formed during dielectrophoresis. In the random composites, the PZT particles are homogeneously distributed in the epoxy matrix (Fig. 5.1c for set 3, and 5.1d for a reference random post-curing-poled sample). For the conditions of set 1 (a strong AC field), the microstructure (Fig. 5.1a) shows a well developed fibrillar structure, which resembles the structure of a reference quasi 1-3 sample produced by successive DEP and poling process steps (Fig. 5.1d). Application of a lower AC field strength (set 2, Fig. 5.1b) leads to well oriented particles, but a less well developed fibrillar structure, with wider particle free regions separating the particle chains. This difference is in excellent qualitative accordance with the results of the computational DEP model (Chapter 3) which show that formation of orientational order precedes the thread formation (Fig. 3.8 and Fig. 3.14).

The average orientation of the individual chains can be quantified via the \bar{P}_2 average orientation factor as shown in 3.11 [110]. \bar{P}_2 ranges between 0 for a random microstructure and 1 for a fully aligned situation. The \bar{P}_2 parameter calculated for set 1, set 2 and the reference

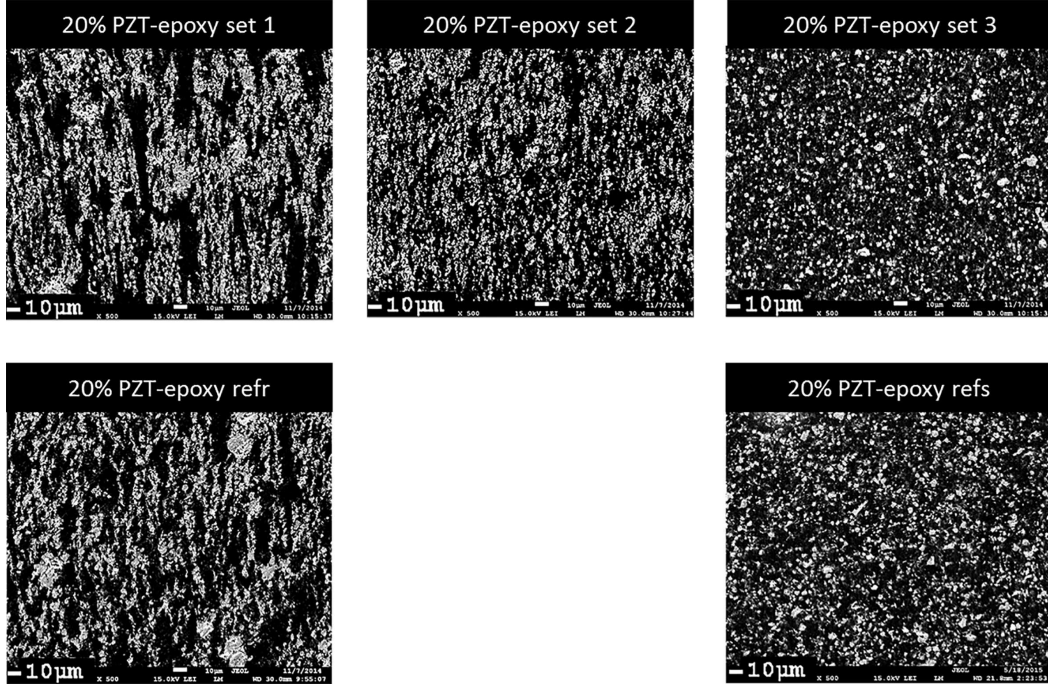


Figure 5.1: SEM micrographs of 20% PZT-epoxy composites prepared using conventional and in-situ techniques. refr and refs stand for reference random and reference structured samples.

structured composites are 0.99, 0.91, and 0.94 respectively. The \bar{P}_2 for set 3 and the reference random composite are 0. A slightly higher degree of orientation is observed for set 1, compared to set 2, as a result of larger driving force acting on the particles, in response to a larger imposed electric field [85].

5.3.2 Functional properties

The dielectric properties of the composites are shown in Fig. 5.2 for PZT volume fractions ranging from 0% to 50%. The models proposed by Yamada [36] (Eq. 2.2) and Bowen [33] (Eq. 2.3) are used to describe the dielectric properties of the random and structured composites, respectively.

The input parameters, for both random and structured composite modeling, are listed in Table 5.2. It is assumed, that the piezoelectric properties of the particles are equal to the bulk ceramic values, as the particle properties could not be measured directly.

Materials	ϵ at 1 kHz	d_{33} (pC/N)	Y (GPa)
PZT5A4	1850 [120]	460 [120]	70
Epoxy Epotek	4.6	0	1.7 [31]

Table 5.2: Properties of ceramic and polymer phases at 25 °C.

The best fit of the experimental data to Yamada's model, for both the reference random composite and the in-situ poled random composite, was obtained for $n = 4.4$, which is an indication of particles having an aspect ratio of 1.3, which is close to an equiaxed shape. The best fit of the experimental data to Bowens's model for the structured composites of set 1, set 2, and the reference structured sample, was obtained for R values of 11, 9 and 13, respectively.

The piezoelectric charge coefficients, d_{33} , of the composites, are shown in Fig. 5.3 where the experimentally observed d_{33} values of both structured and random composites are plotted in combination with the predictions of the models proposed by Yamada (Eq. 2.4) and Van den Ende (Eq. 2.5).

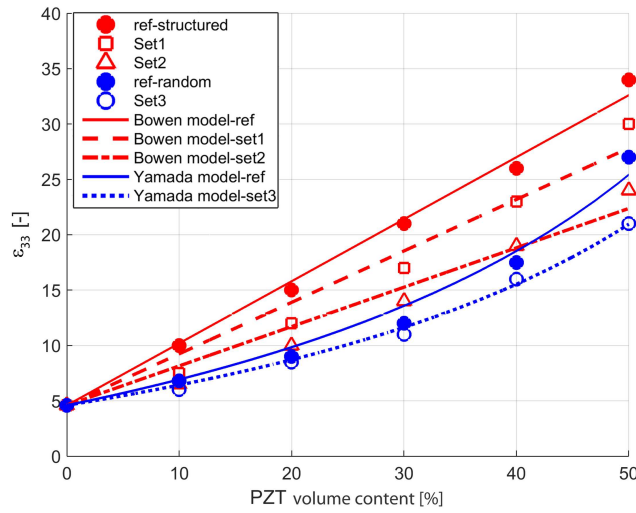


Figure 5.2: The dielectric constant data for PZT-epoxy composites with their associated models.

The best fit of the experimental d_{33} data to Yamada's model was obtained for $\alpha = 0.85$ and 1 for the reference random composite and the in-situ poled random composite, respectively. This is a clear indication of higher poling efficiency for the in-situ poled composites than for conventionally poled samples, in which the matrix was fully cross-linked.

The electrical conductivity (σ) and permittivity (ϵ) of a fully cured epoxy polymer is compared to that of an uncured epoxy in Table 5.3. The conductivity of the uncured epoxy measured at 20 °C is more than an order of magnitude higher than that of the cured epoxy tested at 100 °C, which is the poling temperature in the conventional method [31]. Higher permittivity of the uncured state also results in an enhanced poling efficiency in the uncured matrix. This shows that poling the particulate composites at room temperature is possible at much lower electric fields, when the polymer matrix is still in the liquid state, and has a relatively high permittivity and electrical conductivity.

The best fit of the experimental data to Bowens's model for the structured composites of set 1, set 2, and the reference structured sample, was obtained for R values of 16, 8, and 12 respectively. The interparticle distances calculated based on the obtained R values and

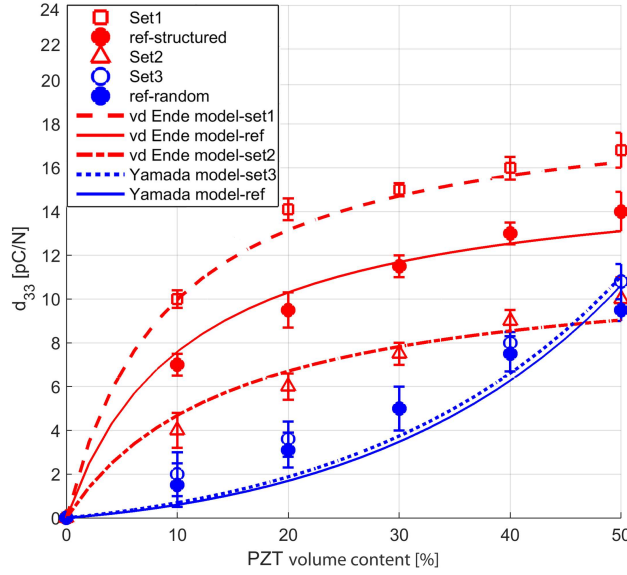


Figure 5.3: The d_{33} data for PZT-epoxy composites with their associated models.

Polymer	Test T ($^{\circ}\text{C}$)	σ (S/cm)	ϵ
Uncured epoxy	20	1.1×10^{-8}	12
Cured epoxy	100	8×10^{-10}	10.5

Table 5.3: Comparison of dielectric and electrical properties of cured and uncured epoxy polymer at 1 kHz.

the measured average particle size are $0.12 \mu\text{m}$, $0.25 \mu\text{m}$, and $0.16 \mu\text{m}$ for set 1, set 2, and the reference structured sample respectively. A higher degree of perfection during dielectrophoresis is realized for the chains formed in in-situ structured and poled samples, which can also be deduced from the SEM microstructures in Fig. 5.1.

The interparticle distance is an important parameter influencing the local electric field acting on the ceramic particles. The interparticle distances at the various volume fractions and poling conditions have been estimated independently by fitting the model to the experimental data. The correlation between the d_{33} of the random and structured composites and their respective average interparticle distance is shown in Fig. 5.4. The d_{33} values increase non-linearly with decreasing the interparticle distance.

The piezoelectric voltage coefficient, g_{33} , calculated by dividing the d_{33} values by their corresponding dielectric constant values, are plotted as a function of PZT volume fraction in Fig. 5.5.

The maximum value obtained for the conventionally prepared random composite is 48 mV.m/N at a PZT volume fraction of 40%, while for the in-situ poled random composite a maximum value of 58 mV.m/N is obtained, at a PZT volume fraction of 50%. All sets of structured composites show a comparable behavior as a function of PZT content, and peak at a volume fraction of 10% PZT. For the reference structured composite a maximum g_{33}

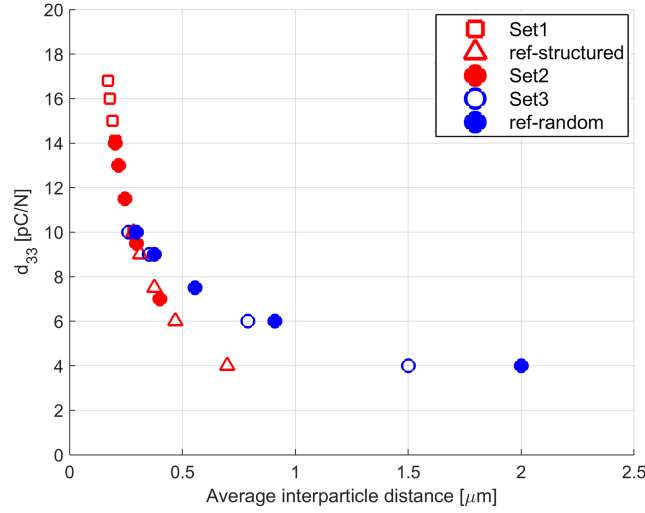


Figure 5.4: The d_{33} as a function of interparticle distance for random and structured composites.

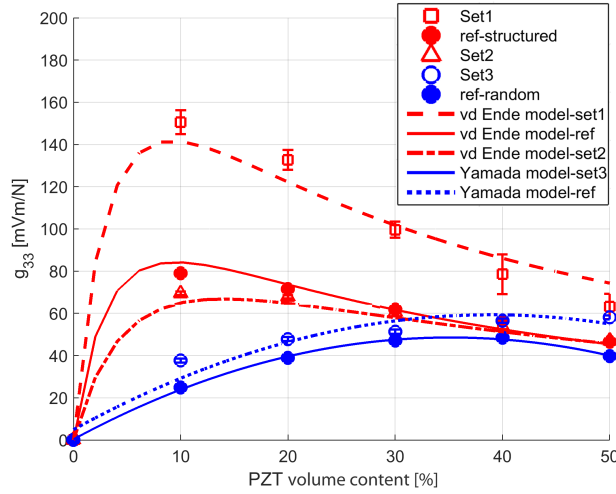


Figure 5.5: The g_{33} data for PZT-epoxy composites.

value of 79 mV.m/N is obtained. The in-situ structured and poled samples of set 1 and set 2, with high and low degree of chain perfection, show maximum g_{33} value of 151 mV.m/N and 69 mV.m/N at a PZT volume fraction of 10%, respectively. Superior g_{33} values, obtained for in-situ structured and poled samples, are attributed to a higher chain perfection degree, and a higher poling efficiency. The reason for the deviation of the experimentally determined g_{33} values from the predictions of the model is due to a few air voids in the sample.

5.4 Conclusions

A significant improvement in piezoelectric properties of quasi 1-3 composites can be achieved by a simultaneous combination of the dielectrophoretic alignment of the ceramic particles and the poling process while the polymer matrix is still in the liquid state, and has a relatively high permittivity as well as electrical conductivity compared to a fully cured system. The proposed method offers new avenues in low cost manufacturing of composite pressure sensitive materials for demanding long term sensor applications.

Chapter 6

Structure and properties of PT-polyethylene oxide composites, and accurate determination of their pyroelectric properties *

6.1 Introduction

In recent years, composites based on ferroelectric ceramics and polymers have attracted particular attention in the context of the piezoelectric and pyroelectric sensors, because their physical properties can be optimized for different applications. Granular composites, which consist of ferroelectric ceramic particles randomly distributed in a polymer matrix, known as 0-3 composites, are interesting candidates for various applications, due to their ease of fabrication, tunable electroactive properties, high mechanical stability, ability to cover a large area, versatile product size range and low manufacturing cost [38–40]. Moreover, they can be flexible if a properly selected polymer matrix material is used and the ceramic volume fraction is kept low. However, below the percolation threshold, there is no continuous path of connected particles from one electrode to another. In such cases, the poling efficiency as

*This work has been published as:

1. Khanbareh, H., van der Zwaag, S., Groen, W. A., Piezoelectric and pyroelectric properties of conductive lead titanate-polyethylene oxide composites, *Journal of Smart Materials and Structures*, Vol. 24, No. 04, pp. 045020, 2015.
2. Khanbareh, H., Schelen, B., van der Zwaag, S., Groen, W. A., A multi-mode temperature oscillation instrument based on discrete sampled data and mathematical lock-in method to determine pyroelectric properties of materials at low frequencies, *Review of Scientific Instruments*. 86, pp. 105111, 2015.

well as the electroactive properties depend even more strongly on the electrical conductivity of the polymer matrix [41–43].

Recent investigations have shown, that the electrical conductivity of the constituents has a significant effect on the dielectric, piezoelectric and pyroelectric properties of the granular composites, as discussed in Chapter 1 [42, 49–54]. These results have stimulated the research into other polymeric materials with higher conductivity, to further enhance the pyroelectricity. Chau et al. [48] reported on the application of polyethylene oxide (PEO), a well known polymer electrolyte used for lithium battery, in pyroelectric composites. In PZT-PEO composites, the pyroelectric and piezoelectric coefficients of the samples were greatly enhanced, compared to other PZT polymer composites with negligible conductivity. In order to improve the pyroelectric sensitivity of these composites even further, it is possible to replace PZT with a ceramic of higher pyroelectric activity and lower dielectric constant. Lead titanate (PT) is regarded as a good pyroelectric material among various kinds of commercially available ferroelectric ceramics for sensing applications [81, 82]. PEO is a synthetic polymer used in its pure non-ionic state as a surfactant, as a water-soluble thermoplastic resin as well as an ionic conducting polymer for Li-batteries, displays, sensors, and other electrochemical devices [124]. The interesting properties of PEO are a good structural integrity, a low glass transition temperature, flexibility, low toxicity and biocompatibility. Pure PEO has an electrical conductivity of 5.6×10^{-9} S/cm at room temperature, which can be improved substantially by incorporating salts into the polymer [125–127]. In the current study, the dielectric, piezoelectric and pyroelectric properties of PT-PEO composites are investigated, to elucidate the effect of the electrical conductivity of the matrix on the sensitivity and poling efficiency of the PT-PEO composites.

Furthermore, in this chapter, a novel method is proposed to determine the pyroelectric properties of materials at low frequency, ranging 0.001–0.250 Hz. The pyroelectric coefficient can be defined based on the generated pyroelectric current, as a result of a temperature change in a pyroelectric material. There are four main approaches in the literature for measuring the pyroelectric constant of a material.

1. The charge integration method, also known as the static method, is based on the integration of charge which develops on the crystal faces as the temperature increases. This method is restricted to ferroelectrics, and results are affected by ohmic conductivity and trapped charges in the bulk material and at the sample-contact interface [128, 129].
2. The radiant heating or pulse method, also known as the dynamic method [130], in which the sample is continuously heated by modulated light. Assuming that all radiation is absorbed and converted to thermal energy, the spontaneous polarization of the sample changes and a pyroelectric current is measured [16, 81, 130]. This method is less sensitive to the effect of trapped charges. A disadvantage is the uncertainty in the amount of energy actually absorbed which can lead to large errors.
3. The direct temperature ramp method, in which the poled sample is uniformly heated at a constant rate. The most important disadvantage of this simple method is that

thermally activated charges, induced during the poling process, are measured as an indistinguishable part of the pyroelectric current [131].

4. The continuous temperature oscillation method which is specially designed for separating the pyroelectric current from the non-pyroelectric current, and is a modified version of the direct temperature ramp method [131–134].

Since the continuous temperature oscillation method is the basis of the device presented in this chapter, it is elaborated in more detail below. This method is based on the difference in the thermal relaxation time of pyroelectric current and that of the thermally stimulated current. In fact, the pyroelectric current is directly proportional to the derivative of the temperature with respect to time, while the non-pyroelectric current is either constant or proportional to the temperature. When the sample is heated with a small sinusoidal temperature wave, an AC current is produced by the sample. The amplitude and phase of the current define the ratio of pyroelectric and non-pyroelectric currents. The AC component, which is in phase with the temperature wave, is the non-pyroelectric current. However, if the AC component precedes the temperature wave by 90° , the origin is a pyroelectric current [131, 132, 134]. The amplitudes of the non-pyroelectric current, I_n , pyroelectric current, I_p , and the phase angle are given by:

$$I_{ac} = I_{peak} \sin(\omega t + \theta) \quad (6.1)$$

$$I_{peak} = (I_n^2 + I_p^2)^{1/2} \quad (6.2)$$

$$I_n = RT \quad (6.3)$$

$$I_p = pAT\omega \quad (6.4)$$

$$\theta = \tan^{-1} \left(\frac{I_p}{I_n} \right) = \tan^{-1} \left(\frac{pA\omega}{R} \right) \quad (6.5)$$

where R is a temperature coefficient of the non-pyroelectric current, A is the electroded area of the pyroelectric material, p is the component of the pyroelectric coefficient normal to the electrodes, ω is the angular frequency of the sinusoidal temperature component, and T is its amplitude. This equation holds, provided that the measurements are carried out under constant mechanical stress and electric field, so as to avoid piezoelectric, ferroelastic and ferroelectric contributions [15, 20]. The frequencies involved in this technique typically vary in the range of 0.2–0.02 Hz [129]. However, some applications for pyroelectric materials, in both sensing and energy harvesting domains, may exist that require the characteristics of the materials over larger bandwidths, especially at lower frequencies. For instance, human motion detectors are sensors for slow thermal processes such as motion of the human body, whose frequency spectrum is located in the region of the infra-low frequencies of order of 0.1 to 1 Hz [135]. In this chapter, the experimental set-up of a simplified version of the temperature modulation method is presented. Detailed analysis of the test unit, sensitivity, accuracy as well as noise is discussed. The method is validated using LiTaO_3 single crystals and used to characterize the pyroelectric properties of PT-PEO composites. The signal

analysis procedure mathematically mimics the ideal lock-in character, via a unique combination of Fast Fourier Transform (FFT) with Heaviside threshold, to filter residual noise. The phase difference between the peaks of the temperature and current waves is calculated using a folded correlation [32].

6.2 Experimental procedure

6.2.1 Composite manufacturing

Lead titanate (PT) powder was calcined at 800 °C for 2 h to develop single phase PbTiO_3 . The agglomerated powder was then dry-milled using 5-mm zirconium balls for 2 h in a single G90 jar mill. The particle size distribution of milled powder in an aqueous solution with 10% isopropyl alcohol, measured by a Beckman Coulter LS230 laser diffraction analyzer, was found to be $d(10) = 2.4 \mu\text{m}$, $d(50) = 4.5 \mu\text{m}$, and $d(90) = 8.1 \mu\text{m}$. The powder was stored in a drying oven at 120 °C for 24 h prior to the experiment, to avoid moisture adsorption. Commercial PEO powder with a molecular weight of $6 \times 10^5 \text{ g/mole}$ (Sigma Aldrich), with a chemical structure as shown in Fig. 6.1, was used as the polymer matrix. A standard solution cast technique was used to prepare composite films. The PEO and PT powders were mixed to the specific volume fractions of 0%, 10%, 20% and 30%, respectively. The mixed powder was then dissolved in de-ionized water, stirred for 30 min at 70 °C until the dissolution is complete, followed by stirring at room temperature for 20 min. The resulting viscous liquids were degassed and cast on the glass substrates for the preparation of the thin films. Subsequently, the samples were dried in an oven at 50 °C for 12 h. The final thickness of the dried samples varied between 280 and 300 μm . Finally, gold electrodes of 9.2 mm diameter and 50 nm thickness were deposited on both sides of the composite samples by sputtering (Balzers Union, SCD 040). The samples were poled at room temperature in a water-cooled Julabo, SE Class III, 12876 oil bath. The effects of electric field and poling time were studied via poling at different electric fields of 1, 5, 10 and 15 kV/mm for times ranging between 1 to 120 min. The samples were then stored at 50 °C for 24 h, with their electrodes short circuited prior to the measurements, in order to remove the injected charges during the polarization and the thermally stimulated discharge current, caused by polarization of the polymer matrix. .

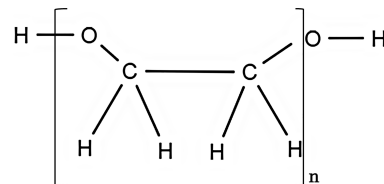


Figure 6.1: Chemical structure of PEO.

6.2.2 Measurement procedure

Dielectric, and piezoelectric measurements

The dielectric constant of the composites were determined using a broadband spectrometer (Novocontrol), in conjunction with a Cryostat high temperature sample cell, using an Agilent E4991A impedance analyzer at 1 V and 1 kHz. The piezoelectric coefficient, d_{33} , measurements were performed with a high precision PM300 Piezometer (Piezosystems) at 110 Hz under static and dynamic forces of 10 N and 0.25 N, respectively. At least five samples of each composite were tested.

6.3 Novel device for pyroelectric measurements

6.3.1 Basic concept

A schematic diagram of the test set-up, and the realized device, are shown in Fig. 6.2 and Fig. 6.3, respectively. The measurement equipment consists of an Aluminum Faraday cage, equipped with a heat sink on top of which the test cell is located. A MCPE1-07106NC-S Peltier cooler receives sinusoidal signals from a power supply, and generates the temperature modulation. To ensure uniform temperature, a 1 mm thick Copper plate is mounted on top of the Peltier cooler. A thin layer of thermal conductive paste is used on the interface between the Peltier and the Copper plate, to ensure proper thermal conductivity. The pyroelectric sample is placed on the Copper plate, and probed with a gold plated pin electrode. The temperature sensor, a MCP9701A SOT23 thermistor device with a fast response time of under 0.6 second from Microchip, is mounted very close to the sample. The temperature control unit is based on the ATMEGA5 Xplained development board from Atmel. The 12 bit Xmega on board ADC is used with 128 times oversampling, to create a signal of 16 bit capable of running at an effective sample rate up to 1 kHz. Using this mode of the ADC, together with an accurate 2.5 V (LM4040 device) reference voltage results in an overall resolution of $67.3 \mu\text{V/bit}$. The combination with the MCP9701 sensor device, which has a sensitivity of 19.5 mV/K makes it possible to control the temperature with a precision of 3.913 mK . The software is programmed to ensure that this precision is always maintained, resulting in the smallest digital temperature disturbance possible. The 1K temperature sine amplitude is generated in 256 steps of 3.913 mK . The sine period is discretized with 1606 ($2\pi \cdot 1\text{K}/3.913\text{mK}$) time steps, independent of the frequency range of 1 mHz to 250 mHz. A temperature set point generator is realized, that always uses the smallest temperature step possible. The same method is used to generate temperature ramping. The sine frequency or temperature ramping rate is controlled with the frequency of the steps. The parameters for the temperature profiles can be set by USB as communication port.

6.3.2 Temperature controller and noise analysis

A timer controlled routine, running at 500 Hz, starts the ADC temperature measurement. Once the ADC flag is set to ready, the update process of the PID controller with the gen-

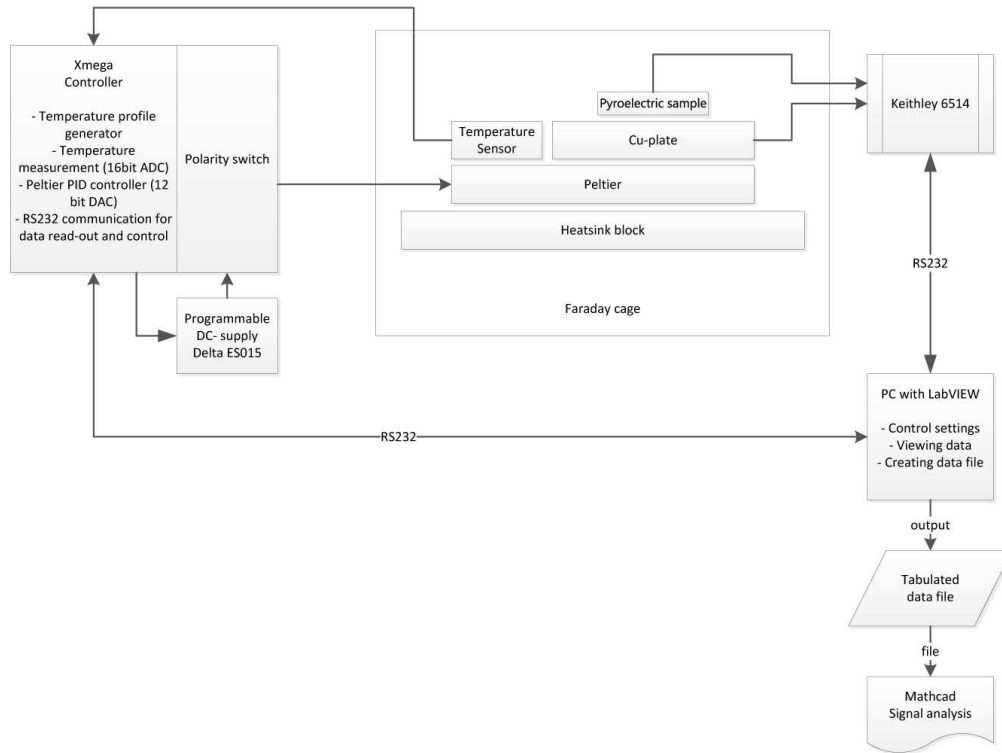


Figure 6.2: Schematic diagram of the set-up for the direct pyroelectric current measurement.

erated temperature profile as input starts. The 500 Hz frequency is half the maximum rate of the ADC, and is considered to be high enough for the sampling rate of the temperature control loop to cope with the thermal time constant of the Peltier element. The sign of the output of the PID controller is checked, to operate the polarity switch for the Peltier element. This polarity switch is constructed by 4 Avagos, optically controlled, SSR switches in between the power supply output and the Peltier element. The modulus of the PID result is converted with the internal 12 bit DAC to a voltage that drives the Delta ES150-10 power supply as a power amplifier for proportional control of the Peltier current. This combination is able to provide the Peltier element with 40W of bipolar power at a 500 Hz sample rate. The PID controller, used with 500 Hz sampling rate, allows for a high closed loop bandwidth. The bandwidth can be controlled with the PID parameters, so as to reduce closed loop temperature noise. Noise in the temperature signal translates to current noise from the sample. For frequency and phase measurements, this noise is easily eliminated by the Fast Fourier transformation (FFT) convolution (shown in the data processing section). For direct measurement of the temperature ramping current, this could result in a too low overall signal to noise ratio figures at low ramping rate. Therefore, a different set of PID parameters for sine modulation and temperature ramping is preferred. The temperature signal to noise ratio at the lowest possible amplitude of 1 K, with a frequency of 1 mHz sine modulation is 30 dB or 0.03 K RMS as measured in the temperature data sampled with 2 Hz. Due to alias-

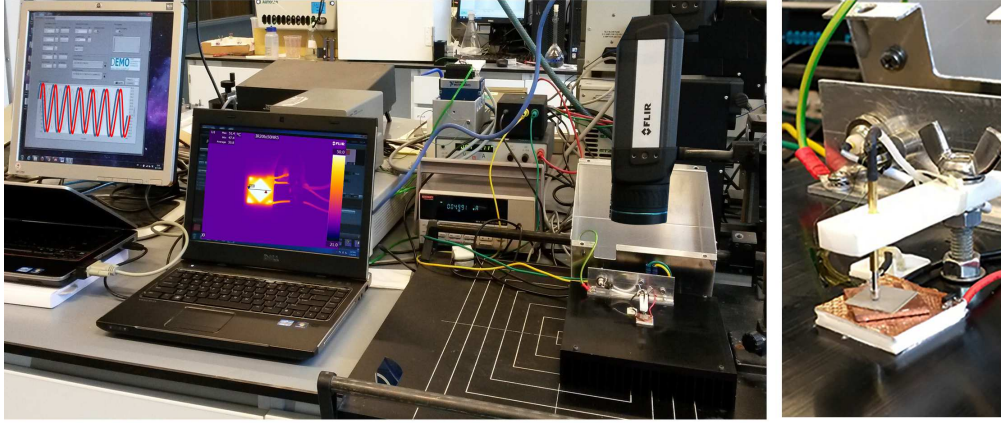


Figure 6.3: Newly developed set-up for pyroelectric current measurements. Figure on the right shows a sample being tested.

ing, the spectral noise is slightly folded around the bandwidth (1 Hz) of Peltier controller. The pyroelectric current signal to noise ratio (SNR) is much lower due to its principle dT/dt character which gives a 6dB rise per octave of the noise with frequency.

The absolute current accuracy, as specified for the Keithley electrometer in the current range is 0.2%. This accuracy affects the accuracy of pyroelectric current, but does not have an effect on the phase accuracy. The character of the noise on both temperature and current is mainly correlated due to the common source. The SNR on the current, being mainly a transformation of the noise on temperature, is barely depending on the current amplitude. Basically, the cross correlation convolution method in the frequency domain multiplies the temperature-frequency spectrum and the current-frequency spectrum element by element, resulting in a product of both individual SNRs. The SNR of the result is at least equal to the individual sum of both SNRs in dB. In fact, it will be higher, because uncorrelated noise in the individual spectra is greatly reduced. For the current, the signal to noise ratio evaluates to 3dB at the lowest frequency of 1 mHz. The applied correlation makes use of all recorded samples and is, therefore, improving the overall SNR with the square root out of the total number of samples per each fully logged modulation cycle at 1 mHz. By logging more than one full modulation cycle the overall SNR can be further improved.

Temperature and current sampling

The temperature controller determines the overall sampling rate if used in auto transmit temperature mode, via the USB port. Although the controller is capable of 500 measurements per second, the Keithley electrometer can only perform 2 measurements per second when using the standard RS232 bus as in the current study. Therefore, all measurements were performed using this sample rate, allowing frequency measurements up to half of the Shannon

frequency or 1 Hz. The temperature controller is used with the temperature measurement in average mode set to 250 for a 500 Hz effective sampling rate. Settings and file I/O is done by LabVIEW software running on a PC or Laptop. This software allows to control the settings of the temperature unit, and has a graphical viewer for the output data, such as temperature and current and user controlled logging. Once the Keithley Electrometer receives data from the temperature controller a new measurement is triggered. This pair of correlated data, both temperature and current are stored into a data file. Logging is done by starting the instrument and acquiring at least 1 complete period of the modulation frequency data. In case of ramping, the logging is started just before the ramp and stopped after reaching the final temperature. At 1 mHz with 2 Hz sampling, this results in a measurement of approximately 20 min with 2000 data points. For higher modulation frequencies, the measurement time is proportionally shorter.

Data processing

The goal is to measure the phase difference between the pyroelectric current and the modulated temperature, as well as the pyroelectric current amplitude. The collected raw data is used in the signal processing phase. This allows to process the data for new findings in multiple perspectives. Currently, the raw data are imported in the commercial tool Mathcad, but it can be imported in any other mathematical program as well. The measured temperature and current are read as a vectored data set. From the acquired data, the number of full modulation cycles is extracted, to avoid errors due to incomplete cycles. This could otherwise results in foreign frequencies of phase-like modulation in the frequency domain. Since both sampling rate and modulation frequencies are synchronized and known, full measurement cycles can be isolated exactly. The time related signals of temperature and current are transformed to the frequency domain by using a Fast Fourier transformation (FFT). By applying the complex conjugate on the current signal and performing a convolution within the frequency domain, the correlation between the signals is calculated. The DC component is removed from the result, as it adds to the real component of the correlation. The phase between both signals is calculated by the arc tangents of the DC free results.

The procedure described above results in a signal to noise ratio of 30 dB on the temperature measurement and only 3 dB on the current measurement. The extracting method is accurate to within a phase error of less than 0.25° at the low frequency of 1 mHz, which improves with increasing the frequency. This method clearly eliminates the need for costly lock-in amplifiers for this application.

Phase correction for systematic errors

To calculate the actual phase angle between the pyroelectric current and the temperature signals, the FFT driven phase is corrected for heat transfer and instrument delays.

The phase delay due to the heat transfer is firstly discussed. The overall control loop is shown in Fig. 6.4.

The feedback element of the Peltier surface temperature is the MCP9701, with a thermal

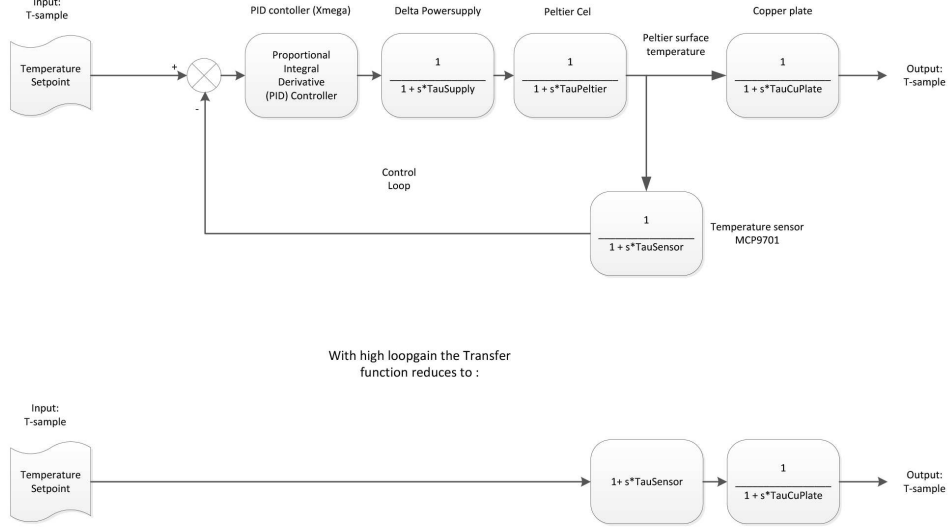


Figure 6.4: Simplified temperature control loop.

time constant of only 0.6s. On top of the Peltier, a thin (1 mm) Copper plate is used to create a uniform temperature signal, as well as a smooth surface, to mount the sample on. Copper, with low thermal resistance and relative low thermal capacity is suited to act as an additional noise filter for the temperature. This Copper filter is kept outside the electrical PID loop as it would otherwise give rise to instability, and thereby canceling its positive noise filtering effects. The loop-gain is sufficiently high (see diagram 6.4) to reduce the Laplacian overall transfer function to:

$$H_{transfer} = \frac{s \cdot \tau_{plate} + 1}{s \cdot \tau_{sensor} + 1} \quad (6.6)$$

$$s = 2\pi i f \quad (6.7)$$

The heat transfer function, $H_{transfer}$, is calculated based on the thermal time constant of the temperature sensor, τ_{sensor} , and that of the Copper plate τ_{plate} . The thermal time constant of the plate is determined by comparing the recorded temperature signal, measured by the thermistor in the unit and the temperature of the plate monitored using a IR camera (as shown in Fig. 6.3) at different test frequencies. The final heat transfer phase delay, ϕ_{heat} , is then calculated as:

$$\phi_{heat} = \arctan\left(\frac{Im(H_{transfer})}{Re(H_{transfer})}\right) \quad (6.8)$$

Where $Re(H_{transfer})$ and $Im(H_{transfer})$ are the real and imaginary components of the heat transfer function.

Finally, a small compensation is added for the overall instrument delay. Since the overall sampling rate is kept constant at 2 Hz, the averaging of temperature inside the control unit, as well as the fixed sample delay of the Keithley electrometer adds a small compensation for this quantity. The instrument delay, ϕ_{inst} , consists of two components, delay of the electrometer and delay of the temperature control unit as follows:

$$\phi_m = t_m 2\pi f \quad (6.9)$$

$$\phi_t = t_t 2\pi f \quad (6.10)$$

$$\phi_{inst} = \phi_m - \phi_t \quad (6.11)$$

where ϕ_m and ϕ_t are the phase angles, corresponding to the sampling delays of the electrometer and temperature control unit. t_m and t_t are the sampling times of the electrometer and temperature control unit, f is the frequency of the thermal sine wave, respectively.

In order to determine the actual phase angle between the temperature and the current signals, the sum of the instrumental and heat transfer phase corrections, $\phi_{correction}$, is added to the calculated phase shift, based on the Fourier transformation.

$$\phi_{correction} = \phi_{inst} + \phi_{heat} \quad (6.12)$$

Measurements and validation

The device and the data processing protocol were validated using LiTaO₃ single crystals, whose properties are well documented, and have low sample to sample variations. Fully poled commercial LiTaO₃ wafers of 5 mm by 5 mm by 0.2 mm were obtained from Infratec, Germany. The measured absolute values of pyroelectric properties as a function of frequency from 1 mHz to 250 mHz at 25 °C are listed in Table 6.1, and compared to the reported values from literature, obtained by the continuous temperature oscillation method.

Frequency (mHz)	Phase angle (°)	I_{peak} (A)	$p_{measured}$ ($\mu\text{C}\cdot\text{m}^{-2}\cdot^\circ\text{C}^{-1}$)	$p_{reported}$ ($\mu\text{C}\cdot\text{m}^{-2}\cdot^\circ\text{C}^{-1}$)	Ref.
1	89.5	2.75×10^{-11}	175.1	Not reported	-
5	89	1.35×10^{-10}	171.8	175	[132]
10	88.7	2.68×10^{-10}	170.5	175	[132]
30	92	8.3×10^{-10}	176	Not reported	-
60	91	1.65×10^{-9}	175.1	172.7	[136]
100	97.9	2.41×10^{-9}	152	175	[132]
150	99	3.90×10^{-9}	163.2	Not reported	-
200	101	5.64×10^{-9}	176.3	160	[132]
250	104	7.14×10^{-9}	176.5	Not reported	-

Table 6.1: Measured pyroelectric properties of LiTaO₃ chip at 25 °C and $\Delta T = 1$ °C.

The phase difference between the temperature and current signals is determined, to establish which type of current is present. When both pyroelectric and non-pyroelectric currents are

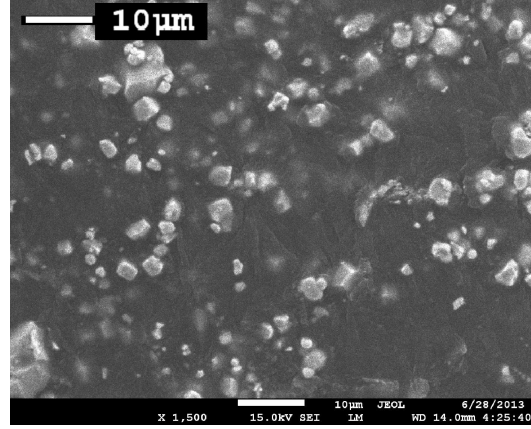


Figure 6.5: SEM microstructure of 20%PT-PEO composite.

present, the phase angle varies. The fractions of current associated with pyro and nonpyro effects are then calculated using Eq. 6.5. For the calculation of the pyroelectric coefficient, the peak current (I_{peak}) is measured and the pyroelectric coefficient is calculated using Eq. 1.3.

Three samples are tested at each frequency. No dependencies of pyroelectric current to frequency is observed, indicating a pure pyroelectric behavior for LiTaO_3 . The measured phase shifts at all frequencies show values close to 90° , indicating that the AC current has almost no non-pyroelectric component [132]. The calculated pyroelectric coefficients in the range of 1 to 250 mHz are in agreement with the reported values from literature ($170\text{--}190 \cdot 10^{-10} \mu\text{C} \cdot \text{m}^{-2} \cdot ^\circ\text{C}^{-1}$) [132, 136, 137]. Therefore, it can be stated the accuracy of the test unit is high over the whole frequency range of 1 to 250 mHz.

6.4 Results and discussion

6.4.1 Microstructure of composites

Fig. 6.5 shows an SEM image of a 20% PT-PEO composite. The PT particles are homogeneously distributed in the PEO matrix, and do not show signs of agglomeration. The average particle size matches very well with the result of the particle size analysis.

6.4.2 Dielectric results

The dielectric constants of the PT-PEO composites, poled at 10 kV/mm for 15 min, are presented in Fig. 6.6 for PT volume fractions from 0% to 30%. The analytical model used to describe the dielectric properties of the 0-3 composites is the model formulated by Yamada et al. [36], as presented in Chapter 2.

The physical parameters for the constituent phases, adopted in the theoretical calculations are listed in Table 6.2. The good agreement between the measured and theoretical values

supports the assumed 0-3 connectivity pattern. In the current work n was obtained by the least square fitting method. The best fit of the experimental data to model predictions for PT-PEO composites was obtained for $n = 5$.

Materials	ϵ at 1 kHz	d_{33} (pC/N)	d_{31} (pC/N)	σ (S/cm)	$\tan \delta$ at 1 kHz
PT	200 [81]	50 [81]	-4.2 [81]	10^{-13}	0.02
PEO	8	0	0	5.6×10^{-9}	0.15

Table 6.2: Properties of ceramic and polymer phases at 25 °C .

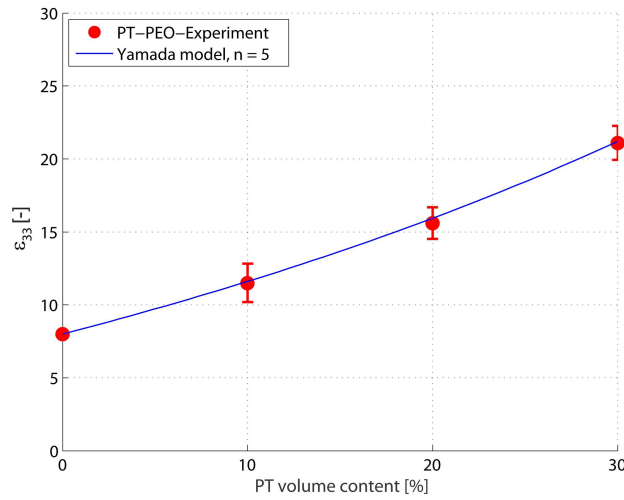


Figure 6.6: Measured dielectric constant values for PT-PEO composites poled at 10 kV/mm for 15 min with the associated model.

6.4.3 Piezoelectric analysis

The model formulated by Yamada et al., as discussed in Chapter 2, is also used to analyze the piezoelectric properties of the current granular composites, [36] as shown in Fig. 6.7.

The best fit of the experimental data for PT-PEO composites, poled at 10 kV/mm for 15 min, to the model predictions was obtained assuming a poling ratio, $\alpha = 1$. Clearly, the high electrical conductivity of PEO has resulted in a high poling efficiency of the particles embedded in the polymer matrix. Although most saturated polymers are classified as insulators, both low and high molecular weight polyethylene oxide polymers have been reported to have high conductivities, even when the possibility of ionic transport, resulting from the presence of impurities, was eliminated. It has been shown by Binks et al. [138], that an inherent ionic process is operative in PEO polymers, involving in the generation of protons and their subsequent transport through the ethereal oxygen by local segmental motion. For the mechanism to operate, two requirements need to be fulfilled: the presence of proton-accepting atoms (in this case oxygen) in the polymer chains; and proximity to the melting

point to ensure adequate chain-mobility [138, 139].

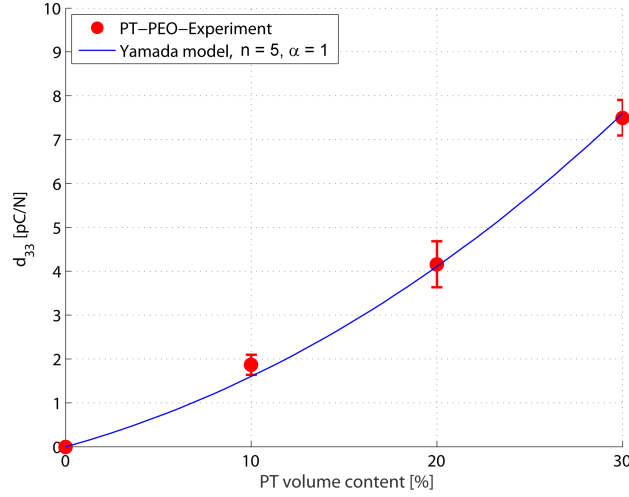


Figure 6.7: d_{33} values for PT-PEO composites poled at 10 kV/mm for 15 min and fitted model prediction.

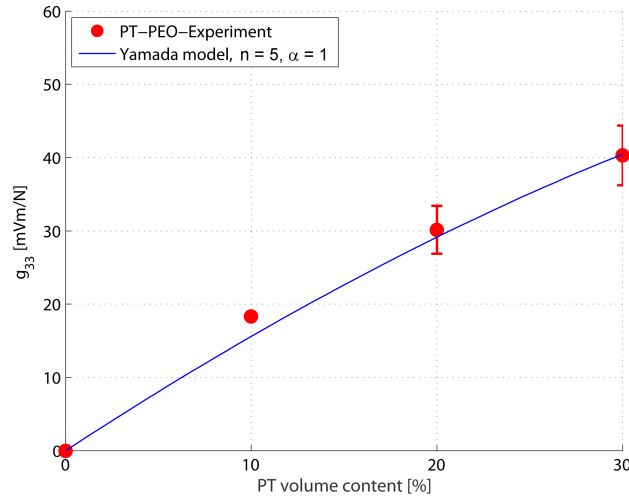


Figure 6.8: g_{33} values for PT-PEO composites poled at 10 kV/mm for 15 min and fitted model prediction.

The piezoelectric voltage coefficient, g_{33} , can be calculated by dividing the d_{33} of the composite by their respective permittivity. The variation of g_{33} of the composites as a function of PT volume fraction is presented in Fig. 6.8. The maximum g_{33} value obtained for PT-PEO is 44 mV.m/N at a PT volume fraction of 30%.

6.4.4 Pyroelectric properties

The pyroelectric coefficients of PT-PEO composites, poled at 10 kV/mm for 15 min, are presented in Fig. 6.9.

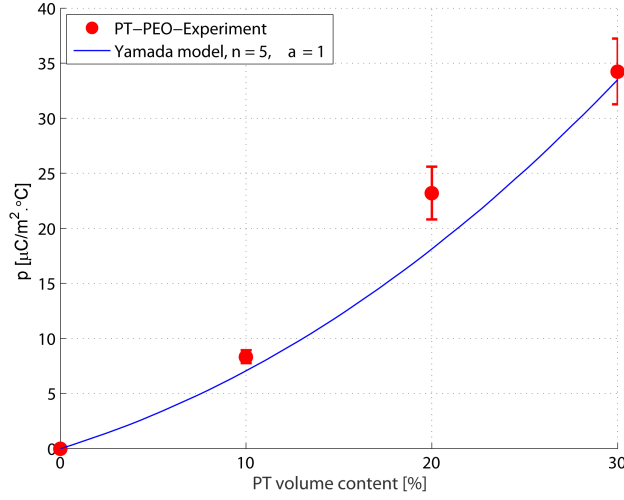


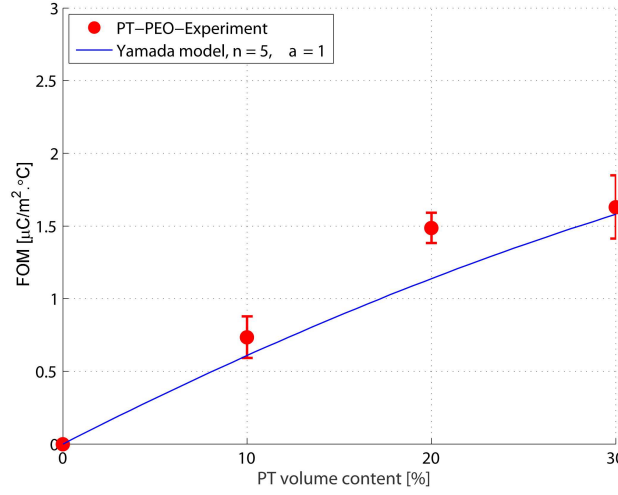
Figure 6.9: Pyroelectric coefficient, p , of PT-PEO composites poled at 10 kV/mm for 15 min and the model predictions.

These composites show superior pyroelectric sensitivity over the whole range of volume fractions, owing to the higher conductivity of the polymer matrix. Such a result is in agreement with other results reported in literature for carbon-modified PZT-PU [46], PANi coated PZT-PVDF [45, 47] and LiClO_4 doped PZT-PU composites [53]. The reason for enhanced properties is that the dielectric permittivity mismatch decreases when a conducting matrix is used [45, 53]. Such a matrix creates an electrical flux path between the ceramic particles [45]. As a result, the local electric field acting on the ceramic particle is enhanced, making the poling process more efficient [140]. The model proposed by Yamada (Eq. 6.13) is fitted to the experimental data by using the least square method with n and α as the fitting parameters. Interestingly, the best fit for PT-PEO composites was obtained for $n = 5$ and $\alpha = 1$, which is in excellent agreement with the parameters calculated by fitting the model to the d_{33} data. The calculated phase angle between temperature modulation, and the current for all of the samples, is listed in Table 6.3. The lower phase angle at lower ceramic volume fractions is indication of a larger contribution of non-pyroelectric current in the total thermally stimulated current signal.

$$p = \frac{\phi \alpha n \epsilon_{\text{comp}} p_c}{n \epsilon_{\text{comp}} + \epsilon_c - \epsilon_{\text{comp}}} \quad (6.13)$$

The pyroelectric figure of merit (FOM) can be calculated by dividing the pyroelectric coefficient of the composite by its dielectric permittivity (p/ϵ). As demonstrated in Fig 6.10, with increasing volume fraction of PT an improvement in pyroelectric coefficient is observed. PT-PEO composites show a maximum FOM of $1.6 \mu\text{C} \cdot \text{m}^{-2} \cdot ^\circ\text{C}^{-1}$ for 30%PT-PEO

Material	PEO10PT	PEO20PT	PEO30PT
Phase angle °	55	61	63

Table 6.3: Phase angle between temperature and current signals at 5 mHz and 25 °C.**Figure 6.10:** Pyroelectric FOM of PT-PEO composites poled at 10 kV/mm for 15 min and the model predictions.

composite, which is more than 10 times higher than that for the reference 30%PT-epoxy composite. A comparison between the pyroelectric FOM of 30%PT-PEO with that of different classes of materials is presented in Fig. 6.11. 30%PT-PEO reaching 25% of the performance of LiTaO₃ single crystals can be manufactured in large area and is flexible.

6.4.5 Poling study

The effect of poling time and temperature on the piezoelectric charge constants of the PT-PEO composites is shown in Fig. 6.12 and Fig. 6.13.

The electric field was kept constant at 10 kV/mm while investigating the effect of poling time, and poling time was held constant at 15 min during the electric field magnitude study. The graphs show, that under an electric field of 10 kV/mm, the values of d_{33} significantly increase within the first 15 min of poling, and saturate thereafter. The fact that the d_{33} parameter saturates within 15 min indicates that the poling is complete within a very short time. The effects of electric field magnitude on the d_{33} is also presented in Fig. 6.13. The d_{33} values of the composites enhance with increasing the electric field up to 10 kV/mm, and levels off afterward. This is also a clear indication of complete poling at 10 kV/mm. During the poling process, the mobility of charges in the polymer matrix is a key parameter in defining the final poling efficiency. The effective charge relaxation time is defined as:

$$\tau = \frac{3\phi\epsilon_m + (1 - \phi)(\epsilon_c + 2\epsilon_m)}{3\phi\sigma_m + (1 - \phi)(\sigma_c + 2\sigma_m)} \quad (6.14)$$

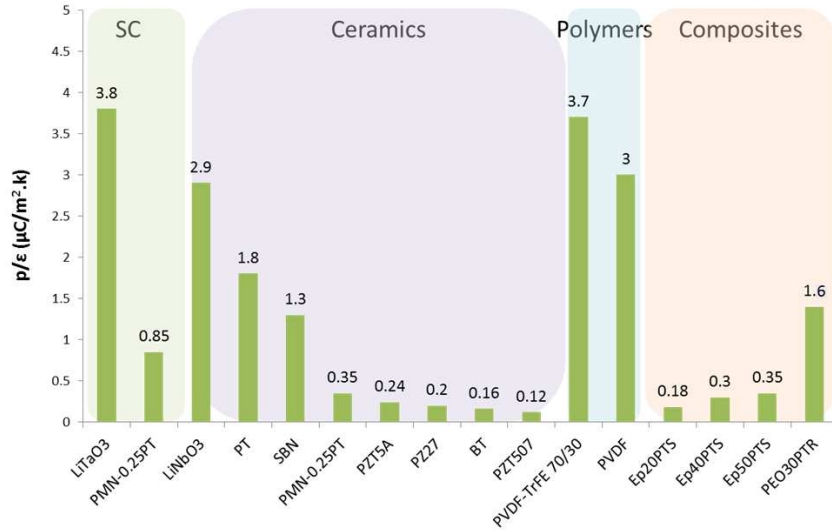


Figure 6.11: Pyroelectric FOM of different classes of materials.

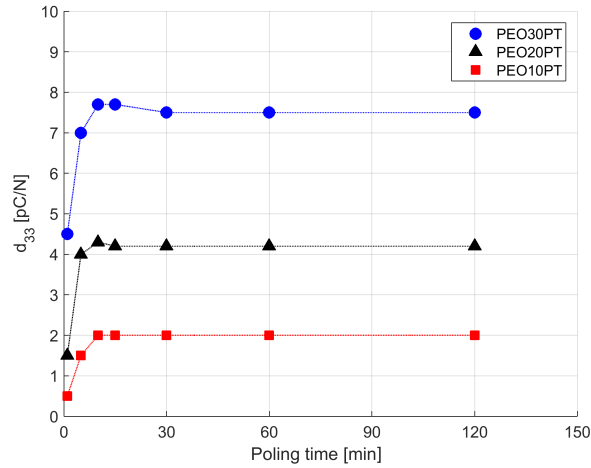


Figure 6.12: Variation of d_{33} with poling time in the poling study of the PT-PEO composites.

where σ is electrical conductivity, and subscripts c and m denote ceramic and polymer matrix, respectively. ϕ and ϵ are volume fraction and dielectric permittivity of the constituents, respectively. It has been shown, that if the poling time is substantially longer than the charge relaxation time, the ceramic phase will be fully polarized [41,42]. The effect of permittivity and electrical conductivity of the matrix on the relaxation time is shown in Fig. 6.14.

As the permittivity of PT is much higher than that of the polymer matrix, τ , is mainly governed by the electrical conductivity of the matrix. The higher conductivity of the polymer matrix in ferroelectric composites shortens the time required for the electric field acting on

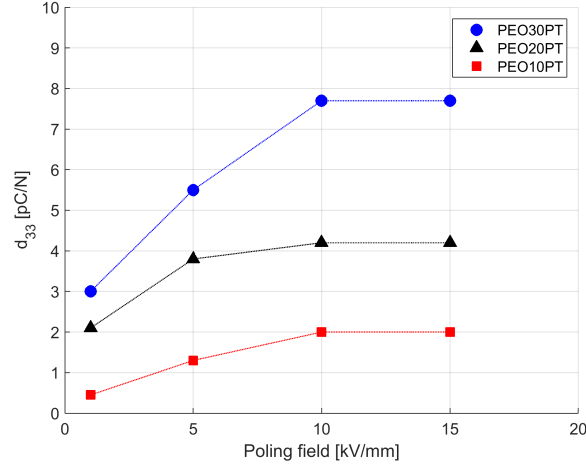


Figure 6.13: Variation of d_{33} with the electric field in the poling study of the PT-PEO composites.

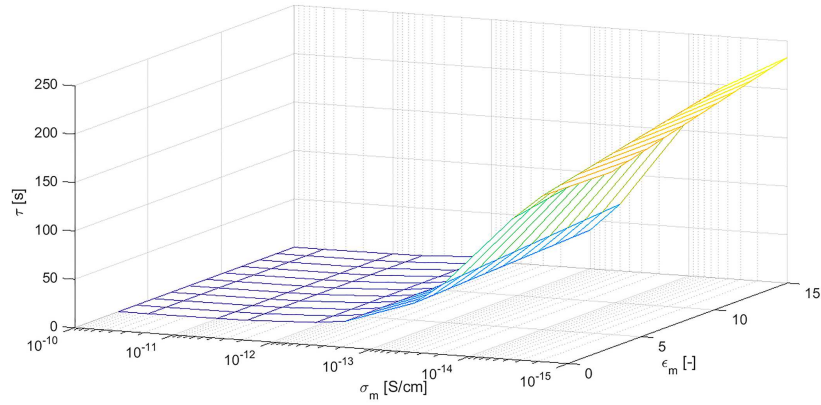


Figure 6.14: Variation of charge relaxation time with σ_m and ϵ_m for 30% PT-PEO.

the ceramic inclusion to reach saturation, thereby making the poling of the ceramic phase more efficient [49, 122]. When σ_p is increased from 10^{-15} S/cm of epoxy to 5.6×10^{-9} S/cm of PEO the charge relaxation time decreases to less than a second, resulting in a faster poling process. Moreover, as stated by several researchers, the increase of the electrical conductivity and dielectric permittivity of the polymer matrix in the composite can enhance its piezo- and pyroelectric activities, due to an increase in the local electric field, sensed by the ceramic particles [42, 45, 140]. When the DC poling voltage is applied for a period longer than the relaxation time, the voltage applied on the particles depends on the electrical conductivity ratio of polymer with respect to ceramic phase, as shown in Fig 6.15 [50, 122]. The effective electric field on the ceramic particles in a polymer matrix can be calculated

using:

$$E_{effective} = \frac{3\sigma_m E_{applied}}{(1 - \phi)\sigma_c + (2 + \phi)\sigma_m} \quad (6.15)$$

where $E_{applied}$ is the applied poling electric field, and $E_{effective}$ is the electric field experienced by the ceramic phase. The effective electric field on PT particles in a PEO matrix is more than 20 times higher than the field experienced by the particles in an epoxy matrix, with electrical conductivity of 10^{-15} S/cm. Therefore, PT-PEO composites can be efficiently poled at lower electric fields and within a shorter time and under lower temperatures than similar composites with a non-conductive polymer matrix.

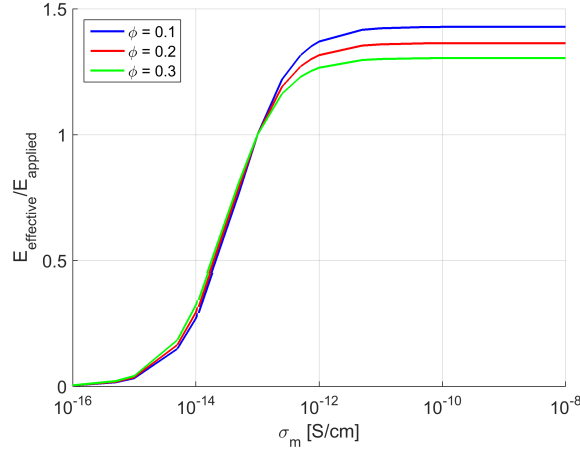


Figure 6.15: Variation of effective electric field with σ_m .

6.5 Conclusions

The accurate determination of the pyroelectric coefficient of materials by applying a simple digital signal processing method on the discrete sampled data obtained in temperature oscillation technique has been presented. Using the proposed approach, the FFT analysis can be performed to combine residual noise filtration and phase shift analysis between temperature modulation and current. The phase shift is accurately corrected, based on the instrument and heat transfer delays of the test unit. The method has been proven to be suitable for testing pyroelectric materials in the ultra low frequency spectrum of 1 to 250 mHz, without using costly lock-in amplifiers. Moreover, the importance of electrical conductivity of the polymer matrix, and its effect on dielectric, piezoelectric and pyroelectric properties of granular ferroelectric composites, has been demonstrated. PT-PEO composites were fabricated and their properties were evaluated and compared with the predictions of the analytical models. Substantial improvement in the pyroelectric activity resulting from the high electrical conductivity of PEO is observed for composites of 10%, 20% and 30% PT-PEO, compared to

composites with a matrix of lower electrical conductivity. 30%PT-PEO composite shows a pyroelectric figure of merit of $1.6 \mu\text{C} \cdot \text{m}^{-2} \cdot ^\circ\text{C}^{-1}$, which is comparable to that of monolithic PT ceramics. Efficient poling of the composites is possible at room temperature, with short poling times and under relatively low electric fields.

Enhancing the sensitivity of PZT-polyurethane composites by reducing the dielectric permittivity of the matrix

7.1 Introduction

Several types of polymeric materials can be foamed to low densities for applications that require properties such as weight-reduction, insulation, buoyancy, energy dissipation, mass transport as well as convenience and comfort [58]. More recent advances include polymeric foam scaffolds for tissue engineering [59], shape memory polymer foams for biomedical and aerospace applications [60–63], membranes for gas separation or filtration [64, 65], polymeric electrolytes in lithium-ion batteries [66, 67] and hydrogen storage [68, 69].

Recent developments in the field of electronics have encouraged fabrication of ultra low permittivity dielectrics for the next generations of microchips. They require interlayer of dielectrics with dielectric constants below 2.2. Therefore, a new concept has been developed, based on porous structures, achieved mainly by thermal decomposition of a block copolymer composed of a thermally stable block and a thermally unstable one [70]. These porous materials show a clear relation between decreasing permittivity and increasing porosity. The macroscopic behavior of such polymer foams is determined by a combination of the intrinsic constitutive behavior of the polymeric material, and the microstructure. There are numerous models in literature that relate material properties of the polymer foam to the intrinsic properties of the constituent phases. A simple simulation based on the mixed connectivity model, as presented in Chapter 2, in a serial and a parallel arrangement, can be used to estimate the dielectric properties of the polymer foam. A two-phase dielectric material, consisting of spherical gaseous inclusions in a polymer matrix, is assumed. In the serial

mode (0-3), the porosities are homogeneously distributed in the polymer matrix. In the parallel mode (1-3), the microstructure can be considered as the columns of porosity, elongated in the thickness direction. With increasing the gaseous content, the dielectric constant of the polymer foam decreases linearly. However, in a system of homogeneously distributed air inclusions in the polymer matrix, the dielectric constant of the polymer foam decreases exponentially with increasing gaseous content [58, 71]. Therefore, a polymer foam consisting of randomly distributed closed cells, has an effectively reduced dielectric constant compared to the bulk polymer.

As far as piezoelectric properties of the ceramic-polymer composite sensors are concerned, optimization of the dielectric properties of the polymer matrix plays an important role in controlling the output voltage of the di-phase composites [57]. The piezoelectric voltage coefficient, g_{33} , is calculated by dividing the d_{33} of the composites by their relative permittivity. Therefore, the piezoelectric performance of the di-phase systems can be enhanced by adding a gaseous phase to the polymer matrix, in form of a homogeneously distributed porosity (0-3 connectivity) to decrease the dielectric constant, while d_{33} is kept unchanged. Since DEP alignment of piezo particles improves the piezoelectric charge constant of the composites, while foaming significantly decreases the permittivity of the composites, a combination of both will result in enhanced electromechanical behavior. The behavior of a tri-phase piezoelectric composite materials is controlled by geometrical, topological, elastic, dielectric, and piezoelectric parameters. In this chapter, the influence of topological parameters on the properties of the polyurethane (PU) foam is mapped in detail. Tri-phase composites of PZT-porous PU are manufactured and their functional properties are investigated.

7.2 Experimental procedure

7.2.1 Composite manufacturing

Lead zirconate titanate ceramic powder (PZT5A4), provided by Morgan Electro Ceramics, was calcined at 1150 °C 1 h in a closed zirconia crucible according to the optimized scheme reported by Van den Ende [11]. After calcination, the powder was dry ball milled for 2 h in a Gladstone-Engineering G90 jar mill. Subsequently, the particles were sieved for 20 min, using a Haver & Boecker EML Digital Plus test sieve shaker with stacked sieves with mesh sizes of 125 μm and 63 μm . The powder was dried for at least 2 h to prevent agglomerations due to moisture, as well as chemical interaction between the polymer and moisture from the particles. The particle size distribution of milled powder in an aqueous solution with 10% isopropyl alcohol, measured by a Beckman Coulter LS230 laser diffraction analyzer, was found to be $d(10) = 0.8 \mu\text{m}$, $d(50) = 1.8 \mu\text{m}$, and $d(90) = 6 \mu\text{m}$.

A two component urethane rubber, Smooth-on-Econ 80 Polyurethane, is used to serve as the polymer phase in the composites studied in this chapter. This polymer is composed of di-isocyanate (component A) resin and polyol (component B) was used (see Fig. 7.1). Gas formation is observed upon addition of water to the uncured polymer, due to a chemical

reaction between the di-isocyanates component and water, which leads to the formation of poly(urea-urethane), and the release of CO₂ (Fig. 7.2).

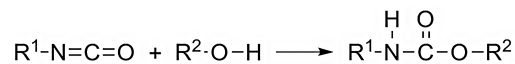


Figure 7.1: Chemical reaction of di-isocyanates with polyols.

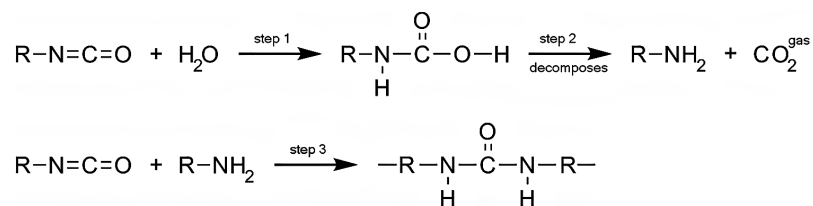


Figure 7.2: Chemical reaction of di-isocyanates with water and the release of CO₂.

To study the effect of demineralised water (D-water) on gas formation in PU, component A was magnetically stirred at 600 RPM for 6-7 min at room temperature. In the meantime, component B and a varying amount of D-water, from 0 to 0.5%, was mixed using a Speed-mixer DAC 150.1 FVZ at 3500 RPM for 5 min. Subsequently, component A, B and D-water were magnetically stirred at 600 RPM, until viscosity increased enough to stop the magnet from rotating (see Fig. 7.3). A tape-cast-film was made on an Aluminum substrate, using a doctor blade that was set at 1 mm. The amount of D-water that was added to 10 mL PU is in the μL range. Influences from moisture in the air can thus be significant, which is why the samples were covered and if possible produced on the same day. The microstructures of the samples are discussed later in Fig. 7.5.

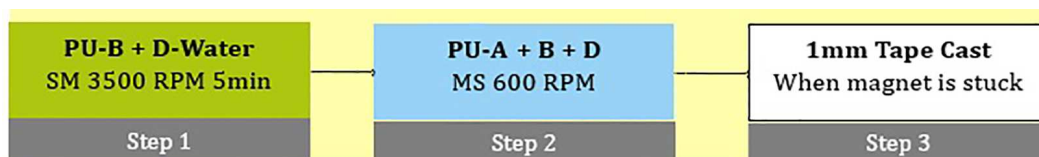


Figure 7.3: PU foam production route. SM stands for speed mixed and MS stands for magnetically stirred.

Thermogravimetric Analysis (TGA) of the polymer is performed using Perkin Elmer Pyris Diamond at 20°C/min under a nitrogen atmosphere. The results show that, at 200°C, less than 2wt% loss is registered. Subsequently, Differential Scanning Calorimetry (DSC) was performed, at a heating rate of 20 °C/min under a nitrogen atmosphere, using the Perkin Elmer Sapphire to find the glass transition temperature, T_g , of -7.6 °C. The T_g of the polymer does not appear to be significantly affected by post curing at 100 °C.

The production route, that was used for the production of the D-water range of 0 to 0.5%, as explained before (see Fig. 7.3), was also used for the production of the first batch of random (0-3) tri-phase composites. However, for the 20 vol% PZT, the initial viscosity of

the system due to the presence of the PZT was too high to allow for magnetic stirring. The production route was adapted accordingly, and is shown in Fig. 7.4.

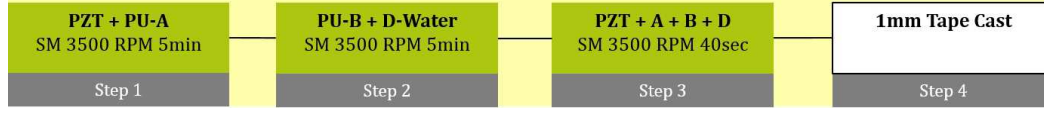


Figure 7.4: PZT-porous PU composite production route.

In the new production route, the magnetic stirring step is eliminated. Foams were able to form nonetheless. To check the necessity of the magnetic stirring in the D-water sample production, a PU cast was made where PU component A, component B and the D-water were mixed all at once for 60 seconds at 3500 RPM. The result was a cast with large (>1 mm) through-thickness voids and some smaller voids of approximately $100\ \mu\text{m}$, distributed throughout the cast. This rules out self-nucleation as a possible reason for the foaming of non-mechanically stirred PZT-PU foam samples, and proves that micro-voids are essential in order to obtain a desirable foam micro-structure. It also proves, that PZT particles are able to function as void nucleation sites, thereby replacing the functionality of micro-voids which are introduced by magnetic stirring.

To prepare the composites, the PZT particles were dispersed in the mixture of polymer resin and demineralized-water (D-water) to the specific volume fractions of 0%, 20%, 30% and 40% and mixed at 3500 RPM for 1 min. 0-3 samples were produced by casting the slurry on an Aluminum substrate using a doctor blade at the thickness of 1 mm. The surface of the film was exposed to air. Quasi 1-3 samples were produced in a closed mold format using a Teflon mold of 1 mm thick. The details of the mold layout are presented in Chapter 2. For random and structured samples, the optimum volume fraction of D-water, resulting in maximum reduction of dielectric constant of the polymer matrix is found to be 0.4 vol% and 0.2 vol%, respectively. This optimization will be discussed in detail in the following section. The closed mold used in preparation of DEP structured samples restricts the water evaporation from the mixture, therefore, a lower water content of 0.2 vol% results in similar gas content of 60 vol% similarly as in random composites prepared by casting. The dielectrophoretic structuring is performed on uncured composites by applying an electric field of 3 kV/mm at 3 kHz for 1.5 h, using a function generator (Agilent, 33210A) coupled to a high voltage amplifier (Radiant Technologies Inc., T6000HVA-2), until the polymer matrix is fully cured. After curing, flexible films of 1 mm thickness were obtained. The samples were then poled for 2 h, using a Heinzinger 30000-5 30kV DC amplifier, a Haake N3 digital circulating hot oil bath filled with silicone oil and a custom made sample holder at $100\ ^\circ\text{C}$, 5 kV/mm.

7.2.2 Measurement procedure

Circular discs of 16 mm were produced, and electrodes were made by sputtering of Gold for 20 min on both sides using a Quorum Q300T D sputter coater. Subsequently, all samples were punched using a 16 mm punch, thereby removing the material at the edges to prevent

leakage current. The dielectric constant of the composites was determined using an Agilent 4263B & 16034E - Inductance Capacitance Resistance Meter (LCR) by the parallel plate capacitor method at 1 V and 1 kHz. The d_{33} of the poled samples were determined using the Piezotest PiezoMeter System PM300 - Berlincourt d_{33} meter, under a 10 N static force and a 0.25 N dynamic force at a frequency of 110 Hz. At least three samples of each composite were tested. For microstructural analysis, the samples were sectioned using scissors along the thickness, and the cross sections were observed using a field emission-scanning electron microscope (FE-SEM) (JEOL, JSM-7500F).

7.3 Results and discussion

7.3.1 Microstructure analysis

Microstructures of porous PU-polymer

The effect of D-water content, ranging from 0 to 0.5%, on the microstructures of PU, prepared by the process shown in Fig. 7.3, is investigated. The microstructures are shown in Fig. 7.5. The increase of the gaseous volume fraction and sample thickness with increasing water content is clearly visible.

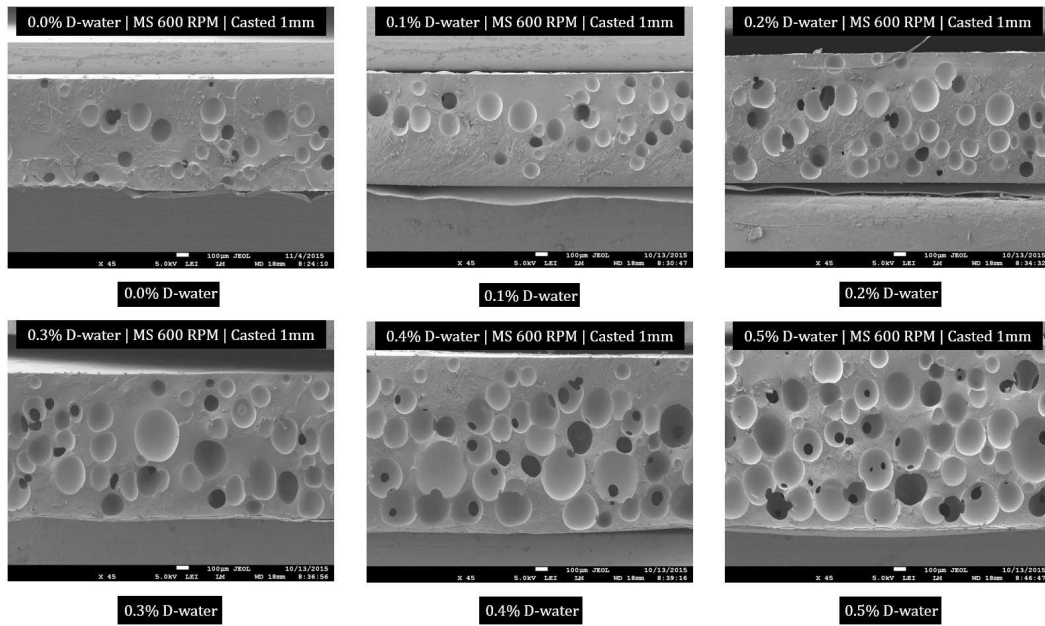


Figure 7.5: SEM microstructures of neat PU samples containing different volume fractions of D-water, ranging from 0.0% to 0.5% prepared by the route shown in Fig. 7.3. MS stands for magnetically stirred.

The SEM images are processed using the Image Processing Toolbox of MATLAB, in order to quantify the gaseous volume fraction, pore size and morphology. The images are binarized, and the area fraction of the gaseous phase, as an indication of the volume fraction of

this phase, is subsequently calculated. An example is provided in Fig. 7.6, where a 0.4% D-water sample is processed.

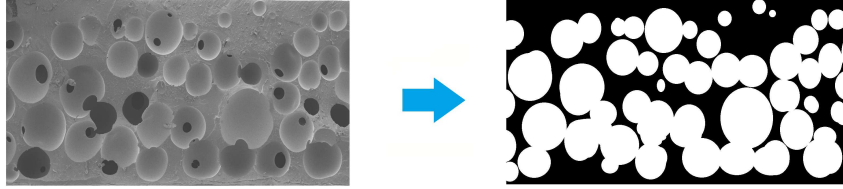


Figure 7.6: Example of image processing of a microstructure of PU Foam with 0.4% D-water analyzed to calculate gas volume fraction.

The results of image processing are used to plot the variation of gas content present in the PU polymer, as a function of volume fraction of D-water in the polymer as shown in Fig. 7.7. A linear correlation is observed between the gas content and the corresponding water content. Increasing the D-water content results in increasing the gas production in the polymer, which is entrapped in a form of a mostly closed cell structure.

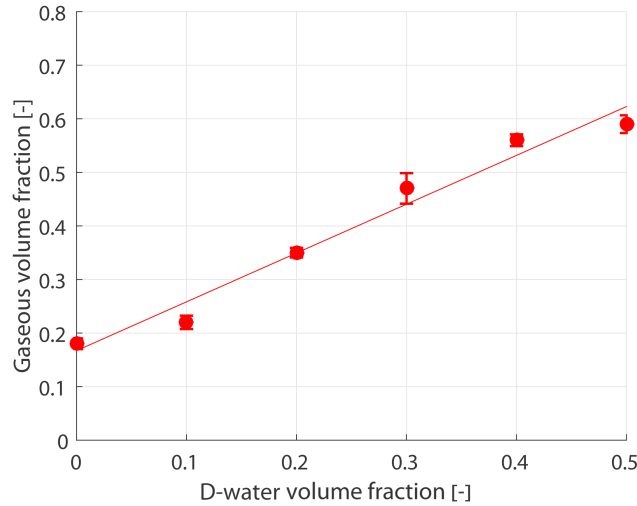


Figure 7.7: Variation of air content present in neat PU, prepared by the route shown in Fig. 7.3, as a function of D-water content.

The pore size distribution, quantified in the form of a maximum, minimum and average pore diameter, is shown in Fig. 7.8. The diameter is an equivalent circular diameter, calculated by conversion of the pore area to the diameter of a circular pore. The minimum diameter does not show significant changes with increasing the water content. However, the average and maximum diameters increase with rising the D-water content. The 0.5% D-water sample shows the highest average diameter of $260 \mu\text{m}$.

The volume fraction of the open cells, observed on the porous-PU microstructures, is calculated using the area fraction of the open cells with respect to the total area of the cells. The results at different D-water contents are shown in Fig. 7.9. Increasing the water content,

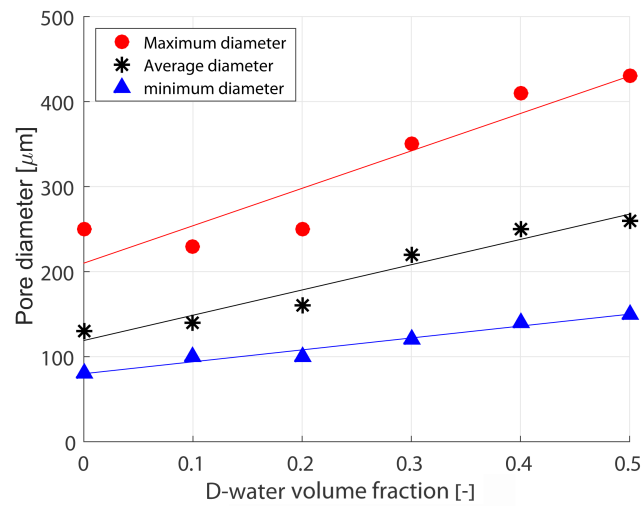


Figure 7.8: Variation of pore size present in neat PU, prepared by the route shown in Fig. 7.3, as a function of D-water content.

thus increasing the gas volume fraction, leads to cell walls merging that results in a higher content of open cells.

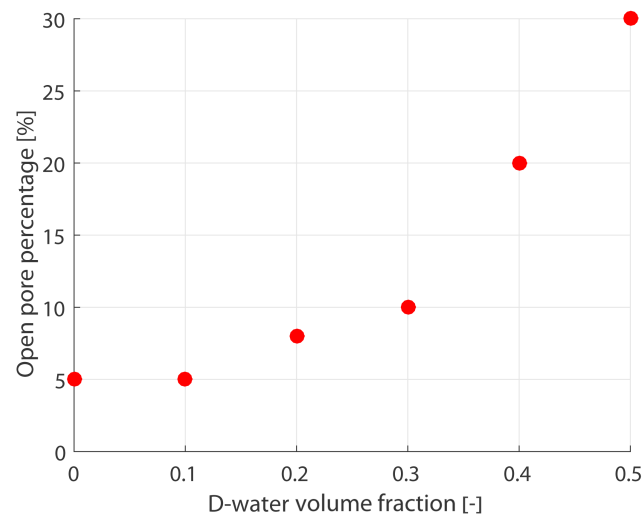


Figure 7.9: Open pore content in neat PU, prepared by the process shown in Fig. 7.3, as a function of D-water content.

The pore shape is quantified using the aspect ratio, AR, as a measure of elongation, calculated by dividing the maximum to minimum calipers. AR approaches infinity for a long object, while a more isotropic object has AR of 1. As shown in Fig. 7.10, the pore AR at different D-water content is very close to 1, which signifies that the pores resemble almost perfect spheres.

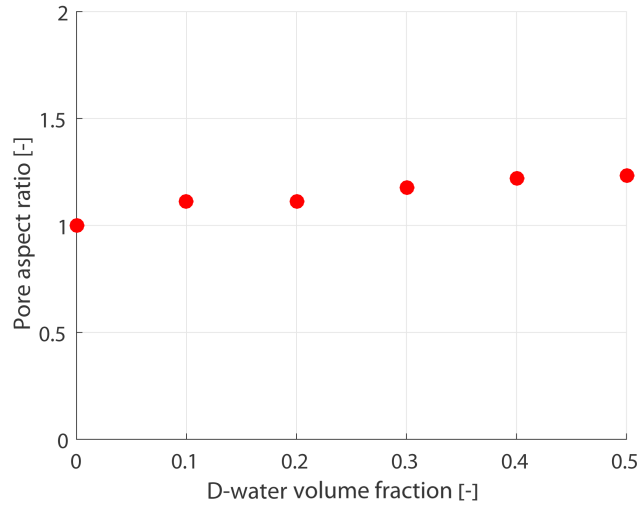


Figure 7.10: Average aspect ratio of pores present in neat PU, prepared by the process shown in Fig. 7.3, as a function of D-water content.

Microstructures of PZT-porous polymer composites

The microstructures of random PZT-porous PU composites, containing a range of PZT volume contents from 0 to 40%, are shown in Fig. 7.11. Samples show a uniform distribution of ceramic particles. Agglomerations are only observed at 40 vol% PZT. Pore free layers of about 300 μm and 100 μm are observed adjacent to the substrate on the 10% PZT-porous PU and 20% PZT-porous PU microstructures, respectively. The presence of this layer can be attributed to ceramic sedimentation, as well as lower viscosity of the low PZT content samples compared to the magnetically stirred mixtures, as shown in Fig. 7.5, which is more likely to keep the gas pores entrapped until the polymer matrix is cured. Increasing the PZT volume fraction results in a higher content of interface porosity.

The microstructures of dielectrophoretically (DEP) structured PZT-porous PU foam composites, containing a range of PZT volume content from 0 to 40%, are shown in Fig. 7.12. The pores show a uniform distribution through the thickness, likely to be affected by the application of the AC electric field during DEP. The chain formation is clearly visible in the cell walls, especially at lower PZT content. The structured 40% PZT-porous PU sample shows a very rough surface, containing a very high degree of interface porosity.

The variation of gas content, present in the random and structured PZT-porous PU composites is shown in Fig. 7.13. Addition of 0.4% D-water in the random composites of 0, 10% and 20% PZT in PU has successfully resulted in roughly 60 vol% of gas in these samples. In structured composites of 0, 10% and 20% PZT in PU, prepared in a closed mold, addition of 0.2% D-water has resulted in almost 60 vol% of gaseous phase. The structured 30% PZT and 40% PZT-porous PU samples show very rough cross sections with a high degree of interface porosity which makes the microstructural analysis less accurate. It is presumed that this is the reason for the gas volume content of these two samples, shown in Fig 7.13,

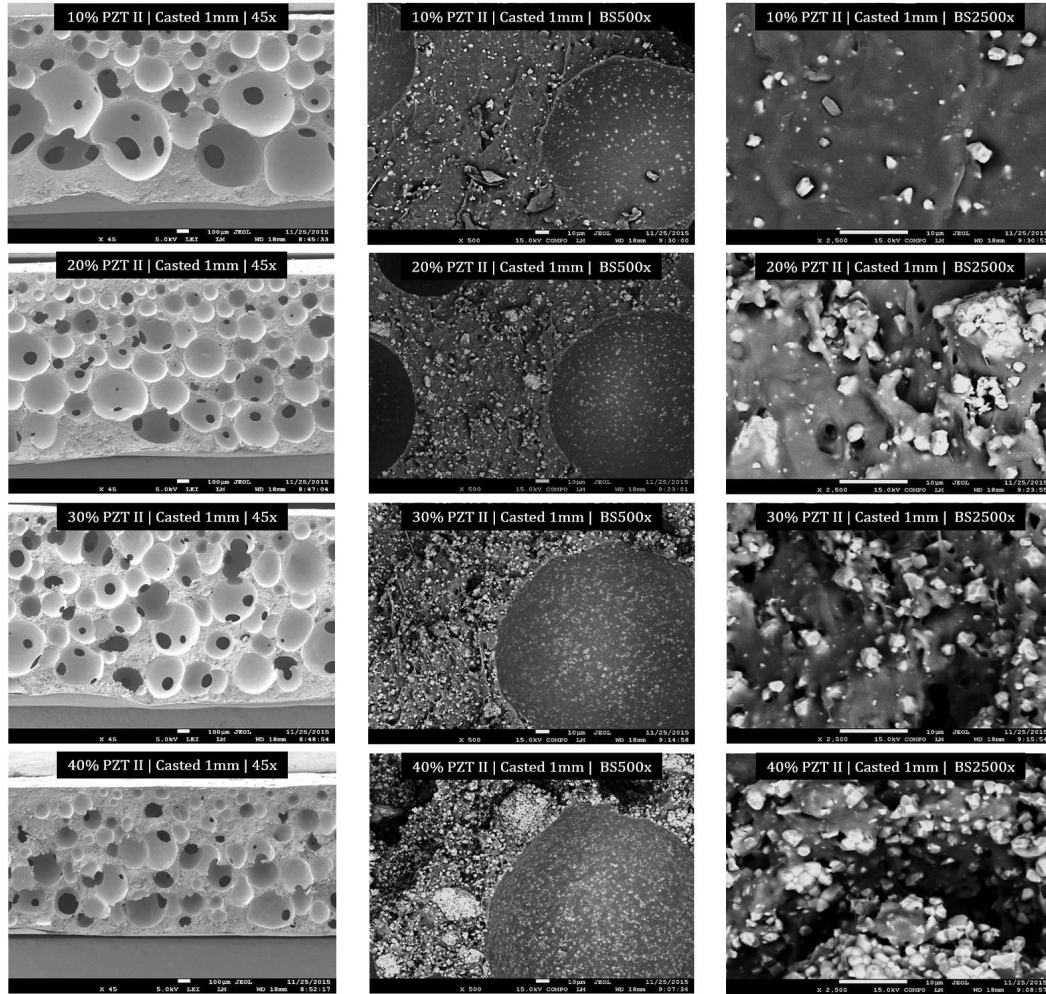


Figure 7.11: SEM micrographs of the 0-3 tri-phase sample range prepared using 0.4 vol% D-water.

to deviate from the expected trend.

The average pore diameters, quantified for random and structured PZT-porous PU composites, are presented in Fig. 7.14. The average pore size in structured composites varies from $250\ \mu\text{m}$ to $100\ \mu\text{m}$ with increasing the PZT content from 0% to 40%, respectively. Increasing the PZT volume fraction results in higher viscosity of the composites, which restricts the pore growth. The same trend is observed in random composites, containing PZT ranging from 20% to 40%. However, the random 10% PZT-porous PU sample shows an extremely large average pore diameter of $400\ \mu\text{m}$. The reason can be attributed to the low viscosity of this sample which accommodates the voids on the bottom of the film to merge until they form large pores, while the smaller voids closer to the top escape the film.

The aspect ratios of the pores in the random and structured PZT-porous PU composites are shown in Fig. 7.15. The random composites of varying PZT content show consistent

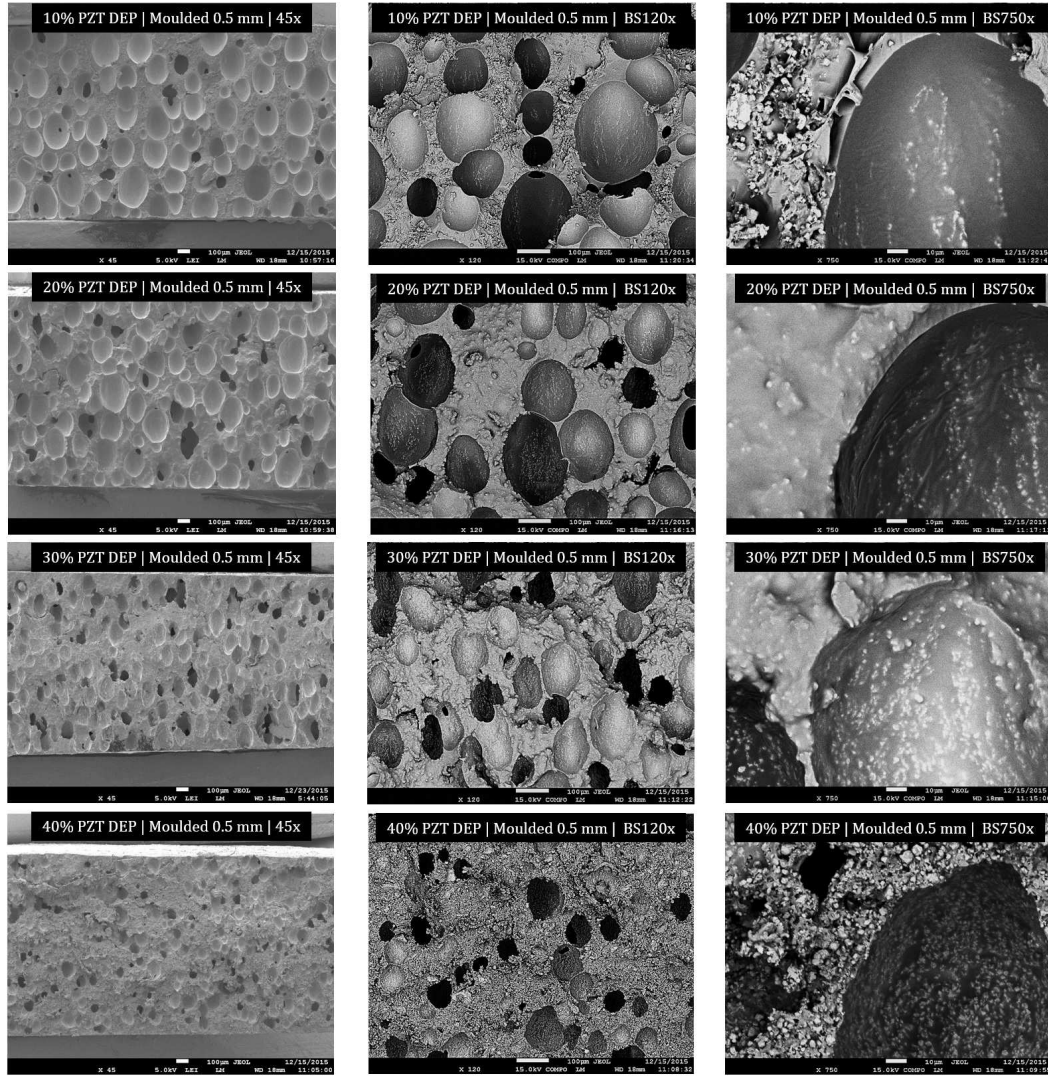


Figure 7.12: SEM micrographs of the 1-3 tri-phase DEP sample range prepared using 0.2 vol% D-water.

AR, close to 1, which indicates spherical voids as shown in Fig. 7.11. However, the DEP structured composites show elongated pores in the field direction, as presented in Fig. 7.12. A maximum AR of 1.7 is observed for the structured 30% PZT-porous PU composite.

The open pore content as a function of PZT content is shown in Fig. 7.16 for random and structured composites of PZT-porous PU. Increasing the PZT volume content from 0 to 40% results in a small increase of open pore content, in both random and structured composites. A maximum pore volume fraction of 0.3 is observed for the 40% PZT-porous PU sample.

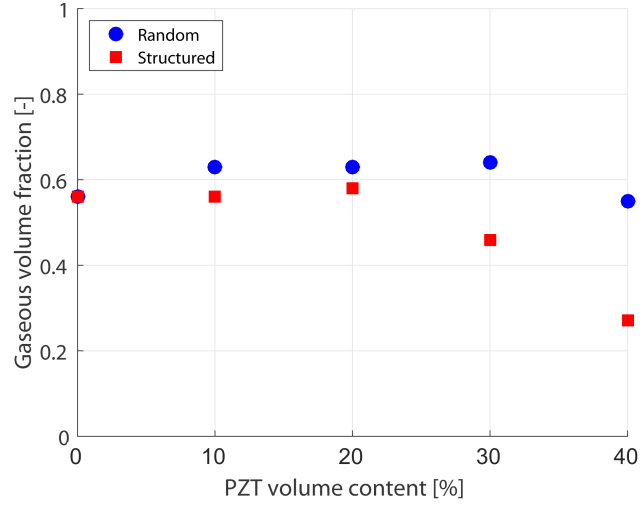


Figure 7.13: Variation of gaseous volume content in PZT-porous PU random and structured composites as a function of PZT content.

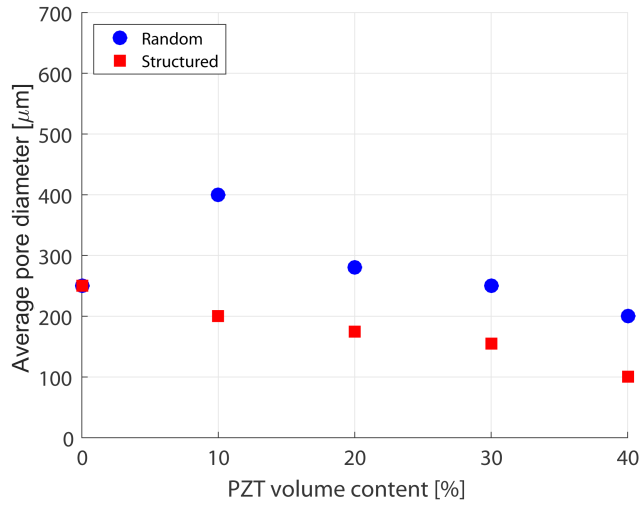


Figure 7.14: Variation of pore size in PZT-porous PU random and structured composites as a function of PZT content.

7.3.2 Properties of composites

The effect of gaseous volume fraction on the dielectric constant (ϵ_{33}) of the PZT-PU tri-phase composites at 1 kHz is shown in Fig. 7.17. The dielectric constant decreases noticeably with increasing porosity, as the increasing amount of air ultimately leads to a permittivity of one. The presence of 56 vol% gas results in a 62% reduction in the dielectric constant from 11.1 to 4.2.

Considering the polymer foam a di-phase composite, consisting of a gaseous phase in a

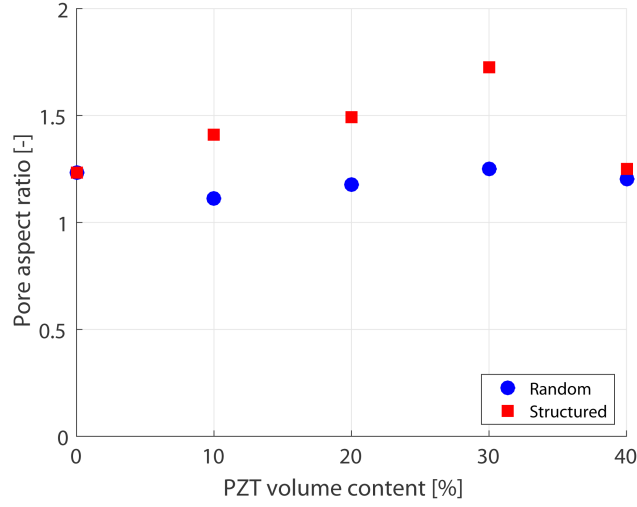


Figure 7.15: Average aspect ratio of pores present in PZT-porous PU random and structured composites as a function of PZT content.

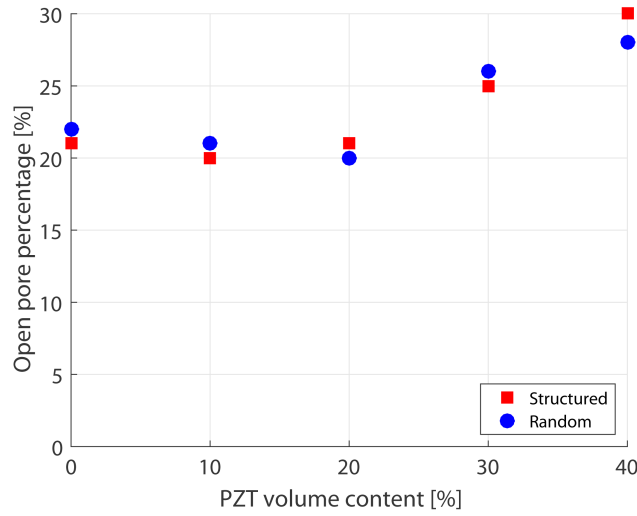


Figure 7.16: Open pore content in in PZT-porous PU random and structured composites as a function of PZT content.

polymer matrix, the properties of the foam can be simulated using Yamada's model (Eq. 2.2). The dielectric constant of the neat PU polymer is measured to be 11.1 at 1 kHz. To fit the experimental data to the model an n value of 3 is used, which corresponds to aspect ratios of 1, which is an indication of spherical gas inclusions. This is in agreement with the AR of the porosities presented in Fig. 7.10, that can also be seen from the SEM microstructures, shown in Fig. 7.5. The lower and upper bounds of the dielectric constant can be simulated using serial and parallel arrangements, based on the mixed connectivity model [12]. In

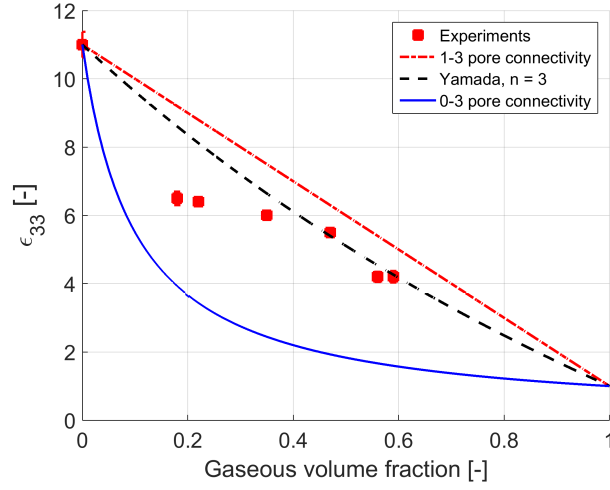


Figure 7.17: Variation of dielectric properties of neat PU foams at 1 kHz with the containing gas volume fraction.

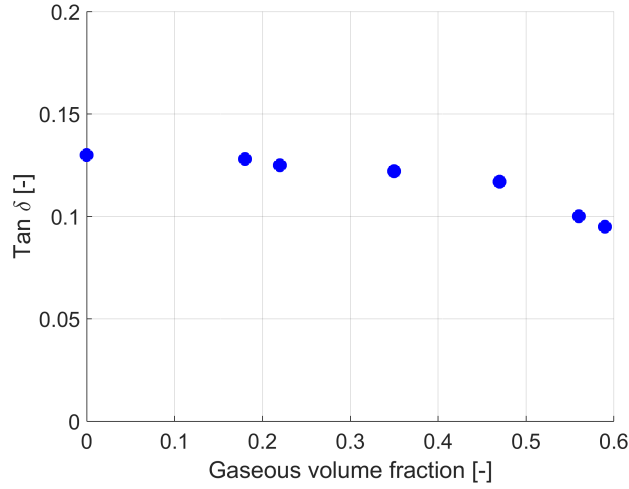


Figure 7.18: Variation of dielectric loss of neat PU foams at 1 kHz with the containing gas volume fraction.

the serial mode (0-3), the porosities are homogeneously distributed in the polymer matrix. However, in the parallel mode (1-3), the microstructure can be considered as columns of porosity, elongated in the thickness direction. The dielectric constant, as a function of the gas content at low gas volume fractions, shows a good agreement to the predictions of the serial model.

The effect of gaseous volume fraction on the dielectric loss, $\tan \delta$, of the PZT-PU tri-phase composites at 1 kHz, is shown in Fig. 7.18. $\tan \delta$ is taken as measure of dielectric loss and is known as loss tangent. In a perfect insulator, there is no consumption of energy, and electric

current leads the applied voltage by 90° . However, for commercial dielectrics, this phase angle is less than 90° by an angle δ , which is called dielectric loss angle. As shown in Fig. 7.18 $\tan \delta$ seems to slightly decrease with increasing the gaseous volume fraction which is in agreement with the documented behavior of polymer foams [70, 141].

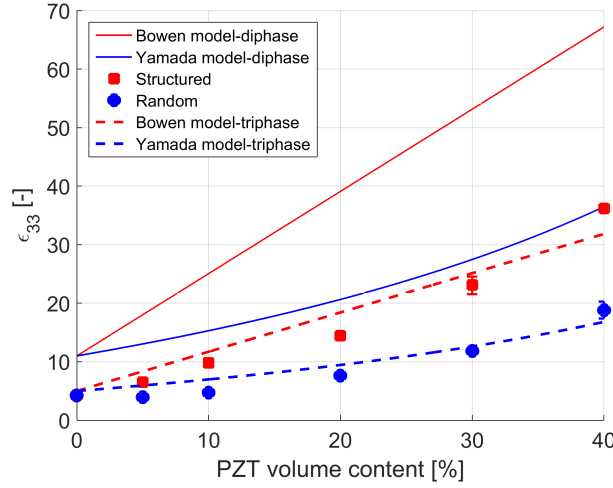


Figure 7.19: Measured dielectric constant values at 1 kHz for structured and random composites with their associated models. Dashed lines indicate the model predictions for PZT-porous PU composites, and the solid lines show properties of PZT-bulk PU composites.

The dielectric properties of the tri-phase composites, containing PZT powder ranging from 0 vol% to 40 vol% in PU polymer foam matrix, are shown in Fig. 7.19. The dielectric constant of the polymer foam, used as an input for modeling the properties of the tri-phase composites, is experimentally determined as 4.7 for a PU sample containing approximately 60 vol% of gaseous phase. The properties of the random and structured composites are fitted to the models proposed by Yamada (Eq. 2.2) and Bowen (Eq. 2.3), respectively. The best fit of the experimental data to Yamada's model, for the random composites, was obtained for $n = 3.6$, which indicates spherical particles. The best fit of the experimental data to Bowens's model, for the structured composites, was obtained for R values of 15. The predictions of the associated models for di-phase composite system, consisting of PZT particles and PU polymer, are also presented for comparison. Both random and structured di-phase PZT-bulk PU composites show higher dielectric constant than the tri-phase foam based composites. For the whole PZT range, the improvement in dielectric constant of the tri-phase composites is in accordance with the change in the permittivity of the polymer phase upon addition of the gaseous phase. The gas volume content of random and structured composites (Fig. 7.11 and Fig. 7.12) are shown in Fig. 7.13.

The influence of DEP structuring on piezoelectric charge constant, d_{33} , of the tri-phase composites is shown in Fig. 7.21. The Young's modulus of the porous-PU, as an input for the Van den Ende model, is calculated using the mixed connectivity model, for a perfect 0-3 composite in the serial mode, as shown in Fig. 7.20. The stiffness of a di-phase material in

a serial arrangement follows a rule of mixtures:

$$C_{33} = Q_1 \cdot C_{331} + Q_2 \cdot C_{332} \quad (7.1)$$

where C_{33} is the stiffness in the thickness direction, Q is the volume content of the constituent phases, and subscripts 1 and 2 denote the phases, respectively. The input stiffness values for the d_{33} simulations was chosen based on the gas content of the composite. The neat PU has a modulus of 4.6 MPa, which decreases significantly with increasing the gas content.

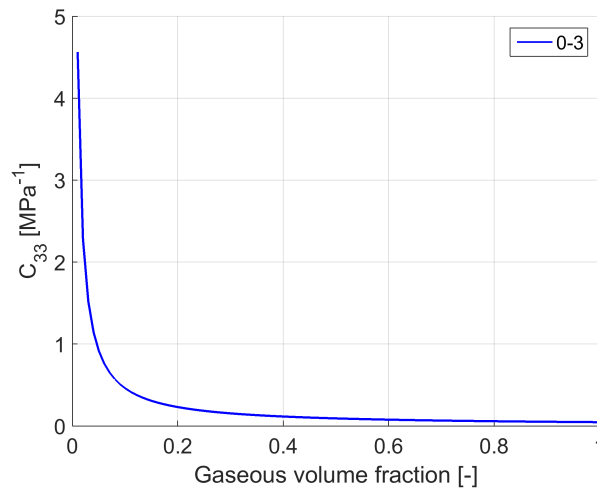


Figure 7.20: Variation of stiffness of the porous PU material with the gaseous volume content.

The measured d_{33} values of structured and random composites are compared with their associated models (Eq. 2.4 and Eq. 2.5). However, the change in the stiffness of the polymer matrix does not seem to affect the d_{33} of the PZT-PU composites (see Fig. 7.21), as both di-phase and tri-phase composites show similar behaviors. The best fit of the experimental d_{33} data of the random composites to Yamada's model was obtained for $n = 3.6$ and $\alpha = 1$. This is a clear indication of efficient poling. The best fit of the experimental data to Bowens's model for the structured composites was obtained for R values of 10. The maximum d_{33} value of 25 pC/N is obtained for 40% PZT-PU tri-phase composite, which is twice that of the d_{33} value of 40% PZT-epoxy composite [11]. Moreover, adding the gaseous phase results in a decrease in the stiffness of the polymer matrix, which consequently leads to higher d_{33} values compared to a stiffer polymer matrix [57]. A matrix stiffness assures a minimal absorption of mechanical energy by the matrix upon loading. This results in higher effective strains in the piezoelectric composite material.

The piezoelectric voltage coefficient, g_{33} , calculated by dividing the d_{33} of the composites by their relative permittivity, is plotted as a function of the PZT volume fraction in Fig. 7.22. The maximum value obtained for the random composites is 94 mV.m/N, at a PZT volume fraction of 40%, while for the structured porous composite, a value of 166 mV.m/N

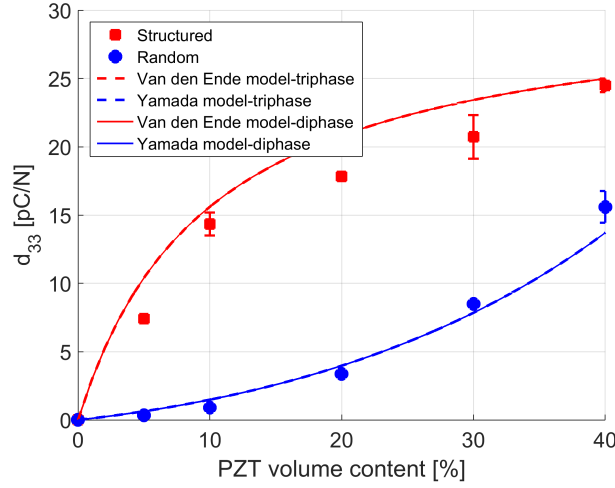


Figure 7.21: d_{33} values for structured and random composites with their associated models. Dashed lines indicating the predictions for PZT-porous PU composites coincide with the solid lines showing properties of PZT-bulk PU composites.

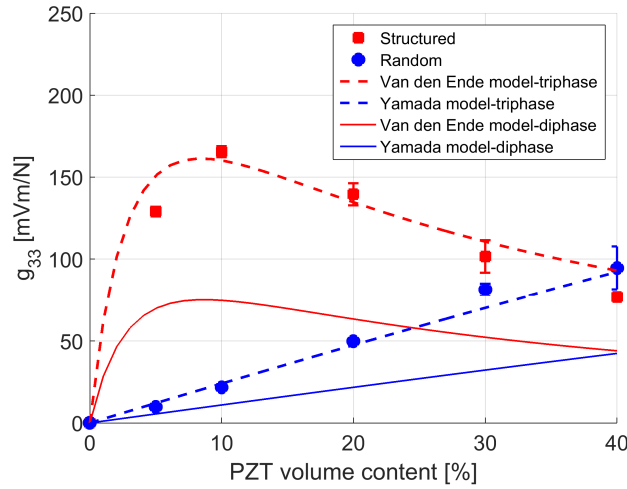


Figure 7.22: g_{33} values for structured and random composites with their associated models. Dashed lines indicate the model predictions for PZT-porous PU composites, and the solid lines show properties of PZT-bulk PU composites.

is obtained at a PZT volume fraction of 10%. The predictions of the models for the random and structured bulk di-phase systems are also shown. At 10 vol%, the maximum g_{33} of a structured bulk di-phase composite is approximately 80 mV.m/N. Therefore, a factor of two improvement in g_{33} is obtained in 10% PZT-porous PU composites by decreasing the dielectric constant of the polymer phase when adding a gaseous content of 60 vol%. The maximum g_{33} reported for structured bulk di-phase particulate composites ranges between

70-90 mV.m/N [11, 32]. Addition of the third gaseous phase significantly improves the g_{33} performance of the particulate composites.

7.4 Conclusions

The addition of a gaseous phase in the form of spherical well-distributed inclusions effectively reduces the dielectric permittivity of PU polymer, which improves the piezoelectric voltage coefficient of the PZT-PU-gas tri-phase composites significantly. The unique combination of dielectrophoretic structuring of PZT particles and the addition of a gaseous phase to the polymer resin results in the best performance of the particulate composite sensors reported in the literature so far. The g_{33} values of the newly developed triphase composites exceed those of the structured di-phase PZT-bulk PU composites (80 mV.m/N), as well as those of the structured PZT-epoxy composites (72-78 mV.m/N) by a factor of two, and more than five times the g_{33} of the bulk PZT ceramics (24-28 mV.m/N).

High temperature PT-polyetherimide composites

8.1 Introduction

High temperature piezoelectric materials for application in automotive, aerospace and energy production have been a growing area of research [72]. In automotive electronics, repeated thermal cycles of up to 150 °C are currently the norm, with temperatures as high as 500 °C being expected for the near future. In aerospace industry, structural health monitoring of the engines requires sensors to be as close as possible to the engine, leading to exposure to high temperatures. Moreover, exploration of new sources for clean energy, such as nuclear and wind power, as well as geothermal and electrical energy, has significantly motivated the development of high temperature electronic materials. High temperature sensors for structure health monitoring can ensure enhanced lifetime and reliability, less maintenance and downtime, and can thus reduce the overall cost of renewable energy sources [73, 74]. Piezoelectric materials can also be used for mechanical energy harvesting converting the vibrations, present in the environment, into electrical energy. An example of energy harvesting under extreme conditions is in oil producing wells, where the ambient pressures may reach to 200 MPa, and the temperature reaches 200 °C. In this case local power production is crucial, since transmitting power from the surface is complicated, due to the difficulty of making reliable electrical connections in harsh environments [142].

The use of conventional piezocomposites in high temperature applications has been limited, due to the reduced sensing capability of the piezoceramic at elevated temperatures, increased conductivity and mechanical attenuation, as well as variation of the piezoelectric properties of the ceramic phase with temperature. Most importantly, the low glass transition temperature and high thermal expansion of the polymer matrix limit the operational temperature range of a piezocomposites. High T_c piezo-ceramics can be embedded in high temperature polymers to overcome this problem. In practice, the operating temperature must be substantially below the Curie temperature of the piezoceramic phase, in order to

minimize thermal aging and property degradation.

High performance amorphous polyimides are interesting candidates for the applications mentioned above [75,76,78–80]. Growing interest for viable, multifunctional and lightweight materials for demanding space applications has lead into developing new series of such polymers [75–77] with superior mechanical and chemical properties. Some of the polymer systems in this family have been reported to show insignificant piezoelectric properties [75,78]. One of the most widely reported piezo polyimide polymers is a polyimide, containing a single nitrile group, (b-CN)APB/ODPA. As opposed to the well-known semicrystalline PVDF polymer family, the high temperature performance of this polyimide allows these films to retain 50% of the room temperature remnant polarization at temperatures up to 150 °C [78]. However, the remnant polarization of this system is very low, 14 mC/m², when poled at 100 kV/mm, for 1 h above T_g . Therefore, the piezoelectric charge coefficient of this polyimide is much lower than that of PVDF [75, 78]. Limited chain mobility in the imidized film restricts the preferential alignment of the dipoles upon application of an electric field. To solve this problem, new polymers have been synthesized, with different types and concentrations of the polar groups [79]. Despite the interesting research outcomes, the polyimide systems exhibit very low piezoelectric responses that are not high enough to attract commercial interest [75, 76, 79, 143].

To overcome these limitations, and to achieve adequate combinations of mechanical, thermal, dielectric and electroactive properties, researchers have embedded ferroelectric ceramic particles within polyimide polymers. Structuring the ceramic particles into a chain form configuration, by means of dielectrophoresis (DEP), has been shown to improve the dielectric, piezoelectric, and pyroelectric properties of such piezoceramic-polymer composites over those of random composites [31–33]. In this work, processing of high temperature lead titanate-polyimide composites is presented. Among various kinds of commercially available ferroelectric ceramics for sensing applications, lead titanate (PT) is a good high temperature piezoelectric material with a very high Curie temperature of 490 °C, exhibiting a large spontaneous polarization and a small relative dielectric constant [23, 144]. Therefore, it serves as a viable candidate for integration with high temperature polyimide films. In this chapter the manufacturing procedure of PT-ODPA/ODA composites is discussed, and the microstructures, as well as functional properties of the composites are assessed.

8.2 Experimental procedure

8.2.1 Composite manufacturing

The polyimide studied, ODA/ODPA, was prepared using a standard 2-step synthesis method via a polyamic-acid solution in N-Methyl-2-pyrrolidone (NMP). The scheme is shown in Fig. 8.1. The thermal properties of the films were determined by Thermogravimetric Analysis (TGA), using a Perkin Elmer Pyris Diamond, as well as Differential Scanning Calorimetry (DSC), using a Perkin Elmer Sapphire DSC. Samples were heated at a rate of 20 °C/min under a nitrogen atmosphere to 550 °C. Dynamic Mechanical Thermal Analysis (DMTA) was performed in the tensile mode, at a frequency of 1 Hz and a heating rate of 2.0 °C/min,

using films of approximate dimensions of $20 \times 3 \times 0.005$ mm.

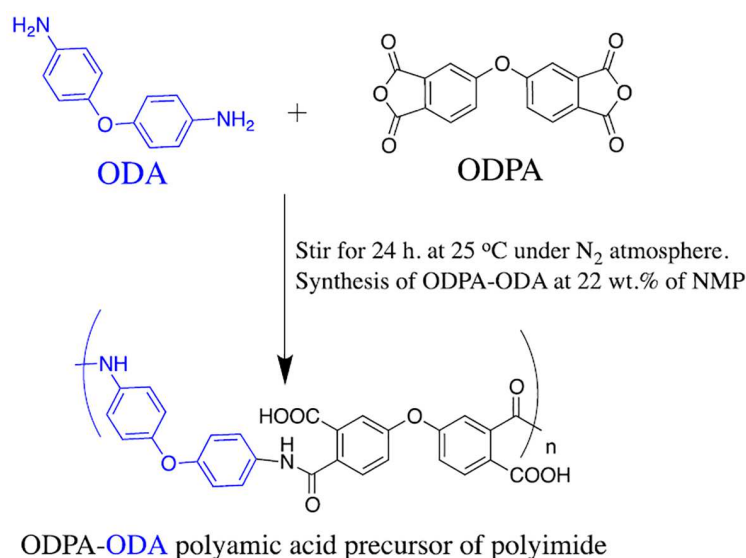


Figure 8.1: Scheme of (b-CN)APB/ODPA polymerization.

Lead titanate (PT) powder, purchased from Sigma Aldrich, was calcined at 800 °C for 2 h to develop single phase PbTiO_3 . The agglomerated powder was then dry-milled, using 5-mm zirconium balls for 2 h in a single G90 jar mill. The particle size distribution of milled powder in an aqueous solution with 10% isopropyl alcohol, measured by a Beckman Coulter LS230 laser diffraction analyzer was found to be $d(50) = 3 \mu\text{m}$. The powder was stored in a vacuum drying oven at 120 °C for 24 h prior to the experiment to avoid moisture absorption. The dried PT powder is predispersed in NMP, stirred for 1 h, and added to the polyamic acid. The mixture was cast on an Aluminum foil using a doctor blade, with an initial film thickness of 600 μm . Structuring of the particles in the polyamic acid polymer was realized by a dielectrophoresis process, in which an electric field of 2 kV/mm and a frequency of 2 kHz was applied to the composite medium of particles dispersed in PAA, using a function generator (Agilent, 33210A) coupled to a high voltage amplifier (Radiant Technologies Inc., T6000HVA-2) at room temperature (RT) for 1 h in an Argon purged oven. Once the structuring of the particles was realized, the film was dried at 60 °C for 1.5 h under the same atmosphere and electric field. The randomly dispersed samples were obtained by the process described above, only without applying an electric field by oven curing at 60 °C for 1.5 h, using inert Argon gas as the surrounding medium. The free standing films were then removed and cut to discs of 7 mm diameter. Au electrodes were sputtered on the samples, and they were poled at 150 °C for 30 min with an electric field of 20 kV/mm. The poled films were then imidized in a vacuum oven at 200 °C and 300 °C, each for 1 h. The resulting films have a fully imidized chemical structure as shown in Fig. 8.2.

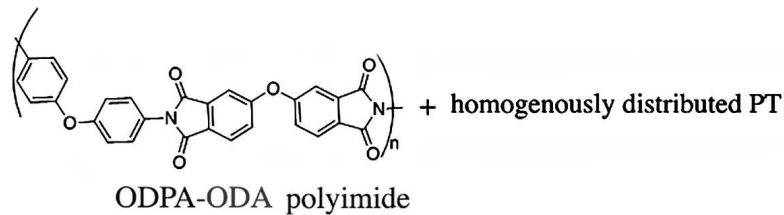


Figure 8.2: Chemical structure of fully imidized 20% PT-ODPA/ODA composite.

8.2.2 Measurement procedure

A Novocontrol Broadband Dielectric Spectroscopy (BDS) is used in conjunction with a Cryostat high temperature sample cell and an Agilent E4991A impedance analyzer at 1 V and 1 kHz to measure the dielectric properties as well as electrical conductivity of the polymer films. The dielectric constant of the composites was determined using the parallel plate capacitor method with an Agilent 4263B LCR meter at 1 V and 1 kHz. The piezoelectric coefficient, d_{33} , measurements were done with a high precision PM300 Piezometer, Piezosystems, at 110 Hz and under a static and dynamic force of 10 N and 0.25 N, respectively. Before performing the d_{33} measurements, the samples were grounded with their electrodes shorted at 100 °C for 24 h to remove any remaining space charges. To test the d_{33} of the composites at elevated temperatures, a modified sample holder was manufactured and connected to the CF technologies PM3001 d_{33} meter, as shown in Fig. 8.3. The sample was placed on a Copper electrode and heated uniformly using two integrated programmable heaters. The fixture was thermally insulated using Kapton foils, and the set-up was calibrated using reference PZT ceramics with known properties. It has to be noted that the maximum test temperature is above the advised operating temperature of the set-up. The pyroelectric properties were determined at 25 °C at 5 mHz, using the AC method as described in Chapter 6.

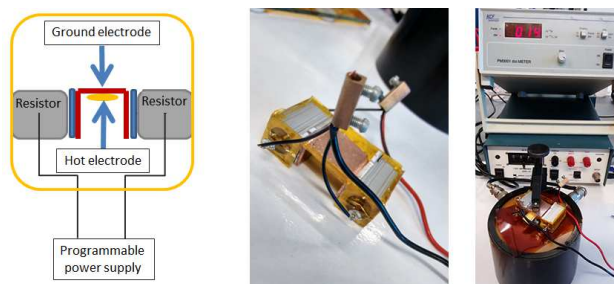


Figure 8.3: The sample holder used in conjunction with PM3001 d_{33} meter for d_{33} measurements at elevated temperatures. Figure on the right shows a sample being tested.

8.3 Results and discussion

8.3.1 Microstructure analysis

The effect of DEP structuring on the SEM microstructures of the 20% PT-ODPA/ODA composite samples is shown in Fig. 8.4. A clear difference can be observed between random and structured composites. It can be seen that during dielectrophoresis, ceramic particles form chain like structures along the electric field direction. The degree of alignment which affects the final dielectric and electroactive properties of the composites depends on the force acting on the particles, as a consequence of the imposed electric field.

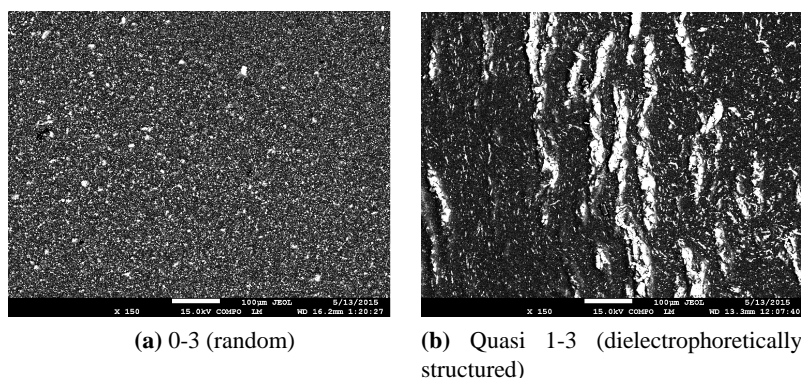


Figure 8.4: SEM microstructures of fully imidized 20% PT-ODPA/ODA.

8.3.2 Thermo-mechanical analysis

The TGA result of fully imidized ODPA/ODA is shown in Fig. 8.5a. A 2% weight loss is observed at 520 °C. The DMTA results, presented in Fig. 8.5-b, show a storage modulus of 4.0 GPa, at room temperature for neat ODPA/ODA and ODPA/ODA with 20 vol% PT. The T_g remains unchanged at 265 °C.

8.3.3 Dielectric, piezoelectric and pyroelectric analysis

The dielectric and resistivity of fully imidized, as well as partially imidized ODPA/ODA are shown in the frequency range of 100 Hz to 1 MHz in Fig. 8.6. The glass transition of imidized ODPA/ODA can be observed in the real permittivity spectrum, as the temperatures exceeds 260 °C. At temperatures below T_g the polymer shows a stable dielectric behavior. However, the partially imidized ODPA/ODA film shows a frequency dependent dielectric constant, and is more conductive than the fully imidized ODPA/ODA as also reported in literature [145].

The resistivity plots show that the electrical conductivity of partially imidized ODPA/ODA at 100 °C is more than two orders of magnitude higher than that of fully imidized ODPA/ODA

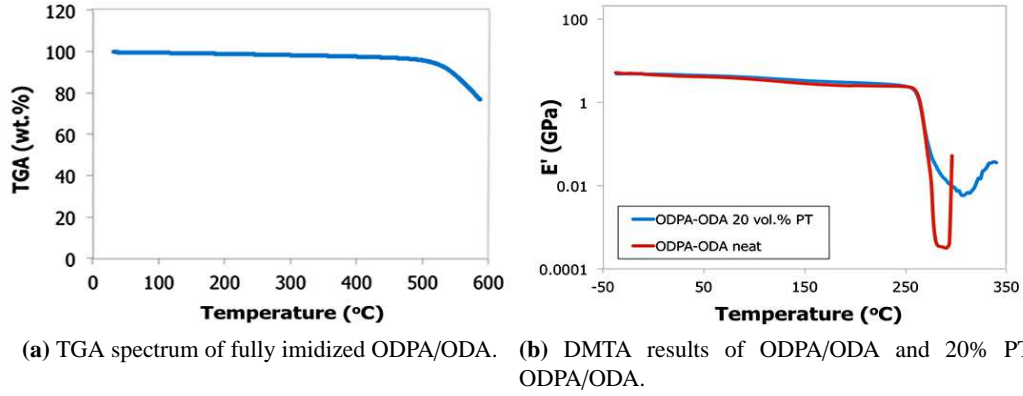


Figure 8.5: Thermo-mechanical properties of fully imidized PT-ODPA/ODA.

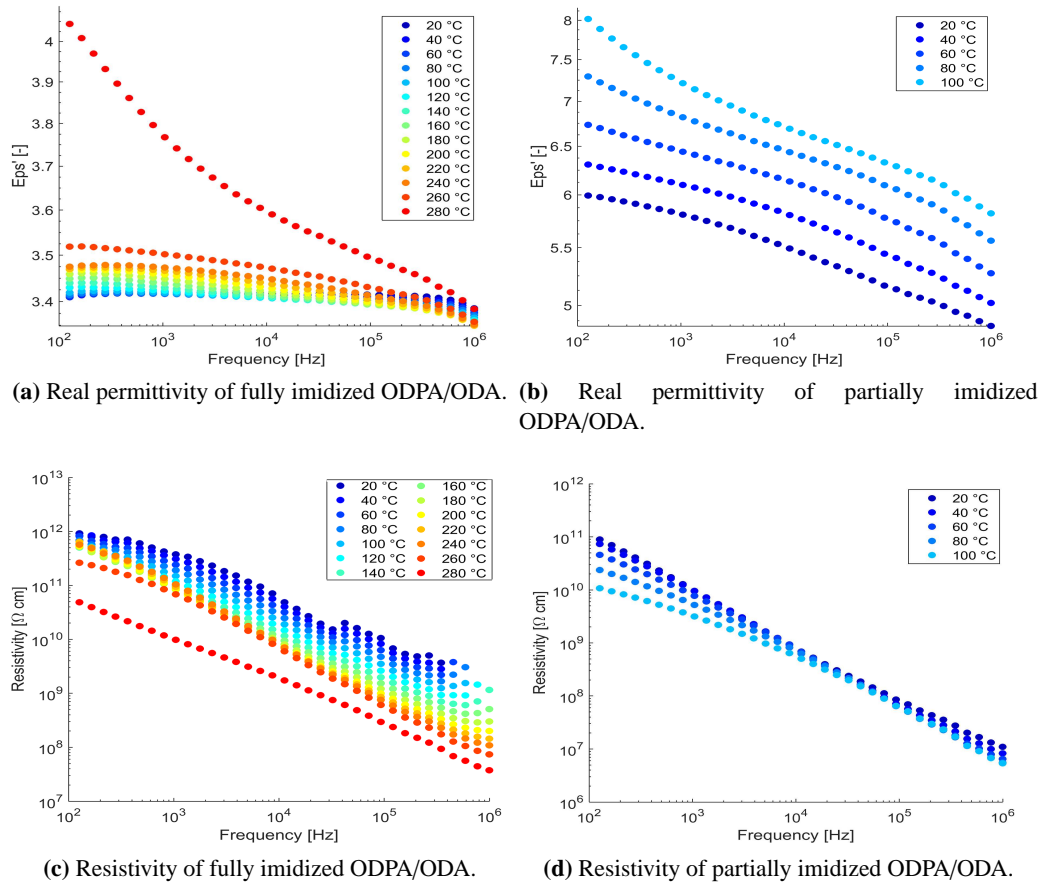


Figure 8.6: Dielectric and electrical resistivity properties of fully and partially imidized ODPA/ODA.

at this temperature. This is in agreement with the results of Park et al., who investigated the effect of processing parameters such as curing conditions on (b-CN)APB/ODPA systems [75]. It has been shown that the partially cured (b-CN)APB/ODPA, in other words polyamic acid with open imide rings, exhibit a higher net dipole moment than the fully imidized closed ring [75, 76, 79].

The lower resistivity of the partially imidized ODPA/ODA causes efficient poling of the composites. During poling, the mobility of charges in the polymer matrix is a key parameter in defining the final poling efficiency. As the permittivity of PT is much higher than that of the polymer matrix, as shown in Chapter 6, the charge relaxation time is mainly governed by the electrical conductivity of the matrix. The higher conductivity of the partially imidized ODPA/ODA shortens the time required for the electric field acting on the ceramic inclusion to reach saturation, thereby making the poling of the ceramic phase more efficient [49, 122]. $\tan \delta$, as an indication of dielectric loss angle, is 0.001 and 0.02 for fully imidized and partially imidized ODPA/ODA films at 20 °C and 1 kHz, respectively.

The effect of DEP structuring on dielectric constant of the 20% and 30% PT-ODPA/ODA composites is shown in Fig. 8.7. The experimental data for random composites are fitted to Yamada's model, using an n value of 5. Dielectric properties of the structured composites are fitted to Bowen's model [33], using an R value of 10.

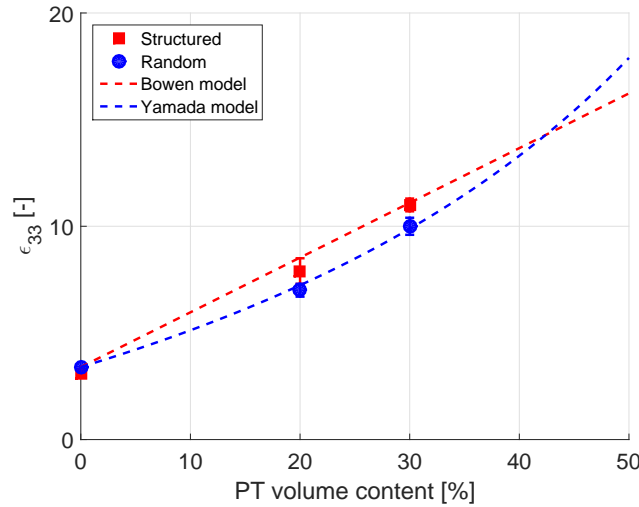


Figure 8.7: Dielectric constant values of structured and random 20% and 30% PT-ODPA/ODA composites composites with their associated models.

The influence of DEP structuring on piezoelectric charge constant, d_{33} , of the composites is shown in Fig. 8.8, where the experimental d_{33} values of random and structured 20% and 30% PT-ODPA/ODA composites are compared with the predictions of Yamada's and Van den Ende's models described in chapter 2. The best fit of the experimental data to the model predictions was obtained for $n = 5$, $R = 10$ and $\alpha = 1$, which is an indication of high poling efficiency attributed to the relatively low electrical resistivity of the partially imidized ODPA/ODA.

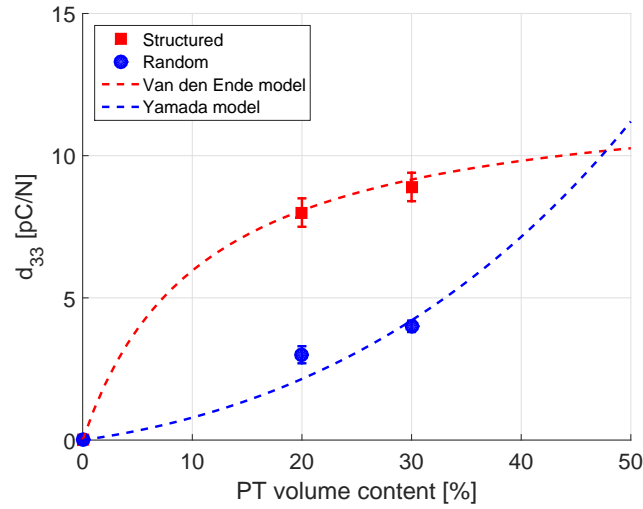


Figure 8.8: d_{33} values of structured and random PT-epoxy 20% and 30% PT-ODPA/ODA composites with their associated models.

The d_{33} of 20% and 30% PT-ODPA/ODA composites are tested as a function of temperature, as shown in Fig. 8.9. A stable behavior is observed over the temperature range from room temperature to 175 °C. The room temperature d_{33} value can be retained upon cooling back. This stability is caused by the thermally stable dielectric and piezoelectric properties of the high T_c lead titanate [14], as well as stable dielectric properties of the ODPA/ODA in this temperature range, as shown in Fig. 8.10.

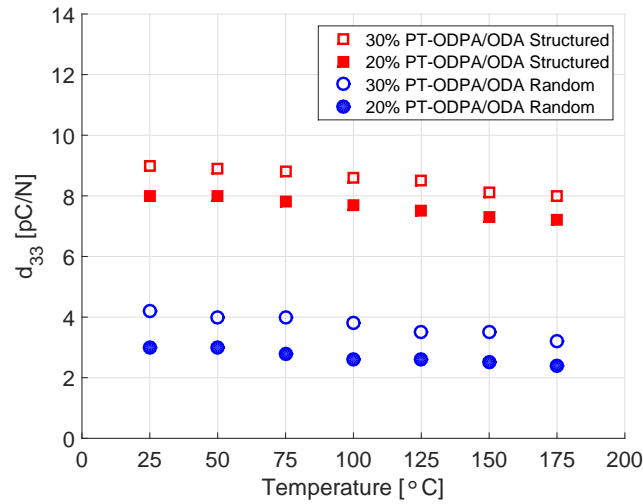


Figure 8.9: d_{33} of fully imidized random and structured 20% and 30% PT-ODPA/ODA composites as a function of temperature.

The piezoelectric voltage coefficient values, g_{33} , at room temperature which were calculated

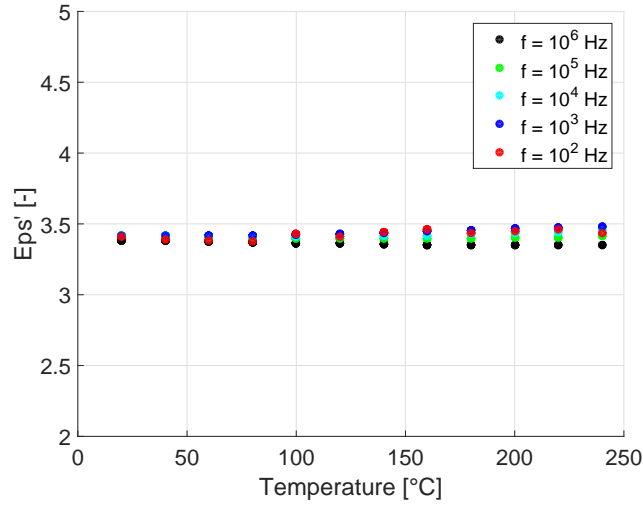


Figure 8.10: Relative permittivity of fully imidized ODPA/ODA polymer as a function of temperature at different frequencies.

by dividing the d_{33} of the composites by their dielectric constant, are 48 mV.m/N and 114 mV.m/N for random and structured 20% PT-ODPA/ODA composites, respectively. The g_{33} for random and structured 30% PT-ODPA/ODA composites are 45 mV.m/N and 90 mV.m/N, respectively. The room temperature g_{33} values for the PT-ODPA/ODA composites are compared to those of PT-epoxy reference composites, as presented in Chapter 2, in Fig. 8.11. The DEP structured 20% PT-ODPA/ODA composites show 30% improvement in g_{33} compared to the structured 20% PT-epoxy composites, which is mainly due to their lower dielectric constant.

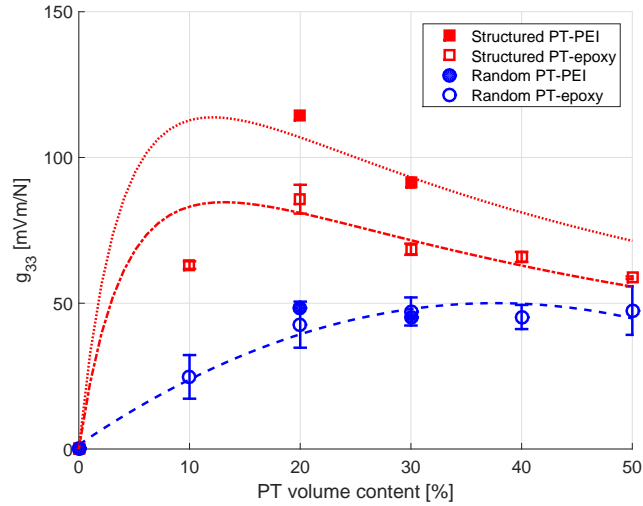


Figure 8.11: Comparison of room temperature g_{33} values for structured and random PT-epoxy and PT-PEI composites with their associated models.

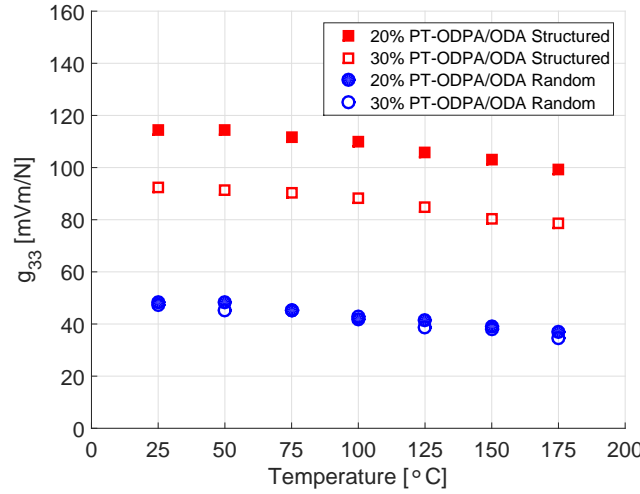


Figure 8.12: g_{33} of fully imidized random and structured 20% and 30% PT-ODPA/ODA composites as a function of temperature.

The g_{33} of 20% and 30% PT-ODPA/ODA composites are calculated as a function of temperature and are shown in Fig. 8.12. Structured 20% PT-ODPA/ODA composites maintain their high g_{33} values of over 100 mV.m/N over the temperature range from room temperature to 175 °C. The stable g_{33} behavior of all composites over the mentioned temperature range is attributed to the thermally stable piezoelectric properties of the high T_c lead titanate [14], as well as stable dielectric properties of the ODPA/ODA in this temperature range, as shown in Fig. 8.10.

The pyroelectric coefficients of the composites are calculated based on the pyroelectric current at 5 mHz temperature oscillation at 25 °C, using the device presented in Chapter 6. The values of pyroelectric coefficient are $0.37 \mu\text{C.m}^{-2}.\text{°C}^{-1}$ and $0.62 \mu\text{C.m}^{-2}.\text{°C}^{-1}$ for the random and structured 20% PT-ODPA/ODA composites, respectively. In comparison to 20% PT-ODPA/ODA composites, 30% PT-ODPA/ODA composites show higher pyroelectric coefficients of $0.55 \mu\text{C.m}^{-2}.\text{°C}^{-1}$ and $0.90 \mu\text{C.m}^{-2}.\text{°C}^{-1}$ for the random and structured composites, respectively.

8.4 Conclusions

High temperature PT-ODPA/ODA composites, prepared by solution casting in the forms of 0-3 and quasi 1-3, show thermally stable dielectric and piezoelectric properties in the temperature range from room temperature to 175 °C. Thermally stable dielectric and piezoelectric properties of the high T_c lead titanate [14], as well as stable dielectric properties of the fully imidized ODPA/ODA polymer matrix result in an improved temperature functionality of these high performance composites. Relatively high electrical conductivity as well as permittivity of the partially imidized ODPA/ODA polymer matrix provides a high poling efficiency. After full imidization at 300 °C the imide rings completely close, resulting in

a thermally stable polymer with a very low dielectric loss that maintains the piezoelectric sensitivity up to 175 °C.

Summary

The main objective of the research described in this thesis is to explore several new piezoelectric ceramic-polymer composite materials and relate the effect of topology, processing and intrinsic properties of the constituent materials, mainly the polymer phase, to piezo-, pyro-, and ferroelectric properties of the di-phase and tri-phase composites.

In Chapter 2, functional composites of lead titanate (PT) particles in an epoxy matrix, prepared by dielectrophoresis, are shown to have enhanced dielectric, piezoelectric and pyroelectric properties compared to 0-3 composites (i.e. composites consisting of granular, non-connected particles in a continuous polymer matrix) for different ceramic volume contents ranging from 10% to 50%. The degree of structuring, as well as the electrical properties of the constituents, are shown to be the most important parameters controlling the overall properties of the composites. Two structuring parameters, the interparticle distance and the percentage of 1-3 connectivity (i.e. a continuous one-dimensional fibrillar connectivity of the functional ceramic particles in a polymer matrix) are determined on the basis of Bowen's model and the mixed connectivity model, respectively. The degree of structuring, calculated according to both models, correlates well with the increase in piezoelectric and pyroelectric sensitivities of the composites. Higher sensitivity values of the functional properties are observed at higher ceramic volume fractions. The effect of electrical conductivity of the matrix on the pyroelectric responsivity of the composites is demonstrated to be a key parameter in governing the pyroelectric properties of the composites.

In Chapter 3, a novel multi-physics finite element model is proposed for qualitative simulation of the structure formation during dielectrophoresis of particles suspended in a dielectric Newtonian liquid between parallel-plate electrodes. Upon application of an electric field, particles reorient with respect to the imposed electric field, involving fast particle rotation, followed by slower lateral and axial displacement until a chain-like structure of connected particles is formed. The performance of the model is illustrated for a number of idealized starting configurations. The influence of parameters such as particle size, particle aspect ratio and particle size distribution is studied for the purpose of obtaining insight in the ideal conditions required to obtain a desired structure. In a system containing particles of different sizes, the largest particles play a key role in the development of the chain structure. The quality of the structure evolution is investigated by using a set of geometric parameters. A

new topological parameter, the chain perfection degree, relating the microstructure to the overall performance of the piezoelectric composite, is proposed and calculated for the various cases considered.

In Chapter 4, the particulate composites are studied under high electric fields. Ferroelectric polarization and strain response of 0-3 and quasi 1-3 lead zirconate titanate (PZT)-epoxy composites are investigated. The properties of the composites are evaluated and compared with those of the bulk ceramic. A new analytical model is developed to describe the properties of composites with a chain-like arrangement of particles. This model, which takes both piezoelectric and electrostrictive effects into account, shows a good agreement with the experimental results. The effect of interparticle distance on the final polarization and strain properties is shown. The model predictions correlate well with experimental strain values for the studied particulate composites. Increasing the amount of parallel connectivity via higher packing of particles inside the chains leads to larger strains at a given electric field.

In Chapter 5, PT ceramic particulates are incorporated into a relatively conductive polyethylene oxide (PEO) matrix to develop sensitive and simultaneously flexible composites. PT particles are dispersed in PEO at various volume fractions, and the composite films are prepared by solution casting. The dielectric and piezoelectric properties are determined using conventional techniques. For accurate determination of the pyroelectric properties, a new device is developed. This device requires relatively simple hardware and works without using costly lock-in amplifiers. This novel technique consists of applying a digital signal processing method on the discrete sampled data, which was obtained in a temperature oscillation measurement. The pyroelectric coefficient is calculated from the component of the generated current, which is 90° out of phase with respect to the sinusoidal temperature wave. The novelty of the proposed approach lies in the signal analysis procedure, which implements a simple Fast Fourier Transform (FFT) that filters residual noise through convolution and calculates the phase difference between the peaks of the temperature and current waves. From these data the pyroelectric figures of merit of the composite films are calculated. In order to determine the effect of electrical conductivity of the polymer matrix on the poling efficiency and the final properties, a poling study was performed. Improving the electrical conductivity of the polymer phase enhances the poling process significantly. It is found that both the piezoelectric and the pyroelectric figures of merit increase with PT ceramic concentration. PT-PEO composites show superior pyroelectric sensitivity compared to other composites with less electrically conductive polymer matrices.

In Chapter 6, composites of lead zirconate titanate particles in an epoxy matrix are prepared in the form of 0-3 and quasi 1-3 with different ceramic volume contents, ranging from 10% to 50%. Two different processing routes are tested. Firstly, a conventional dielectrophoretic structuring is used to induce a chain like particle configuration, followed by curing the matrix and poling at a high temperature and under a high voltage. Secondly, a simultaneous combination of dielectrophoresis and poling is applied at room temperature while the polymer is in the liquid state followed by subsequent curing. This new processing

route is applied to an uncured thermoset system while the polymer matrix still possess a relatively high electrical conductivity. Composites with different degrees of alignment are produced by altering the magnitude of the applied alternating electric field. A significant improvement in piezoelectric properties of quasi 1-3 composites can be achieved by a combination of simultaneous dielectrophoretic alignment of the ceramic particles and poling. The degree of structuring as well as the functional properties of the in-situ structured and poled composites enhance significantly compared to those of the conventionally manufactured structured composites.

In Chapter 7, tri-phase PZT-porous polyurethane (PU) composites are investigated. The main goal is to reduce the dielectric constant of the polymer matrix, and improve flexibility of traditional diphasic piezo-composites, consisting of ceramic particles in a dense polymeric matrix, by adding a third (gaseous) phase to the system. The presence of the gaseous component in the polymer matrix in the form of well-distributed spherical inclusions effectively decreases the polymer dielectric permittivity, which increases the piezoelectric voltage constant of the composites significantly. The unique combination of dielectrophoretic structuring of PZT particles and the addition of a gaseous phase to the polymer resin results in the highest performance of the particulate composite sensors reported in the literature so far. The g_{33} values of the newly developed triphase composites are twice that of the structured di-phase PZT-bulk PU composites (80 mV.m/N) and more than five times the g_{33} value of bulk PZT ceramics (24-28 mV.m/N).

In Chapter 8, high temperature PT-polyetherimide (PEI) composites are presented as promising candidates for high temperature piezoelectric sensing applications. High temperature PT-ODPA/ODA composites, prepared by solution casting, show thermally stable dielectric and piezoelectric properties in the temperature range from room temperature to 175 °C. Dielectrophoretic structuring is used to induce chain-like particle configuration, followed by curing the matrix to form free standing films. Subsequently, poling is performed under high voltages at temperatures above the glass transition temperature of the partially imidized matrix. The relatively high electrical conductivity as well as permittivity of the partially imidized ODPA/ODA polymer matrix yields a high poling efficiency. The composites are subsequently imidized to form fully imidized films, and their piezoelectric and pyroelectric properties are tested at elevated temperatures. Thermally stable dielectric and piezoelectric properties of the high T_c PT, as well as stable dielectric properties of the fully imidized ODPA/ODA polymer matrix result in a high temperature functionality of these high performance composites. After full imidization at 300 °C the imide rings completely close, resulting in a thermally stable polymer with a very low dielectric loss that maintains the piezoelectric sensitivity up to 175 °C.

In the Appendix, a model for the effect of topological imperfections on the electromechanical properties of structured particulate composites is presented. A novel method based on the Mori-Tanaka method with Eshelby tensors for piezoelectric composite materials is developed to predict the effective electro-elastic properties d_{33} and g_{33} of structured granular

piezoelectric composites with improved accuracy, by means of a single parameter related to the spatial distribution of imperfectly aligned rod-like PZT particles. The Virtual Particle Mori Tanaka (VPMT) method is found to have excellent prediction capabilities. Extending the approach, several newly defined functions are presented to capture the drop in piezoelectric composite's electro-elastic properties as a function of topological imperfections. These imperfections are related to longitudinal and lateral interparticle spacings and the topology of the chain-like structures themselves. The functions are evaluated in detail and show physically consistent behavior.

Samenvatting

Het hoofddoel van het onderzoek als beschreven in dit proefschrift is het verkennen van nieuwe granulair piezo-elektrische keramiek-polymeer composieten en het relateren van het effect van topologie, processing en intrinsieke eigenschappen van de individuele componenten, hoofdzakelijk de polymeerfase, aan piezo-, pyro-, en ferro-elektrische eigenschappen van twee- en driefasen composieten.

In hoofdstuk 2 worden de onderzoeksresultaten van functionele composieten bestaande uit loodtitanaatdeeltjes (PT) in een epoxy matrix gepresenteerd, die dankzij dielectroforese verbeterde dielektrische, piezo-elektrische en pyro-elektrische eigenschappen vekregen hebben ten opzichte van soortgelijke 0-3 composieten (dat wil zeggen composieten bestaande uit korrelvormige, niet-verbonden deeltjes in een continue polymeermatrix). Deze verbetering geldt voor het bereik van 10-50 volumeprocent PT deeltjes. Er is aangetoond dat de mate waarin de deeltjes geordend zijn (de connectiviteit) en de elektrische eigenschappen van de individuele componenten de voornaamste factoren zijn die de eigenschappen van het composiet beïnvloeden. Twee parameters die de mate van ordening kunnen beïnvloeden zijn de afstand tussen de deeltjes en het percentage van 1-3 connectiviteit (dat wil zeggen continue één-dimensionale vezelachtige connectiviteit van de functionele keramische deeltjes in een polymeermatrix) worden respectievelijk gebruikt op basis van het Bowen model en het mixed connectivity model. De mate van orde berekend volgens beide modellen komt goed overeen met de toename in piezo-elektrische en pyro-elektrische gevoeligheid van de composieten. Hogere keramische volumepercentages resulteren in betere functionele eigenschappen. Er is aangetoond dat de elektrische geleidbaarheid van de matrix de belangrijkste factor is die de pyro-elektrische eigenschappen van de composieten beïnvloedt.

In hoofdstuk 3 wordt een nieuw multi-physics eindige elementen model gepresenteerd voor kwalitatieve berekening van ketenvorming tijdens dielectroforese van piezoelektrische deeltjes in een vloeibare matrix tussen twee parallelle plaalectrodes. Door het aanbrengen van een elektrisch veld oriënteren de deeltjes zich ten opzichte van het opgelegde elektrische veld, middels een snelle rotatie van de deeltjes gevolgd door een langzamere laterale en axiale verplaatsing totdat een keten van aaneengesloten deeltjes is verkregen. Het voorspellend vermogen van het model is toegelicht aan de hand van een aantal geïdealiseerde begin configuraties. De invloed van parameters zoals deeltjesgrootte, "aspect ratio" en deeltjes-

grootteverdeling is bestudeerd om inzicht te verkrijgen in de ideale condities die vereist zijn om de gewenste structuur te bereiken. In een systeem met deeltjes van verschillende grootte zijn het de grote deeltjes die de ketenvorming bepalen. De kwaliteit van structuuronwikkeling is onderzocht met behulp van een set van geometrische parameters. Een nieuwe topologische parameter, ketenperfectiegraad, die de microstructuur aan de eigenschappen van het piezo-elektrische composiet verbindt, wordt geïntroduceerd en doorerekend voor de verschillende beginsituaties.

In hoofdstuk 4 wordt het gedrag van deeltjescomposieten onderzocht als zij blootgesteld worden aan sterke elektrische velden. De ferro-elektrische polarisatie en rek van 0-3 en quasi 1-3 lood-zirkonaat-titanaat (PZT)-epoxy composieten worden bestudeerd. De eigenschappen van de composieten worden geëvalueerd en vergeleken met die van bulk keramieken. Een nieuw analytisch model is ontwikkeld om de eigenschappen van composieten met een ketenachtige rangschikking van deeltjes te beschrijven. Dit model neemt zowel piezo-elektrische als elektro-restrictieve effecten in acht en laat een goede overeenstemming met experimentele resultaten zien. Het effect van de afstand tussen deeltjes op eindpolarisatie en rekeigenschappen is weergegeven. De voorspellingen van het model komen goed overeen met de experimentele rekken voor het bestudeerde deeltjescomposiet. Toename in de hoeveelheid parallelle connectiviteit als gevolg van een hogere deeltjesdichtheid in de ketens leidt tot een grotere rek bij een gegeven elektrisch veld.

In hoofdstuk 5 worden keramische loodtitanaat (PT) deeltjes verwerkt in een matrix van het relatief goed (electrisch) geleidend polyethyleenoxide (PEO) om composieten te creëren die zowel flexibel zijn als een hoge contactgevoeligheid hebben. Hiertoe worden PT-PEO composieten met verschillende PT vulgraden gemaakt die via 'solution casting' tot dunne films uitgegoten worden. De dielektrische en piezoelektrische eigenschappen zijn in eerste instantie bepaald met behulp van conventionele technieken. Voor een accurate meting van de piezoelektrische eigenschappen is echter een nieuw apparaat ontwikkeld. Dit apparaat vereist relatief simpele hardware en werkt zonder gebruik van kostbare lock-in versterkers. Deze nieuwe techniek is gebaseerd op een numerieke analyse van periodiek gesamplede data welke tijdens cyclische temperatuursveranderingen verkregen zijn. De pyroelectrische coëfficiënt is berekend vanuit de de stroomsterkte die 90 graden uit fase is met het opgelegde sinusvormige temperatuurspatroon. 90 graden uit fase met betrekking tot de sinusoidale temperatuurgolf. Het nieuwe van de geïntroduceerde aanpak is gelegen in de gebruikte procedure om het signaal te verwerken, waarbij, na filteren van de ruis, het faseverschil tussen de pieken voor temperatuur en stroom berekend wordt. Uit dergelijke data kunnen de de pyroelektrische kentallen van de composietfilms bepaald worden. Een polingstudie is uitgevoerd om het effect van geleidbaarheid van het matrixpolymeer op poling efficiëntie en uiteindelijke eigenschappen van het composiet te bepalen. Er is gebleken dat een verbetering van de elektrische geleidbaarheid van het polymeer leidt tot een significante verbetering van het polingsproces. Tevens is ontdekt, dat zowel waarden van de piezoelektrische als pyroelektrische kentallen toenemen met toenemende PT keramiek concentratie. PT-PEO composieten vertonen superieure pyroelektrische sensitiviteit in vergelijking met andere

composieten met een minder elektrisch geleidende matrix.

In hoofdstuk 6 worden lood zirkonaat titanaat (PZT) deeltjes in een epoxy matrix verwerkt in de vorm van 0-3 en quasi 1-3 composieten met verschillende volumefracties tussen 10% en 50%. Twee verschillende productieprocessen zijn getest. Allereerst een conventionele manier van het aanbrengen van een ketenstructuur middels dielektroforese gevolgd door het laten uitharden van de matrix en poling op hoge temperaturen bij een hoog voltage. In de tweede route worden dielektroforese en poling gelijktijdig en bij kamertemperatuur uitgevoerd, waarna het composiet uitgehard wordt. Dit nieuwe proces is toegepast op een niet-uitgeharde thermoharder, op het moment dat de polymeermatrix nog steeds een redelijk hoge elektrische geleiding vertoont. Composieten met verschillende gradaties in ketenvorming zijn geproduceerd door de grootte van het toegepaste elektrische (AC) veld te variëren. Een significante verbetering in piezoelektrische eigenschappen van quasi 1-3 composieten kan worden gerealiseerd door dielektroforese en poling gelijktijdig uit te voeren. De mate van ketenvorming en de functionele eigenschappen van de in-situ gestructureerde en gepoolde composieten blijken significant te verbeteren ten opzichte van gestructureerde composieten die op een conventionele manier zijn geproduceerd. De kwaliteitsverbetering kan vooral toegeschreven worden aan verbetering van de topologische kwaliteit van de ketens.

In hoofdstuk 7 worden drie-fase PZT-lucht-polyurethaan (PU) composieten onderzocht. Het hoofddoel van het gebruik van een poreuze PU matrix is om de dielektrische constante en flexibiliteit van de polymeermatrix te verbeteren ten opzichte van de traditionele twee-fase composieten, bestaande uit keramische deeltjes in een dichte polymeermatrix. De aanwezigheid van deze gasvormige component in de polymeermatrix in de vorm van goed verdeelde bolvormige poriën is een effectieve manier om de dielektrische permittiviteit te reduceren. Dit leidt uiteindelijk tot een significante toename in de piezoelektrische voltage constante van de composieten. De unieke combinatie van het aanbrengen van ruimtelijke ordening van de PZT deeltjes via dielektroforese met behulp van dielektroforese van de PZT deeltjes en het toevoegen van de gasvormige fase aan de polymeerhars, resulteert in de hoogst behaalde prestaties van sensoren bestaande uit deeltjescomposieten, die tot dusver gerapporteerd is in de literatuur. De g_{33} waarden van de nieuw ontwikkelde tri-fase composieten zijn dubbel zo hoog als de di-fase PZT-bulk PU composieten (80 mV.m/N) en meer dan vijf maal de g_{33} waarden van bulk PZT keramieken (24-28 mV.m/N).

In hoofdstuk 8 worden PT-polyetherimide (PEI) composieten gepresenteerd als veelbelovende kandidaten voor sensortoepassingen bij hoge temperatuur. Bij PT-ODPA/ODA composieten, geproduceerd met behulp van 'solution casting', zijn stabiele dielektrische en piezoelektrische eigenschappen waargenomen over het temperatuurbereik van kamertemperatuur tot 175 °C. Dielektroforese is toegepast om ketenachtige deeltjesconfiguratie te realiseren, gevolgd door het uitharden van de matrix om vrijstaande films te laten vormen. Vervolgens wordt er gepoold bij hoge voltages en temperaturen boven de glasovergangstemperatuur van de partieel geïmideerde matrix. De relatief hoge elektrische geleidbaarheid en

permittiviteit van de partieel geïmidiseerde ODP/ODA polymeermatrix leidt tot een hoge poling efficiëntie. De composieten worden daarna verhit om volledig geïmidiseerde films te vormen en hun piezoelektrische en pyroelektrische eigenschappen te meten bij hoge temperaturen. Na volledige imidisatie bij 300 °C sluiten de imide-ringen volledig, wat resulteert in een thermisch stabiel polymeer met zeer een zeer laag dielektrisch verlies dat piezoelektrische sensitiviteit behoudt tot 175 °C.

In de appendix wordt het effect van topologische imperfecties op de elektromechanische eigenschappen van gestructureerde deeltjescomposieten beschreven. Een nieuwe methode, gebaseerd op de Mori-Tanaka methode met Eshelby tensors voor piezoelektrische composieten, is ontwikkeld om de effectieve elektro-elastische eigenschappen, d_{33} en g_{33} van gestructureerde piezoelektrische deeltjescomposieten te kunnen voorspellen, met een hogere precisie door middel van een enkele parameter gerelateerd aan de ruimtelijke verdeling van imperfect uitgelijnde staafachtige PZT deeltjes. Er is geconstateerd dat de Virtual Particle Mori Tanaka (VPMT) methode uitstekende voorspellende eigenschappen bezit. Uitbreiding van deze aanpak, met behulp van verschillende nieuw gedefinieerde functies, heeft aangetoond dat de afname in elektro-elastische eigenschappen van piezoelektrische composieten als functie van topologische imperfecties succesvol vast kan worden gelegd. Deze imperfecties zijn gerelateerd aan de longitudinale en laterale afstand tussen de deeltjes en de topologie van de ketenachtige structuur zelf. De functies worden in detail gevalueerd en tonen fysiek consistent gedrag.

Bibliography

- [1] Ferreira, A. D. B., Nvoa, P. R., and Marques, A. T., “Multifunctional Material Systems: A State-of-the-Art Review,” *Composite Structures*, 2016, pp. –.
- [2] Lin, Y. and Sodano, H. A., “Concept and model of a piezoelectric structural fiber for multifunctional composites,” *Composites Science and Technology*, Vol. 68, No. 78, 2008, pp. 1911 – 1918.
- [3] Wang, Y. and Inman, D. J., “Adaptive multifunctional composites,” *Proceedings of SPIE - The International Society for Optical Engineering*, Vol. 8725, 2013.
- [4] Wang, Y. and Inman, D. J., “Experimental and finite element analysis for a multifunctional beam with frequency-dependent viscoelastic behavior,” *54th AIAA/ASME/ASCE/AHS/ASC Structures, Structural Dynamics, and Materials Conference*, 2013.
- [5] Wang, Y. and Inman, D. J., “Experimental validation for a multifunctional wing spar with sensing, harvesting, and gust alleviation capabilities,” *IEEE/ASME Transactions on Mechatronics*, Vol. 18, No. 4, 2013, pp. 1289–1299.
- [6] Wang, Y. and Inman, D. J., “Simultaneous energy harvesting and gust alleviation for a multifunctional composite wing spar using reduced energy control via piezoceramics,” *Journal of Composite Materials*, Vol. 47, No. 1, 2013, pp. 125–146.
- [7] Anton, S. R., Erturk, A., and Inman, D. J., “Multifunctional unmanned aerial vehicle wing spar for low-power generation and storage,” *Journal of Aircraft*, Vol. 49, No. 1, 2012, pp. 292–301.
- [8] Anton, S. R. and Inman, D. J., “Electromechanical modeling of a multifunctional energy harvesting wing spar,” *Collection of Technical Papers - AIAA/ASME/ASCE/AHS/ASC Structures, Structural Dynamics and Materials Conference*, 2011.
- [9] Matic, P., “Overview of Multifunctional Materials,” *Proceedings of SPIE - The International Society for Optical Engineering*, Vol. 5053, 2003, pp. 61–69.

- [10] National Academy of Engineering, *Frontiers of Engineering: Reports on Leading-Edge Engineering from the 2004 NAE Symposium on Frontiers of Engineering*, The National Academies Press, 2005.
- [11] van den Ende, D. A., *Structured piezoelectric composites, materials and applications*, Ph.D. thesis, Faculty of Aerospace Engineering, Delft University of Technology, The Netherlands, 2012.
- [12] Dias, C., *Ferroelectric composites for pyro- and piezoelectric applications*, Ph.D. thesis, School of electronic engineering and computer systems, University of Wales, Bangor, UK, 1994.
- [13] Bertotti, G. and Mayergoyz, I., *The Science of Hysteresis*, Academic press, 1st ed., 2005.
- [14] Jaffe, B., Cook Jr., W., and Jaffe, H., *Piezoelectric Ceramics*, Academic Press Inc., London & New York, 3rd ed., 1971.
- [15] Lang, S. B., "Pyroelectricity: From Ancient Curiosity to Modern Imaging Tool," *Physics Today*, Vol. 58, No. 8, 2005, pp. 31–36.
- [16] Lang, S. B., *Sourcebook of Pyroelectricity*, Routledge, 1974.
- [17] Srinivasan, M., "Pyroelectric materials," *Bulletin of Materials Science*, Vol. 6, 1984, pp. 317–325.
- [18] Chew, K.-H., Shin, F. G., Ploss, B., Chan, H. L. W., and Choy, C. L., "Primary and secondary pyroelectric effects of ferroelectric 0-3 composites," *Journal of Applied Physics*, Vol. 94, No. 2, 2003, pp. 1134–1145.
- [19] Scott, R., "Development of MEMS based pyroelectric thermal energy harvesters," Vol. 8035, SPIE, 2011, p. 80350V.
- [20] Whatmore, R. W. and Watton, R., "Pyroelectric Materials and Devices," *Infrared Detectors and Emitters: Materials and Devices*, Vol. 8, Springer US, 2001, pp. 99–147.
- [21] Whatmore, R. W., "Pyroelectric devices and materials," Vol. 49, 1986, p. 1335.
- [22] Holterman, J. and Groen, P., *An Introduction to Piezoelectric Materials and Applications*, Stichting Applied Piezo, Apeldoorn, 1st ed., 2013.
- [23] Jaffe, B., Roth, R. S., and Marzullo, S., "Piezoelectric Properties of Lead Zirconate-Lead Titanate Solid-Solution Ceramics," *Journal of Applied Physics*, Vol. 25, No. 6, 1954, pp. 809–810.
- [24] Moulson, A. J. and Herbert, J., *Electroceramics: Materials, Properties, Applications, second edition*, John Wiley and Sons Inc, 2003.

- [25] Heywang, W., Lubitz, K., and Wersing, W., editors, *Piezoelectricity Evolution and Future of a Technology*, Springer, 2008.
- [26] Yamaka, E., "Pyroelectric IR sensor using vinylidene fluoride-trifluoroethylene copolymer film," *Ferroelectrics*, Vol. 57, No. 1, 1984, pp. 337–342.
- [27] "A 3×1 integrated pyroelectric sensor based on VDF/TrFE copolymer," *Sensors and Actuators A: Physical*, Vol. 52, No. 13, 1996, pp. 103 – 109.
- [28] Nalwa, H. S., *Ferroelectric Polymers: Chemistry: Physics, and Applications*, CRC Press, 1995.
- [29] Newnham, R. E., D. S. and Cross, L., "Connectivity and piezoelectric-pyroelectric composites," *Materials Research*, Vol. 13, 1978, pp. 525–536.
- [30] Wilson, S. A. and Whatmore, R. W., "Structure modification of piezoelectric ceramic polymer composites through dielectrophoresis," *Journal of Physics D: Applied Physics*, Vol. 38, 2005, pp. 175–182.
- [31] van den Ende, D., Bory, B., Groen, W., and van der Zwaag, S., "Improving the d33 and g33 properties of 0-3 piezoelectric composites by dielectrophoresis," *Journal of Applied Physics*, Vol. 107, No. 2, 2010.
- [32] Khanbareh, H., van der Zwaag, S., and Groen, W., "Effect of dielectrophoretic structuring on piezoelectric and pyroelectric properties of PT-epoxy composites," *Smart Materials and Structures*, Vol. 23, No. 10, 2014, pp. 105030.
- [33] Bowen, C. P., Newnham, R. E., and Randall, C. A., "Dielectric properties of dielectrophoretically assembled particulate-polymer composites," *Journal of Materials Research*, Vol. 13, 1998, pp. 205–210.
- [34] Tang, H., Lin, Y., and Sodano, H. A., "Synthesis of High Aspect Ratio BaTiO₃ Nanowires for High Energy Density Nanocomposite Capacitors," *Advanced Energy Materials*, Vol. 2, No. 451-456, 2012, pp. 451–456.
- [35] Tang, H., Malakooti, M. H., and Sodano, H. A., "Relationship between orientation factor of lead zirconate titanate nanowires and dielectric permittivity of nanocomposites," *Applied Physics Letters*, Vol. 103, No. 22, 2013, pp. 222901–222905.
- [36] Yamada, T., Ueda, T., and Kitayama, T., "Piezoelectricity of a high-content lead zirconate titanate polymer composite," *Journal of Applied Physics*, Vol. 53, 1982, pp. 4328.
- [37] Lee, Y. H., Safari, A., and Newnham, R. E., "Preparation of PT powder for a flexible 0-3 piezoelectric composite," 1986, pp. 318–322.

- [38] van den Ende, D. A., van de Wiel, H. J., Groen, W. A., and van der Zwaag, S., "Direct strain energy harvesting in automobile tires using piezoelectric PZT-polymer composites," *Smart Materials and Structures*, Vol. 21, No. 1, 2012, pp. 1–11.
- [39] Li, X. and Zhang, Y., "A Constitutive Model for Piezoelectric Paint with Mixed Connectivity," *Journal of Intelligent Material Systems and Structures*, Vol. 21, No. 12, 2010, pp. 1213–1225.
- [40] Payo, I. and Hale, J., "Sensitivity analysis of piezoelectric paint sensors made up of PZT ceramic powder and water-based acrylic polymer," *Sensors and Actuators A: Physical*, Vol. 168, No. 1, 2011, pp. 77 – 89.
- [41] Lau, S. T., Kwok, K. W., Shin, F. G., and Kopf, S., "A poling study of lead zirconate titanate/polyurethane 0–3 composites," *Journal of Applied Physics*, Vol. 102, No. 4, 2007, pp. 044104.
- [42] Wong, C. and Shin, F., "Effect of electrical conductivity on poling and the dielectric, pyroelectric and piezoelectric properties of ferroelectric 0-3 composites," *Journal of Materials Science*, Vol. 41, 2006, pp. 229–249.
- [43] Dias, C. J. and Das-Gupta, D. K., "Poling behaviour of ceramic/polymer ferroelectric composites," *Ferroelectrics*, Vol. 157, No. 1, 1994, pp. 405–410.
- [44] Renxin, X., Wen, C., Jing, Z., Yueming, L., and Huajun, S., "Dielectric and piezoelectric properties of 0-3 PZT-PVDF composite doped with polyaniline," *Journal of Wuhan University of Technology-Mater. Sci. Ed.*, Vol. 21, 2006, pp. 84–87.
- [45] de Campos Fuzari Jr, G., Orlandi, M. O., Longo, E., de Barros Melo, W. L., and Sakamoto, W. K., "Effect of controlled conductivity on thermal sensing property of 0-3 pyroelectric composite," *Smart Materials and Structures*, Vol. 22, No. 2, 2013, pp. 025015.
- [46] Sakamoto, W., Marin-Franch, P., and Das-Gupta, D., "Characterization and application of PZT/PU and graphite doped PZT/PU composite," *Sensors and Actuators A: Physical*, Vol. 100, No. 23, 2002, pp. 165 – 174.
- [47] Sakamoto, W. K., de Campos Fuzari Jr, G., Zaghete, M. A., and de Freitas, R. L. B., "Lead Titanate-Based Nanocomposite: Fabrication, Characterization and Application and Energy Conversion Evaluation," *Ferroelectrics - Material Aspects*, 2011.
- [48] Chau, K. H., Wong, Y. W., and Shin, F. G., "Enhancement of piezoelectric and pyroelectric properties of composite films using polymer electrolyte matrix," *Applied Physics Letters*, Vol. 91, No. 25, 2007, pp. 252910.
- [49] Or, Y. T., Wong, C. K., Ploss, B., and Shin, F. G., "Modeling of poling, piezoelectric, and pyroelectric properties of ferroelectric 0–3 composites," *Journal of Applied Physics*, Vol. 94, No. 5, 2003, pp. 3319–3325.

- [50] Sa-Gong, G., Safari, A., Jang, S. J., and Newnham, R. E., "Poling flexible piezoelectric composites," *Ferroelectrics Letters Section*, Vol. 5, No. 5, 1986, pp. 131–142.
- [51] Sakamoto, W. K., Souza, E. d., and Das-Gupta, D. K., "Electroactive properties of flexible piezoelectric composites," *Materials Research*, Vol. 4, 07 2001, pp. 201 – 204.
- [52] Liu, X. F., Xiong, C. X., Sun, H. J., Dong, L. J., li, R., and Liu, Y., "Piezoelectric and dielectric properties of PZT-PVC and graphite doped with PZT-PVC composites," *Materials Science and Engineering: B*, Vol. 127, No. 2-3, 2006, pp. 261 – 266.
- [53] Ploss, B. and Krause, M., "Optimized pyroelectric properties of 0-3 composites of PZT particles in polyurethane doped with lithium perchlorate." *IEEE transactions on ultrasonics, ferroelectrics, and frequency control*, Vol. 54, No. 12, 2007, pp. 2479–81.
- [54] Ploss, B. and Krause, M., "Doped Polymers as Matrix Materials for Ferroelectric Composites," *Ferroelectrics*, Vol. 358, No. 1, 2007, pp. 77–84.
- [55] Tsunemi, K., Ohno, H., and Tsuchida, E., "A mechanism of ionic conduction of poly (vinylidene fluoride)-lithium perchlorate hybrid films," *Electrochimica Acta*, Vol. 28, No. 6, 1983, pp. 833 – 837.
- [56] Furukawa, T., Takahashi, Y., and Yasuda, K., "Dielectric and Conductive Spectra of the Composite of Barium Titanate and LiClO₄ -Doped Polyethylene Oxide," *IEEE Transactions on Dielectrics and Electrical Insulation*, Vol. 11, No. 1, 2004, pp. 65–71.
- [57] Van Kempen, S., *Optimisation of Piezoelectric Composite Materials Design through Improved Materials Selection and Property Prediction Methods*, Master's thesis, Faculty of Aerospace Engineering, Delft University of Technology, Delft, The Netherlands, 2012.
- [58] Khemani, K. C., *Polymeric Foams*, American Chemical Society, Washington, DC, 1997.
- [59] Shastri, V. P., Martin, I., and Langer, R., "Macroporous polymer foams by hydrocarbon templating," *Proceedings of the National Academy of Sciences*, Vol. 97, No. 5, 2000, pp. 1970–1975.
- [60] Fabrizio, Q., Loredana, S., and Anna, S. E., "Shape memory epoxy foams for space applications," *Materials Letters*, Vol. 69, 2012, pp. 20 – 23.
- [61] Santo, L., Quadrini, F., Mascetti, G., Dolce, F., and Zolesi, V., "Mission STS-134: Results of Shape Memory Foam Experiment," *Acta Astronautica*, Vol. 91, 2013, pp. 333 – 340.

- [62] Li, G. and John, M., "A self-healing smart syntactic foam under multiple impacts," *Composites Science and Technology*, Vol. 68, No. 1516, 2008, pp. 3337 – 3343.
- [63] Song, W., Wang, L., and Wang, Z., "Synthesis and thermomechanical research of shape memory epoxy systems," *Materials Science and Engineering: A*, Vol. 529, 2011, pp. 29 – 34.
- [64] Yin, J. and Deng, B., "Polymer-matrix nanocomposite membranes for water treatment," *Journal of Membrane Science*, Vol. 479, 2015, pp. 256 – 275.
- [65] Alzahrani, S. and Mohammad, A. W., "Challenges and trends in membrane technology implementation for produced water treatment: A review," *Journal of Water Process Engineering*, Vol. 4, 2014, pp. 107 – 133.
- [66] Xiao, Q., Wang, X., Li, W., Li, Z., Zhang, T., and Zhang, H., "Macroporous polymer electrolytes based on PVDF/PEO-b-PMMA block copolymer blends for rechargeable lithium ion battery," *Journal of Membrane Science*, Vol. 334, No. 12, 2009, pp. 117 – 122.
- [67] Xi, J., Qiu, X., Li, J., Tang, X., Zhu, W., and Chen, L., "PVDF-PEO blends based microporous polymer electrolyte: Effect of PEO on pore configurations and ionic conductivity," *Journal of Power Sources*, Vol. 157, No. 1, 2006, pp. 501 – 506.
- [68] Banyay, G., Shaltout, M., Tiwari, H., and Mehta, B., "Polymer and composite foam for hydrogen storage application," *Journal of Materials Processing Technology*, Vol. 191, No. 13, 2007, pp. 102 – 105, Advances in Materials and Processing Technologies, July 30th - August 3rd 2006, Las Vegas, Nevada.
- [69] Jurczyk, M. U., Kumar, A., Srinivasan, S., and Stefanakos, E., "Polyaniline-based nanocomposite materials for hydrogen storage," *International Journal of Hydrogen Energy*, Vol. 32, No. 8, 2007, pp. 1010 – 1015.
- [70] Krause, B., Koops, G.-H., van der Vegt, N. F., Wessling, M., Wubbenhorst, M., and van Turnhout, J., "Ultralow-k dielectrics made by supercritical foaming of thin polymer films," *Advanced Materials*, Vol. 14, No. 15, 2002, pp. 1041–1046.
- [71] Chand, N. and Sharma, J., "Influence of porosity on resistivity of polypropylene foams," *Journal of Cellular Plastics*, Vol. 48, No. 1, 2012, pp. 43–52.
- [72] Li, L., Zhang, S., Xu, Z., Wen, F., Geng, X., Lee, H. J., and Shrout, T. R., "1?3 piezoelectric composites for high-temperature transducer applications," *Journal of Physics D: Applied Physics*, Vol. 46, No. 16, 2013, pp. 165306.
- [73] Lee, J. and Choi, B., "Development of a piezoelectric energy harvesting system for implementing wireless sensors on the tires," *Energy Conversion and Management*, Vol. 78, 2014, pp. 32–38.

- [74] Xue, Q., Stanton, M., and Elfbaum, G., "A high temperature and broadband immersion 1-3 piezo-composite transducer for accurate inspection in harsh environments," *Proceedings of the IEEE Ultrasonics Symposium*, Vol. 2, 2003, pp. 1372–1375.
- [75] Park, C., Ounaies, Z., Wise, K. E., and Harrison, J. S., "In situ poling and imidization of amorphous piezoelectric polyimides," *Polymer*, Vol. 45, No. 16, 2004, pp. 5417 – 5425.
- [76] Ounaies, Z., Park, C., Harrison, J. S., Smith, J. G., and Hinkley, J., "Structure-property study of piezoelectricity in polyimides," *Proceedings of SPIE - The International Society for Optical Engineering*, Vol. 3669, 1999, pp. 171–178.
- [77] Ounaies, Z., Park, C., Harrison, J., and Lillehei, P., "Evidence of piezoelectricity in SWNT-polyimide and SWNT-PZT-polyimide composites," *Journal of Thermoplastic Composite Materials*, Vol. 21, No. 5, 2008, pp. 393–409.
- [78] Atkinson, G. M., Pearson, R. E., Ounaies, Z., Park, C., Harrison, J. S., Dogan, S., and Midkiff, J. A., "Novel piezoelectric polyimide MEMS," *TRANSDUCERS 2003 - 12th International Conference on Solid-State Sensors, Actuators and Microsystems, Digest of Technical Papers*, Vol. 1, 2003, pp. 782–785.
- [79] Ounaies, Z., Park, C., Harrison, J. S., Smith, J. G., and Hinkley, J., "Structure-property study of piezoelectricity in polyimides," *Proceedings of SPIE - The International Society for Optical Engineering*, Vol. 3669, 1999, pp. 171–178.
- [80] Simpson, J., Ounaies, Z., and Fay, C., "Polarization and piezoelectric properties of a nitrile substituted polyimide," *Materials Research Society Symposium - Proceedings*, Vol. 459, 1997, pp. 59–64.
- [81] Xu, Y., *Ferroelectric Materials and Their Applications*, North Holland, 1991.
- [82] Beerman, H. P., "Investigation of pyroelectric material characteristics for improved infrared detector performance," *Infrared Physics*, Vol. 15, No. 3, 1975, pp. 225 – 231.
- [83] Dias, C. and Das Gupta, D., "Inorganic ceramic polymer ferroelectric composite electrets," *IEEE Transactions on Dielectrics and Electrical Insulation*, Vol. 3, No. 5, 1996, pp. 706–734.
- [84] Byer, R. and Roundy, C. B., "Pyroelectric Coefficient Direct Measurement Technique and Application to a Nsec Response Time Detector," *Sonics and Ultrasonics, IEEE Transactions on*, Vol. 19, No. 2, 1972, pp. 333–338.
- [85] Jones, T. B., *Electromechanics of Particles*, Cambridge University Press, 2005.
- [86] Chambion, B., Goujon, L., Badie, L., Mugnier, Y., Barthod, C., Galez, C., Wiebel, S., and Venet, C., "Optimization of the piezoelectric response of 0-3 composites: a modeling approach," *Smart Materials and Structures*, Vol. 20, No. 11, 2011, pp. 1–8.

- [87] Sakamoto, W. K., Kanda, D., and Das-Gupta, D., "Dielectric and pyroelectric properties of a composite of ferroelectric ceramic and polyurethane," *Materials Research Innovations*, Vol. 5, No. 6, 2002, pp. 257–260.
- [88] Marin-Franch, P., Martin, T., Tunnicliffe, D., and Das-Gupta, D., "PTCa/PEKK piezo-composites for acoustic emission detection," *Sensors and Actuators A: Physical*, Vol. 99, No. 3, 2002, pp. 236–243.
- [89] Marin-Franch, P., Tunnicliffe, D., and Das-Gupta, D., "Pyroelectric properties of the PTCa/PEKK composite transducers," *Dielectric materials, measurements and applications, conference publications, IEEE2000*, No. 473, 2000, pp. 386–391.
- [90] Abdullah, M. and Das-Gupta, D., "Electroactive properties of polymer-ceramic composites," *Ferroelectrics*, Vol. 87, 1988, pp. 213–228.
- [91] Bowen, C. P., Shrout, T. R., Newnham, R. E., and Randall, C. A., "A study of the frequency dependence of the dielectrophoretic effect in thermoset polymers," *Journal of Materials Research*, Vol. 12, 1997, pp. 2345–2356.
- [92] van den Ende, D. A., Bory, B. F., Groen, W. A., and van der Zwaag, S., "Properties of Quasi 1-3 Piezoelectric PZT-epoxy Composites Obtained by Dielectrophoresis," *Integrated Ferroelectrics*, Vol. 114, No. 1, 2010, pp. 108–118.
- [93] Chan, H. L. W., Unsworth, J., and Bui, T., "Mode coupling in modified lead titanate/polymer 1-3 composites," *Journal of Applied Physics*, Vol. 65, No. 4, 1989, pp. 1754–1758.
- [94] Dias, C., Igreja, R., Marat-Mendes, R., Inacio, P., Marat-Mendes, J., and Das-Gupta, D., "Recent advances in ceramic-polymer composite electrets," *IEEE Transactions on Dielectrics and Electrical Insulation*, Vol. 11, No. 1, 2004, pp. 35–40.
- [95] Savakus, H., Klicker, K., and Newnham, R., "PZT-epoxy piezoelectric transducers: A simplified fabrication procedure," *Materials Research Bulletin*, Vol. 16, No. 6, 1981, pp. 677–680.
- [96] Pardo, L., Mendiola, J., and Alemany, C., "Theoretical treatment of ferroelectric composites using Monte Carlo calculations," *Journal of Applied Physics*, Vol. 64, No. 10, 1988, pp. 5092–5097.
- [97] Dias, C. and Das-Gupta, D., "Electroactive Polymer-Ceramic Composites," *Proceedings of the 4th international conference on properties and applications of dielectric materials*, 1994, pp. 1–4.
- [98] Peláiz-Barranco, a. and Marin-Franch, P., "Piezo-, pyro-, ferro-, and dielectric properties of ceramic/polymer composites obtained from two modifications of lead titanate," *Journal of Applied Physics*, Vol. 97, No. 3, 2005, pp. 0341041–0341045.

- [99] Martin, T., Marin-Franch, P., and Das-Gupta, D., "Evaluation of PTCa-PEKK Composites for Acoustic Emission Detection," *IEEE Transactions on Dielectrics and Electrical Insulation*, 2004, pp. 50–55.
- [100] Khanbareh, H., van der Zwaag, S., and Groen, W., "Piezoelectric and pyroelectric properties of conductive polyethylene oxide-lead titanate composites," *Smart Materials and Structures*, Vol. 24, No. 4, 2015, pp. 5020.
- [101] Patil, S. K., Koledintseva, M. Y., Schwartz, R. W., and Huebner, W., "Prediction of Effective Permittivity of Diphasic Dielectrics Using an Equivalent Capacitance Model," *Journal of Applied Physics*, Vol. 104, 2008, pp. 074108–1.
- [102] Andrews, C., Lin, Y., and Sodano, H. A., "The effect of particle aspect ratio on the electroelastic properties of piezoelectric nanocomposites," *Smart Materials and Structures*, Vol. 19, 2010, pp. 025018.
- [103] Tang, H., Zhou, Z., and Sodano, H. A., "Relationship between BaTiO₃ Nanowire Aspect Ratio and the Dielectric Permittivity of Nanocomposites," *ACS Applied Materials & Interfaces*, Vol. 6, No. 8, 2014, pp. 5450–5455.
- [104] Jones, T. B., "Multipole corrections to dielectrophoretic force," *IEEE Transactions on Industry Applications*, Vol. IA-21, No. 4, 1985, pp. 930–934.
- [105] Jones, T., "Dielectrophoretic force in axisymmetric fields," *Journal of Electrostatics*, Vol. 18, No. 1, 1986, pp. 55–62.
- [106] Green, N. and Jones, T., "Numerical determination of the effective moments of non-spherical particles," *Journal of Physics D: Applied Physics*, Vol. 40, No. 1, 2007, pp. 78–85.
- [107] Techaumnat, B., Eua-arporn, B., and Takuma, T., "Electric field and dielectrophoretic force on a dielectric particle chain in a parallel-plate electrode system," *Journal of Physics D: Applied Physics*, Vol. 37, No. 23, 2004, pp. 3337–3346.
- [108] Stein, E., Borst, R. D., and Hughes, T. J. R., *Encyclopedia of Computational Mechanics*, John Wiley and Sons, Ltd, 2004.
- [109] Wriggers, P. and Zavarise, G., *Computational Contact Mechanics*, John Wiley and Sons, Ltd, 2004.
- [110] Spencer, N. D. and Moore, J. H., *Encyclopedia of Chemical Physics and Physical Chemistry*, Institute of Physics Publishing, Bristol, UK, 2001.
- [111] Okamoto, S., Kuwabara, K., and kakurou Otsuka, "Electrical stimuli-induced deformation and material properties of electro-active polymer Nafion117," *Sensors and Actuators A: Physical*, Vol. 125, No. 2, 2006, pp. 376 – 381.

- [112] Pelrine, R., Kornbluh, R., Joseph, J., Heydt, R., Pei, Q., and Chiba, S., “High-field deformation of elastomeric dielectrics for actuators,” *Materials Science and Engineering: C*, Vol. 11, No. 2, 2000, pp. 89 – 100.
- [113] Pelrine, R. E., Kornbluh, R. D., and Joseph, J. P., “Electrostriction of polymer dielectrics with compliant electrodes as a means of actuation,” *Sensors and Actuators A: Physical*, Vol. 64, No. 1, 1998, pp. 77 – 85, Tenth {IEEE} International Workshop on Micro Electro Mechanical Systems.
- [114] Cheng, Z.-Y., Bharti, V., Xu, T.-B., Xu, H., Mai, T., and Zhang, Q., “Electrostrictive poly(vinylidene fluoride-trifluoroethylene) copolymers,” *Sensors and Actuators, A: Physical*, Vol. 90, No. 1-2, 2001, pp. 138–147.
- [115] Li, J. and Rao, N., “Dramatically enhanced effective electrostriction in ferroelectric polymeric composites,” *Applied Physics Letters*, Vol. 81, No. 10, Sep 2002, pp. 1860–1862.
- [116] Pawlik, B., Schirrmann, C., Bornhorst, K., and Costache, F., “Strain-enhanced Nanocomposites of Electrostrictive Polymers and High-k Nanofillers for Micro-actuation Applications,” *Procedia Engineering*, Vol. 87, No. 0, 2014, pp. 1601 – 1604, EUROSENSORS 2014, the 28th European Conference on Solid-State Transducers.
- [117] James, N. K., Van den Ende, D., Lafont, U., van der Zwaag, S., and Groen, W. A., “Piezoelectric and mechanical properties of structured PZTepoxy composites,” *Journal of Materials Research*, Vol. 28, 2013, pp. 635–641.
- [118] Kanda, M., *High strain electrostrictive polymers : elaboration methods and modeling*, Ph.D. thesis, School of Doctorate: Electronic, Electrotechnic and Automatic, 2011.
- [119] Nelson, L. J., Bowen, C. R., Stevens, R., Cain, M., and M., S., “High field behaviour of piezoelectric fibre composites,” *Proc. SPIE - Int. Soc. Opt. Eng.*, 2003, pp. 544–555.
- [120] Morgan Electro-ceramics, “PZT500 Series, Piezoelectric Ceramics, Morgan Electro Ceramic,” 2015, [Online; accessed 5-August-2015].
- [121] Eury, S., Yimnirun, R., Sundar, V., Moses, P. J., Jang, S.-J., and Newnham, R. E., “Converse electrostriction in polymers and composites,” *Materials Chemistry and Physics*, Vol. 61, No. 1, 1999, pp. 18 – 23.
- [122] Kwok, K. W., Lau, S. T., Wong, C. K., and Shin, F. G., “Effect of electrical conductivity on poling of ferroelectric composites,” *Journal of Physics D: Applied Physics*, Vol. 40, No. 21, 2007, pp. 6818–6823.

- [123] Lau, S., "A poling study of lead zirconate titanate/polyurethane 03 composites.pdf," 2007.
- [124] Bravina, S., Morozovsky, N., Kulek, J., and Hilczer, B., "Pyroelectric Thermowave Probing and Polarization Reversal in TGS/PEO Composites," *Molecular Crystals and Liquid Crystals*, Vol. 497, No. 1, 2008, pp. 109/[441]–120/[452].
- [125] Chandra, A., Chandra, A., and Thakur, K., "Synthesis, characterization and ion transport properties of hot-pressed solid polymer electrolytes PEO-KI," *Chinese Journal of Polymer Science*, Vol. 31, No. 2, 2013, pp. 302–308.
- [126] Andreev, Y. G., Seneviratne, V., Khan, M., Henderson, W. A., Frech, R. E., and Bruce, P. G., "Crystal Structures of Poly(Ethylene Oxide)₃:LiBF₄ and (Diglyme)_n:LiBF₄ (n = 1,2)," *Chemistry of Materials*, Vol. 17, No. 4, 2005, pp. 767–772.
- [127] Stoeva, Z., Martin-Litas, I., Staunton, E., Andreev, Y. G., and Bruce, P. G., "Ionic Conductivity in the Crystalline Polymer Electrolytes PEO₆:LiXF₆," *Journal of the American Chemical Society*, Vol. 125, No. 15, 2003, pp. 4619–4626.
- [128] Hatano, J., Takeuchi, H., Harazaki, M., and Watanabe, T., "Compensation for Ferroelectric Hysteresis Loop Distortion and Its Application to Phase Transition Studies," *Japanese Journal of Applied Physics*, Vol. 31, No. 9S, 1992, pp. 3235.
- [129] Lubomirsky, I. and Staffsudd, O., "Invited Review Article: Practical guide for pyroelectric measurements," *Review of Scientific Instruments*, Vol. 83, No. 5, 2012, pp. 051101.
- [130] Chynoweth, A. G., "Dynamic Method for Measuring the Pyroelectric Effect with Special Reference to Barium Titanate," *Journal of Applied Physics*, Vol. 27, No. 1, 1956, pp. 78–84.
- [131] Garn, L. E. and Sharp, E. J., "Use of low-frequency sinusoidal temperature waves to separate pyroelectric currents from nonpyroelectric currents. Part I. Theory," *Journal of Applied Physics*, Vol. 53, No. 12, 1982, pp. 8974–8979.
- [132] Sharp, E. J. and Garn, L. E., "Use of low-frequency sinusoidal temperature waves to separate pyroelectric currents from nonpyroelectric currents. Part II. Experiment," *Journal of Applied Physics*, Vol. 53, No. 12, 1982, pp. 8980–8987.
- [133] Dias, C. and Das-Gupta, D., "Measurement of the pyroelectric coefficient in composites using a temperature-modulated excitation," *Electronic Engineering*, Vol. 106, 1993.
- [134] Lam, K. S., Wong, Y. W., Tai, L. S., Poon, Y. M., and Shin, F. G., "Dielectric and pyroelectric properties of lead zirconate titanate/polyurethane composites," *Journal of Applied Physics*, Vol. 96, No. 7, 2004, pp. 3896–3899.

- [135] Kang, S. J., Samoilov, V., and Yoon, Y. S., "Low-frequency response of pyroelectric sensors," *Ultrasonics, Ferroelectrics, and Frequency Control, IEEE Transactions on*, Vol. 45, No. 5, Sept 1998, pp. 1255–1260.
- [136] Movchikova, A., Tech. rep., Infratec, Dresden, Germany, 2013.
- [137] Byer, R. and Roundy, C., "Pyroelectric Coefficient Direct Measurement Technique and Application to a Nsec Response Time Detector," *Sonics and Ultrasonics, IEEE Transactions on*, Vol. 19, No. 2, april 1972, pp. 333 –338.
- [138] Binks, A. E. and Sharples, A., "Electrical conduction in olefin oxide polymers," *Journal of Polymer Science Part A-2: Polymer Physics*, Vol. 6, No. 2, 1968, pp. 407–420.
- [139] Bailey, F. E. and Koleske, J. V., *Poly (Ethylene Oxide)*, Academic Press, 1976.
- [140] Wei, N., Zhang, D., Yang, F., Han, X.-y., Zhong, Z.-c., and Zheng, K.-y., "Effect of electrical conductivity on the polarization behaviour and pyroelectric, piezoelectric property prediction of 03 ferroelectric composites," *Journal of Physics D: Applied Physics*, Vol. 40, No. 9, May 2007, pp. 2716–2722.
- [141] Martin Straat, Igor Chmutin, A. B., "Dielectric Properties of Polyethylene Foams at Medium and High Frequencies," *Annual Transactions of the Rheology Society*, Vol. 18, 2010, pp. 1–10.
- [142] Lee, H. J., Zhang, S., Bar-Cohen, Y., and Sherrit, S., "High temperature, high power piezoelectric composite transducers," *Sensors (Switzerland)*, Vol. 14, No. 8, 2014, pp. 14526–14552.
- [143] Park, C., Su, P. O., Su, J., Smith, J. G., Jr., and Harrison, J. S., "Polarization Stability Of Amorphous Piezoelectric Polyimides," 1999.
- [144] "Special Issue on Transducers Materials for high temperature acoustic and vibration sensors: A review," *Applied Acoustics*, Vol. 41, No. 4, 1994, pp. 299 – 324.
- [145] Kremer, Friedrich, S. A., editor, *Broadband Dielectric Spectroscopy*, Springer, 2004.
- [146] Aboudi, J., *Mechanics of composite materials: A Unified Micromechanical Approach*, Elsevier Science Publishers B.V., 1991.
- [147] Benveniste, Y., "A new approach to the application of Mori-Tanaka theory in composite materials," *Mechanics of Materials*, Vol. 6, 1987, pp. 147–154.
- [148] Dunn, M. and Taya, M., "An analysis of piezoelectric composite materials containing ellipsoidal inhomogeneities," *Proc. R. Soc.*, Vol. 443, 1993, pp. 265–287.
- [149] Barnett, D. M. and Lothe, J., "Dislocations and line charges in anisotropic piezoelectric insulators," *physica status solidi (b)*, Vol. 67, No. 1, 1975, pp. 105–111.

- [150] Fakri, N., Azrar, L., and Bakkali, L. E., "Electroelastic behavior modeling of piezoelectric composite materials containing spatially oriented reinforcements," *International Journal of Solids and Structures*, Vol. 40, No. 2, 2003, pp. 361 – 384.
- [151] Odegard, G., "Constitutive modeling of piezoelectric polymer composites," *Acta Materialia*, Vol. 52, No. 18, 2004, pp. 5315 – 5330.
- [152] Van den Ende, D., Bory, B., Groen, W., and Van Der Zwaag, S., "Improving the d33 and g33 properties of 0-3 piezoelectric composites by dielectrophoresis," *Journal of Applied Physics*, Vol. 107, No. 2, 2010.
- [153] Van den Ende, D. A., van Kempen, S. E., Wu, X., Groen, W. A., Randall, C. A., and van der Zwaag, S., "Dielectrophoretically structured piezoelectric composites with high aspect ratio piezoelectric particles inclusions," *Journal of Applied Physics*, Vol. 111, No. 12, 2012.
- [154] Feenstra, J. and Sodano, H. A., "Enhanced active piezoelectric 0-3 nanocomposites fabricated through electrospun nanowires," *Journal of Applied Physics*, Vol. 103, No. 12, 2008.
- [155] Gutiérrez, M., Khanbareh, H., and van der Zwaag, S., "Computational modeling of structure formation during dielectrophoresis in particulate composites," *Computational Materials Science*, Vol. 112, Part A, 2016, pp. 139 – 146.
- [156] Schjødt-Thomsen, J. and Pyrz, R., "The Mori-Tanaka stiffness tensor: Diagonal symmetry, complex fibre orientations and non-dilute volume fractions," *Mechanics of Materials*, Vol. 33, No. 10, 2001, pp. 531–544.
- [157] Damjanovic, D., Demartin, M., Shulman, H., Testorf, M., and Setter, N., "Instabilities in the piezoelectric properties of ferroelectric ceramics," *Sensors and Actuators A: Physical*, Vol. 53, No. 13, 1996, pp. 353 – 360, Proceedings of The 8th International Conference on Solid-State Sensors and Actuators.
- [158] Roelofs, A., Schneller, T., Szot, K., and Waser, R., "Piezoresponse force microscopy of lead titanate nanograins possibly reaching the limit of ferroelectricity," *Applied Physics Letters*, Vol. 81, No. 27, 2002, pp. 5231–5233.
- [159] Kamel, T. M. and de With, G., "Grain size effect on the poling of soft Pb(Zr,Ti)O₃ ferroelectric ceramics," *Journal of the European Ceramic Society*, Vol. 28, No. 4, 2008, pp. 851 – 861.
- [160] Randall, C. A., Kim, N., Kucera, J. ., Cao, W., and Shrout, T. R., "Intrinsic and extrinsic size effects in fine-grained morphotropic-phase-boundary lead zirconate titanate ceramics," *Journal of the American Ceramic Society*, Vol. 81, No. 3, 1998, pp. 677–688.

- [161] Gent, A. N. and Lindley, P. B., "Internal Rupture of Bonded Rubber Cylinders in Tension," *Proceedings of the Royal Society of London A: Mathematical, Physical and Engineering Sciences*, Vol. 249, No. 1257, 1959, pp. 195–205.
- [162] Tan, P. and Tong, L., "Micro-electromechanics models for piezoelectric-fiber-reinforced composite materials," *Composites Science and Technology*, Vol. 61, No. 5, 2001, pp. 759 – 769.
- [163] Fu, S.-Y., Feng, X.-Q., Lauke, B., and Mai, Y.-W., "Effects of particle size, particle/matrix interface adhesion and particle loading on mechanical properties of particulate–polymer composites," *Composites Part B: Engineering*, Vol. 39, No. 6, 2008, pp. 933–961.
- [164] Park, C. and Robertson, R. E., "Aligned microstructure of some particulate polymer composites obtained with an electric field," *Journal of Materials Science*, Vol. 33, No. 14, 1998, pp. 3541–3553.
- [165] Winter, W. T. and Welland, M. E., "Dielectrophoresis of non-spherical particles," *Journal of Physics D: Applied Physics*, Vol. 42, No. 4, 2009, pp. 045501.

Effect of topological imperfections on the electromechanical properties of structured particulate composites

A.1 Introduction

Production of 1-3 composites is a complex process which often results in composites with a significant amount of microstructural imperfections, making it hard to predict their effective electromechanical properties using existing analytical models [11, 31, 146]. As the current models do not incorporate microstructural imperfections they generally overestimate the effective electromechanical properties. Better predictions may be obtained by using numerical schemes, such as the self-consistent and generalized self-consistent schemes or finite element modeling [146], but these are time consuming and computationally expensive due to the large amount of iterations involved. In this chapter a novel computational method is proposed to predict the electromechanical properties of structured piezo-polymer composite materials with improved accuracy, taking into account several (quantified) topological imperfections in the arrangement of the piezo electric particles. The method is essentially based on the established Mori-Tanaka model (MT) reformulated by Benveniste [147] and adopted by Dunn and Taya [148] who expanded the Eshelby tensor to incorporate piezo-electric behavior. The Mori-Tanaka theory considers a single inclusion in an infinite matrix aligned in a specified direction and has been proven to be an accurate and effective model for the homogenization of particulate composites. For this study a numerical approximation for the Eshelby tensor is used which has been extensively described and validated in a FEM analysis by Andrews et al. [102].

A.2 Theory

A.2.1 Piezoelectric constitutive equations

The constitutive equations for a linearly piezoelectric material are defined as:

$$\sigma_{ij} = C_{ijmn} \epsilon_{mn} - e_{nij} E_n \quad (\text{A.1})$$

$$D_i = e_{imn} \epsilon_{mn} + k_{in} E_n \quad (\text{A.2})$$

where σ_{ij} , C_{ijmn} , ϵ_{mn} , e_{nij} , E_n , D_i and k_{in} are defined as the stress, the elastic moduli (for a constant electric field), the elastic strain, the piezoelectric stress moduli (for a constant strain or constant electric field), the electric field, the electric displacement and the dielectric moduli (for constant strain), respectively. The piezoelectric stress coefficient can be related to the elastic and piezoelectric strain coefficient, d_{mn} , using the following equation:

$$e_{nij} = C_{ijmn} d_{mn} \quad (\text{A.3})$$

In this case, e_{nij} can be reduced to e_{ij} because of the symmetry present in the piezoelectric material. The independent variables, the strain and the electric field, can be expressed with the following equations:

$$\epsilon_{mn} = \frac{1}{2} (u_{m,n} + u_{n,m}) \quad (\text{A.4})$$

$$E_n = -\phi_{,n} \quad (\text{A.5})$$

where u_i is the elastic displacement and ϕ is the electric potential. In the absence of body forces elastic equilibrium applies. With free charge Gauss' law of electrostatics is applicable as well, which yields the following relations:

$$\sigma_{ij,j} = 0 \quad (\text{A.6})$$

$$D_{i,i} = 0 \quad (\text{A.7})$$

Equations 1-7 define the static theory of piezoelectricity. In the modeling of piezoelectric materials it is considered more convenient to rewrite the equations such that the elastic and electric variables are combined. This notation was proposed by Barnett and Lothe [149] and is identical to conventional (Einstein) indicial notation with the exception that lower case subscripts range from 1-3 and capitalized subscripts range from 1-4, with repeated

capitalized subscripts summed over 1-4. The stress and electric displacement, Σ_{iJ} , can be presented as:

$$\Sigma_{iJ} = \begin{cases} \sigma_{ij}, & J = 1, 2, 3 \\ D_i, & J = 4 \end{cases} \quad (\text{A.8})$$

The combination of the elastic strain and electric field, Z_{Mn} , can be expressed as:

$$Z_{Mn} = \begin{cases} \epsilon_{mn}, & M = 1, 2, 3 \\ E_n, & M = 4 \end{cases} \quad (\text{A.9})$$

The electro-elastic moduli, E_{iJMn} , can be written as:

$$E_{iJMn} = \begin{cases} C_{ijmn}, & J, M = 1, 2, 3 \\ e_{nij}, & J = 1, 2, 3, M = 4 \\ e_{imn}, & J = 4, M = 1, 2, 3 \\ \kappa_{in}, & J, M = 4 \end{cases} \quad (\text{A.10})$$

The above expressions yield the following equation that fully describes the constitutive equations as:

$$\Sigma_{iJ} = E_{iJMn} Z_{Mn} \quad (\text{A.11})$$

An essential footnote to Eq. 11 is that the entries are not conventional tensors and expression of these equations in different coordinate systems requires separate transformation of each individual tensor. The factors themselves are represented by the following tensors:

$$\Sigma_{iJ}^t = [\sigma_{11} \quad \sigma_{22} \quad \sigma_{33} \quad \sigma_{23} \quad \sigma_{13} \quad \sigma_{12} \mid D_1 \quad D_2 \quad D_3] \quad (\text{A.12})$$

$$Z_{Mn}^t = [\epsilon_{11} \quad \epsilon_{22} \quad \epsilon_{33} \quad \gamma_{23} \quad \gamma_{13} \quad \gamma_{12} \mid E_1 \quad E_2 \quad E_3] \quad (\text{A.13})$$

$$E_{iJMn} = \begin{bmatrix} C_{ijmn} & e_{nij}^t \\ e_{imn} & -\kappa_{in} \end{bmatrix} \quad (\text{A.14})$$

where C_{ijmn} , e_{nij} , and κ_{in} are the elastic stiffness matrix, the piezoelectric stress constant matrix and the permittivity matrix, respectively. Fully written, the constitutive matrix equation

is defined as:

$$\begin{bmatrix} \sigma_{11} \\ \sigma_{22} \\ \sigma_{33} \\ \sigma_{23} \\ \sigma_{13} \\ \sigma_{12} \\ D_1 \\ D_2 \\ D_3 \end{bmatrix} = \begin{bmatrix} C_{11} & C_{12} & C_{13} & 0 & 0 & 0 & 0 & 0 & e_{31} \\ C_{12} & C_{22} & C_{23} & 0 & 0 & 0 & 0 & 0 & e_{32} \\ C_{13} & C_{23} & C_{33} & 0 & 0 & 0 & 0 & 0 & e_{33} \\ 0 & 0 & 0 & C_{44} & 0 & 0 & 0 & e_{15} & 0 \\ 0 & 0 & 0 & 0 & C_{55} & 0 & e_{15} & 0 & 0 \\ 0 & 0 & 0 & 0 & 0 & C_{66} & 0 & 0 & 0 \\ 0 & 0 & 0 & 0 & e_{15} & 0 & -\kappa_1 & 0 & 0 \\ 0 & 0 & 0 & e_{15} & 0 & 0 & 0 & -\kappa_2 & 0 \\ e_{31} & e_{32} & e_{33} & 0 & 0 & 0 & 0 & 0 & -\kappa_3 \end{bmatrix} \begin{bmatrix} \varepsilon_{11} \\ \varepsilon_{22} \\ \varepsilon_{33} \\ \gamma_{23} \\ \gamma_{13} \\ \gamma_{12} \\ E_1 \\ E_2 \\ E_3 \end{bmatrix} \quad (\text{A.15})$$

The full constitutive matrix is orthotropic and the contracted Voigt notation is used. In this case the 3-axis of the particles is the principle direction of polarization. It should be noted that for the matrix to be reduced to the form shown in Eq. 15, it is assumed that the piezoelectric material is tetragonal and has symmetry 4mm, known as di-tetragonal pyramidal. Key parameters such as the piezoelectric charge coefficients, d_{mn} , the piezoelectric voltage coefficients, g_{mn} , and the energy efficiency, Q_{mn} , can be obtained using:

$$d_{mn} = e_{nij} C_{ijmn}^{-1} \quad (\text{A.16})$$

$$g_{mn} = \frac{d_{mn}}{\kappa_{mn}} \quad (\text{A.17})$$

$$Q_{mn} = d_{mn} g_{mn} \quad (\text{A.18})$$

These parameters are also referred to as performance parameters since they can be used to characterize a piezoelectric (composite) material and provide useful information on the material's capabilities. Another important parameter for piezoelectric materials is the piezoelectric coupling coefficient, k_{ij} , which can be extracted from the electro-elastic matrix using:

$$k_{ij} = \frac{d_{ij} \sqrt{C_{ij}^E}}{\sqrt{\varepsilon_{ii}^T}} \quad (\text{A.19})$$

A.2.2 Homogenization of 0-3 composites

To approximate the full set of electro-elastic properties of a 0-3 composite with significant accuracy, the Mori-Tanaka method (MT) can be applied to homogenize the effective properties. It is assumed that the particles are aligned in the poling direction and that the

inter-particle distance is large. By itself, the MT method cannot be used for piezoelectric composites, which was addressed by Dunn and Taya [148] who derived the following relation for the effective electro-elastic modulus, E_c , of a particulate electroactive composite.

$$E_c = E_1 + \sum_{r=2}^N c_r (E_r - E_1) A_r \quad (\text{A.20})$$

where E_r , c_r , N and A_r are the electro-elastic moduli of the r^{th} phase, the volume fraction of the r^{th} phase, the total number of phases (including the matrix material) and the concentration tensor for the r^{th} phase, respectively. The first phase is the matrix phase and it is denoted with subscript 1. Of all available methods that have relatively short computation times, the MT method has proven to give the most accurate results [102, 149–151]. The MT method uses a concentration tensor which is represented by:

$$A_r = A_r^{dil} \left[c_1 I + \sum_{r=2}^N c_r A_r^{dil} \right]^{-1} \quad (\text{A.21})$$

A_r^{dil} is the dilute concentration tensor which is expressed as:

$$A_r^{dil} = \left[I + S_r E_1^{-1} (E_r - E_1) \right]^{-1} \quad (\text{A.22})$$

where S_r is the Eshelby or constraint tensor for the r^{th} phase. The Eshelby tensor is a function of the geometry of the ellipsoidal particle or inclusion with semi-axes a , b and c , and the electro-elastic properties, E_1 , of the matrix phase.

$$S_r = f(E_1, a^r, b^r, c^r) \quad (\text{A.23})$$

For an ellipsoidal inclusion the following relations define three distinct particle shapes:

$$\text{Spherical particle} \quad a^r = b^r = c^r \quad (\text{A.24})$$

$$\text{Long cylinders} \quad a^r = b^r < c^r \quad (1 < c^r < 100) \quad (\text{A.25})$$

$$\text{Continuous fibre} \quad a^r = b^r, c^r \rightarrow \infty \quad (\text{A.26})$$

A numerical approximation of the constraint and Eshelby tensors is provided by Andrews et al. [102].

To approximate the effective properties of composites with randomly oriented particles the MT method can be applied in combination with the rule of mixtures. The first step is to calculate the effective electro-elastic properties for composites with aligned slender cylindrical particles, oriented in discretized Euler rotations, which replicate all possible directions. It should be noted that the poling axis remains in the 3-direction for all these composites. The

previously discussed Eshelby tensor can be rotated with tensor transformation laws which allows the generation of electro-elastic properties for composites with slender cylindrical particles with different orientations. Because the electro-elastic Eshelby tensor is an extension of the Voigt notation and essentially not a true tensor the transformation laws cannot be applied directly. Therefore, the transformation laws should first be applied to the separate parts of the tensor before it is recompiled in the Voigt extension. The modeling of 0-3 composites with randomly oriented particles using the rule of mixtures is elaborated in more detail by Andrews et al. [102].

A.2.3 Homogenization of 1-3 composites

In this section a new method is presented for the prediction of the effective properties of structured piezoelectric composite materials, also referred to as (quasi) 1-3 composites, with the piezoelectric charge constant d_{33} and the composite permittivity, κ , in particular since they can be used to determine the piezoelectric voltage coefficient, g_{33} , and the energy efficiency, Q using (Eq. 16). The theory behind the model will be elucidated and an experimental validation is performed to demonstrate the models capabilities. Columnisation of particles and its effect on the properties of the ceramic-polymer composite materials has been described by Bowen et al. [33] and Van den Ende et al. [11, 152, 153] who showed that columnisation can significantly improve the effective electro-elastic properties of PCMs in the poling direction. They proposed models for the prediction of the composite permittivity and the d_{33} , respectively. Bowen's model for the permittivity assumes perfectly stacked particles with a discrete inter-particle spacing in the poling direction, also referred to as axial particle misalignment. Van den Ende's model for the d_{33} and g_{33} expands on this by additionally taking angular misalignment of the cylindrical particles into account. These models give good preliminary prediction results for 1-3 composites with a limited amount of imperfections and act as the upper limit for the newly developed model in which additional topological imperfections will cause a further reduction of the composite's properties. Benveniste [147] concluded that the MT method already takes particle interaction into account up to a certain extent which implies that it can be used for homogenization of composites where particle interaction is present even though an infinite particle spacing is assumed initially. In the current approach the MT method with Eshelby tensors is used twice in succession to determine the properties of composites with columnised particles by redefining a column as a single virtual particle (VP) which is in essence a composite in its own right [152]. The particulate columns or chains have a high aspect ratio and the proposed method originates from the fact that for these high aspect ratios the values of the composite performance parameters as a function of the particle volume fraction converge towards a common limit [102]. The contour of the limit for high aspect ratios is traversed by varying the volume fraction of particles within the column. For construction of a VP it is assumed that the particles in the column are close to each other within a section that can be captured by a rectangle and that the formed chains or columns have an aspect ratio of at least 20, but preferably 100 and up because the numerical error is smaller for higher aspect ratios. To have the geometry of the VP comply with the MT method requirements an ellipse is fitted

over the rectangle which incidentally also reduces the very high particle volume fraction within the rectangle, increasing calculation accuracy. A schematic representation of a VP is shown in Fig. A.1.

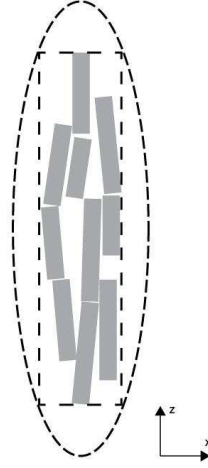


Figure A.1: Schematic representation of the virtual particle boundary for homogenization of columnised particles.

The effective composite properties depend on several non-linear functions, which are mainly influenced by the volume fraction and aspect ratio of the piezoceramic phase [102, 151–155]. In order to correct for the high VP volume fraction [150, 156] and incorporate columnisation and imperfections through manipulation of the volume fraction of the VP the novel Virtual Particle Mori-Tanaka (VPMT) method is proposed. The VPMT method is a derivative of a non-dilute MT method proposed by Schjødt-Thomsen and Pyrz [156] where an intermediate step with a comparison medium is used to account for high volume fraction deviations. For structured composites this comparison medium is defined as being a two-phase particulate piezoelectric composite with the same initial phases as the basic composite. The volume fraction, c_{VP} , of this composite can be adjusted to account for the high-volume fraction error and non-linear conversion effects when using the VP with the MT method in a similar way that Schjødt-Thomsen and Pyrz determine the non-dilute solution for the MT method. The method employs an intermediate value for the dilute concentration tensor, $A_{r,cm}^{dil}$, which captures the homogenized properties of a VP.

$$A_{r,cm}^{dil} = \left[I + S_p E_m^{-1} (E_p - E_m) \right]^{-1} \quad (\text{A.27})$$

where I is the identity tensor, S_p is the Eshelby or constraint tensor for the piezoelectric phase, E_m is the electro-elastic tensor of the matrix and E_p is the electro-elastic tensor of the piezoelectric material. $A_{r,cm}^{dil}$ is used in the MT method to calculate the comparison medium's electro-elastic tensor E_{cm} with c_{VP} . In the successive step, the dilute concentra-

tion tensor of the VP, $A_{r,VP}^{dil}$, is calculated with E_{cm} instead of E_m , forming:

$$A_{r,VP}^{dil} = [I + S_{VP} E_{cm}^{-1} (E_p - E_{cm})]^{-1} \quad (A.28)$$

where S_{VP} is the constraint tensor for the virtual particle. is used with a the VP's aspect ratio and a corrected composite volume fraction, c_{VPMT} , which is expressed as a function of the piezoelectric material's initial volume fraction in the VP, c_{VP}^0 , and its original volume fraction, c_p .

$$c_{VPMT} = \frac{c_p}{c_{VP}^0} \quad (A.29)$$

The volume fraction that is used in the second step of the VPMT method is larger than the original volume fraction because there is also matrix material included in the VP. This method distinguishes itself from the non-dilute MT method through the change of the particle geometry and volume fraction by means of a VP which accounts for the chain formation. The bounds for c_{VP} are $0 < c_{VP} \leq m_{VP}^0$. For $c_{VP} = c_{VP}^0 = 1$ the chains in the composite are uninterrupted and perfectly oriented and the results should coincide with the results of the MT method when the particle geometry is taken to be a continuous wire.

A.2.4 Experimental determination of c_{VP}

The value of c_{VP} can be determined experimentally by comparing test results of 0-3 and 1-3 composites and selecting a value for c_{VP} that captures the differences in performance. The accuracy of the prediction of the electro-elastic properties of the structured composite relies on an accurate determination of the properties of the 0-3 composite. To demonstrate the prediction capabilities of the newly proposed method is given by fitting the MT method to the experimental results of measured d_{33} and permittivity of 0-3 composite samples published [152]. Some of the material parameters that are used as input for the MT model may have to be adjusted slightly with respect to the nominal values because the properties of the composites' constituents change due processing of the material. Piezoceramics in particular experience significant changes in piezoelectric and dielectric properties when ground after sintering [157–160] which results in changes of the effective electromechanical properties of the composite in which they are embedded, different particle-matrix interaction [161–163], and different processing behavior [164, 165]. Because the piezoceramic powder is too small to conduct reliable property measurements and because the particle size and shape are not uniform the material properties were altered in such a way that the MT method prediction is accurate. Since the MT method is considered to be very reliable it is expected that the result in this case is similar to the result that would have been calculated had the right material properties been available. Fig. A.2 shows the experimental d_{33} and g_{33} results of 0-3 and 1-3 samples as a function of the volume fraction PZT granulate, as well as the fit prediction of the MT method and the calculated prediction of the newly proposed method for several values of c_{VP} .

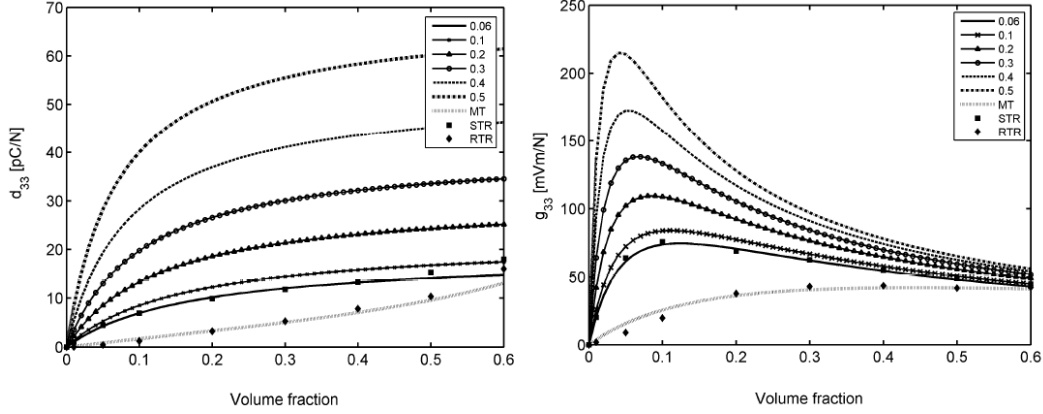


Figure A.2: Test results for measured d_{33} and g_{33} for structured and random with the predicted values of the VPMT method, indicated with a value for c_{VP} , the MT method, structured composite test results (STR), and random composite test results (RTR). Material parameters were based on PZT-5A and fully cured polyurethane resin (Crystal Clear 202). Material properties as defined in the ComSol material database.

It is shown that when the MT method is applied well, the newly proposed method can yield exceptionally well matching predictions for structured composites, here shown for $c_{VP} = 0.06$. The consistency of the analysis is demonstrated by the optimal c_{VP} fit value is the same for d_{33} and g_{33} . The fit value of c_{VP} of 0.06 is considerably lower than the value of $c_{VP} = 0.5$, which was approximately the initial volume fraction in the VP where $c_{VP}^0 = 0.55$. Clearly the actual spatial arrangement of the particles deviates significantly from an equi-spaced perfectly aligned arrangement. The c_{VP} as derived here can serve as a simple yet informative figure of merit to gauge the quality of real dielectrophoretically or otherwise structured PZT-polymer composites.

A.3 Theoretical predictions using imperfection parameters

While the c_{VP} parameter gives an attractive single parameter to cover the effects of all topological imperfections, it is desirable to analyze the effects of specific types of imperfections in more detail. Topological defects can be distinguished at a level of a single strand or chain of quasi-aligned particles and at the level of aggregated chains. These will now be analyzed separately.

A.3.1 Single chain imperfections

The three most commonly observed imperfections in isolated particulate chains are angular misalignment, axial misalignment and lateral misalignment. Single chain formation is most commonly found in composites with low volume fraction of the piezoceramic phase.

Angular misalignment

The misalignment of particles with respect to the direction of the applied electric field causes the effective properties of the composite in the field direction to be reduced. This is due to the fact that the particles are poled in the field direction. A misalignment of the particles will cause the effective particle length in the poling direction to be reduced, therefore the particle aspect ratio as experienced by the composite is smaller as well. The effects of the average orientation angle of chains of particles and the average orientation angle of particles within the chains have been described by Van den Ende et al., as seen in Fig. A.3 [152].

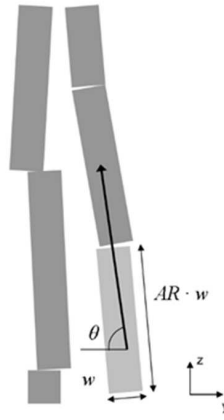


Figure A.3: Schematic of a cross section of aligned cylindrical particles including the particle dimensions, w , AR and average orientation angle, θ [152].

The effective AR of particles is expressed by Van den Ende et al. as:

$$AR_{eff} = 1 + \sin(\theta)(AR - 1) \quad (A.30)$$

The effective AR of chains is expressed in a similar way.

$$AR_{chain_eff} = 1 + \sin(\theta_{chain})(AR_{chain} - 1) \quad (A.31)$$

The effective aspect ratios can directly be used with the VPMT method, leading to a decrease in effective properties when misorientation is added, as is to be expected (Fig. A.4). In the figure it can be seen that the calculated results for the VPMT method are lower than those of the MT method. For structured composites as long as the misorientation angle is less than 100 the conventional MT model describes the properties adequately. For higher misorientation angles the MT method rather over-estimates the properties.

Axial misfit

The average axial misfit, l_{vs} , as shown in Fig. A.5, can directly be used with the VPMT method or alternatively be translated into an efficiency factor for c_{VP} which allows for cross-

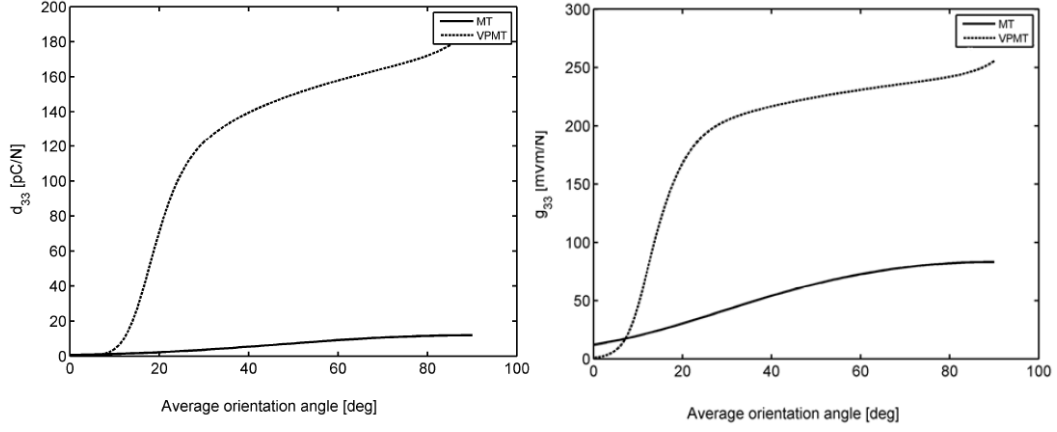


Figure A.4: Effects of particle misorientation on the d_{33} and κ for the VPMT method compared to the MT model for $AR = 5$, $c_p = 0.1$ and $c_{VP} = 0.55$

ing the AR-limit boundary by reducing c_{VP} to mimic the increase of the inter-particle spacing.

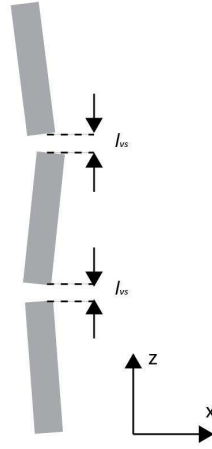


Figure A.5: Schematic representation of the vertical inter-particle spacing definition for the VPMT model.

A decrease of the volume fraction due to an increase in particle spacing will lead to exponentially decaying effective properties [102, 152, 153]. The axial misfit is averaged over the inter-particle spacing between vertically adjacent particles. The proposed function to describe this is:

$$\eta_{ips} = \cos(\tan(l_{vs})) \quad (\text{A.32})$$

In Fig. A.6 it is shown that multiplying c_{VP} by η_{ips} drives the effective properties towards those of the MT model, which is as expected since the MT model assumes an infinite spac-

ing between particles.

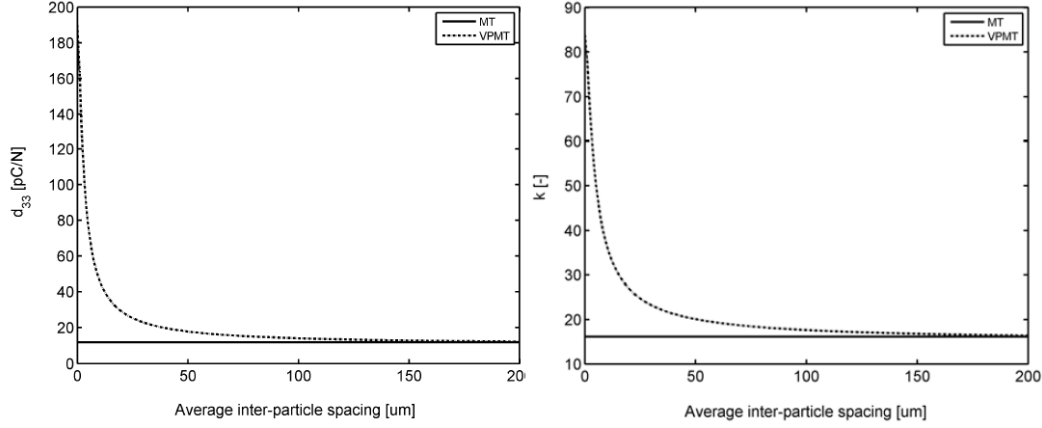


Figure A.6: Comparison of d_{33} and κ of the composite between the VPMT method and analytical models for varying vertical inter-particle spacing with $c_p = 0.1$, $AR = 5$, $c_{VP} = 0.55 \cdot \eta_{ips}$.

The simulations on the effect of axial misfit were made for $AR = 5$. Reducing the aspect ratio decreases the initial values of the VPMT and MT methods for zero spacing and the value for which the VPMT method attains the same value as the MT method and vice versa, which is also found in the literature [33, 102, 151–153].

Lateral misalignment

Another imperfection that can be defined is the average lateral misalignment, l_{lat} , between the ends of adjacent particles in a chain. This parameter will have a large effect in particular for particles with a small aspect ratio, the reason being that the force may not travel efficiently through the particle but can partly bypass it through the matrix. For large particles however, the influence will be less since the force can travel from one particle to another by means of shear and a higher matrix loading in the vicinity of the particle edges, causing a larger portion of the strain energy to travel through the particle instead of the adjacent matrix. The average lateral misalignment is defined as the average of lateral distances between the ends of adjacent particles within a chain (Fig. A.7). It is assumed that the adjacent particles are part of the same chain. To be part of a chain at least one end of a particle should have a lateral misalignment that is smaller than the particle width.

The average lateral misalignment is incorporated in the VPMT model by using it to define an efficiency factor that gauges how longitudinal stress is transferred between particles. For this case the stiffnesses of the composites constituents are deemed unimportant since the force through the thickness of the composite will have an affinity for the stiffest path and these effects are taken into account intrinsically by the MT method. It can be imagined that if the particles are perfectly stacked the load path will travel uninterrupted through the chain. If edge misalignment is introduced, it is logical that an increased amount of energy will be lost to the matrix in order to transfer the load from one particle to another. The amount

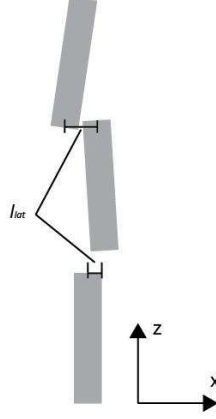


Figure A.7: Schematic representation of the lateral misalignment definition for the VPMT method.

of energy that is lost will be a function of the particle aspect ratio. The efficiency function describes the change in effective properties, such that its impact is low for high aspect ratios and vice versa. It also includes factors that describe the drop in the performance parameters due to increased lateral spacing and hindered stress propagation. The proposed expression that complies with these demands is:

$$\eta_{lat} = 1 - \left[\sin \left(\text{atan} \left(\frac{l_{lat}}{l_{vs} + d_{part}} \right) \right) \left(1 + \frac{l_{lat}}{d_{part}} \right) AR^{-1} \right] \quad (\text{A.33})$$

c_{VP} is multiplied with the efficiency factor to obtain a new c_{VP} value. Even though the actual behavior is highly non-linear the approximation was found to be relatively accurate for lateral spacings that are smaller than twice the particle thickness. Fig. A.8 and Fig. A.9 show the decay of the d_{33} and dielectric constant for different particle aspect ratios. As shown the effect of the lateral displacement is significant and more so for shorter fibers.

A.3.2 Aggregated chain imperfections

The imperfections that occur in single chains also occur in situations where the single chains in a structured composite have agglomerated into multi-chains or columns, a behavior that is found commonly for high volume fractions. Additionally such aggregated chains show two additional topological imperfections: particle overlap and the bridging of gaps by particles. Even though these imperfections may occur in single chains as well, for dielectrophoretically structured composites such forms of topological imperfections are unlikely given the physical force field causing the alignment of the particles.

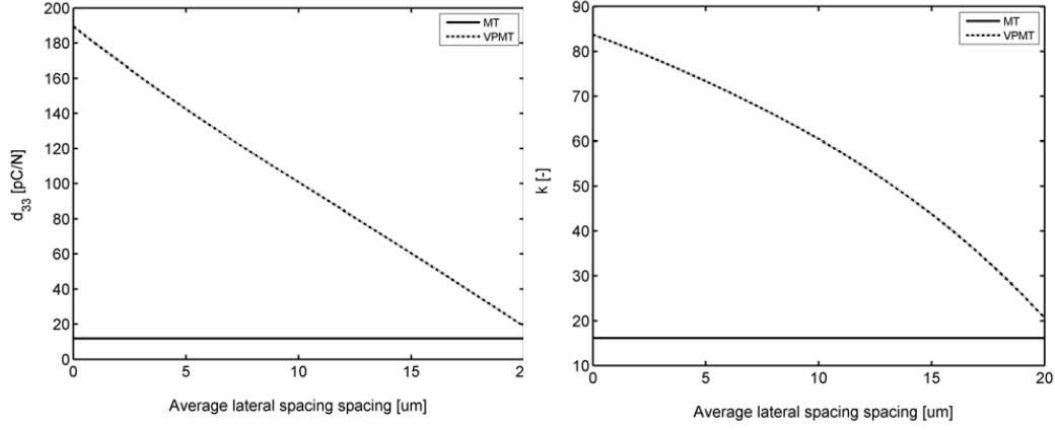


Figure A.8: Effects of lateral misalignment on the composite d_{33} and κ for a particle width of $5 \mu m$. $AR = 5$, $c_p = 0.1$, $c_{VP} = 0.55$.

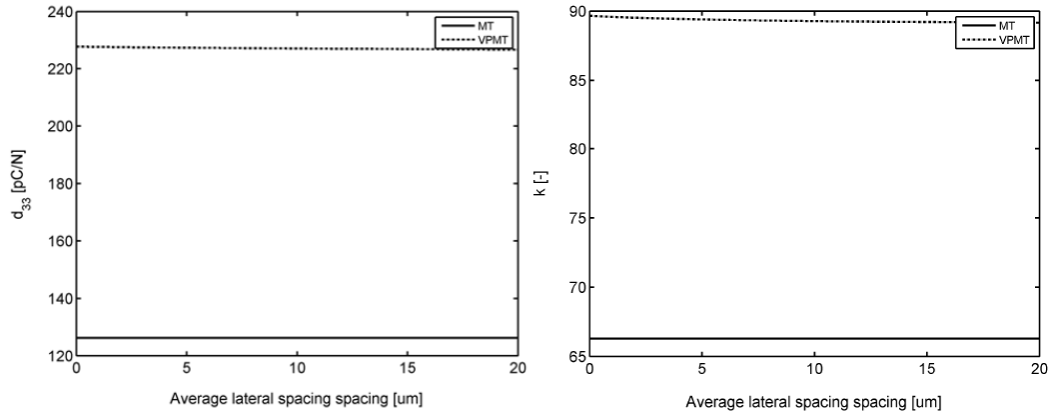


Figure A.9: Effects of lateral misalignment on the composite d_{33} and κ for a particle width of $5 \mu m$. $AR = 20$, $c_p = 0.1$, $c_{VP} = 0.55 * \eta_{lat}$.

Overlap

Particles that overlap cause the surrounding stress-field to be augmented and therefore the strain in each involved particle changes. Because the connection between the particles is through matrix material more energy will be absorbed by the matrix resulting in less strain in the particles and lower effective composite properties. The average overlap length, l_{ol} , is defined as the average fraction of the mean particle length that overlaps with any adjacent particles (Fig. A.10).

In addition to the average overlap length, the efficiency function for the overlap should contain a factor that describes the energy transfer as a function of the material stiffnesses. If the matrix material is considerably less stiff than the piezoelectric material, the piezoelectric material will attract a large portion of stress. However, if the materials have approximately the same stiffness the force will flow straight from the top of the composite to the bottom

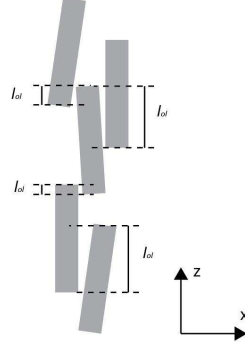


Figure A.10: Schematic representation of the particle overlap definition for the VPMT method.

without alterations in the load path and without being diverted to the piezoelectric particles. The force transfer between particles in a matrix with large differences in stiffness and dependency on particle shape and spacing is highly non-linear. In order to incorporate the energy loss in an efficiency function, the expected physical behavior should be broken down into comprehensible steps. Consider an uninterrupted (ideal) chain with locally a particle that has twice the thickness of other particles and a matrix material with negligible stiffness. In the thicker particle the strain will be half that of the rest of the chain. The total output of this section remains the same since the strain is halved, but the area is doubled. If the particle is split into two equal parts across its length and gradually moved away from the chain it can be imagined that the strain in the particle in the chain will increase and that the strain in the separated particle will decrease. Because the matrix deforms easily the force will be distributed equally over the parts of the split particle for zero lateral spacing and it will be only on the in-chain particle for a large lateral spacing. This is due to the matrix deforming freely causing the strain to be dissipated before it reaches the separated particle. Because the longitudinal strain in a piezoelectric particle is commonly small with respect to the particle's dimensions, it is expected that the force that is transferred to the separated particle diminishes quickly for increased lateral distance. When the matrix material is stiffer, it will absorb more energy upon deformation, but its ability to transfer force between laterally spaced particles becomes more prevalent. The energy that is lost through overlap is proposed to be captured with the following efficiency factor:

$$\eta_{ol} = 1 - \frac{l_{ol}}{1 + l_{olat}} \frac{Y_m}{Y_p} \quad (\text{A.34})$$

The three parameters that influence the overlap efficiency function show different kinds of behavior as shown in Figs. A.11 and A.12 and A.13. Contrary to other imperfection parameters the particle overlap does not converge toward the MT results since it is assumed that there still are columns present in the material. Since the proposed efficiency function does not converge towards the MT model, it is more difficult to fine tune the function and to assess if the impact has the right magnitude. It can however be concluded that the function

is very versatile and therefore it offers good prospects for fine tuning capabilities.

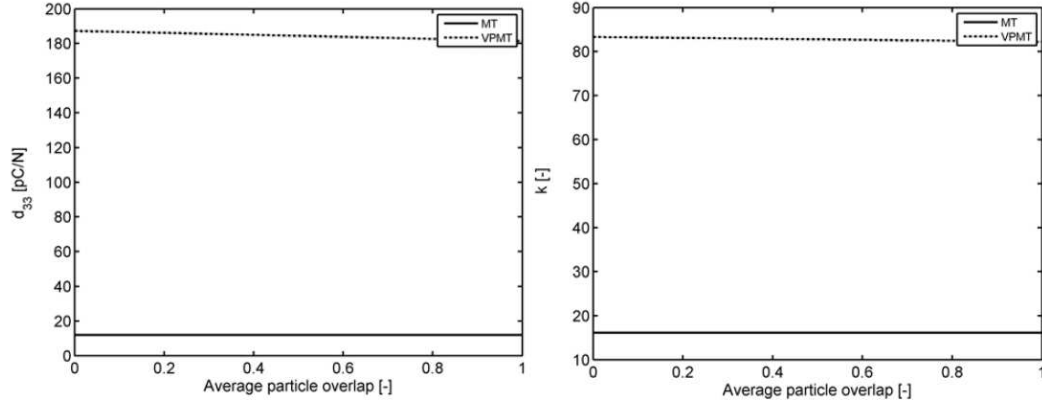


Figure A.11: Effect of particle overlap on the composite d_{33} and κ as a function of overlap length. $AR = 5$, $c_f = 0.1$, $c_{VP} = 0.55 * \eta_{rl}$, $Y_m/Y_p = 0.1$, $l_{olat} = 0.3 \mu m$.

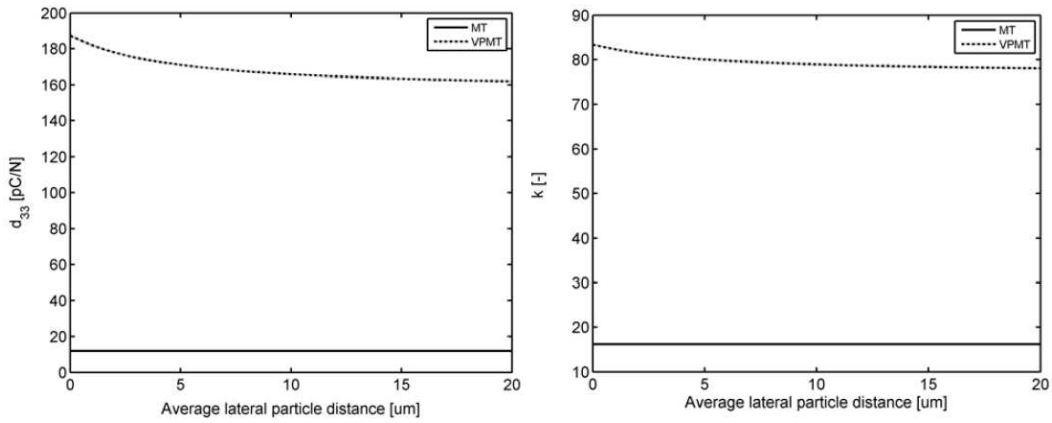


Figure A.12: Effect of particle overlap on the composite d_{33} and κ as a function of lateral distance. $AR = 5$, $c_p = 0.1$, $c_{VP} = 0.55 * \eta_{ol}$, $Y_m/Y_p = 0.1$, $l_{ol} = 0.3 \mu m$.

Gapbridging

The average gap-bridging length, l_b , is defined as the average fraction of the mean particle aspect ratio that is adjacent to a vertical gap between two stacked particles and overlapping both particles' ends (Fig. A.14).

The gap-bridging effect is a positive effect which increases the effective properties of the VP. The spacing between the bridged particles is considered to be axial misalignment. The gap-bridging function converges to its neutral point (which is 1) for a large lateral spacing and high matrix stiffness. The efficiency function for the gap-bridging parameter contains the average fraction of the mean particle length that is bridging a gap, l_b , the average lateral

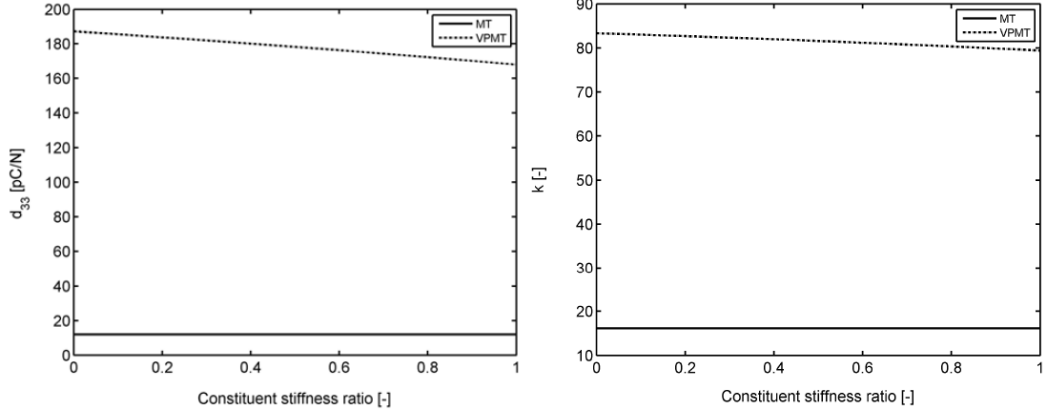


Figure A.13: Effect of particle overlap on the composite d_{33} and κ as a function of Y_m/Y_p ratio. $AR = 5$, $c_p = 0.1$, $c_{VP} = 0.55 * \eta_{ol}$, $l_{ul} = 0.3$, $l_{olat} = 0.3 \mu m$.

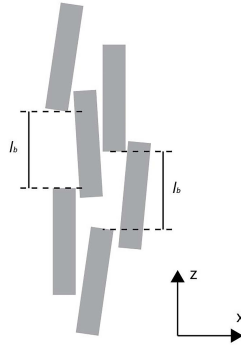


Figure A.14: Schematic representation of particle gap-bridging definition for the VPMT method.

distance of the particle from the gap, l_{olat} , the average number of bridges per particle, n_b , and the stiffnesses of the composites constituents, Y_m and Y_p , for reasons mentioned in the previous section on particle overlap. It is proposed to use an efficiency function similar to the function that was used for the particle overlap. The gap-bridging factor η_b that is proposed is:

$$\eta_b = 1 + \frac{l_{ol}}{1 + l_{olat}} \frac{Y_p}{Y_p + Y_m} l_b n_b \quad (A.35)$$

Since the formula is quite similar to that for particle overlap only the effects of the number of bridges per particle and the bridged length are shown in Fig. A.15 to illustrate that it is a beneficial function and that an optimum can be found for certain combinations of parameters in which the energy is distributed more efficiently over the piezoelectric phase. The impact of gap-bridging has not been researched thoroughly for particulate composites and as for the other imperfections more research is needed to check the validity of

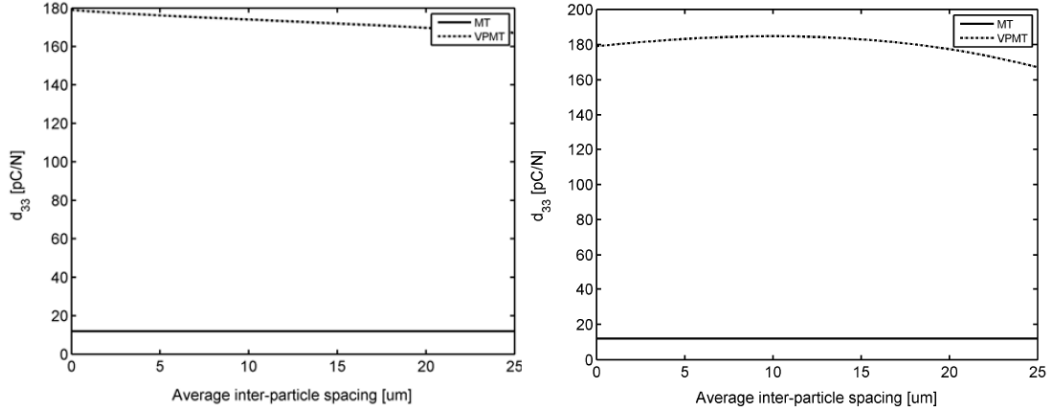


Figure A.15: Effects of gap-bridging on the composite d_{33} for varying average number of bridges per particle ($AR = 5$, $c_p = 0.1$, $c_{VP} = 0.55 * \eta_b$, $Y_m/Y_p = 0.1$, particle length = $25 \mu\text{m}$) $n = 0.3$ (left) and $n = 2$ (right).

the proposed efficiency function. It can however be stated that the trends are as desired. The gap-bridging efficiency function showed trends similar to that of the overlap function and therefore it has the same difficulties with assessment of the magnitude of the impact and fine tuning capabilities. However, the gap-bridging function is very versatile and offer good prospects for fine tuning when more insight is gained in the mechanics behind this imperfection.

Overall Imperfection parameter

The efficiency parameters defined in the previous sections are all multiplication factors to adjust the c_{VP} value and therefore they can be combined using the following equation for a correction factor that takes into account multiple topological imperfections.

$$\eta = \eta_{ips} * \eta_{lat} * \eta_{ol} * \eta_b \quad (\text{A.36})$$

The imperfection volume fraction, c_{imp} , is subsequently expressed as:

$$c_{imp} = c_{VP}^0 * \eta \quad (\text{A.37})$$

The imperfection volume fraction is used in the calculation as input for the VPMT model instead of c_{VP} and shows a lot of potential to obtain accurate property predictions. The range of η is theoretically $0 < \eta \leq 1$. For empirically optimized dielectrophoretically structured composites the imperfection factor is about 0.8 [147,152,153] showing that some significant improvement in properties can be obtained.

A.4 Conclusions

A new VPMT method for the prediction of the properties of particulate composites with imperfections was proposed. The model has the MT model as a lower bound and it coincides with the MT method for high aspect ratios, complying with the desired behavior which ranges between the dilute limit and the saturated limit. Efficiency functions were proposed for angular, axial, and lateral misalignment and particle overlap. Angular misalignment is taken into account in a very direct manner and it has the largest impact on the effective properties, yielding a 10 % decrease in performance parameters for an 8 degree misalignment angle. Axial misfit causes the performance of the composite to converge towards the results of the dilute MT model rapidly depending mainly on the particle aspect ratio. The other imperfection parameters' efficiency functions have a moderate influence but together they can reduce the effective composite properties by a further to 20 %. The only beneficial topological defect leading to an increase in properties over a perfectly structured composite is particle gap-bridging which shows an optimum value for which the strain energy is most efficiently distributed over the surrounding piezoelectric particles. However, the effects of gap-bridging are low compared to the influence of other, clearly detrimental, parameters. Taking realistic degrees of topological imperfections in quasi 1-3 composites it is predicted that the effective dielectric and piezoelectric properties of currently produced quasi 1-3 PZT polymer composites are 20-50 % of the values for perfectly aligned and spaced particulate composites.

Acknowledgments

This thesis is the result of four years of research at the group of Novel Aerospace Materials, in the Faculty of Aerospace Engineering of Delft University of Technology. This work would not have been possible without the supervision, assistance and support of many people to whom I would like to express my sincere gratitude.

Firstly, I would like to thank my promoters Prof. dr. ir. Sybrand van der Zwaag and Prof. dr. Pim Groen for providing me with the means to carry out this Ph.D. project at TU Delft. Their complimentary perspectives opened an entire spectrum of ideas and guidance in front of me. Thank you Sybrand, for giving me the opportunity and lots of freedom to fulfill this task. Thanks for your great ideas, always supporting, correcting and improving mine. I always appreciated that you made time late in the evening, on the plane or on the way back from your vacation to read my manuscripts with interest. I always enjoyed our unplanned early morning or late afternoon corridor discussions. Those were the best meetings, inspiring me throughout the six years of working with you. You were a great mentor and I really enjoyed working for you.

Pim, I especially owe thanks to you for your advice and guidance on the road to this Ph.D. Your academic and industrial experience in the field of inorganic materials and their applications has been of great value to me. You have taught me many things, always motivating and supporting. I would like to thank you particularly for your trust in me and also like to acknowledge that you created the opportunity for me to do an internship at Max Planck Institute for Polymer Research in Germany.

At Max Planck Institute, I had the opportunity to work with Prof. dr. Dago De Leeuw and Dr. Ilias Katsouras at the Department of Molecular Electronics, for the ferroelectric measurements of piezo-ceramics and composites. These exciting measurements provided us with deeper understanding of underlying mechanisms as well as creating new questions that still keep us busy. Dago, I have great appreciation for your enthusiasm and drive. Thanks for challenging me with your interesting questions and keeping me on my toes all the time. Ilias, your effort and guidance is much appreciated. Thanks for taking time to join me during the experiments and discuss my results even when many urgent tasks were at hand. Dr. Asadi, thanks for your guidance and inspiration to set up my own research career. I owe my fellowship to our few motivational talks.

I would like to acknowledge my former supervisor, Prof. dr. Reza Mahmudi from University of Tehran, who was the first person who taught me the alphabet of research at a very

young age during my B.Sc. studies.

At TU-Delft laboratories I am indebted to many people for their assistance. In particular I would like to thank Berthil Grashof, Misja Huizinga, Gertjan Mulder, Frans Oostrum and Lijing Xue for their kind help in the experimental work. I also highly appreciate the input from and discussions with Ben Schelen from DEMO-CEO, Faculty of Electrical Engineering, who helped me to develop the pyroelectric testing device (Kitty). Ben, you did a great job in design and construction of our set-up. Ed Roessen and Rob van der List, thank you for your help in design and preparation of sample holders and test setups.

I would like to thank my officemates, Ranjita and Wouter for making our office such an awesome place to work for four years. Thanks to my pre-Ph.D. officemates, Martino, Jasper and Daniella, who made my integration phase in the faculty during my M.Sc. time a great fun. Thanks to Michael, my neighbor during the most intensive time of thesis-writing, who shared wonderful travel experience/advice, helping me to go through this period with energy, and also assisted me with translations.

I would like to thank Kevin de Boom, who helped me in his graduation project, with the development of our tri-phase piezo-composites, that outperform all the other particulate composites so far. Kevin, working with you was a great pleasure. Your dedication, experimental skills, critical thinking and striving for excellence, as well as positive attitude gave ANTWAN the best possible character I could wish for, since I had the initial spark in mind. Your indefinite supply of caffeine helped me a lot in the last phase of the project.

Thanks to the members of smart materials team, Daan, Nijesh, Daniella, Jibrán, Stanley, Frederik, Kevin, Ryan, Amal, George and Neola. Nijesh, you kindly accommodated me in the lab, as an unofficial daily supervisor, in the beginning of my project, always ready to support, help, and discuss with a positive and friendly attitude. You are a great teacher, thanks. Daniella, our scientific discussions/arguments were one of the most enjoyable times I had in NovAM.

Throughout all of the six years in NovAM, I had the great fortune to surround myself with a group of bright, interesting and friendly people. I will miss you guys. Ugo, I appreciate your valuable assistance in the starting phase of my Ph.D., helping me with characterization techniques and interpretation of my experimental results. I would have not been able to successfully make a great network of specialists all over the university without you. Maruti, thank you for the help to synthesize the high performance composite sensors that turn out to be of very high scientific/industrial interest in our field. Miguel, we definitely were a great team working on computational modeling of structure formation, thanks. My special thanks to Shanta for her kind assistance.

I was also very fortunate to have a group of friends that made me enjoy all the other aspects of life, besides work. Many thanks to Casper and Anna for always being there for me. Charlotte, a huge thank you, for your care and support. I never forget your past-midnight cup of tea, and when you kindly accepted to fly all the way from Berlin to be my paranymph. Maaike, Manon and Michelle, my dear friends, our meet-ups, food-fests and sportive activities over the last few years are unforgettable. Romy and Janneke, you made me feel at home in the Netherlands. My volleyball teammates, Dames, ik wil jullie bedanken voor jullie energie en gezellige tijden, ze hebben een belangrijke rol gespeeld.

I would like to thank my Comma-man for spending days into proof reading the manuscript, making the book heavier but certainly very well readable. Special thanks to Ulla for her love and always-welcoming open arms.

Also, I need to thank Dr. Holakouee, who taught me the most important life lessons. Without him, I may never have gotten to where I am today.

Ali, thank you for supporting me all the time, since I started my studies in Delft, through up and down, encouraging on each and every step, helping and sharing ideas and solutions. I would have not made it here without you. Last but by no means least, I would like to express my deepest gratitude to my parents, my lovely brother, Mohamad-reza, and my sweet sister, Latifeh, for all their love and support in all my pursuits. Thanks baba, and maman, for all your unconditional care in the last 29 years, in every aspect of my life. You have been there day after day to make sure my life turns out this way. Mohamad-reza, special thanks for taking so much time and effort into designing such a fantastic thesis cover for me.

I would like to end by having you find my special acknowledgments and saying, I am looking so much forward to the next adventure.

S	M	O	K	L	I	J	I	N	G	L	Y	A	R	H	L	E	E	H	Z	A	M	N	N	J	S	W	Z	E	A
G	E	O	R	G	E	N	A	Z	I	G	L	E	A	S	L	P	R	G	O	J	S	D	R	A	B	Q	E	W	F
V	M	G	S	K	S	P	A	J	C	L	R	E	T	L	R	I	I	E	H	N	H	E	M	M	A	N	U	E	L
B	X	J	B	V	X	N	O	P	U	R	P	C	E	L	K	I	K	J	F	F	G	H	X	S	I	H	W	A	S
D	S	L	A	V	I	S	A	L	E	W	I	H	D	N	K	D	K	N	O	Q	B	L	Q	H	X	B	L	W	D
M	A	C	D	A	L	E	X	T	Y	R	C	A	U	A	U	A	M	A	I	L	Y	S	I	I	C	Y	F	O	F
U	L	N	T	H	E	O	S	J	M	I	L	R	A	Z	I	C	R	A	N	J	I	T	A	D	B	G	X	U	F
N	A	F	I	S	E	H	A	D	M	A	H	L	Y	D	U	D	D	Z	J	T	U	N	V	C	J	H	O	T	A
X	S	R	C	L	F	E	G	D	O	E	A	I	L	I	P	A	G	H	W	F	H	S	I	H	A	L	T	E	R
A	W	E	E	E	L	H	R	G	T	P	O	E	O	I	P	N	X	U	G	E	R	T	J	A	N	M	B	R	H
L	M	Y	V	L	W	E	A	T	Y	I	A	O	P	L	G	I	L	S	E	M	L	A	J	R	N	I	P	A	A
J	I	I	A	U	M	I	E	S	E	T	A	R	E	H	L	E	C	S	A	P	L	M	A	L	E	M	I	R	N
A	G	P	E	L	T	S	C	G	F	P	B	L	V	A	N	L	Z	E	D	O	Z	A	N	O	K	O	V	P	G
S	U	M	E	N	I	L	A	N	N	A	W	R	E	I	O	L	P	I	E	Y	O	R	T	T	E	S	B	A	H
O	E	J	A	L	H	L	H	M	N	E	N	K	O	O	Z	A	Y	N	L	R	V	Y	O	T	W	T	M	U	Z
N	L	S	U	X	N	U	E	T	G	M	J	R	L	M	N	J	T	M	A	R	I	A	N	E	L	A	E	L	S
G	Q	W	Y	G	R	Y	N	J	M	O	P	D	V	V	Y	O	A	N	F	M	A	M	I	J	Z	F	S	B	Q
N	W	Y	D	F	O	L	R	A	A	H	L	C	V	I	O	P	R	N	J	A	A	C	O	A	Y	A	A	F	U
A	C	E	T	R	E	A	I	S	R	A	B	A	O	J	W	E	D	A	K	I	T	R	X	V	E	N	R	A	E
O	C	H	H	A	D	T	E	P	T	M	B	S	M	Q	G	L	M	S	A	C	M	D	C	R	H	A	D	N	L
M	V	W	H	N	W	I	T	E	I	A	Z	P	V	H	H	D	I	C	U	B	W	M	D	I	T	T	I	P	R
I	U	C	U	S	T	F	T	R	N	D	P	E	P	F	O	J	J	Q	A	Z	O	N	Y	N	A	D	U	A	C
V	I	V	Q	A	K	E	E	G	O	R	N	R	D	Y	D	S	I	X	O	T	A	L	A	I	A	S	C	S	C
M	N	I	J	E	S	H	W	G	D	E	D	A	F	L	R	A	E	B	L	F	E	H	F	N	E	E	D	H	K
S	C	U	N	G	X	Z	J	L	C	Z	M	M	D	X	A	G	Z	I	R	E	S	L	T	A	R	O	F	I	S
M	I	N	S	E	W	Y	I	D	A	A	A	F	G	E	T	I	N	E	N	A	L	N	B	D	Z	M	L	R	A
M	A	M	J	O	H	N	A	L	A	N	A	P	E	T	R	A	D	X	L	F	N	O	N	E	A	L	I	I	R
M	A	N	O	N	K	E	V	I	N	I	I	O	A	R	I	J	A	N	A	J	K	A	T	C	Z	J	W	N	A
R	E	H	H	N	A	N	L	V	C	L	K	I	Q	L	A	G	H	A	Q	R	K	U	J	I	L	D	O	U	V
I	L	I	A	S	E	I	D	E	J	J	E	G	S	S	S	I	J	V	N	U	L	A	G	A	E	B	Q	J	F

حمیده خانبهره

Delft, May 2016

Curriculum Vitae

I started my studies in 2004, at the Materials Engineering Department of Tehran University, in Iran. After completing my graduation project, entitled "Investigation the creep behavior of lead-free Sn-9Zn and Sn-8Zn-3Bi solder alloys", I obtained my B.Sc. degree in 2008.

In February 2010, I joined the Novel Aerospace Materials (NovAM) group, at the Faculty of Aerospace Engineering, at TU Delft, to continue with my graduate studies. The research project I chose to work on was entitled "characterization of grain boundaries in the microstructure of Aluminum alloys by means of fractal dimensions". In December 2011, I received my M.Sc. degree, Cum Laude, and proceeded to do my Ph.D. in NovAM in the fascinating world of smart materials.

During the Ph.D. period, I spent two months at the the Department of Molecular Electronics, at Max Planck Institute for Polymer Research in Germany, taking part in research in the field of ferroelectric materials.

In February 2016 I was awarded with the Prize Fellowship at the Faculty of Engineering, University of Bath, which is given to early career researchers with the potential to become research leaders. In summer 2016 I will be starting my new career in Bath.

List of Publications

Journal Papers

1. Khanbareh, H., van der Zwaag, S., Groen, W. A., In-situ poling and structurization of particulate piezoelectric composites, (under review, Journal of Intelligent Material Systems and Structures, 2016)
2. Shaji, A., James, N. K., Khanbareh, H., van der Zwaag, S., Groen, W. A., Structure, dielectric, and piezoelectric properties of soft doped PZT ceramics across the phase diagram (under review, Journal of European Ceramic Society, 2016)
3. Gutiérrez, M.A., Khanbareh, H., van der Zwaag, S., Computational modelling of structure formation during dielectrophoresis in particulate composites, Computational Materials Science, Vol. 112, Part A, 1 pp. 139146, 2016.
4. Khanbareh, H., Schelen, B., van der Zwaag, S., Groen, W. A., A multi-mode temperature oscillation instrument based on discrete sampled data and mathematical lock-in method to determine pyroelectric properties of materials at low frequencies, Review of Scientific Instruments. 86, pp. 105111, 2015.
5. Khanbareh, H., van der Zwaag, S., Groen, W. A., Piezoelectric and pyroelectric properties of conductive lead titanate-Polyethylene oxide composites, Journal of Smart Materials and Structures, Vol. 24, No. 04, pp. 045020, 2015.
6. Khanbareh, H., van der Zwaag, S., Groen, W. A., Effect of dielectrophoretic structuring on piezoelectric and pyroelectric properties of lead titanate-epoxy composites, Journal of Smart Materials and Structures, No. 23, pp. 105030, 2014.
7. Chen, H., Gamsjäger, E., Schider, S., Khanbareh, H., van der Zwaag, S., In situ observation of austenite/ferrite interface migration in a lean Mn steel during cyclic partial phase transformations, Acta Materialia, Vol. 61, Issue 7, pp. 2414-2424, 2013.
8. Khanbareh, H., Wu, X., van der Zwaag, S., Analysis of the fractal dimension of grain boundaries of AA7050 Aluminum alloys and its relationship to fracture toughness, Journal of Materials Science, Vol. 47, pp. 6246-6253, 2012.
9. Mahmudi, R., Geranmayeh, A.R., Khanbareh, H. and Jahangiri, N., Indentation creep of Lead-free Sn-9Zn and Sn-8Zn-3Bi solder alloys, Materials and Design, Vol. 30, No. 3, pp. 574-580, 2009.

10. Mahmudi, R., Geranmayeh, A.R., Noori, H., Khanbareh, H. and Jahangiri, N., A comparison of impression, indentation and impression-relaxation creep of Lead-free Sn-9Zn and Sn-8Zn-3Bi solders at room temperature, *Journal of Materials Science: Materials in Electronics*, Vol. 20, No. 4, pp. 312-318, 2009.
11. Mahmudi, R., Geranmayeh, A.R., Noori, H., Jahangiri, N. and Khanbareh, H., Effect of cooling rate on the room-temperature impression. creep of Lead-free Sn-9Zn and Sn-8Zn-3Bi solders, *Materials Science and Engineering A*, Vol. 487, No. 1-2, pp. 20-25, 2008.
12. Mahmudi, R., Geranmayeh, A.R., Noori, H., Khanbareh, H. and Jahangiri, N. 2010, Effect of isothermal aging on room temperature impression creep of Lead free Sn-9Zn and Sn-8Zn-3Bi solders, *Materials Science and Technology*, Vol. 26, No. 8, pp. 1001-1007, 2008.

Selected Conference Papers

1. Khanbareh, H., Hegde, M., van der Zwaag, S., Groen, W. A., Advanced processing of lead titanate-polyimide composites for high temperature piezoelectric sensing, *IEEE International Symposium on Application of Ferroelectrics (ISAF)*, May 2015, Singapore.
2. Khanbareh, H., van der Zwaag, S., Groen, W. A., Enhancement of pyroelectric properties of particulate composites, *IEEE International Symposium on Application of Ferroelectrics, ISAF 2015*, May 2015, Singapore.
3. Khanbareh, H., van der Zwaag, S., Groen, W. A., Piezoelectric and pyroelectric properties of lead titanate-polyethylene oxide composites. *AIP proceedings of international conference electroceramics14*, June 2014, Romania.
4. Cervone, A., D.J. Kok B.J. Beckers M.R. Haneveer E.J. Hekma J.B. van Ingen D. Jimenez Lluva A. Krikken J.W. Lopes Barreto P. Mesgari L.Z.F. van Rossum H. Khanbareh T. Watts F. Matser H. Klinkenberg, *HIRES: Hollands Intelligence, Reconnaissance, and Earth Surveillance*, 10th IAA Symposium on Small Satellites for Earth Observation, April 2014, Germany.
5. Khanbareh, H., van der Zwaag, S., Groen, W. A., Dielectrophoretically structured piezoelectric composites, *Proceedings of 19th International Conference on Composite Materials*, pp. 4832-4839, July 2013, Canada.